SAE International™

SURFACE VEHICLE INFORMATION REPORT

SAE J2869 AUG2010

Issued 2010-08

Mechanical Systems Physics-of-Failure Analysis Experimental Validation

RATIONALE

Validate the computer simulation models of the trailer.

FOREWORD

This SAE Vehicle Information Report describes, through example, a process to evaluate and reduce the experimental test data needed for a Mechanical Systems Physics-of-Failure analysis. In addition, the report describes the process used to validate the computer simulation models.

TABLE OF CONTENTS

TO PLACE A DOCUMENT ORDER:
Tel: 877-606-7323 (inside USA and Canada)
Tel: +1 724-776-4970 (outside USA)
Fax: 724-776-0790
Email: CustomerService@sae.org
SAE WEB ADDRESS: http://www.sae.org

1. SCOPE

This report details continuing work examining the fatigue life durability of a US Army Trailer. This report describes, through example, a process to evaluate and reduce the experimental data needed for a Mechanical Systems Physics-of-Failure analysis. In addition the report describes the process used to validate the computer simulation models.

1.1 Purpose

Evaluate and reduce the experimental data obtained during testing of an instrumented trailer.

1.2 Project Results

The results of the project can be split into three areas; experimental data evaluation, dynamic model comparison, and fatigue life validation.

In the experimental data evaluation, it was hypothesized that the hydraulic surge brakes contributed to the fatigue-related failures of the trailer drawbar. Using principal component statistical analysis, it is shown that the surge brakes have little effect on the fatigue damage. Additionally, the principal component analysis reveals that the vertical accelerations and the yaw rate of the trailer were the primary contributors to the strain, which was measured close to the point of failure.

The multi-body dynamic simulation model was compared to measured accelerations and angular rates. The longitudinal and vertical accelerations were the best matches, using both Power Spectral Density (PSD) and statistical distribution comparisons. The worst comparison data was the transverse acceleration and yaw rate. Reasons for the poor matches for these signal components are both the tire model, which does not generate lateral forces based on terrain geometry, and the profilometry data used in the simulations, since it represents only the terrain elevation along the longitudinal path of the vehicle and not the spatial geometry of the terrain under the tire contact patch.

Finally, the fatigue life predictions were calculated using both rigid- and flexible-body simulations and experimental results. The fatigue life predictions show that using a CAE procedure for durability analysis is feasible provided that care is taken in the development of the CAD and dynamics models. The flexible body is necessary for obtaining accurate life predictions, however, using the flexible body simulation requires careful selection of the static correction mode shapes. High frequency modes should not be included since the trailer frame is a low frequency structure.

2. REFERENCES

1. Hurty, W.C. “Dynamic Analysis of Structural Systems Using Component Modes,” AIAA Journal, Vol. 3, No. 4, 1965.

2. Craig, R.R. and C.C. Bampton, “Coupling of Substructures for Dynamic Analysis,” AIAA Journal, Vol. 6, No. 7, 1968.

3. Meirovitch, L. Principles and Techniques of Vibrations, Prentice Hall, 1997.

4. DRAW Concept Manual, Center for Computer-Aided Design, The University of Iowa, 1999.

5. Murphy, N.R. Jr. “A Method for Determining Terrain Surface Roughness,” U.S. Army Engineer Waterways Experiment Station, Geotechnical Laboratory, Vicksburg, MS, September 1984.

3. BACKGROUND

The US Army trailer evaluated in this continuing study was instrumented and tested at Aberdeen Test Center (ATC) during the months of June and July, 2001. The objective of this test was to validate the Physics-of-Failure (PoF) simulation results, including the dynamic response and the critical point strain and fatigue life. Therefore, the comparison of the simulation results with the measured results (time domain data) from the Army Trailer is carried out to determine whether the process of simulation is acceptable, find factors that may affect the simulation results, determine whether the flexible body is required for this analysis, and examine the rivet hole sensitivities.

The PoF process used to identify the fatigue life of the trailer is shown in Figure 1. The process began with the development of a Computer Aided Design (CAD) model of the trailer using Pro/Engineer software. From the CAD model, both a rigid-body multi-body dynamic model and a finite element model were developed using DADS and NASTRAN, respectively. These models were validated in a previous report, using both physical measurements and modal (vibration) test results.

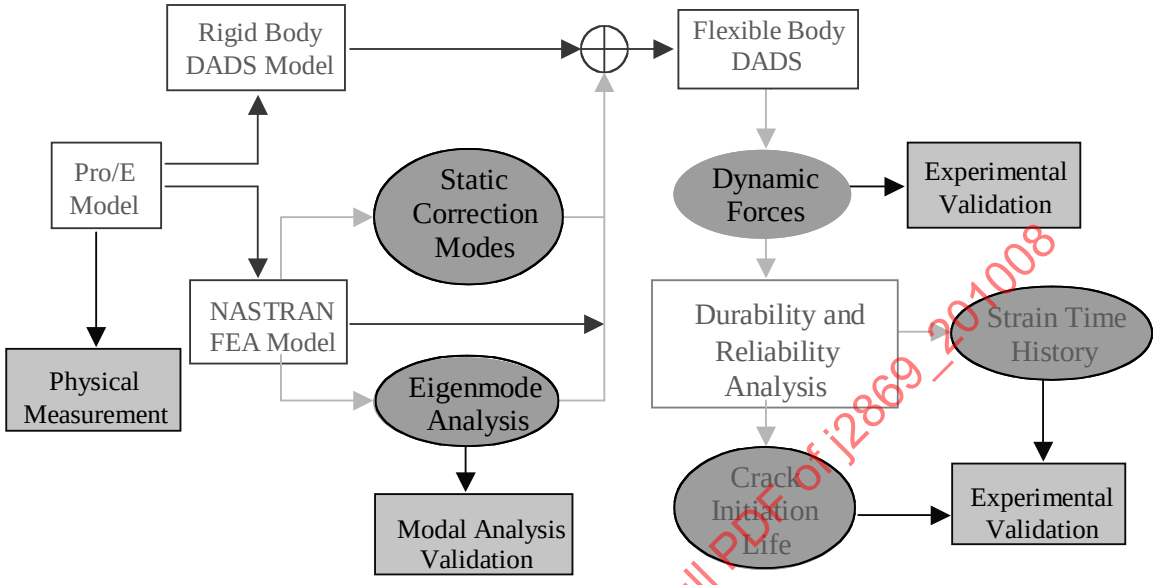

FIGURE 1 - PHYSICS OF FAILURE PROCESS

A flexible-body multi-body dynamic model of the trailer was developed using component-mode synthesis. In particular, the Craig-Bampton [1-3] mode set was analyzed using the NASTRAN FEA model, and then combined with the rigid-body dynamic model. In the simulation-based PoF process, the flexible-body dynamic model was used to generate load histories based on assumed operational usage and measured terrain profiles. The Durability and Reliability Analysis Workspace software (DRAW) [4], developed at the University of Iowa's Center for Computer-Aided Design, used the load histories to create a strain time history, and also to estimate the fatigue durability of the trailer. The fatigue durability criteria used was the formation of a 2 mm crack in any of the model's components. Neither the flexible-body dynamic model, nor the DRAW analysis of the trailer had been previously validated.

In order to verify the simulation results, critical point strain and fatigue life of the trailer, strain gauges were used in the testing. By using the strain gauge data and corresponding FE nodal strain simulation results, validation based on the strain can be performed. The measured strain can also be used as an input of the simulation to predict fatigue life based on experimental strain. The comparison between experimental and simulation-based fatigue life is also carried out.

3.1 Validation Methodology

It is generally acknowledged that mathematical models cannot perfectly simulate real system behavior. One of the reasons for this is that there are always uncertainties in the values of mathematical model parameters and experimental measurement results. Because of this, we require objective, well-found mathematical techniques for model validation. It is desirable to establish a technique for comparing mathematical model behavior to experimental uncertainty. In our validation, the surface roughness of the section of the test course is known to some level of fidelity, but not to the degree of accuracy required for a point-by-point comparison of the mathematical model data and measured data. Therefore, the validation will be done using statistical techniques rather than on a point-by-point basis.

It is important that the data "match" in both the time and frequency domains. In the time domain, histograms of the measured and modeled data should be statistically similar. The first four statistical moments; mean, variance (or standard deviation), skewness and kurtosis for each data channel will be calculated and compared. Additionally, the root mean square (RMS) will be calculated for the time domain data.

In the frequency domain, the PSD will be computed for model and measured data for all the data that are selected. The PSD curves, predicted by the model, will be compared with the measured PSD curves.

The spectral resolution and number of statistical degrees of freedom should be approximately the same for the modeled and measured cases.

3.2 Instrumentation and Transducers

The trailer was instrumented by ATC with a number of strain gauges, accelerometers, rate gyros, linear displacement transducers and pressure transducers. A total of 59 channels were sampled, in the order specified in Table 1. The original sample rate was 1262.626 Hz (7.92E-4 second period).

Analog low-pass anti-aliasing filters were used on every channel, however the cutoff frequency of the filters varied by the type of transducer being measured. Table 2 lists the filter cutoff frequencies and transducer types.

The following subsections provide details of how the test trailer was instrumented and the relationship of the instrumentation locations to the simulation model.

3.2.1 Strain Gauge Setup

The trailer was instrumented with 8 strain gauge rosettes. Based on simulation results, which showed that the critical region is located at the bottom of the straight drawbar, the strain gauges were arranged around the critical region and some complicated structural locations. Four of the strain gauge rosettes were located on the bottom-side of the straight drawbar, and the other four rosettes were placed near complicated structural locations on the upper and lower triangle plates and the angle plate. The instrumented locations are shown in Figures 2 and 3.

Strain gauge locations are shown relative to the FEA mesh in Figure 4, which also indicates the corresponding FE node numbers. The finite element model is created based on the mid surface of the component and does not consider the small joint attached parts and hole, while the strain gauges are attached on the surface of the component. It is difficult to position the strain gauges at exactly the same location as the FE model nodes, especially near the joints and holes. Therefore, the strain gauges are located as close as possible to the corresponding FE node. Table 3 indicates the coordinates of each strain gauge rosette location and their differences from the closest FE node locations, in which the differences are the comparison between their distances from origin of the reference frame.

TABLE 1 - POF EXPERIMENTAL DATA FILE FORMAT

Col #	Description	Units	Col. #	Description	Units
1	Time	seconds	31	Lunette Accel (T)	g's
2	Btm Drwbr Cntr (T) strain	μ inch	32	Lunette Accel (L)	g's
3	Btm Drwbr Cntr (45) strain	μ inch	33	Tongue Accel (V)	g's
4	Btm Drwbr Cntr (L) strain	μ inch	34	Tongue Accel (T)	g's
5	Btm Drwbr Cntr Aft (T) strain	μ inch	35	Tongue Accel (L)	g's
6	Btm Drwbr Cntr Aft (45) strain	μ inch	36	Trailer CG Accel (V)	g's
7	Btm Drwbr Cntr Aft (L) strain	μ inch	37	Trailer CG Accel (T)	g's
8	Btm Drwbr CS Edge (T) strain	μ inch	38	Trailer CG Accel (L)	g's
9	Btm Drwbr CS Edge (45) strain	μ inch	39	CS Forward Accel (V)	g's
10	Btm Drwbr CS Edge (L) strain	μ inch	40	CS Forward Accel (T)	g's
11	Btm Drwbr CS Edge Aft (T) strain	μ inch	41	CS Forward Accel (L)	g's
12	Btm Drwbr CS Edge Aft (45) strain	μ inch	42	CS Aft Accel (V)	g's
13	Btm Drwbr CS Edge Aft (L) strain	μ inch	43	CS Aft Accel (T)	g's
14	Top Triang Plate Corner (T) strain	μ inch	44	CS Aft Accel (L)	g's
15	Top Triang Plate Corner (45) strain	μ inch	45	RS Forward Accel (V)	g's
16	Top Triang Plate Corner (L) strain	μ inch	46	RS Forward Accel (T)	g's
17	Btm Triang Plate Corner (T) strain	μ inch	47	RS Forward Accel (L)	g's
18	Btm Triang Plate Corner (45) strain	μ inch	48	RS Aft Accel (V)	g's
19	Btm Triang Plate Corner (L) strain	μ inch	49	RS Aft Accel (T)	g's
20	Left Angle Plate Lower (V) strain	μ inch	50	RS Aft Accel (L)	g's
21	Left Angle Plate Lower (45) strain	μ inch	51	Trailer CG Pitch Rate	deg/sec
22	Left Angle Plate Lower (L) strain	μ inch	52	Trailer CG Roll Rate	deg/sec
23	Left Angle Plate Upper (V) strain	μ inch	53	Trailer CG Yaw Rate	deg/sec
24	Left Angle Plate Upper (45) strain	μ inch	54	CS Shock Absorber Disp	Inches
25	Left Angle Plate Upper (L) strain	μ inch	55	RS Shock Absorber Disp	inches
26	CS Axle Accel (V)	g's	56	Surge Brake Pressure	psi
27	CS Frame Accel (V)	g's	57	CS Wheel Brake Pressure	psi
28	RS Axle Accel (V)	g's	58	RS Wheel Brake Pressure	psi
29	RS Frame Accel (V)	g's	59	Long. Ground Speed	mph
30	Lunette Accel (V)	g's			

TABLE 2 - ANALOG LOW-PASS ANTI-ALIASING CUTOFF FREQUENCIES

Transducer Type	Filter Cutoff Frequency
Strain gauge	100 Hz
Accelerometer	200 Hz
Rate gyro	20 Hz
Linear position	20 Hz
Pressure	100 Hz

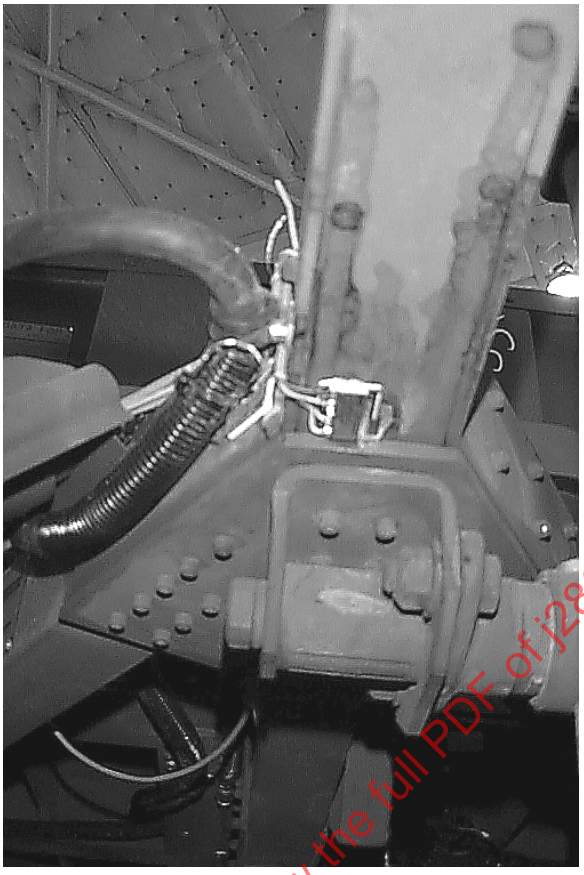

FIGURE 2 - LOCATION AND INSTALLATION OF THE STRAIN GAUGE ROSETTES

FIGURE 3 - LOCATION AND INSTALLATION OF THE STRAIN GAUGE ROSETTES

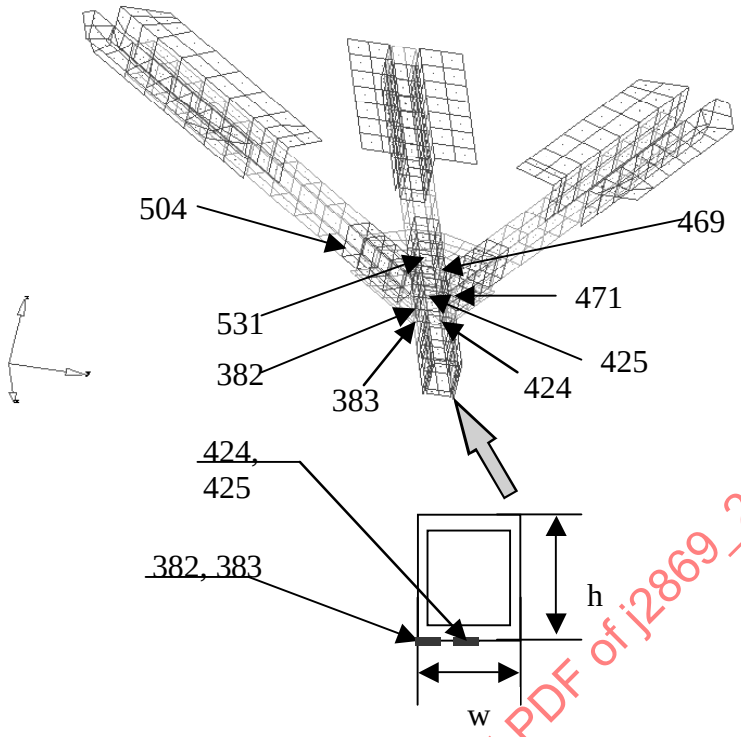

FIGURE 4 - THE LOCATION OF THE STRAIN ROSETTES ON THE FINITE ELEMENT MODEL

TABLE 3 - DISTANCE BETWEEN STRAIN GAUGE LOCATION AND CORRESPONDING FE NODE LOCATION

Distance Between FE Node and Gauge Location					
Node	Model	x	y	z	Distance (in)
382	FE Model	21.23076	-1	-3.25	0.29
	Gauge	21.375	-1	-3.5	
383	FE Model	25.15384	-1	-3.25	0.25
	Gauge	25.15	0	-3.5	
424	FE Model	25.15384	0	-3.25	0.25
	Gauge	25.15	0	-3.5	
425	FE Model	21.23076	0	-3.25	0.29
	Gauge	21.375	0	-3.5	
469	FE Model	21.12	1.25	-0.06	0.33
	Gauge	21.37	1.35	-0.25	
471	FE Model	21.12	1.25	-3.44	0.33
	Gauge	21.37	1.35	-3.25	
504	FE Model	14.26999	-5.94999	-3.5	0.47
	Gauge	14.34	-5.5	-3.6	
531	FE Model	21.12	-1.5	0	0.52
	Gauge	20.62	-1.38	0.1	

Figure 5 indicates the detailed location of all eight strain gauges on the FE model, while Figure 6 shows the detailed locations of four of strain gauges along the bottom of the straight drawbar.

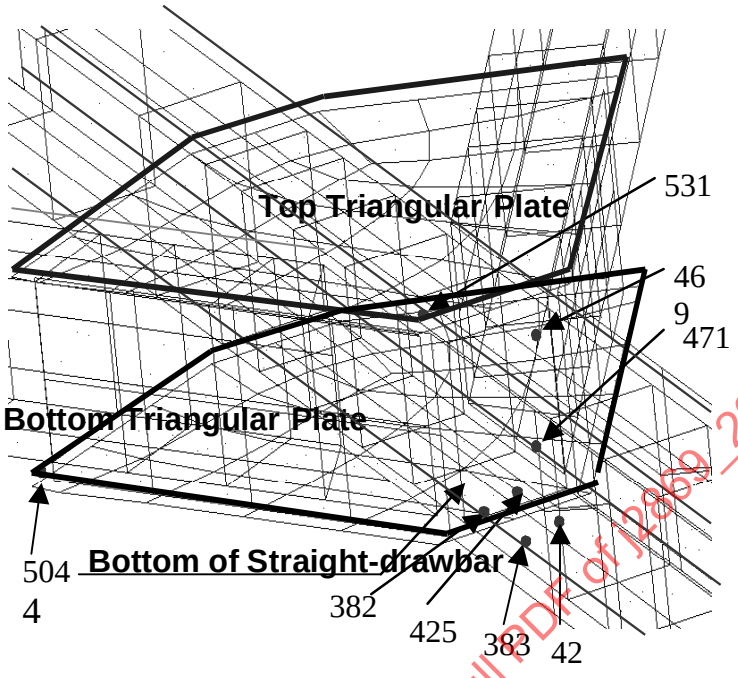

FIGURE 5 - LOCATION OF FOUR OF THE STRAIN ROSETTES ON THE BOTTOM-SIDE OF THE DRAWBAR

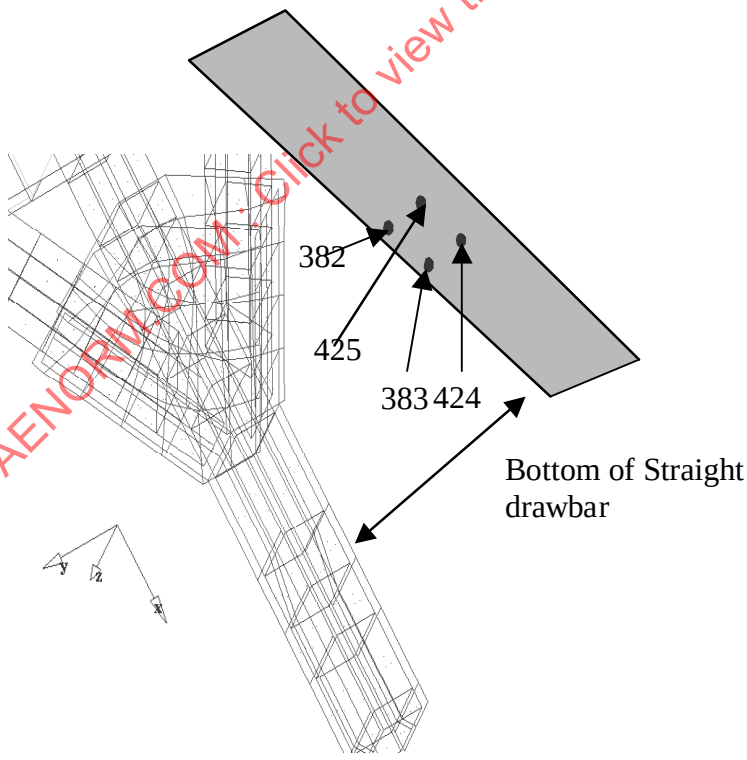

FIGURE 6 - LOCATION OF THE STRAIN ROSETTES (ENLARGEMENT)

Two of the strain gauge rosettes were located on the upper and lower triangle plates, and the remaining two were located on the angle plate, as shown in Figures 7 and 8 respectively.

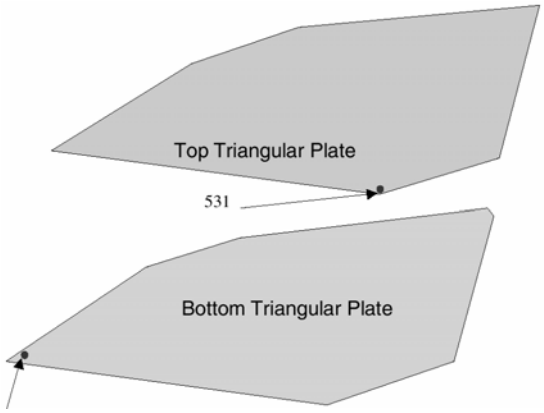

FIGURE 7 - DETAILED LOCATION OF THE STRAIN ROSETTES ON UPPER AND LOWER TRIANGLE PLATES

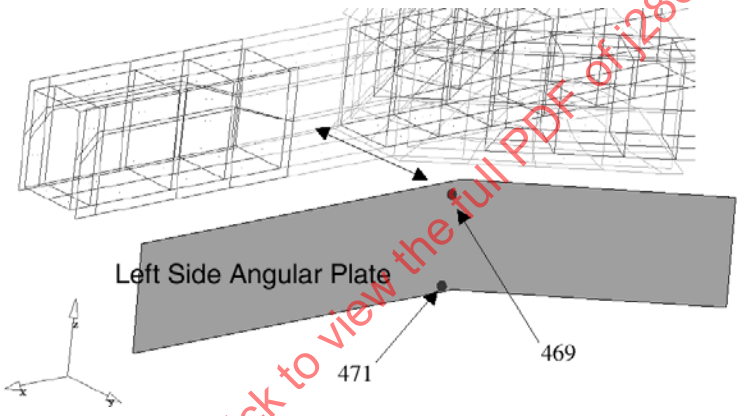

FIGURE 8 - DETAILED LOCATION OF THE STRAIN ROSETTES ON LEFT-SIDE ANGLE PLATES

3.2.2 Accelerometer Setup

A total of seven tri-axial and four single axis accelerometers were used during the trailer testing. One of the tri-axial accelerometers was located on the lunette, and another on the trailer tongue. Significant differences between these two sets of transducers should only exist for experimental runs where the surge brake was active. Another tri-axial accelerometer was located near the trailer CG, as shown in Figure 9. The remaining four tri-axial accelerometers were located at the corners of the cargo box, as shown in Figure 10. The four single axis accelerometers were either located at the frame attachment point for both the curbside and roadside suspension road arms or close to the axle location on the road arms. The axis of the axle accelerometers changes due to jounce/rebound of the suspension.

FIGURE 9 - TRIAXIAL ACCELEROMETERS AND RATE GYROS NEAR TRAILER CENTER OF GRAVITY (CG) LOCATION

FIGURE 10 - TRIAXIAL ACCELEROMETERS AT TOP CORNERS OF TRAILER CARGO BOX

3.2.3 Angular Rate Gyro Setup

A tri-axial angular rate gyro was used to measure the roll, pitch and yaw rates of the trailer. The transducer was mounted as close to the trailer CG as possible. This is shown in Figure 9. The tri-axial angular rate gyro is packaged with the accelerometer located at the trailer CG.

3.2.4 Linear Displacement Transducer Setup

Linear displacement transducers were used to measure the shock absorber displacements during the trailer testing.

3.2.5 Pressure Transducer Setup

A total of three pressure transducers were used in the trailer instrumentation package. One of the transducers measured the pressure as close to the surge brake master cylinder as possible. The master cylinder is located in the hitch assembly. The other two transducers were used to measure pressures close to the left and right drum brakes. The hydraulic surge brake system layout is shown in Figure 11.

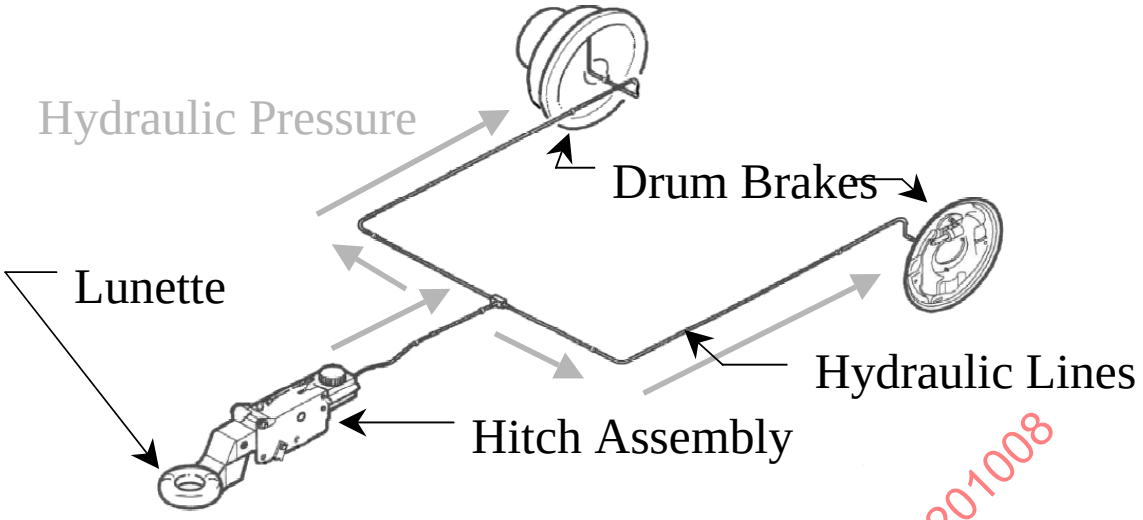

FIGURE 11 - HYDRAULIC SURGE BRAKE SYSTEM LAYOUT

3.3 Test Course Description

Six test courses at the Aberdeen Test Center were utilized for the PoF validation effort. All testing was done when the courses were dry. These test courses are:

1. Test Course A: This is a rough course composed of native soil. When the course is dry, dust is severe. Much of the course is rough due to many years of testing tank-type vehicles.

2. Test Course B: This course is paved with unevenly laid granite blocks forming a surface. It duplicates the rough cobblestone road found in many parts of the world. The course is useful as a standard rough road for accelerated testing of wheeled vehicles, and is generally included in cycles of courses used for vibration studies. The course irregularities vary both along the length of the course and across the width. The motion imparted by the granite paving blocks to a vehicle is a random combination of roll, pitch and high-frequency vibrations.

3. Test Course C: This test course consists of a single 4-inch radius bump. The road surface is concrete. The bump extends across both vehicle wheel tracks, and does not excite the roll degree-of-freedom of the vehicle.

4. Test Course D: This test course is a typical paved primary road segment. The road surface is asphalt.

5. Test Course E: This is a moderate course with a substantial roadbed, composed primarily of quarry spall and bank gravel. The loop includes sharp and sweeping curves, and the surface ranges from smooth to rough, with the roughness due to potholes, wash boarding and rutting.

6. Test Course F: This course is laid out in a loop of moderately irregular terrain. Surfaces range from smooth to rough, and there are sweeping turns. Under dry conditions, the course is extremely dusty.

Measured terrain profiles for the Test Courses A and B as well as Test Courses E and F were used in the simulations.

3.4 Test Matrix

Table 4 lists the data file names associated with the experimental testing. All of the data files were identically formatted comma-separated columns of numbers. The table lists the names of the particular test course, whether the surge brake system was enabled or disabled, and the speed of the test. File names in boldface represent tests that were determined to be good, while file names not in boldface represent data that was determined inconsistent due to a number of possible reasons. All validation work uses the boldfaced experimental test files. The column order, transducer type and units of measurement were previously specified in Tables 1 and 2.

TABLE 4 - TEST MATRIX DATA FILE NAMES

Course/Speed	Brakes	5 mph	10 mph	12 mph	15 mph	20 mph	25 mph	35 mph	50 mph
Test Course A	No		**run032**	**run038**	run039				
			run037		**run055**				
	Yes		**run027**	**run028**	run031				
			run042	run030	**run044**				
				run043	**run049**				
					run050				
					run052				
Test Course B	No				run002	run003	run004		
					run010	**run011**	**run012**		
	Yes				run005	run006	run007		
					run013	**run014**	**run015**		
							run017		
Test Course C	No	**run021**	**run022**	**run023**					
	Yes	**run018**	**run019**	**run020**					
Test Course D	No								**run025**
	Yes								**run026**
Test Course E	No							**run040**	
	Yes							**run041**	
Test Course F	No				**run034**	**run035**	**run036**		
	Yes				**run045**	**run046**	run047		
							run054		

3.5 Data Processing

One of the major lessons learned as a result of this PoF validation project is that all the data, both experimentally measured and simulation generated needed to be processed the same way. Primarily this concerned filtering and decimation of the data, but it also applied to the frequency content required at each stage of the simulation process.

3.5.1 Digital Filtering

The simulation models contain data with varying frequency content. For example, the rigid-body DADS model has a natural frequency for each rigid-body motion, and it has a forced-response frequency spectrum due to the motion of the prime-mover and the irregularity of the terrain profile. The flexible-body DADS model adds the frequencies for the three eigenmodes used in the simulation model. A PSD plot of the center of gravity (CG) vertical (local) acceleration is shown in Figure 12 for both simulation and measured data. Although the output frequency of the simulation was the same as the experimental sample rate, the response spectrum is limited by the model representation.

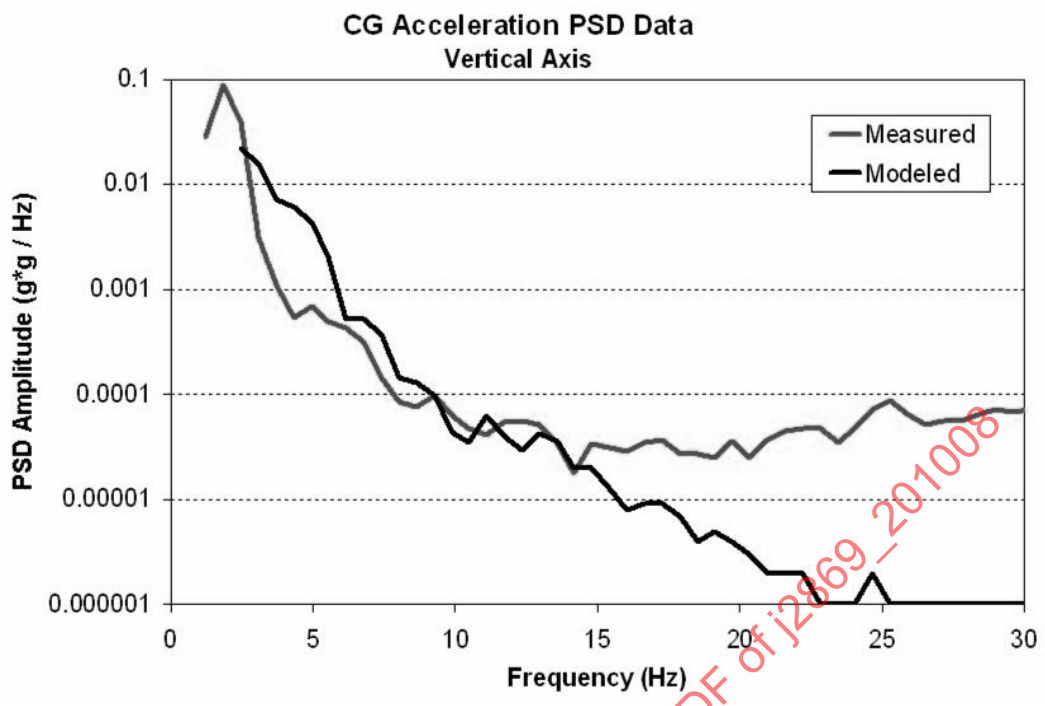

FIGURE 12 - PSD OF SIMULATION AND EXPERIMENTAL CG ACCELERATION

In order to properly compare the simulation and experimental data, the experimental data must be filtered to reduce the effect of any frequency content that is higher than that present in the simulation data. Since the experimental data is being post-processed, the filter can be applied phaselessly (both forward and backward in time).

3.5.2 Principal Strains

For a general loading on a body, the normal strain at a surface point can be determined using a strain rosette, and once readings on the three gauges of the rosette are made, the data can then be used to specify the state of strain at the point. This strain is normally expressed as two principal strains.

Strain deformation was measured using 0-45-90 degree strain gauge rosettes. These can be expressed as principal strains, using the following formulas

$$\varepsilon_{1,2} = \frac{\varepsilon_0 + \varepsilon_{90}}{2} \pm \sqrt{\frac{(\varepsilon_0 - \varepsilon_{45})^2 + (\varepsilon_{90} - \varepsilon_{45})^2}{2}} \quad \text{(Eq. 1)}$$

and

$$\tan(2\alpha) = \frac{\varepsilon_0 - 2\varepsilon_{45} + \varepsilon_{90}}{\varepsilon_0 - \varepsilon_{90}} \quad \text{(Eq. 2)}$$

where $\varepsilon_0, \varepsilon_{45}$ and ε_{90}, are the measured strains, and α is the angle between the reference gauge and the largest principal strain, ε_1. The shear strain, γ, is given by

$$\gamma = 2\sqrt{\frac{(\varepsilon_0 - \varepsilon_{45})^2 + (\varepsilon_{90} - \varepsilon_{45})^2}{2}} \quad \text{(Eq. 3)}$$

Matlab code for reducing the strain data to principal strains is provided in Appendix B.

3.5.3 Decimation and Filtering

The data connection between the multi-body dynamic simulation (DADS) and the finite element analysis was performed at 100 Hz. The decision to use the 100 Hz rates was primarily due to the flexible-body vibration mode frequencies, which were all less than 30 Hz and the computational time required by DRAW to solve the finite element model. This computational time is directly proportional to the frequency (i.e., 200 Hz takes twice the time as 100 Hz). Thus, a requirement exists to decimate the experimental data for comparison to the DRAW results.

Decimation involves both filtering and re-sampling the data. Matlab includes a function ‘decimate’ as part of the Signal Processing Toolkit. This function employs an eighth-order phaseless Chebyshev type-1 low pass filter whose cutoff frequency is set to the Nyquist-rate of the re-sampled data. The filter is applied to the data before it is re-sampled.

For example, in this case the data is originally sampled at 1262.626 Hz and we want to decimate it by a factor of 12, so the re-sampled frequency is 105.22 Hz, which is close to the 100 Hz simulation data. The ‘decimate’ function will first filter the original data at 31.57 Hz, and then resample, using every 12th point.

4. DATA REDUCTION RESULTS

Data reduction was initially performed for all test runs, and then focused specifically on the Test Course A runs, since these were known to cause the failures seen in the field testing of the trailer.

4.1 Speed Data

The foremost variable when validating vehicle models is the experimental test speeds. These speeds must conform with the simulation test speeds in order to make comparisons of the vehicle response.

Table 5 lists the various different test runs, the nominal speed of the run, the average of the actual speed of the run, and some comparisons of the nominal and experimental data. The last two lines of this table are highlighted, since these runs are detailed in further analysis.

The data is easier to understand when presented graphically. Figure 13 shows the minimum, average, and maximum speeds using a stacked bar chart. From this figure, it can be seen that some problems exist with cases 25 and 29. These correspond to two runs on Test Course A (run #32 at 10 mph and run #30 at 12 mph, respectively). Further investigation of the data from these runs shows failures of the vehicle speed sensor.

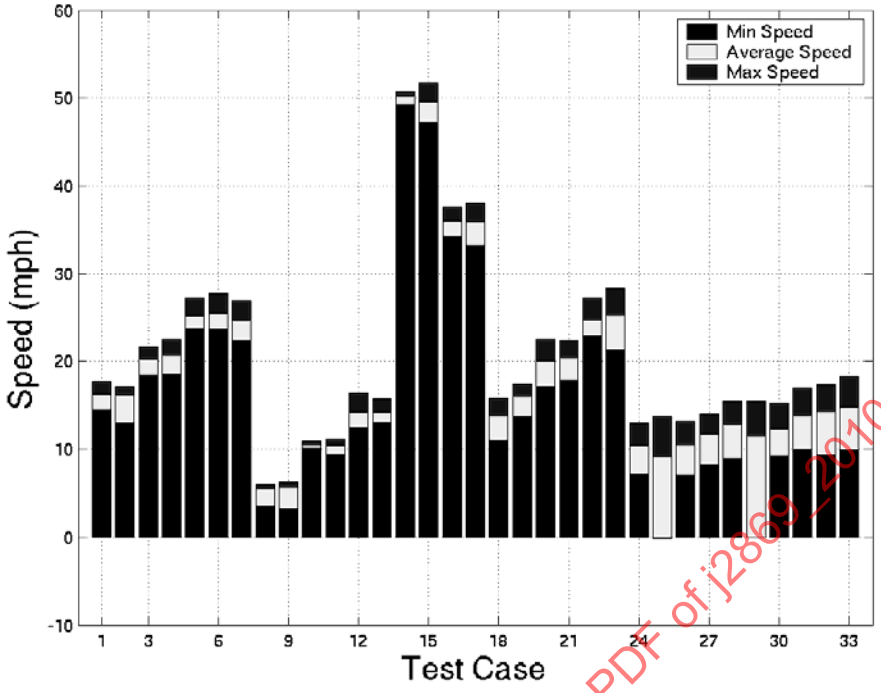

FIGURE 13 - MINIMUM, AVERAGE AND MAXIMUM TEST RUN SPEEDS

TABLE 5 - SPEED DATA STATISTICS FOR EXPERIMENTAL TEST RUNS IN MPH

Course	Case #	Run #	Nominal Speed	Average Speed	Speed Difference	% Speed Difference	Std. Dev.	RMS	-Peak	+Peak
Test Course A	24	27	10	10.32	0.32	3.21	1.28	10.40	7.12	12.97
	25	32	10	9.21	-0.79	-7.91	3.11	9.72	-0.10	13.66
	26	37	10	10.43	0.43	4.26	1.31	10.51	7.05	13.11
	27	42	10	11.66	1.66	16.59	1.05	11.71	8.27	14.01
	28	28	12	12.74	0.74	6.15	1.50	12.83	8.94	15.43
	29	30	12	11.60	-0.40	-3.36	2.48	11.86	-0.05	15.41
	30	38	12	12.26	0.26	2.13	1.17	12.31	9.21	15.25
	31	43	12	13.77	1.77	14.71	1.23	13.82	10.01	16.95
	32	52	15	14.25	-0.75	-5.02	0.97	14.28	9.32	17.30
	33	55	15	14.75	-0.25	-1.64	0.86	14.78	9.85	18.24
Test Course B	1	10	15	16.16	1.16	7.70	0.61	16.17	14.49	17.71
	2	13	15	16.06	1.06	7.06	0.57	16.07	12.96	17.17
	3	11	20	20.17	0.17	0.83	0.58	20.17	18.34	21.60
	4	14	20	20.62	0.62	3.11	1.06	20.65	18.51	22.51
	5	12	25	25.28	0.28	1.12	0.73	25.29	23.81	27.20
	6	15	25	25.48	0.48	1.91	0.85	25.49	23.72	27.77
	7	17	25	24.65	-0.35	-1.41	1.07	24.67	22.37	26.92
Test Course C	8	18	5	5.47	0.47	9.43	0.37	5.48	3.49	5.99
	9	21	5	5.67	0.67	13.41	0.55	5.70	3.17	6.29
	10	19	10	10.43	0.43	4.34	0.20	10.44	10.12	10.97
	11	22	10	10.33	0.33	3.31	0.48	10.34	9.42	11.09
	12	20	12	14.16	2.16	18.02	1.27	14.22	12.49	16.37
	13	23	12	14.21	2.21	18.45	0.81	14.24	13.02	15.73
Test Course D	14	25	50	50.22	0.22	0.44	0.38	50.22	49.28	50.81
	15	26	50	49.56	-0.44	-0.87	1.20	49.58	47.25	51.70
Test Course E	16	40	35	36.04	1.04	2.97	0.98	36.05	34.26	37.66
	17	41	35	35.96	0.96	2.75	0.98	35.98	33.27	38.08
Test Course F	18	34	15	13.76	-1.24	-8.27	0.90	13.79	11.04	15.80
	19	45	15	16.02	1.02	6.83	0.93	16.05	13.66	17.42
	20	35	20	19.99	-0.01	-0.06	1.41	20.04	17.18	22.47
	21	46	20	20.41	0.41	2.06	0.83	20.43	17.77	22.36
	22	36	25	24.76	-0.24	-0.97	0.93	24.77	22.82	27.24
	23	54	25	25.36	0.36	1.44	1.24	25.39	21.26	28.38

Figure 14 shows the difference between the average and nominal speeds for each test run. Since the nominal speeds vary from 5 to 50 mph, it is better to compare the quality of the test using the relative speed difference, shown as a percentage in Figure 15.

Figure 16 shows the standard deviation of the experimental speed data. The large deviations associated with cases 25 and 29 confirm that there are problems with the speed data for those test runs.

Figure 17 shows the difference between the RMS speed values and the nominal values. This plot mirrors the same information as the relative difference plot, Figure 15.

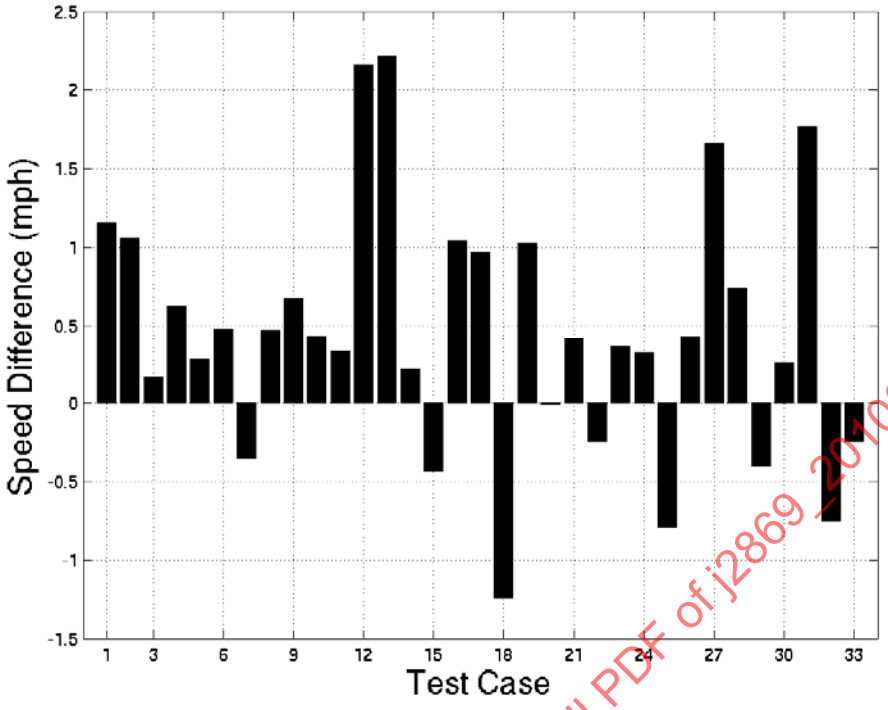

FIGURE 14 - DIFFERENCE BETWEEN AVERAGE AND NOMINAL SPEEDS

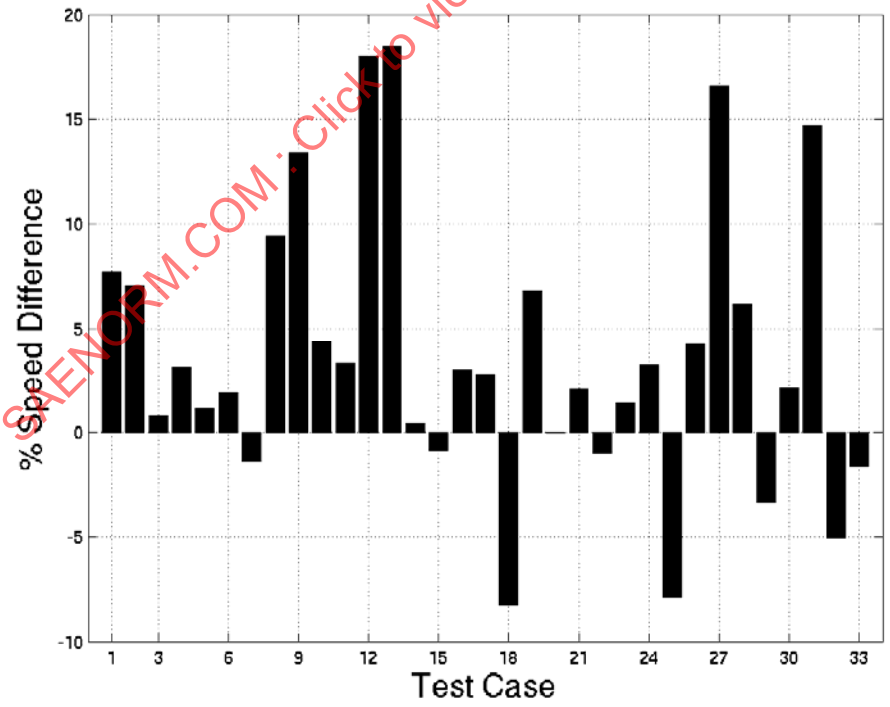

FIGURE 15 - PERCENT SPEED DIFFERENCE (EXPERIMENTAL VS. NOMINAL DATA)

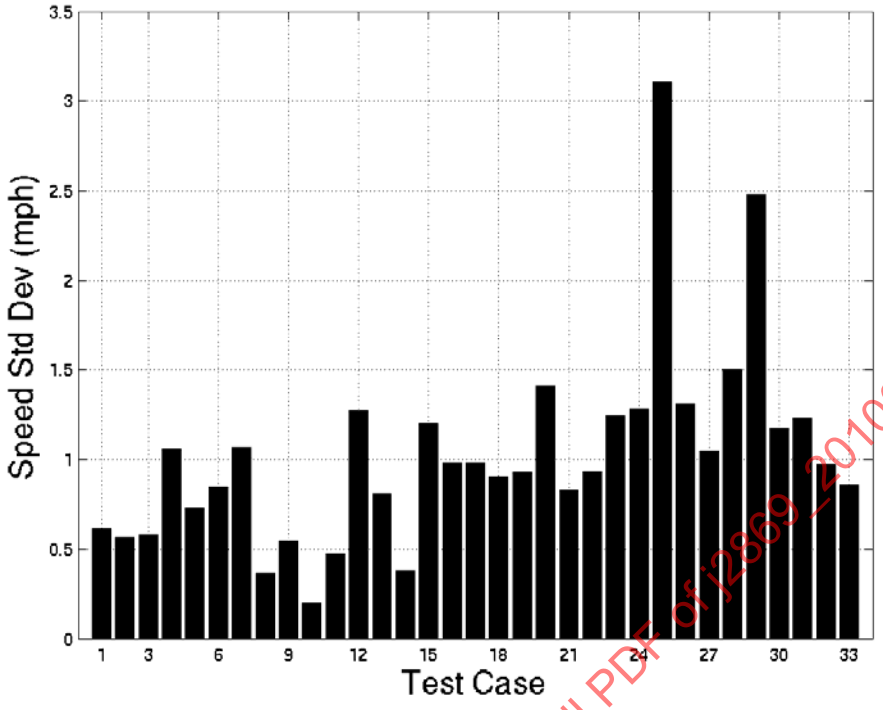

FIGURE 16 - STANDARD DEVIATION (EXPERIMENTAL VS NOMINAL SPEEDS

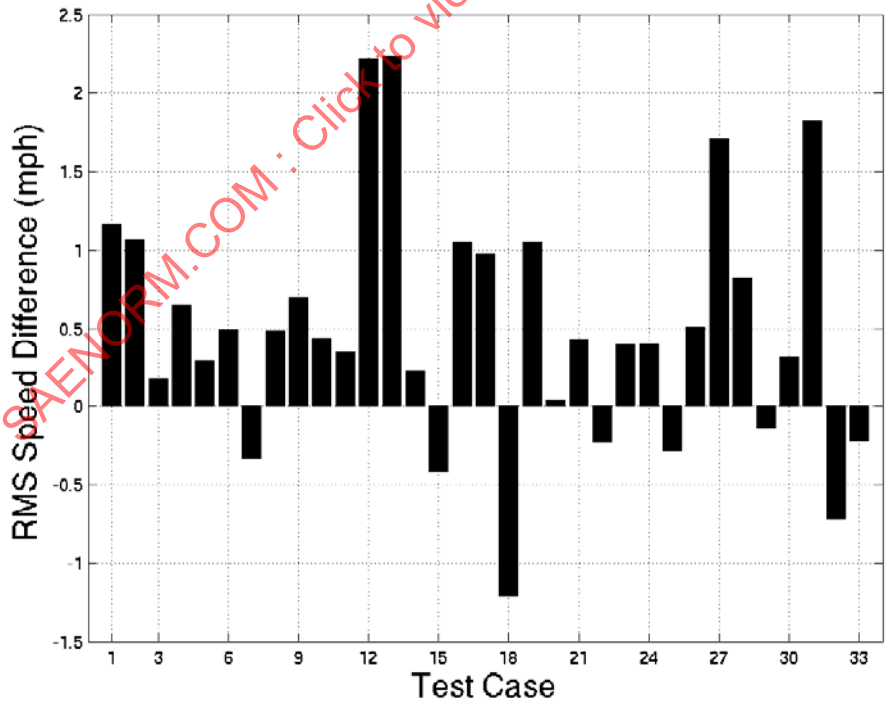

FIGURE 17 - DIFFERENCE BETWEEN RMS AND NOMINAL SPEEDS

The bias in the speed measurements can be accounted for by using the measured average, rather than the nominal speed value, for the dynamic simulations. However, there is no good way to handle the variance unless the position of the vehicle, relative to the terrain, is known. In this case, the measured velocity profile can be integrated with respect to time, and used as a kinematic position driver in the DADS software. Unfortunately, the position of the vehicle was not measured, so the average speed was used for all the dynamic simulations.

4.2 Test Course A

Data reduction results are presented for experimental test runs numbered 52 and 55 (shown in Table 5 as cases #32 and #33), which were collected on Test Course A at a nominal speed of 15 mph with the surge brakes enabled and disabled, respectively. Comparative data for other runs on Test Course A are presented Appendix C.

Amplitude distributions (average, standard deviation, RMS, +peak, -peak, +99.9%, -99.9%, +99%, -99%, +90%, -90%) were performed on all data. Strain gauge data were resolved as principal strains before computing the distributions. All other channels were directly used.

4.2.1 Strain Gauge Data

The principal strains and rotation angle were calculated from the measured gauge data. This is presented in Table 6 for the case with the brakes disabled, and Table 7 for the case with the brakes enabled. In each table, the description identifies both the location of the strain gauge, and the nearest finite element node number.

TABLE 6 - PRINCIPAL STRAIN AMPLITUDE DISTRIBUTION DATA (BRAKES DISABLED)

Description		Ave	Std Dev	Rms	+Peak	-Peak	+99.9	-99.9	+99	-99	+90	-90
Btm Cntr	(ε_1)	242.938	150.225	285.632	880.486	-20.345	857.991	-5.944	690.530	2.054	443.680	50.013
#424	(ε_2)	-87.290	46.750	99.021	-3.956	-430.34	-9.427	-395.83	-14.877	-230.13	-36.162	-145.30
	(α)	-0.179	6.433	6.435	44.782	-44.869	42.740	-42.631	22.807	-22.438	3.785	-4.173
Btm Cntr Aft	(ε_1)	284.480	167.241	329.996	1006.189	-40.338	982.870	-18.012	789.999	22.046	511.970	82.419
#425	(ε_2)	-90.984	59.190	108.542	-4.963	-514.44	-8.766	-489.89	15.835	-276.98	-30.056	-166.05
	(α)	5.114	11.245	12.353	44.937	-44.980	44.564	-44.591	39.708	-39.772	14.548	-0.450
Btm Edge	(ε_1)	191.440	112.308	221.951	651.319	-8.258	642.308	-3.616	525.357	12.180	341.845	52.941
#383	(ε_2)	-77.209	47.480	90.640	-20.508	-339.27	13.857	-295.91	1.502	-222.97	-20.362	-139.56
	(α)	2.759	8.292	8.739	44.961	-44.997	42.995	-43.436	31.042	-30.220	9.272	-2.585
Btm Edge Aft	(ε_1)	219.534	138.438	259.537	791.191	-55.423	786.361	-30.984	635.930	3.046	406.053	48.416
#382	(ε_2)	-83.040	53.540	98.803	65.274	-463.15	44.050	-408.03	7.074	-245.79	-23.520	-151.44
	(α)	1.477	7.692	7.832	44.990	-44.968	43.040	-42.504	31.691	-28.343	6.428	-1.432
Top Plate	(ε_1)	24.597	15.111	28.868	128.575	-0.091	124.926	3.273	86.042	5.985	38.804	11.275
#531	(ε_2)	-13.730	17.111	21.939	0.274	158.78	-1.615	152.29	-3.206	-95.468	-5.233	-23.928
	(α)	15.840	15.060	21.856	44.044	-44.823	43.855	-44.749	41.608	-43.478	0.225	31.164
Btm Plate	(ε_1)	14.077	5.182	15.000	37.045	1.226	34.522	3.566	29.426	4.842	21.222	8.149
#504	(ε_2)	-7.231	4.648	8.596	5.722	-42.737	3.310	-38.794	0.415	-26.830	-2.801	-11.847
	(α)	-14.723	11.936	18.953	44.423	-44.810	19.567	-44.736	15.121	-40.992	2.144	-28.961
Ang. Lower	(ε_1)	264.853	171.321	315.432	828.211	-17.173	758.451	-10.943	671.887	0.038	499.069	27.221
#471	(ε_2)	-54.740	63.711	83.997	14.447	-743.11	10.987	-695.70	-0.738	-365.79	-12.850	-96.577
	(α)	-4.025	9.135	9.982	44.905	-44.930	43.646	-43.765	31.655	-34.105	2.969	-12.086
Ang Upper	(ε_1)	50.794	47.988	69.877	506.827	-10.53	475.728	-6.896	261.520	-3.088	86.524	9.189
#469	(ε_2)	-168.67	136.302	216.854	-3.282	-670.82	-7.397	-657.97	-12.480	-575.06	-32.209	-375.37
	(α)	9.590	12.555	15.798	44.995	-45.00	44.220	-44.55	39.664	-39.79	21.127	-2.490

TABLE 7 - PRINCIPAL STRAIN AMPLITUDE DISTRIBUTION DATA (BRAKES ENABLED)

Description		Ave	Std Dev	RMS	+Peak	-Peak	+99.9	-99.9	+99	-99	+90	-90
Btm Cntr	(ε_1)	218.164	127.738	252.808	666.656	-2.979	658.671	5.521	610.086	30.535	382.589	53.824
#424	(ε_2)	-75.143	36.514	83.545	-14.713	-313.36	-17.453	-296.56	-24.222	-191.40	-36.896	-122.76
	(α)	-8.938	12.900	15.693	44.918	-44.794	44.480	-44.411	39.686	-40.831	-0.919	-22.333
Btm Cntr Aft	(ε_1)	243.083	154.273	287.90	774.404	-41.626	764.828	-24.706	710.929	6.357	441.772	49.657
#425	(ε_2)	-95.015	53.499	109.04	-12.480	-394.90	-18.492	-374.27	-24.186	-260.29	-34.963	-164.73
	(α)	4.773	11.075	12.059	44.910	-44.711	44.298	-43.934	38.246	-37.029	15.801	-3.505
Btm Edge	(ε_1)	157.614	99.048	186.15	490.097	-9.280	485.771	-4.573	449.787	1.657	285.090	34.692
#383	(ε_2)	-68.377	41.352	79.91	5.359	-246.95	2.077	-237.15	-1.611	-194.16	-17.108	-124.59
	(α)	1.593	9.906	10.033	44.996	-44.859	44.374	-44.438	38.555	-37.611	8.869	-4.791
Btm Edge Aft	(ε_1)	174.121	117.657	210.14	598.355	-48.786	588.660	-35.979	523.232	-1.912	325.854	28.977
#382	(ε_2)	-69.101	47.985	84.128	57.870	-432.52	47.495	-342.00	20.270	-202.51	-18.452	-133.44
	(α)	-0.265	7.556	7.561	44.755	-44.895	41.944	-43.349	24.192	-30.904	4.464	-5.253
Top Plate	(ε_1)	26.852	11.623	29.260	84.748	4.055	81.603	7.042	73.976	10.065	41.080	16.229
#531	(ε_2)	-11.878	10.379	15.774	0.719	-87.387	-1.608	-81.635	-3.544	-78.601	-6.221	-18.739
	(α)	-21.364	16.114	26.760	44.898	-44.179	44.852	-44.052	40.305	-42.180	1.044	-35.563
Btm Plate	(ε_1)	28.892	3.540	29.108	40.115	16.989	38.222	18.944	36.610	20.862	33.519	24.288
#504	(ε_2)	-10.250	5.855	11.804	6.054	-38.049	4.421	-35.321	2.934	-30.411	-3.515	-16.355
	(α)	17.418	5.458	18.253	32.763	-9.396	27.982	-4.497	26.113	-0.146	23.617	10.136
Ang. Lower	(ε_1)	193.147	139.823	238.44	631.754	-5.869	610.917	-1.459	533.269	4.910	389.554	23.859
#471	(ε_2)	-49.027	70.741	86.069	11.629	-731.14	9.168	-602.25	2.865	-352.88	-4.924	-117.93
	(α)	-1.082	12.251	12.298	44.790	-44.918	44.161	-44.429	39.315	-39.108	10.552	-13.261
Ang Upper	(ε_1)	56.142	33.830	65.547	268.708	-2.140	247.43	0.377	190.161	5.556	91.777	17.142
#469	(ε_2)	-171.31	135.234	218.25	3.524	-588.83	-0.439	-574.30	-9.340	-547.18	-25.818	-371.99
	(α)	9.196	13.287	16.159	44.929	-44.922	44.814	-44.234	40.255	-40.243	22.129	-2.786

Much of this information is easier to understand graphically. Figure 18 shows the average principal strain for each of the eight rosette positions. In general, it shows that the average strains, along the bottom of the drawbar, were larger for the case #33 (run055) where the surge brake was disabled. However, the average vehicle speed for this run was 3.4% faster than case #32 (run052), with the brake enabled.

The standard deviations of the principal strains for each of the strain gauge locations are shown in Figure 19. In this figure, nearly all of the principal strain standard deviations are larger when the brakes are disabled.

The RMS values of the principal strains for each of the strain gauge locations are shown in Figure 20. As expected, the graphs are qualitatively similar to the standard deviation plots.

Finally, Figures 21 and 22 portray the data range statistics as stacked bar charts. Although the test case with the brakes disabled shows higher peak values of principal strains, the charts look similar. Figure 21 also shows that the largest values of the 1st principal strain occurred at the bottom center aft strain gauge (BCA). The BCA strain gauge was placed closest to the point of failure.

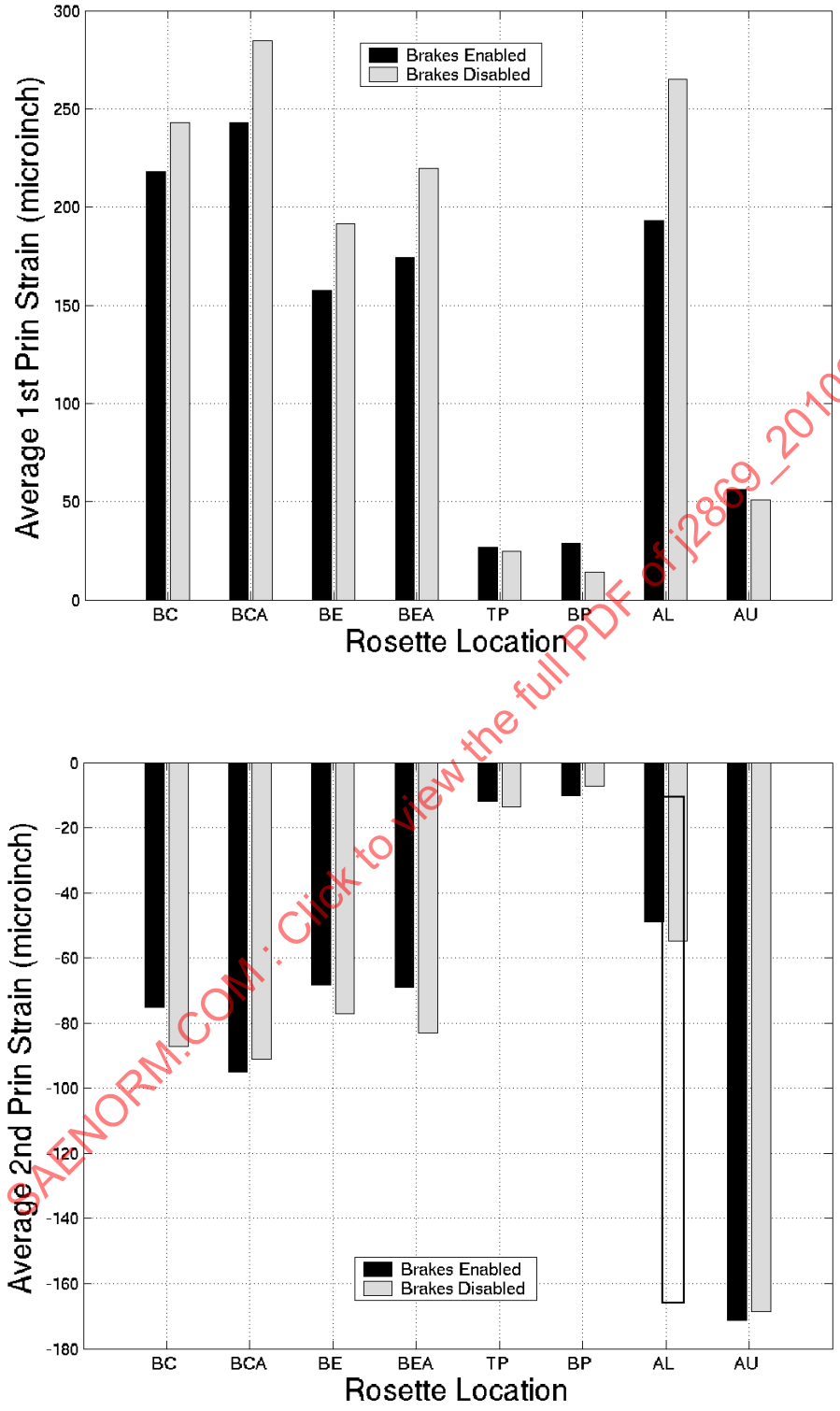

FIGURE 18 - AVERAGE PRINCIPAL STRAINS (TEST COURSE A, 15 MPH)

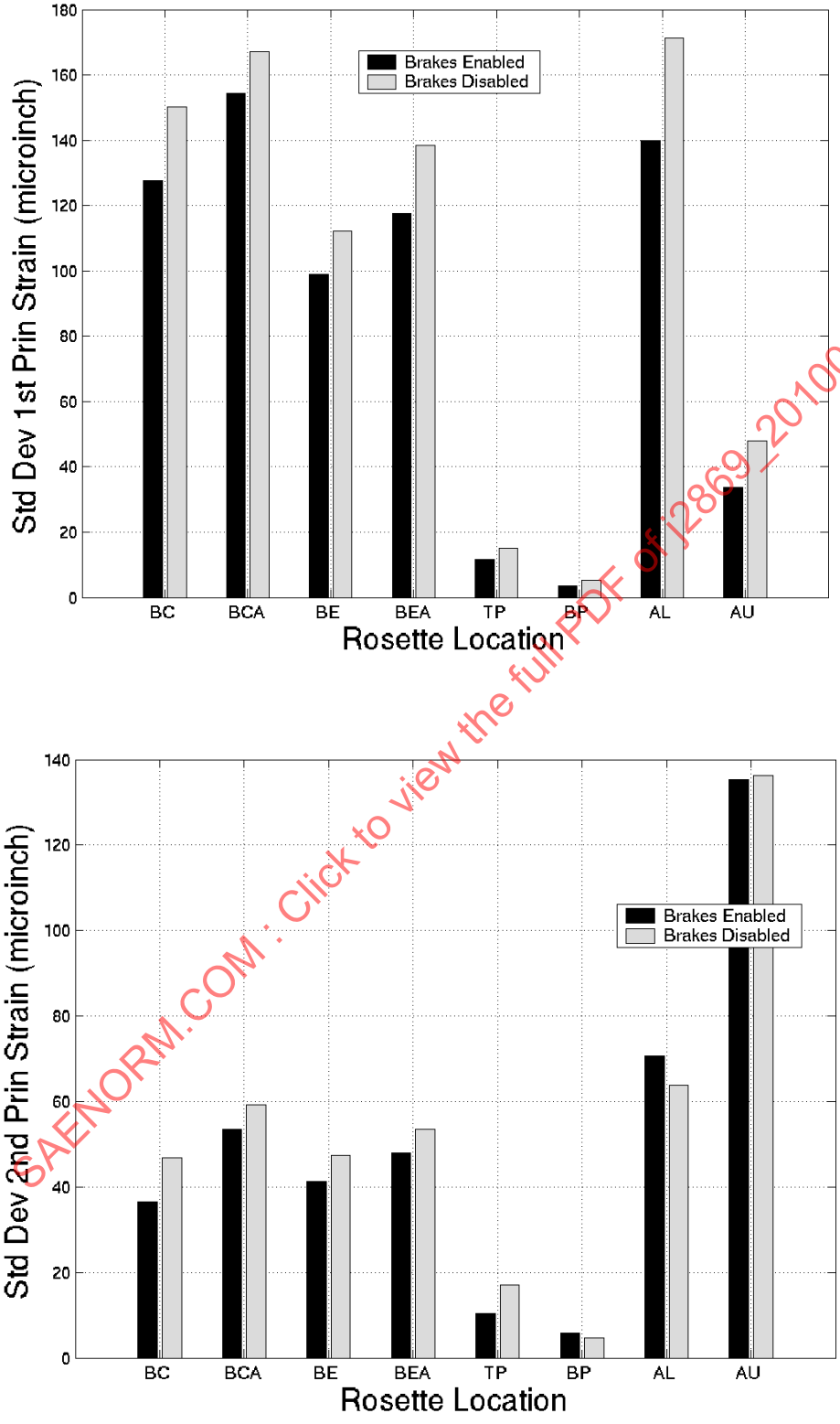

FIGURE 19 - PRINCIPAL STRAIN STANDARD DEVIATIONS (TEST COURSE A, 15 MPH)

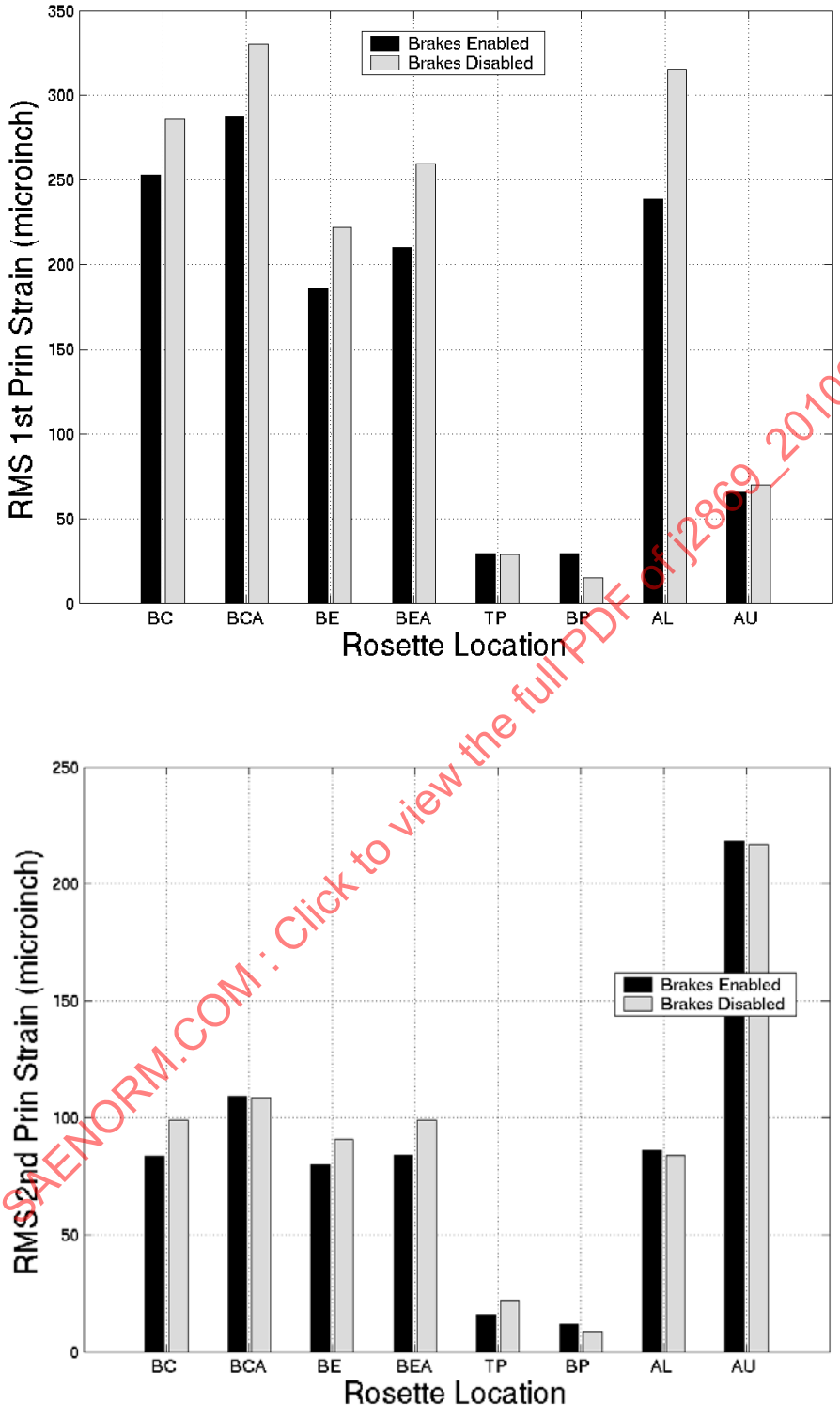

FIGURE 20 - RMS VALUES OF PRINCIPAL STRAINS

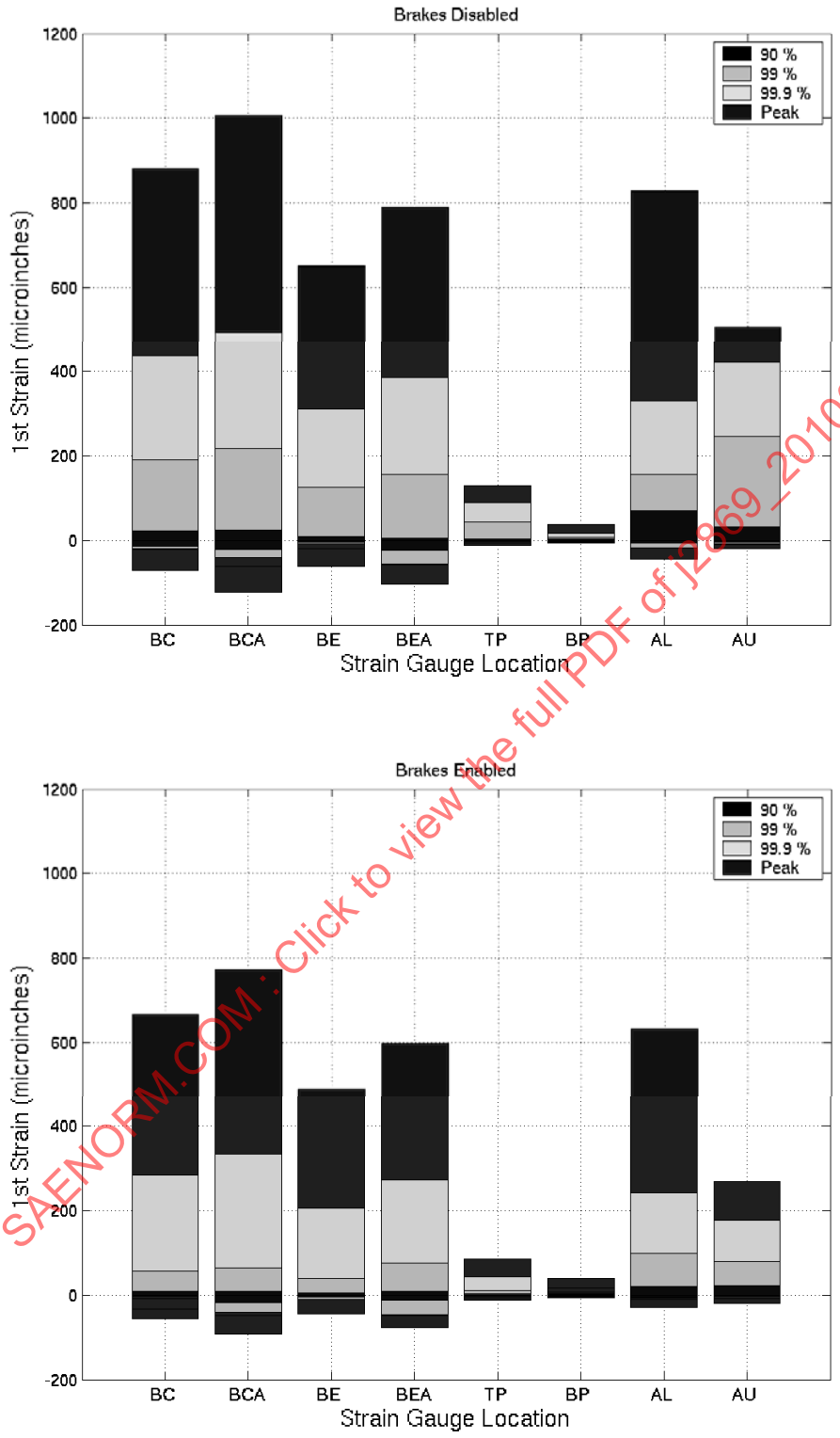

FIGURE 21 - DISTRIBUTION OF FIRST (1^{ST}) PRINCIPAL STRAINS

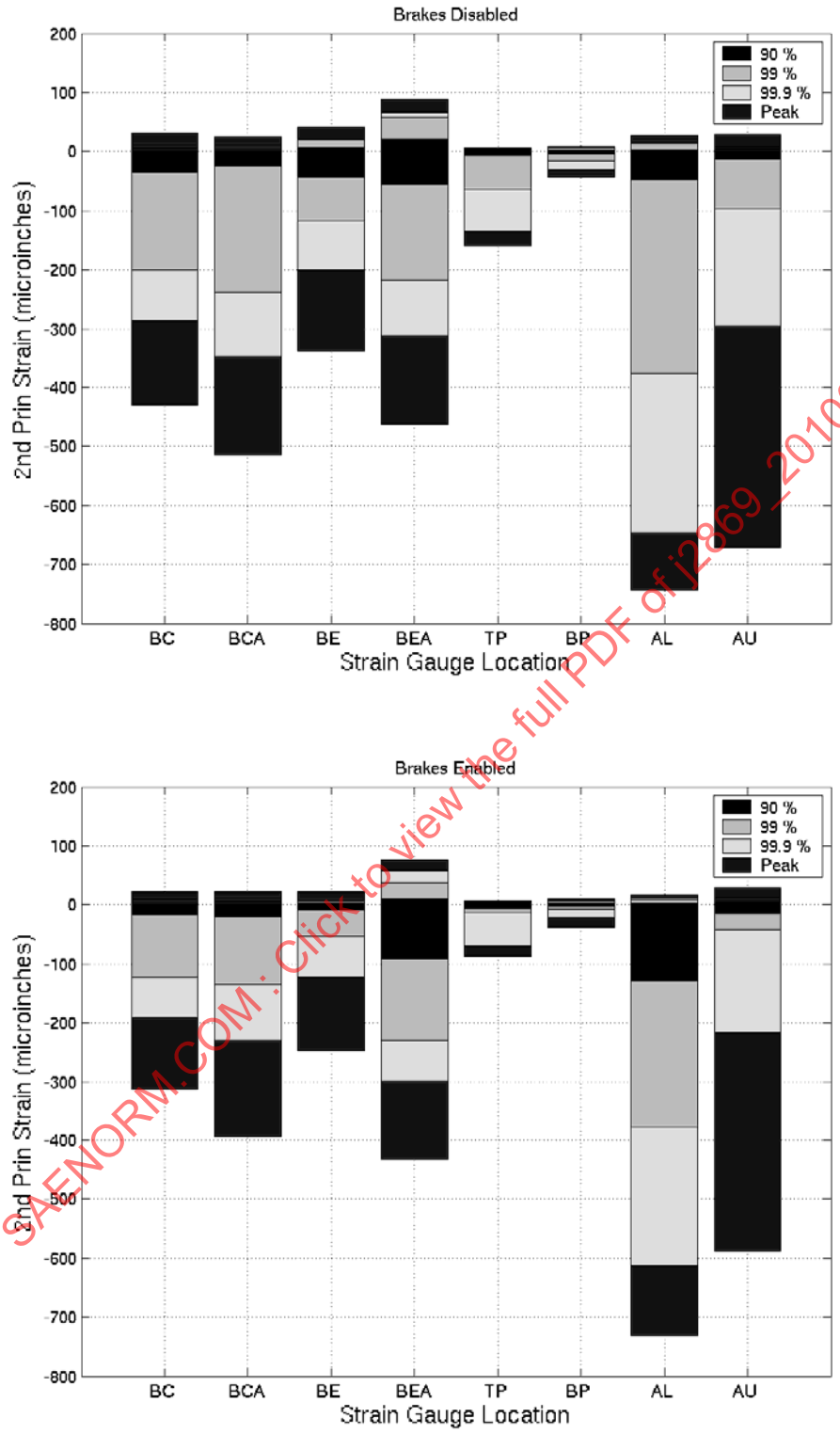

FIGURE 22 - DISTRIBUTION OF SECOND (2^{ND}) PRINCIPAL STRAINS

4.2.2 Accelerometer Data

Statistics about the accelerometer data amplitude distribution are given in Table 8 for the case with the brakes disabled and in Table 9 for the case with the brakes enabled.

Figures 23 through 25 show the average accelerations (vertical, transverse, and longitudinal) for several locations on the trailer. In addition to the lunette, drawbar (tongue) and CG location, the four triaxial accelerometers at the top corners of the trailer box on both the roadside (RS) and curbside (CS) are displayed.

For this type of experimental testing, and the types of accelerometers used, it would be expected that the average accelerations would tend toward zero. As seen in the figures, all of the averages are less than 0.25 g. Since a fairly long sample signal was used, these average values can be assumed to be representative of the instrumentation bias values. For some accelerometers, particularly vertical accelerometers at the CG, curbside forward, and roadside aft locations, the transverse accelerometer on the drawbar (tongue), and the longitudinal accelerometer on the lunette, questions can be raised about the data, instrumentation and/or test procedures, because of the sign reversal (positive/negative) of the average on the brakes disabled and brakes enabled testing.

The standard deviations of the accelerations are graphed in Figures 26 through 28, and the similar appearing RMS accelerations in Figures 29 through 31. These figures show a higher signal variance for the aft mounted accelerometers (both roadside and curbside) in the vertical and transverse directions. This means that the trailer is experiencing significant movement relative to the pintle/lunette, as these accelerometers were the most distant.

Also showing some significance is the longitudinal acceleration of the lunette in Figures 28 and 31. In the case where the brakes are enabled, both the standard deviation and RMS longitudinal accelerations are approximately twice that seen when the brakes are disabled.

Figures 32 through 34 show the statistical distributions of the acceleration data. With the surge brakes enabled, only the peak positive vertical acceleration of the drawbar was greater than the corresponding acceleration with the surge brakes disabled. In some cases, particularly longitudinal accelerations, the difference in the peak accelerations is quite pronounced.

TABLE 8 - ACCELERATION AMPLITUDE DISTRIBUTION DATA (BRAKES DISABLED) IN G'S

Description	Ave	Std Dev	RMS	+Peak	-Peak	+99.9	-99.9	+99	-99	+90	-90
Lunette (V)	0.12168	0.4581	0.4582	0.4583	0.4584	0.4585	0.4586	0.4587	0.4588	0.4589	0.4590
(T)	-0.075	0.3101	0.319	12.632	-8.3959	2.4542	-2.9747	0.5986	-0.7352	0.0754	-0.2314
(L)	-0.0889	0.1779	0.1989	4.0817	-4.6148	1.0331	-1.1936	0.3298	-0.5483	0.0693	-0.2562
Tongue (V)	-0.0525	0.4156	0.4189	13.57	-6.9543	1.996	-3.1291	0.7836	-1.1986	0.3574	-0.4531
(T)	-0.185	0.1688	0.2504	2.5198	-2.6362	1.1419	-1.1759	0.2237	-0.6285	-0.0321	-0.3397
(L)	-0.0053	0.1311	0.1312	1.9064	-1.0406	0.6609	-0.5848	0.3064	-0.3517	0.1384	-0.1608
CG (V)	0.1415	0.3706	0.3967	2.2667	-2.2081	1.6796	-0.8874	1.2249	-0.6657	0.6607	-0.2953
(T)	-0.0683	0.118	0.1363	0.7149	-0.594	0.4068	-0.467	0.2534	-0.3519	0.0749	-0.2094
(L)	0.0299	0.121	0.1266	1.6047	-0.4785	0.636	-0.3985	0.3406	-0.2693	0.1781	-0.1178
CS For. (V)	0.0317	0.3561	0.3575	4.3396	-3.1448	1.88	-1.6149	0.961	-0.8145	0.4544	-0.3714
(T)	0.0499	0.1613	0.1689	1.5647	-1.2575	0.9982	-0.7279	0.4733	-0.3657	0.2247	-0.1282
(L)	0.0808	0.2411	0.2543	1.8408	-1.0989	1.3538	-0.7164	0.7839	-0.5122	0.3503	-0.1999
CS Aft (V)	-0.0208	0.662	0.6623	4.1594	-2.3021	3.2007	-1.7933	2.1049	-1.4319	0.7118	-0.779
(T)	0.1244	0.3633	0.3834	5.6734	-4.6933	2.0413	-1.7544	1.1053	-0.7988	0.515	-0.2643
(L)	-0.1234	0.2317	0.2625	1.5709	-1.2324	1.0813	-0.9077	0.5811	-0.6385	0.1405	-0.3902
RS For (V)	0.0553	0.4088	0.4125	6.2374	-3.5506	2.0098	-2.0374	1.0706	-0.9092	0.544	-0.4075
(T)	-0.0394	0.1727	0.1171	1.5752	-1.3812	0.9449	-0.84	0.4047	-0.4783	0.15	-0.2343
(L)	-0.0745	0.2486	0.2596	1.975	-1.9357	1.1045	-0.8627	0.6167	-0.6569	0.2317	-0.3646
RS Aft (V)	0.0075	0.6042	0.6042	3.1227	-2.2267	2.3379	-1.5632	1.7719	-1.3449	0.7346	-0.6992
(T)	0.1265	0.3075	0.3325	4.2607	-3.6938	1.864	-1.4085	0.9809	-0.6421	0.4597	-0.2044
(L)	0.0394	0.2106	0.21421	1.3207	-0.7322	1.0818	-0.5791	0.65451	-0.4319	0.3096	-0.194
CS Axle (V)	0.0852	0.4934	0.5007	4.3174	-3.36	2.7369	-1.9719	1.5695	-1.0699	0.6409	-0.4585
CS Frame (V)	-0.0525	0.4021	0.4055	1.8081	-1.2716	1.6858	-1.0935	1.2094	-0.9464	0.4166	-0.523
RS Axle (V)	-0.0301	0.3931	0.3943	2.2952	-2.0173	1.7752	-1.4556	1.1079	-0.9078	0.4299	-0.4972
RS Frame (V)	-0.0261	0.3909	0.3917	1.6563	-1.1276	1.4053	-1.0349	1.1184	-0.9349	0.4417	-0.4812

TABLE 9 - ACCELERATION AMPLITUDE DISTRIBUTION DATA (BRAKES ENABLED) IN G'S

Description	Ave	Std Dev	RMS	+Peak	-Peak	+99.9	-99.9	+99	-99	+90	-90
Lunette (V)	0.2202	0.6183	0.6521	21.071	-13.441	4.802	-5.7613	1.5933	-1.4499	0.6616	-0.2016
(T)	-0.1545	0.5104	0.5332	15.779	-20.018	4.5127	-4.4471	1.0028	-1.3463	0.0511	-0.3657
(L)	0.0399	0.6974	0.6985	19.735	-29.825	5.7253	-7.9237	1.5271	-1.6708	0.2877	-0.217
Tongue (V)	0.13324	0.6087	0.6231	10.218	-12.366	4.929	-4.9009	1.5916	-1.559	0.5915	-0.3057
(T)	0.14123	0.2694	0.3041	6.8436	-7.2149	2.2118	-1.8035	0.8591	-0.5756	0.3469	-0.0689
(L)	0.13663	0.2205	0.2594	3.4864	-3.9984	1.9519	-1.5489	0.7293	-0.4116	0.3091	-0.0497
CG (V)	-0.1242	0.4284	0.446	4.5005	-7.6431	2.5262	-1.9716	1.1257	-1.112	0.3346	-0.5775
(T)	-0.0395	0.1547	0.1597	0.9022	-1.7508	0.5993	-0.9303	0.3599	-0.442	0.1384	-0.2067
(L)	0.1465	0.1861	0.2368	3.447	-3.808	1.7097	-1.0958	0.6771	-0.2548	0.311	-0.0186
CS For. (V)	-0.1274	0.4411	0.4591	4.3337	-7.9789	2.3179	-2.6774	1.0904	-1.2897	0.3406	-0.5656
(T)	0.021	0.2111	0.2121	3.1715	-2.8352	1.1754	-1.1853	0.6102	-0.5559	0.2416	-0.1919
(L)	0.1736	0.3394	0.3812	5.0471	-6.0943	2.6709	-2.0454	1.1309	-0.6452	0.4848	-0.1481
CS Aft (V)	0.0349	0.7652	0.766	8.4154	-6.3583	5.4353	-3.0088	2.3397	-1.7089	0.834	-0.7713
(T)	-0.0232	0.5302	0.5307	6.2574	-8.5646	3.6121	-3.5446	1.3968	-1.5638	0.4568	-0.484
(L)	-0.0918	0.3226	0.3354	4.8301	-4.9436	2.3277	-2.0992	0.8744	-0.8165	0.2134	-0.3956
RS For (V)	-0.0498	0.5111	0.5135	8.202	-9.5838	2.807	-2.972	1.3539	-1.406	0.4688	-0.56
(T)	0.1679	0.224	0.2799	3.7841	-4.5178	1.3926	-1.0656	0.7736	-0.4446	0.4001	-0.0569
(L)	-0.1321	0.3325	0.3485	4.3677	-7.5798	2.2229	-2.075	0.7561	-0.9025	0.1827	-0.439
RS Aft (V)	-0.1377	0.6953	0.7088	10.413	-3.8751	5.4252	-2.6428	1.8761	-1.6617	0.6125	-0.8755
(T)	0.139	0.4711	0.4912	9.1632	-8.374	3.4472	-3.4478	1.4288	-1.771	0.531	-0.2463
(L)	0.1491	0.2769	0.3144	4.6166	-3.0698	2.1879	-1.4118	0.9581	-0.446	0.434	-0.1111
CS Axle (V)	-0.0911	0.5322	0.534	4.1965	-2.9852	2.9817	-2.3028	1.5491	-1.3428	0.4993	-0.669
CS Frame (V)	-0.0405	0.4357	0.4376	3.5915	-2.6474	2.5291	-1.4417	1.2945	-1.0205	0.4558	-0.5216
RS Axle (V)	-0.024	0.423	0.4236	4.7063	-3.5782	3.0029	-1.6431	1.2476	-0.9086	0.4925	-0.4463
RS Frame (V)	0.0528	0.4271	0.4303	3.6333	-2.0387	2.6487	-1.2556	1.3515	-0.8782	0.5483	-0.4367

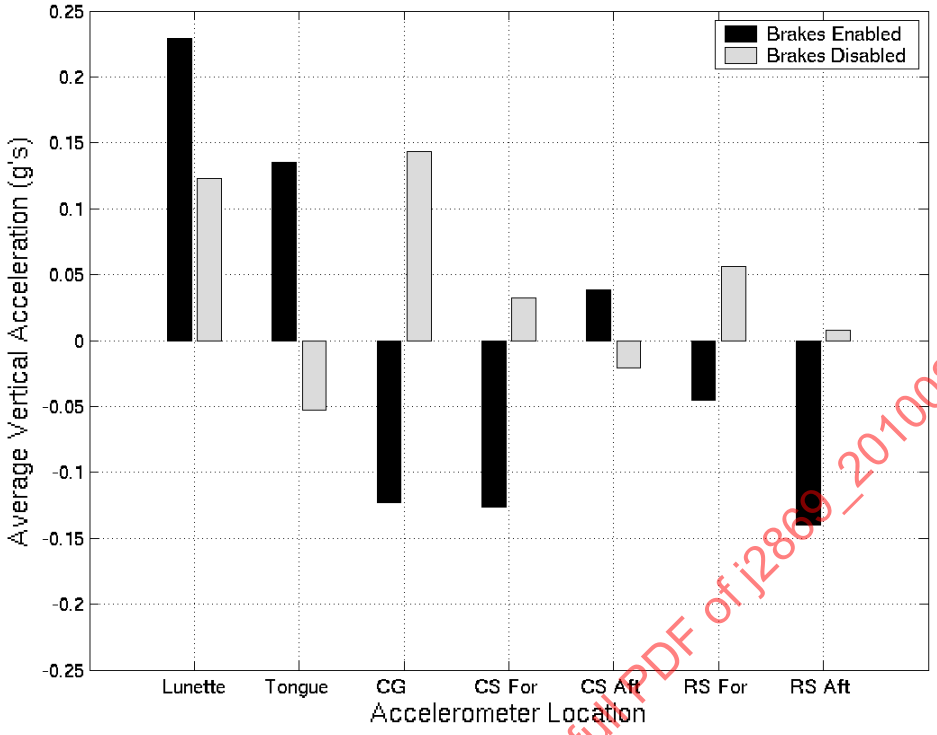

FIGURE 23 - AVERAGE VERTICAL ACCELERATIONS FOR SEVERAL TRAILER LOCATIONS

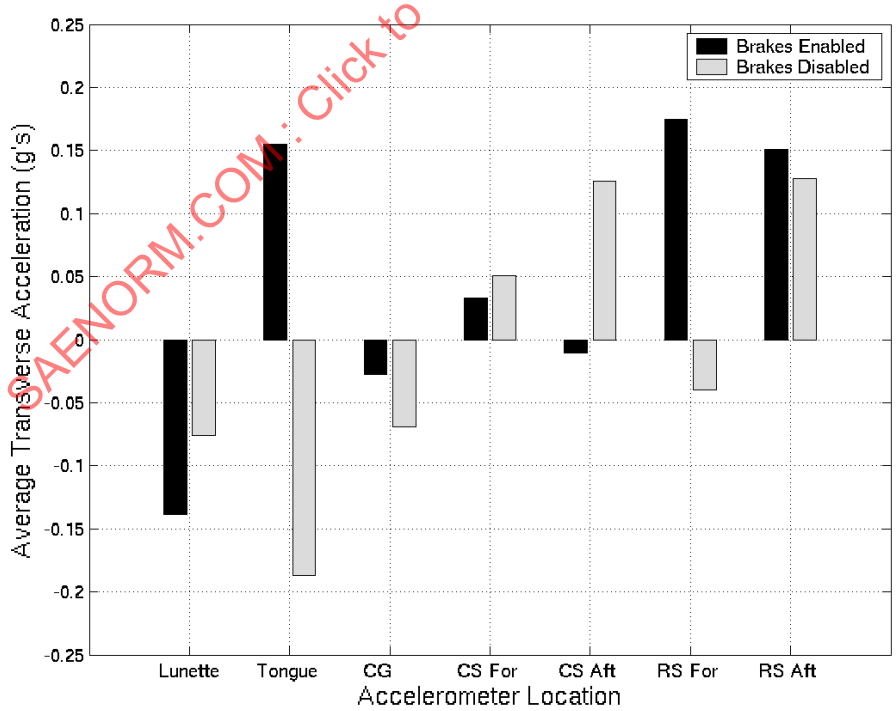

FIGURE 24 - AVERAGE TRANSVERSE ACCELERATIONS FOR SEVERAL TRAILER LOCATIONS

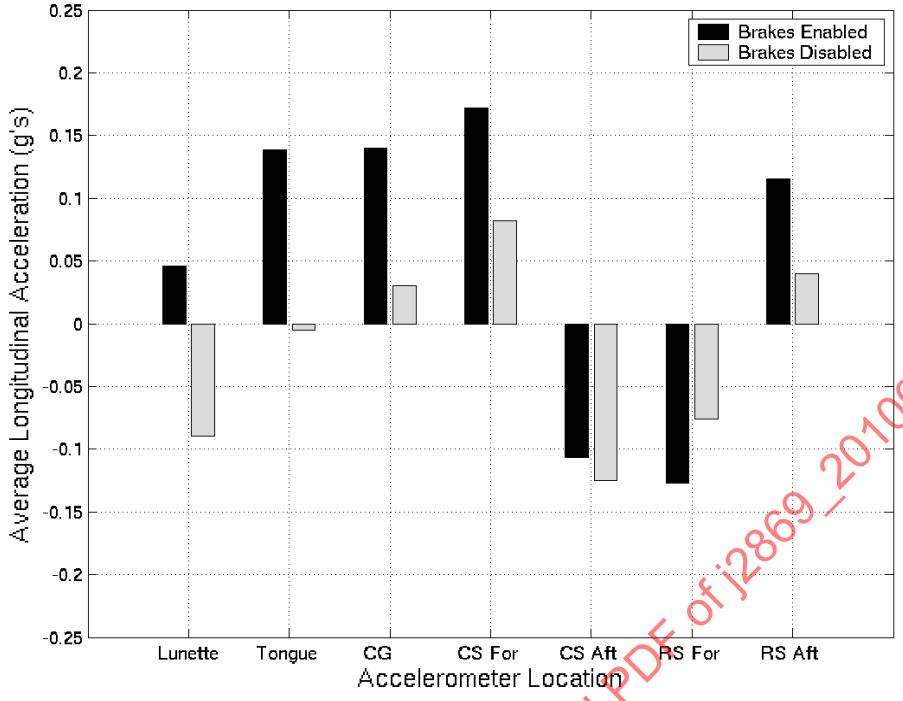

FIGURE 25 - AVERAGE LONGITUDINAL ACCELERATIONS FOR SEVERAL TRAILER LOCATIONS

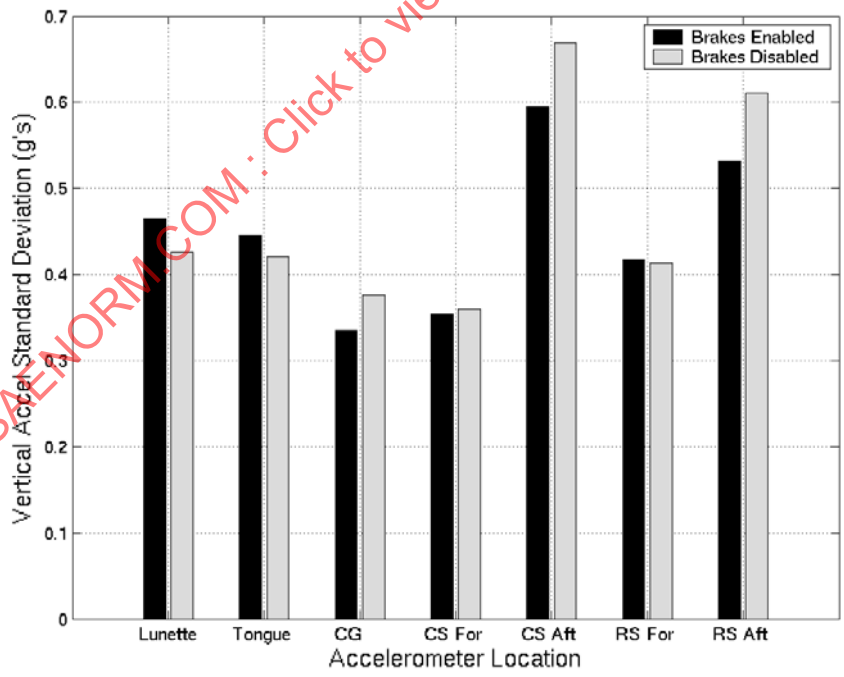

FIGURE 26 - VERTICAL ACCELERATION STANDARD DEVIATION FOR SEVERAL TRAILER LOCATIONS

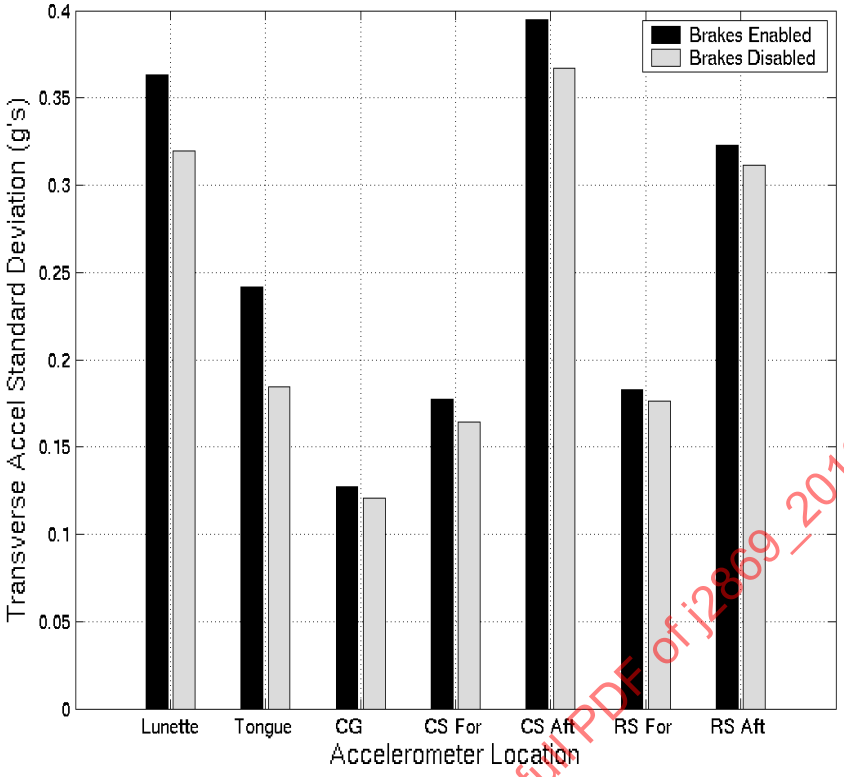

FIGURE 27 - TRANSVERSE ACCELERATION STANDARD DEVIATION FOR SEVERAL TRAILER LOCATIONS

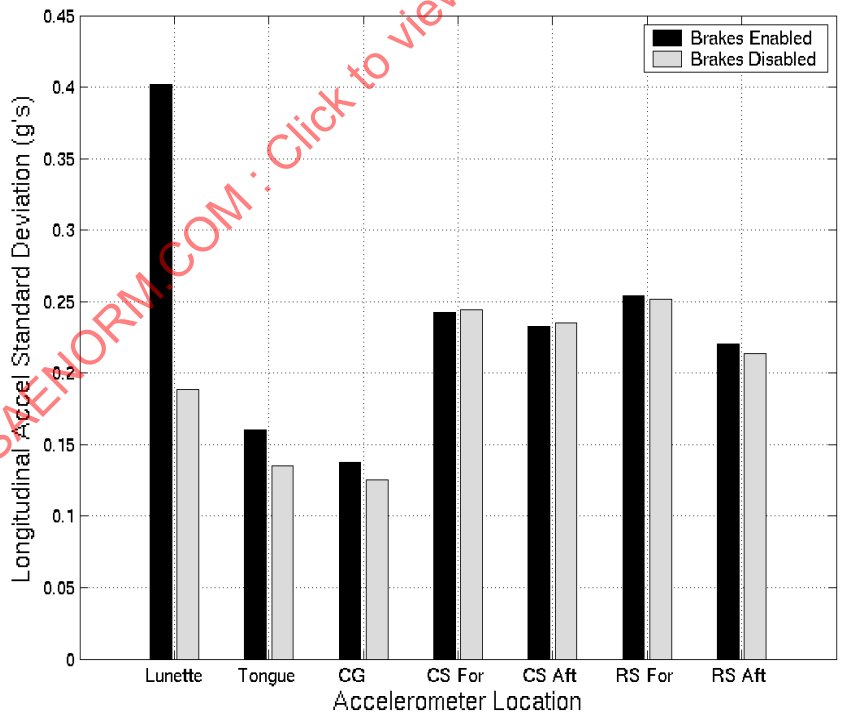

FIGURE 28 - LONGITUDINAL ACCELERATION STANDARD DEVIATION FOR SEVERAL TRAILER LOCATIONS

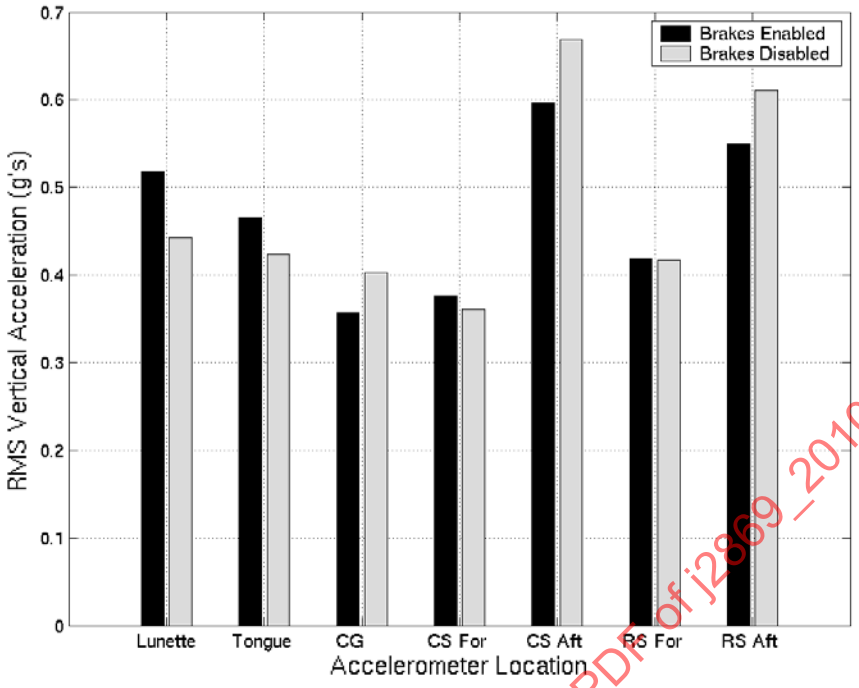

FIGURE 29 - VERTICAL RMS ACCELERATIONS FOR SEVERAL TRAILER LOCATIONS

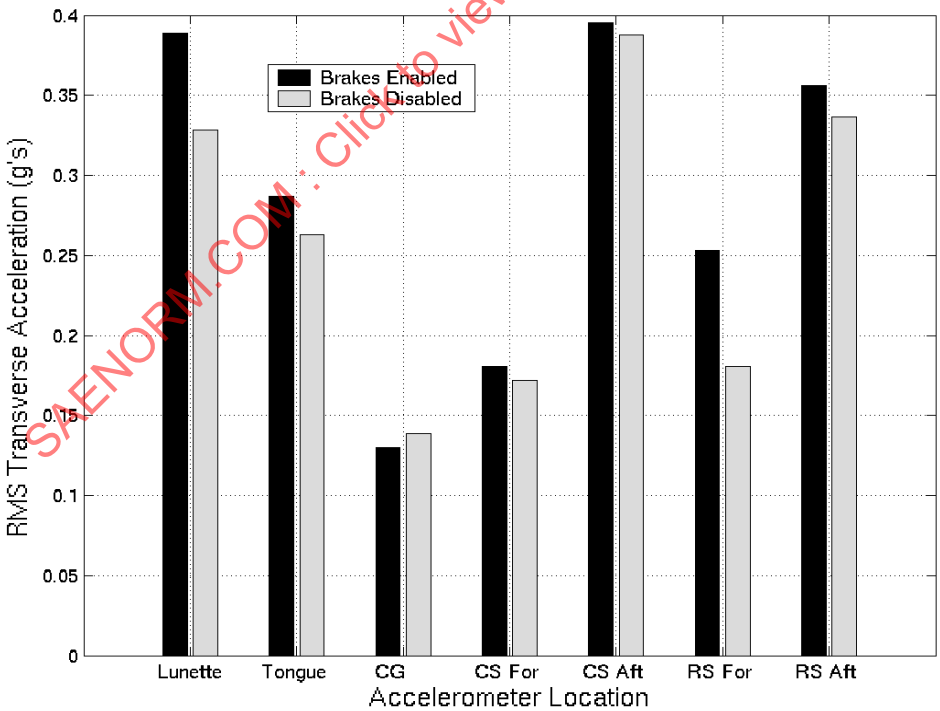

FIGURE 30 - TRANSVERSE RMS ACCELERATIONS FOR SEVERAL TRAILER LOCATIONS

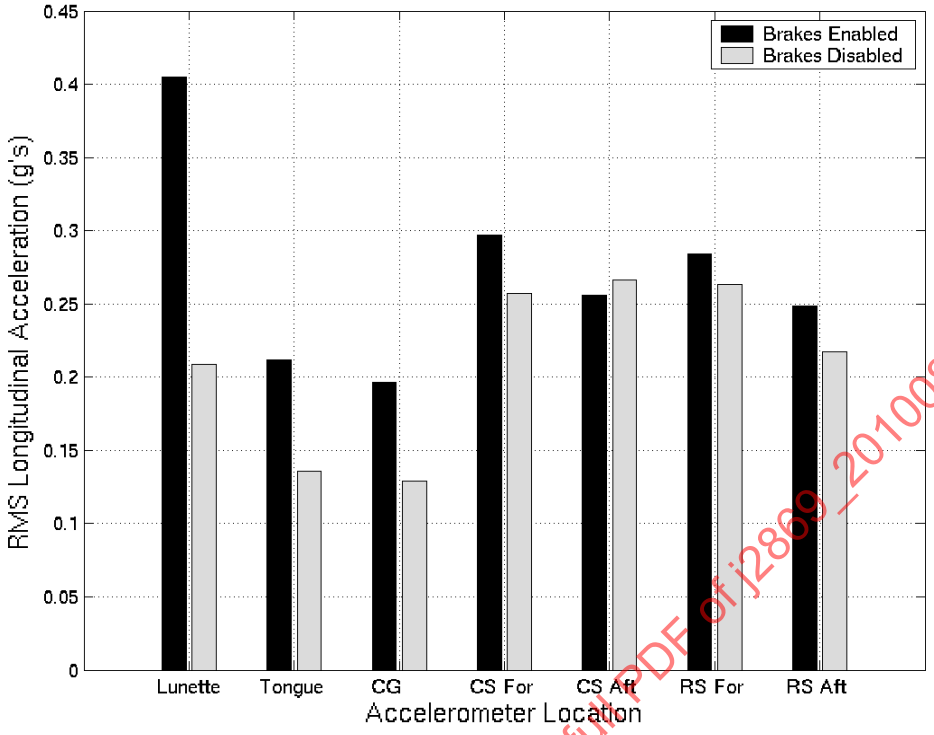

FIGURE 31 - LONGITUDINAL RMS ACCELERATIONS FOR SEVERAL TRAILER LOCATIONS

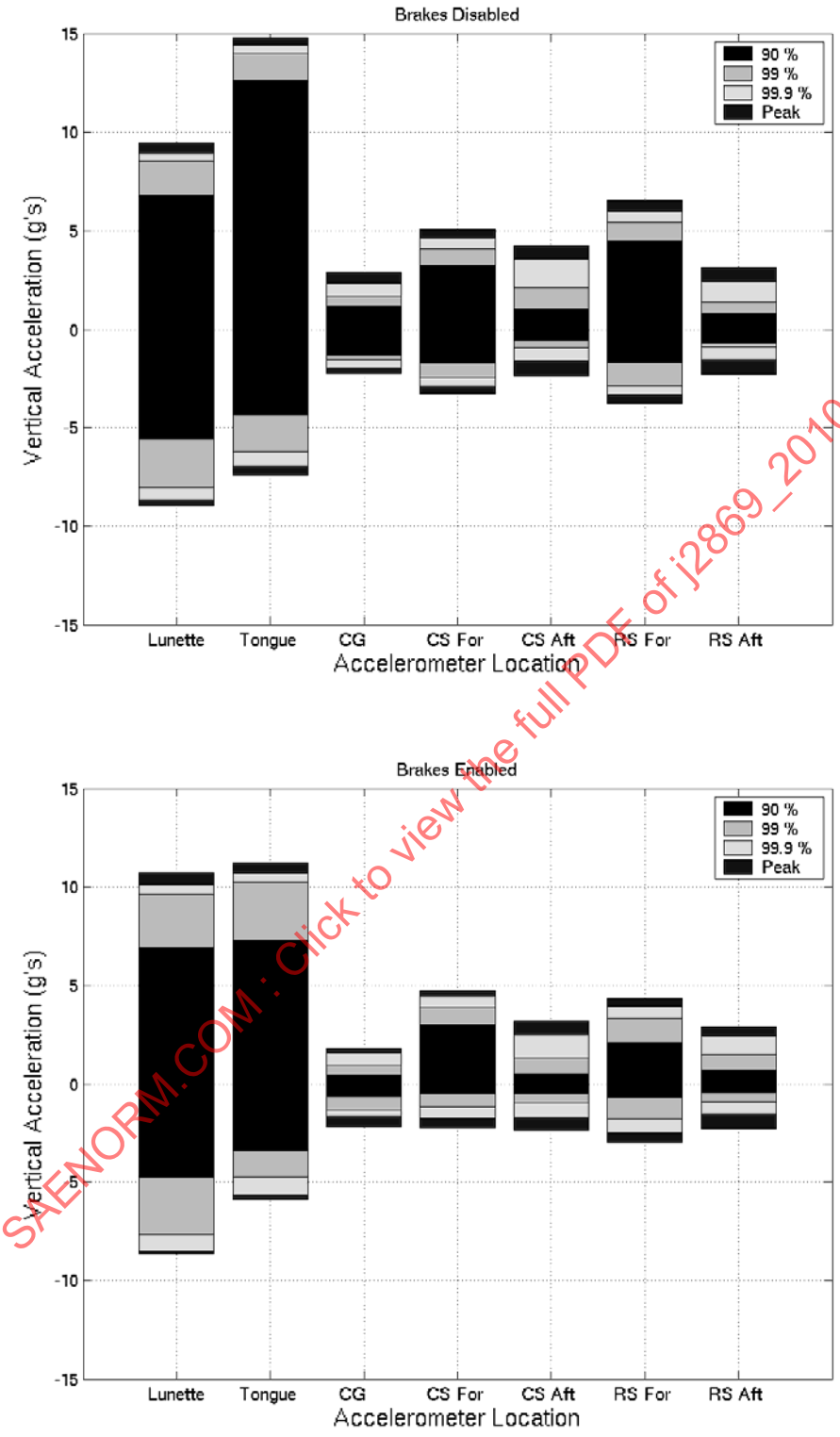

FIGURE 32 - VERTICAL ACCELERATION STATISTICS FOR SEVERAL TRAILER LOCATIONS

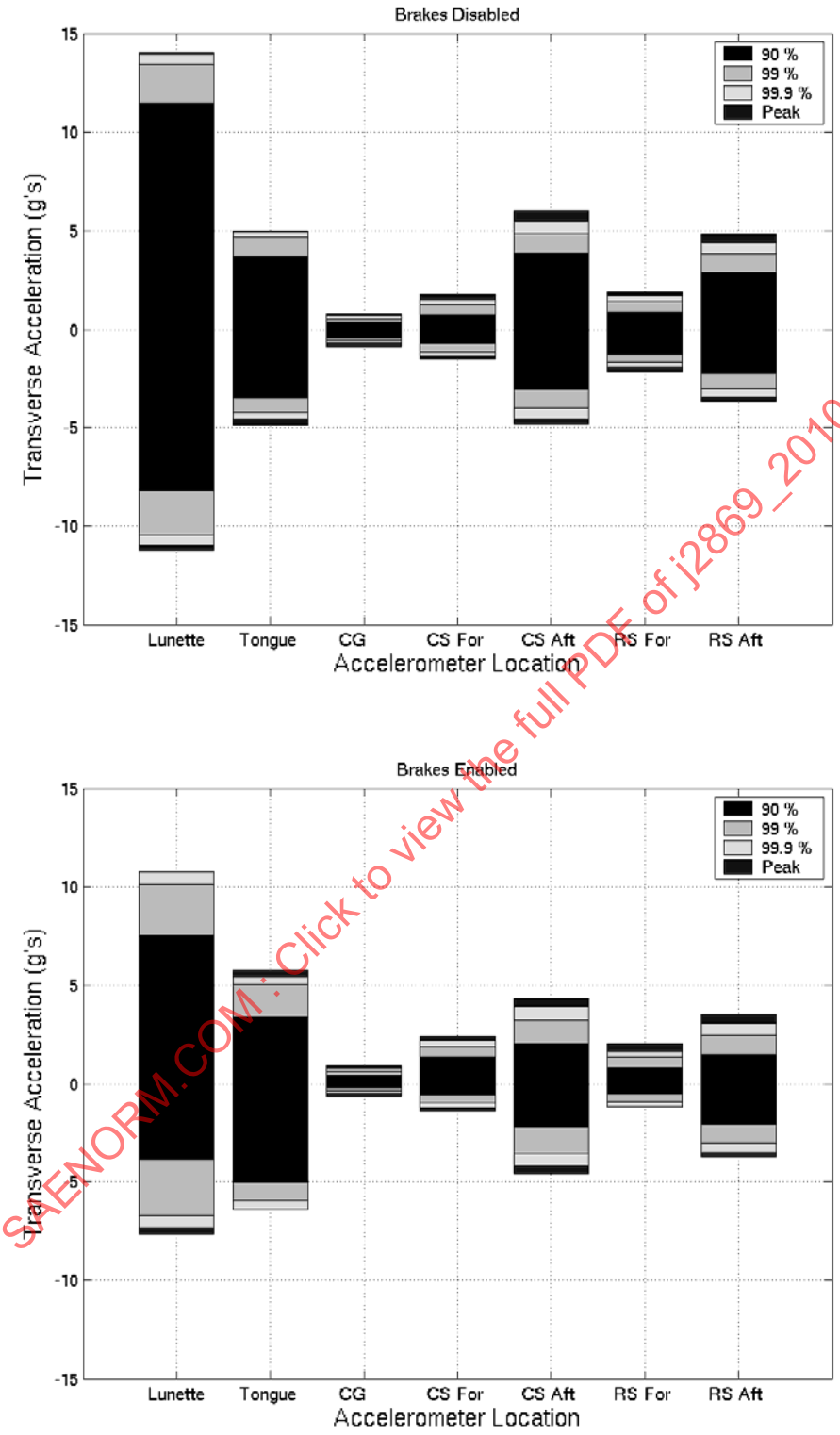

FIGURE 33 - TRANSVERSE ACCELERATION STATISTICS FOR SEVERAL TRAILER LOCATIONS

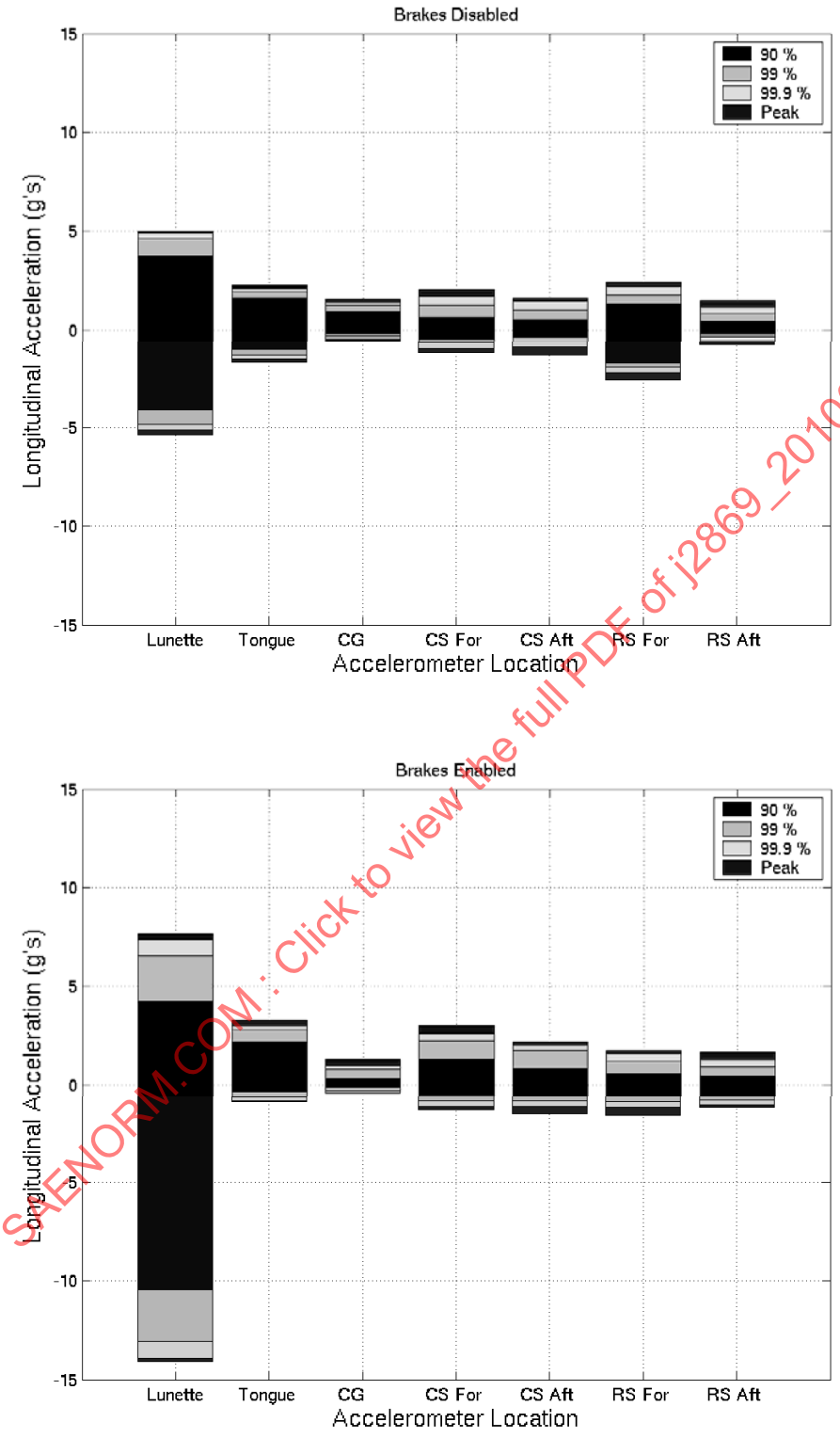

FIGURE 34 - LONGITUDINAL ACCELERATION STATISTICS FOR SEVERAL TRAILER LOCATIONS

4.2.3 Rate-gyro Data

The statistical data for the rate-gyros is provided in Tables 10 and 11 and in Figures 35 through 38. Similar to the accelerometer data, the signal average is expected to be zero; however rate-gyros are notorious for bias drift. In this case, only the pitch rate data average exceeded 0.3 degree/second.

TABLE 10 - RATE-GYRO DISTRIBUTION DATA (BRAKES DISABLED) IN DEGREE/SECOND

Description	Ave	Std Dev	RMS	+Peak	-Peak	+99.9	-99.9	+99	-99	+90	-90
CG Pitch Rate	0.5062	21.129	21.13	86.102	-86.514	82.994	-83.458	65.056	-55.193	24.919	-22.348
CG Roll Rate	0.1854	6.816	6.817	26.256	-28.468	25.406	-26.223	16.541	-16.635	8.6564	-8.4134
CG Yaw Rate	-0.0332	4.5215	4.5206	16.61	-13.423	15.613	-11.701	11.204	-9.9055	6.0071	-5.5888

TABLE 11 - RATE-GYRO DISTRIBUTION DATA (BRAKES ENABLED) IN DEGREE/SECOND

Description	Ave	Std Dev	RMS	+Peak	-Peak	+99.9	-99.9	+99	-99	+90	-90
CG Pitch Rate	0.5062	21.129	21.13	86.102	-86.514	82.994	-83.458	65.056	-55.193	24.919	-22.348
CG Roll Rate	0.1854	6.816	6.817	26.256	-28.468	25.406	-26.223	16.541	-16.635	8.6564	-8.4134
CG Yaw Rate	-0.0332	4.5215	4.5206	16.61	-13.423	15.613	-11.701	11.204	-9.9055	6.0071	-5.5888

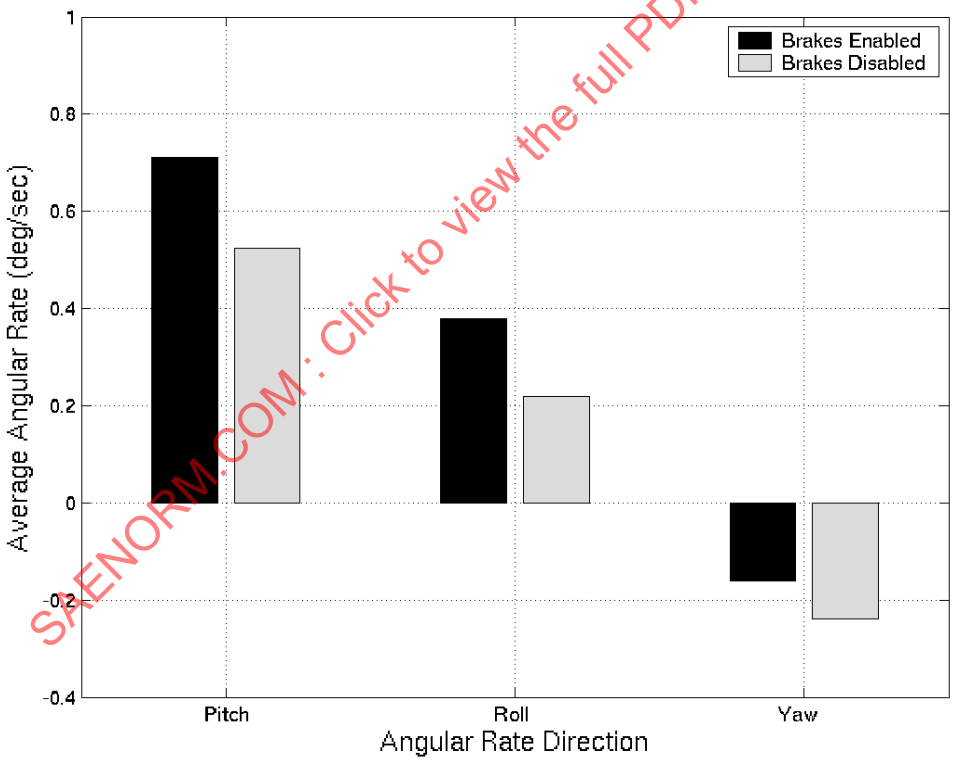

FIGURE 35 - AVERAGE RATE-GYRO ANGULAR RATES

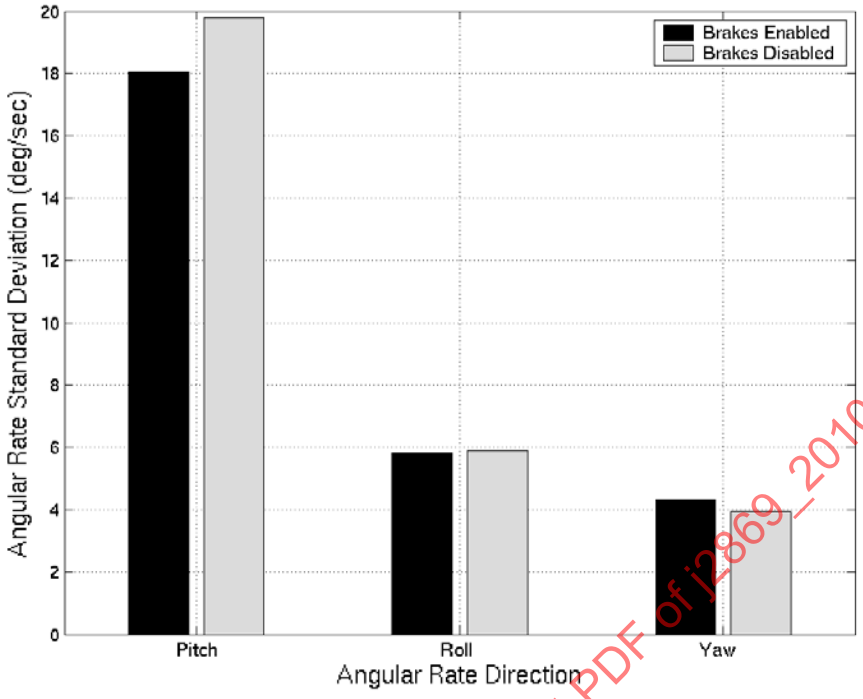

FIGURE 36 - RATE-GYRO ANGULAR RATE STANDARD DEVIATIONS

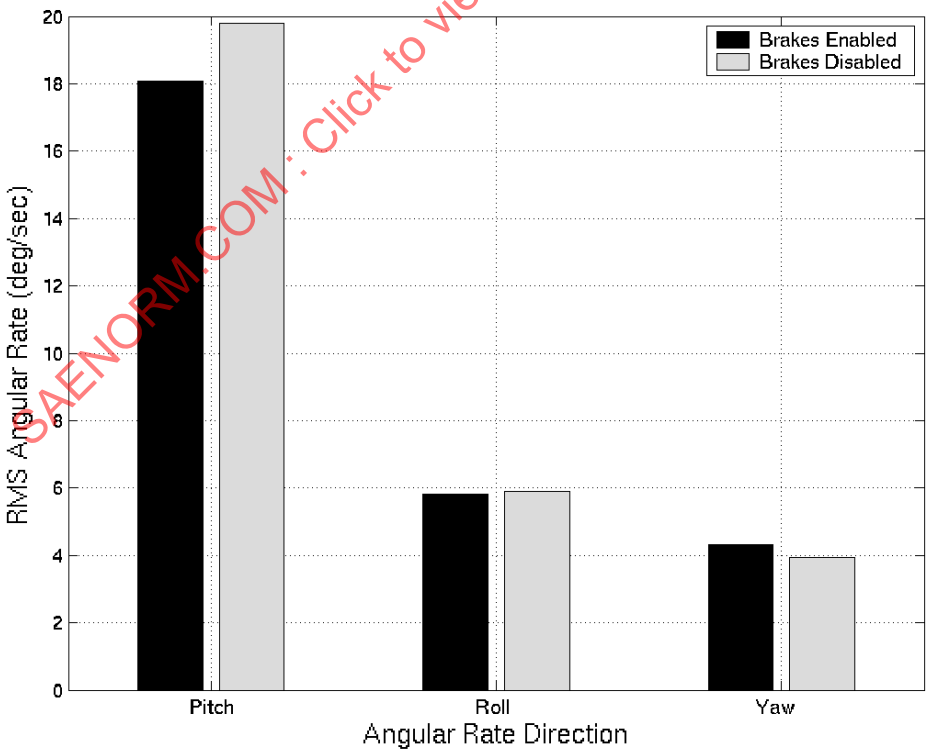

FIGURE 37 - RATE GYRO RMS ANGULAR RATES

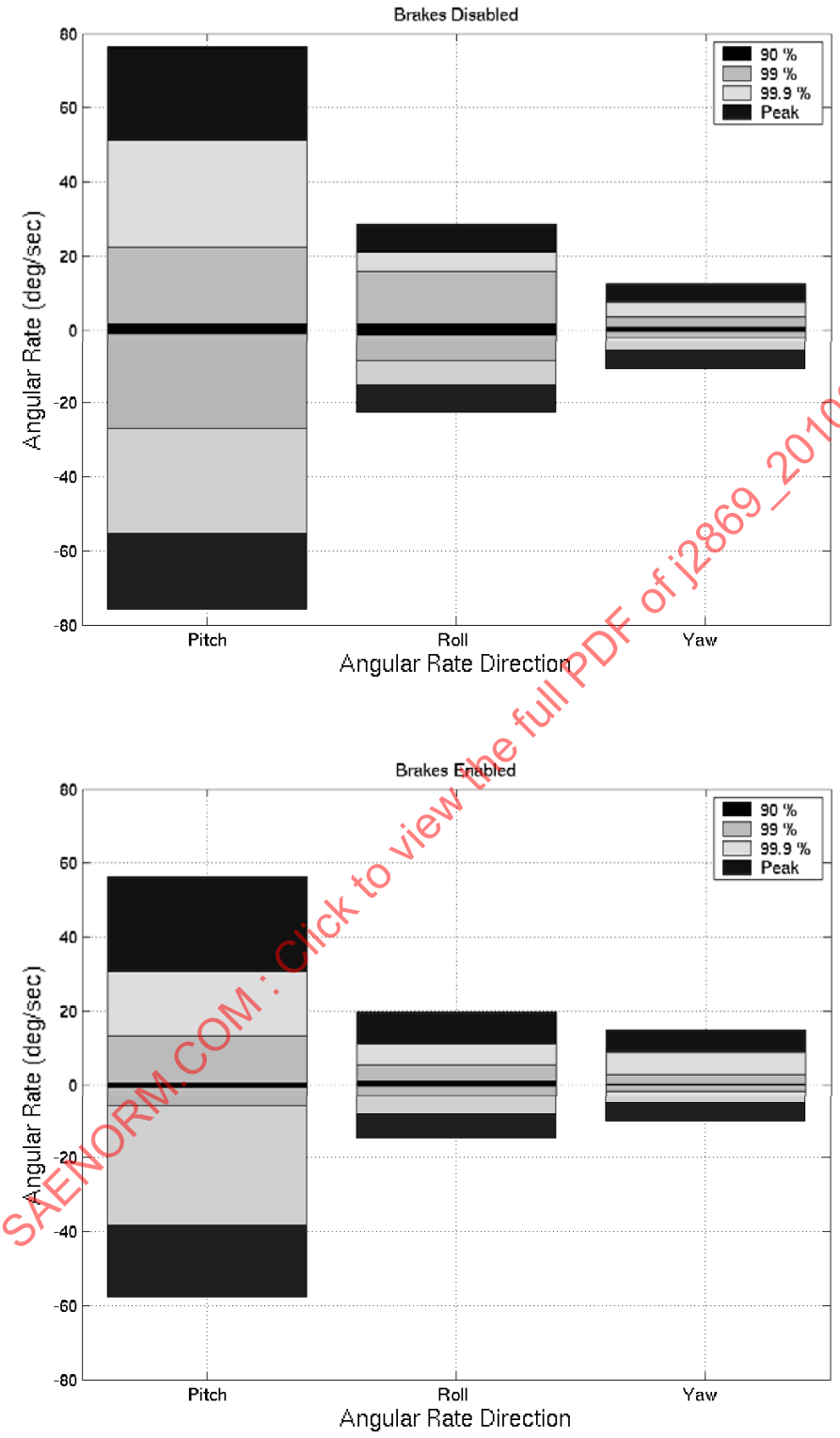

FIGURE 38 - RATE-GYR0 ANGULAR RATE DISTRIBUTIONS

FIGURE 39 - TRAILER SUSPENSION

4.2.4 Linear Displacement Transducer Data

The trailer has a trailing arm suspension, shown in Figure 39. The shock absorber is oriented approximately 90 degrees from the axis of the trailing arm, and the transducer (not shown) was co-linear with the shock. Tables 14 and 15 detail the statistics of the axle displacement with the surge brakes disabled and enabled, respectively.

The average displacements are shown in Figure 40, while the standard deviations and RMS values are shown in Figures 41 and 42. Finally, the statistical distributions are shown in Figure 43.

TABLE 12 - LINEAR DISPLACEMENT DISTRIBUTION DATA (BRAKES DISABLED) IN INCHES

Description	Ave	Std Dev	RMS	+Peak	-Peak	+99.9	-99.9	+99	-99	+90	-90
CS Shock Displacement	0.0305	0.24631	0.2481	0.8698	-0.7029	0.86805	-0.692	0.82091	-0.6177	0.3067	-0.2535
RS Shock Displacement	0.0132	0.0133	0.0134	0.0135	0.0136	0.0137	0.0138	0.0139	0.0140	0.0141	0.0142

TABLE 13 - LINEAR DISPLACEMENT DISTRIBUTION DATA (BRAKES ENABLED) IN INCHES

Description	Ave	Std Dev	RMS	+Peak	-Peak	+99.9	-99.9	+99	-99	+90	-90
CS Shock Displacement	0.0538	0.2594	0.2649	1.1323	-0.6997	1.0674	-0.6905	0.845	-0.5695	0.35244	-0.2458
RS Shock Displacement	0.0258	0.2417	0.243	1.0241	-0.5707	0.9407	-0.5581	0.7497	-0.5421	0.33093	-0.2517

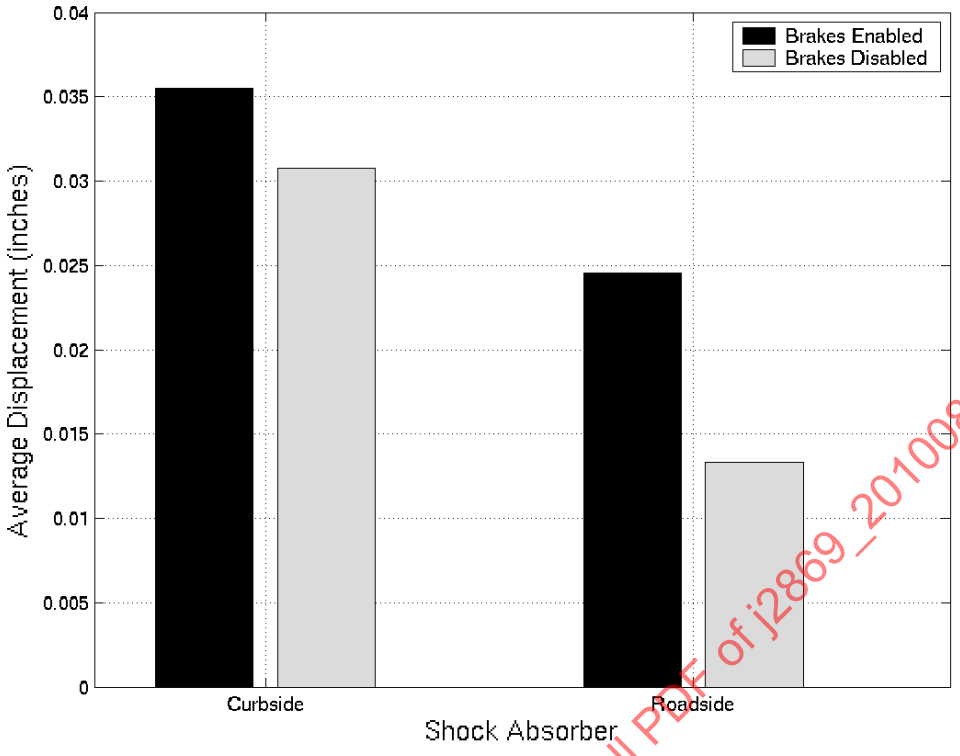

FIGURE 40 - LINEAR DISPLACEMENT AVERAGE VALUE (INCHES)

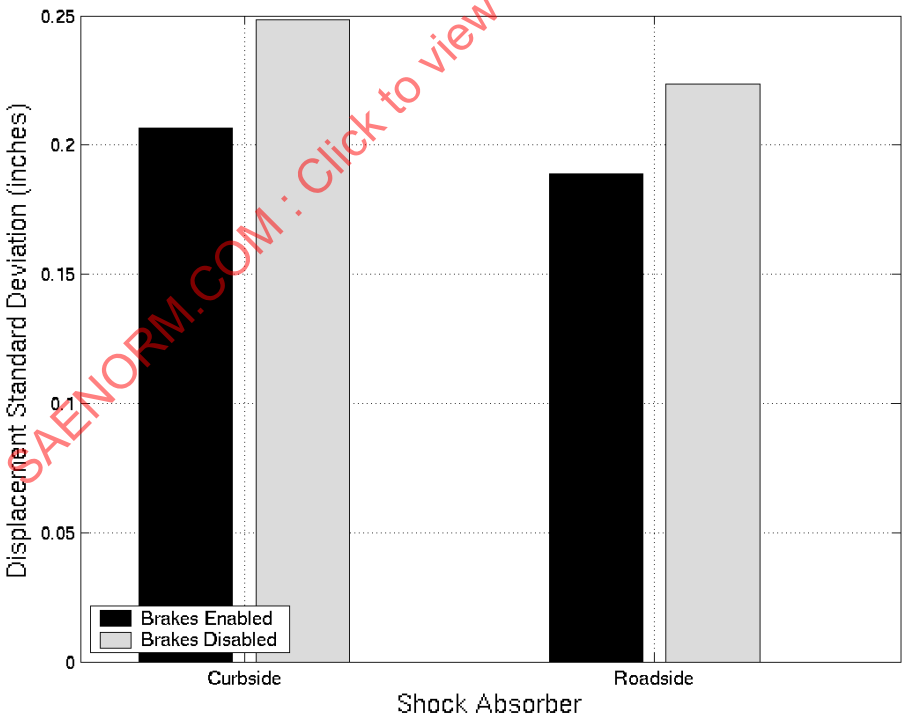

FIGURE 41 - LINEAR DISPLACEMENT STANDARD DEVIATION (INCHES)

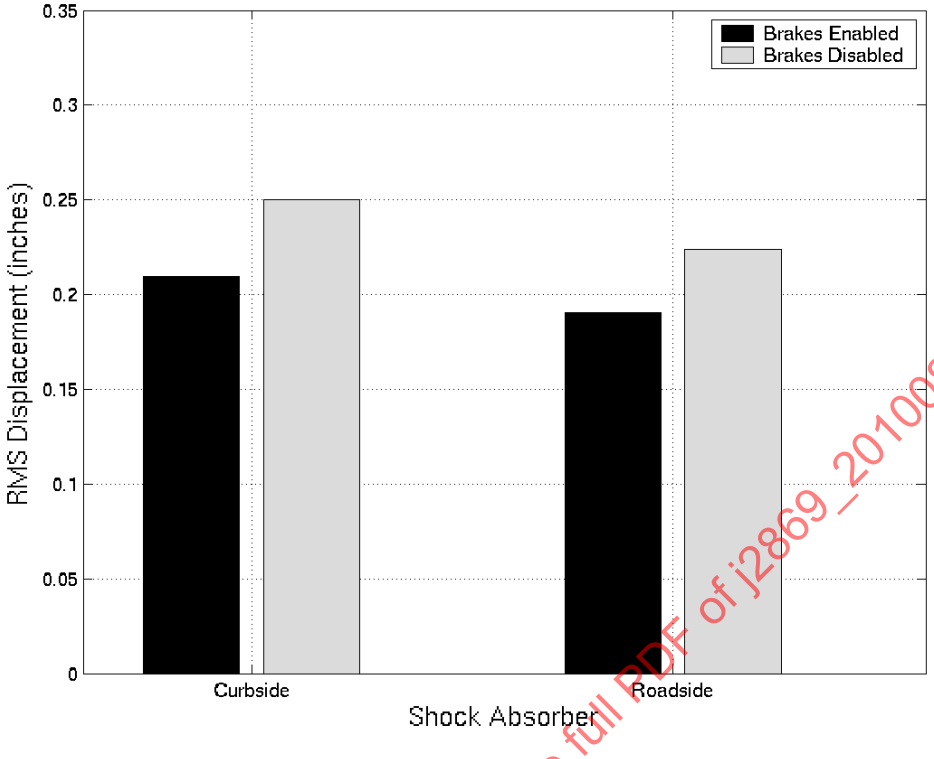

FIGURE 42 - LINEAR DISPLACEMENT RMS VALUE (INCHES)

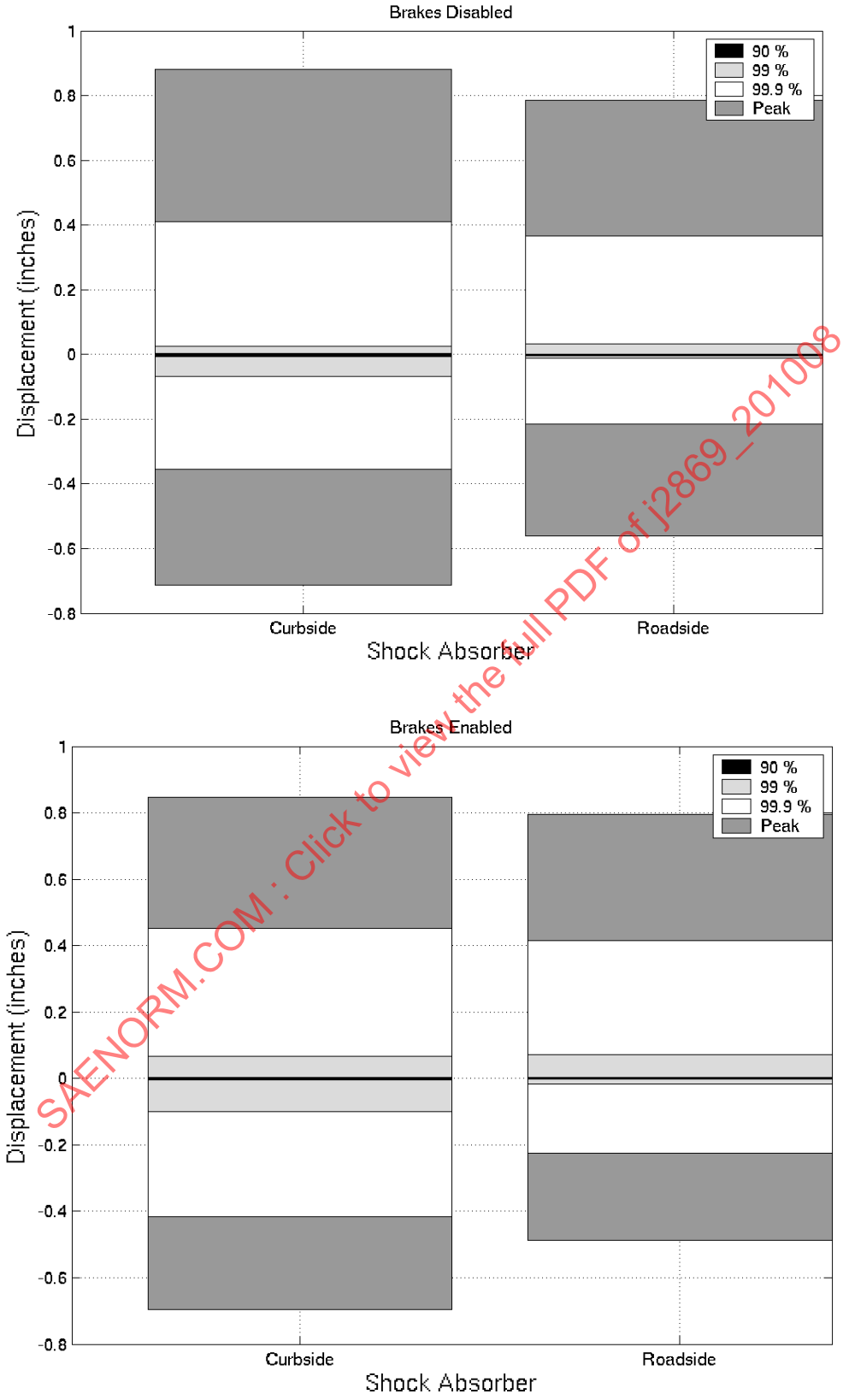

FIGURE 43 - LINEAR DISPLACEMENT DISTRIBUTIONS (INCHES)

4.2.5 Pressure Transducer Data

Analysis of the brake pressure transducer data is given in Tables 14 and 15 for the disabled and enabled brake system, respectively. It was expected that the brake system pressure would be zero when the system was disabled, but this was not true. Figures 44 through 47 provide graphical representations of the statistics to make the data more readable.

TABLE 14 - BRAKE PRESSURE DISTRIBUTION DATA (BRAKES DISABLED) IN PSI

Description	Ave	Std Dev	RMS	+Peak	-Peak	+99.9	-99.9	+99	-99	+90	-90
Master Cylinder Pressure	9.5460	0.6018	9.5650	12.1460	6.6650	11.6480	8.1600	11.1500	8.1600	10.1530	8.6580
CS Wheel Brake Pressure	-1.5119	0.6273	1.6369	4.1900	-2.6010	3.2200	-2.1160	1.7640	-1.6310	-1.6310	-1.6310
RS Wheel Brake Pressure	1.1531	0.4883	1.2522	6.1650	0.0550	5.1470	0.5640	4.1280	1.0740	1.0740	1.0740

TABLE 15 - BRAKE PRESSURE DISTRIBUTION DATA (BRAKES ENABLED) IN PSI

Description	Ave	Std Dev	RMS	+Peak	-Peak	+99.9	-99.9	+99	-99	+90	-90
Master Cylinder Pressure	-13.168	18.8242	22.9726	86.8900	-23.232	85.395	-22.236	77.422	-21.738	2.6790	-21.239
CS Wheel Brake Pressure	-16.225	16.4085	23.0752	67.7330	-24.914	66.277	-24.914	60.457	-24.429	-1.6310	-23.944
RS Wheel Brake Pressure	-16.001	16.9422	23.3035	73.3690	-25.401	71.283	-25.401	62.677	-24.382	1.0740	-23.873

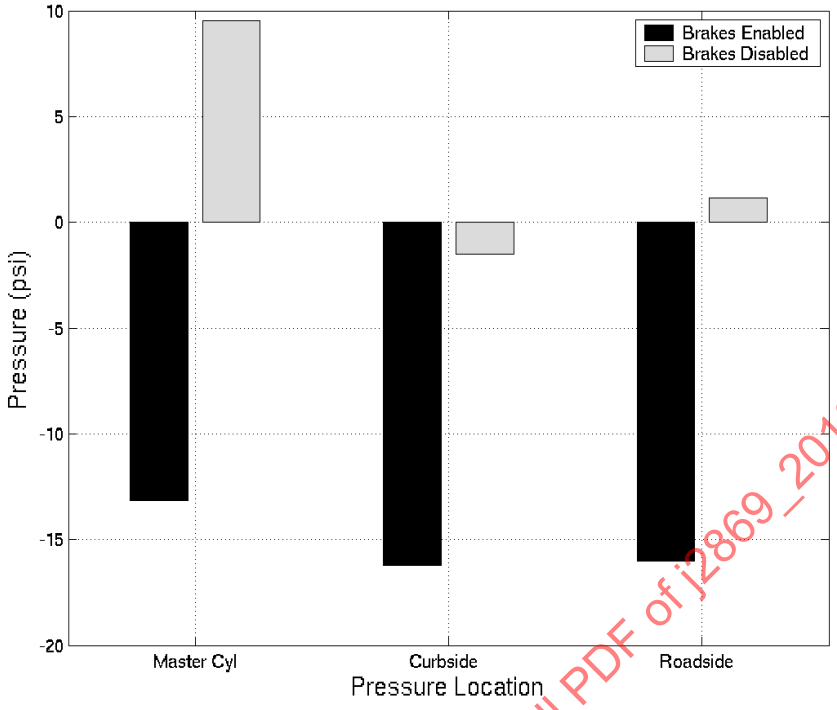

FIGURE 44 - AVERAGE BRAKE PRESSURE VALUES (PSI)

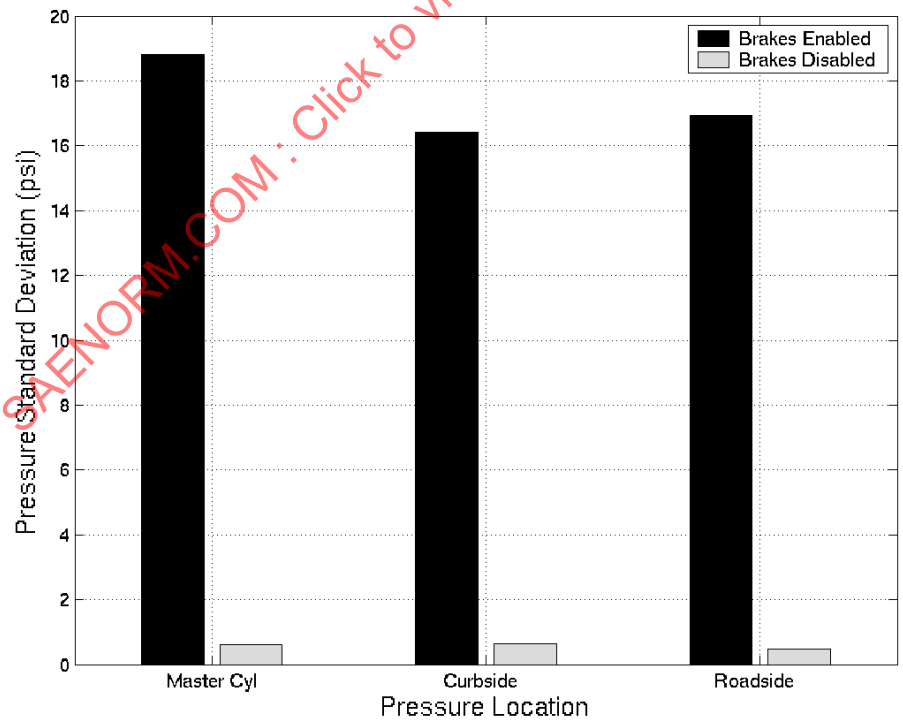

FIGURE 45 -BRAKE PRESSURE STANDARD DEVIATION (PSI)

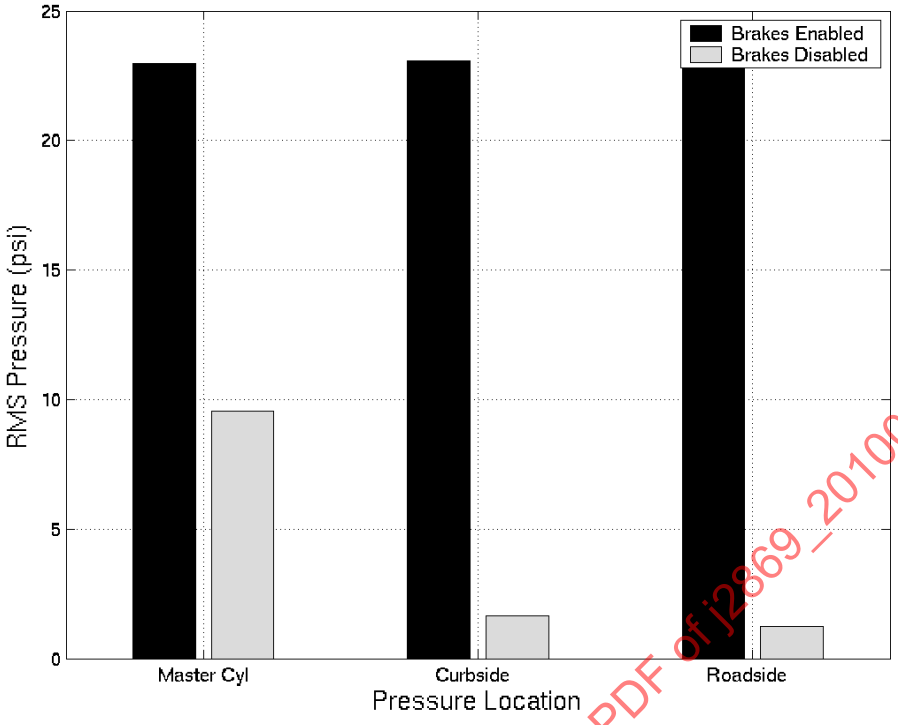

FIGURE 46 - BRAKE PRESSURE RMS VALUES (PSI)

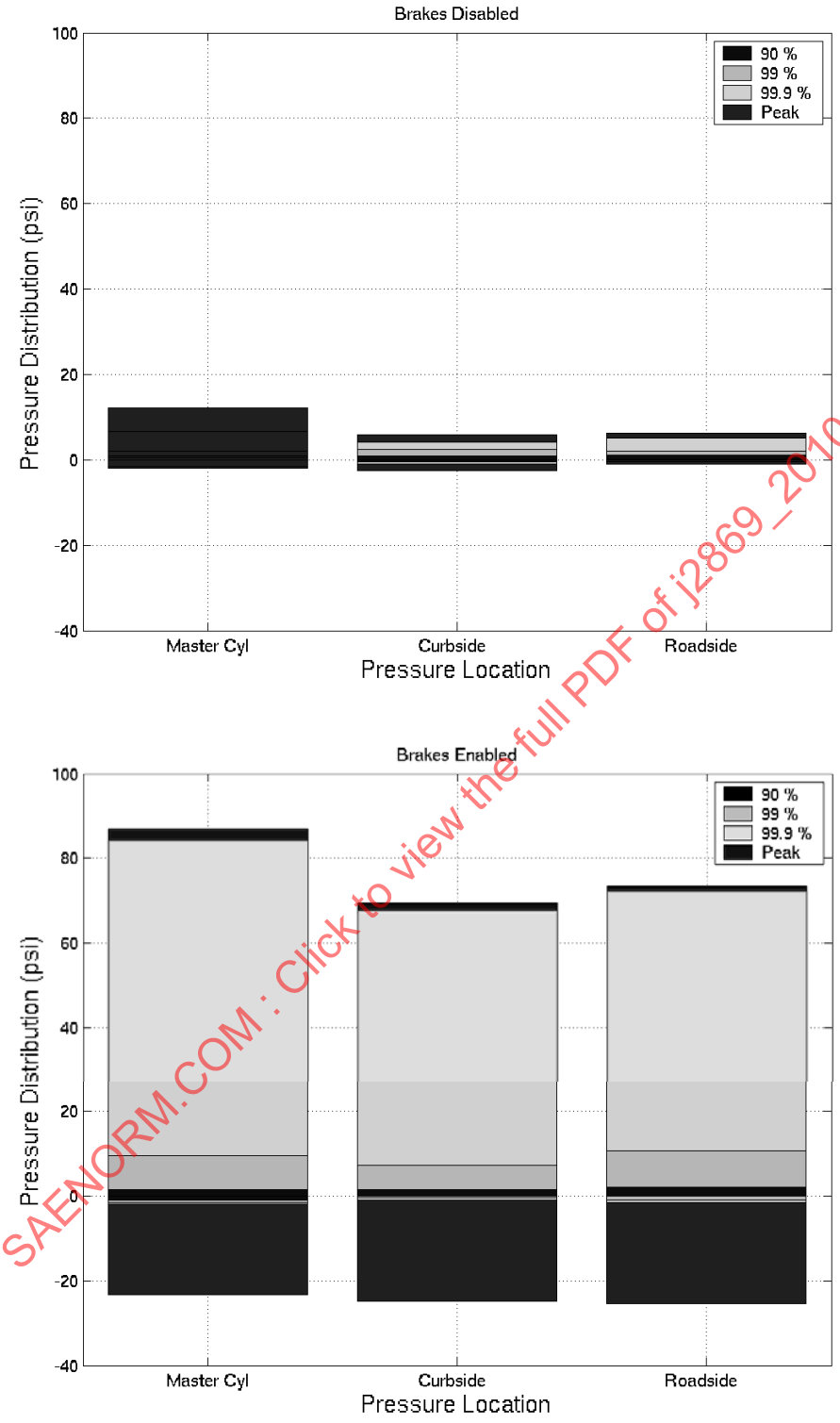

FIGURE 47 - BRAKE PRESSURE VALUE DISTRIBUTIONS (PSI)

4.3 Summary

This section presented a summary of the experimental data collected from the trailer. In particular, runs #52 (case #32, brakes enabled) and #55 (case #33, brakes disabled) were statistically examined. Both of these runs were made on the Test Course A, which was selected because it is known to cause fatigue failures for this trailer. The only problems with the data are the drifting of the transducer offsets between test runs. Further analysis of the data must zero the mean offsets for the transducers which should be generating zero averages.

5. EXPERIMENTAL ANALYSIS OF SURGE BRAKE EFFECTS

Originally, at the beginning of the project, it was assumed that the hydraulic surge brake contributed to the fatigue damage incurred by the trailer. The trailer failures occurred on Test Course A; however, the simulated position of the trailer could not be matched with experimental data since the location was not one of the measured parameters.

In order to analyze the effect of the surge brake on the trailer dynamics, Test Course B was selected as the terrain profile for this analysis since its elevation profile is normally distributed, although non-stationary, with an RMS value of 19 mm (0.75 inch). Data for Test Course B was much more reproducible, using profilometry measurements of the course elevation profile.

A listing of the instrumentation channels appears in Table 16. For this analysis, the data channels were divided into three groups; input channels, output channels, and ignored channels. The output channels consisted of the strain gauge rosette located closest to the predicted point of failure. This is identified as the center-aft rosette in the table. This is at the same location as node 425 in the FE model. Other strain gauge channels, as well as the tow vehicle speed were ignored. This left the accelerometers, rate gyros, pressure transducers, and position transducers to represent the input variables to the system.

Two test runs were performed on Test Course B where the tow vehicle/trailer speed was nominally 12 mph. On one of the test runs, the brake system was operating normally, and on the second run, the brake system was disabled by fixing the lunette and preventing actuation of the brake cylinder. Typical system pressures for normal operation are shown in Figure 48.

The brake pressure data was analyzed to look for errors and potential analysis problems. Table 17 shows a negative offset with the transducer reading when the brakes are not engaged. Table 18 shows the brake pressures to be highly correlated. The left wheel cylinder pressure is not as highly correlated with the master cylinder as the right wheel cylinder, indicating a possible bias in the system. Ideally, the losses between the master and wheel cylinders should be equivalent.

TABLE 16 - LISTING OF DATA ACQUISITION CHANNELS AND GROUPING

a	Description	Group	#	Description	Group
1	Time	Ignored	31	Lunette Trans Accel	Input
2	Btm Drwbr Cntr (T) strain	Ignored	32	Lunette Long Accel	Input
3	Btm Drwbr Cntr (45) strain	Ignored	33	Tongue Vert Accel	Input
4	Btm Drwbr Cntr (L) strain	Ignored	34	Tongue Trans Accel	Input
5	Btm Drwbr Cntr Aft (T) strain	Output	35	Tongue Long Accel	Input
6	Btm Drwbr Cntr Aft (45) strain	Output	36	CG Vert Accel	Input
7	Btm Drwbr Cntr Aft (L) strain	Output	37	CG Trans Accel	Input
8	Btm Drwbr CS Edge (T) strain	Ignored	38	CG Long Accel	Input
9	Btm Drwbr CS Edge (45) strain	Ignored	39	Curbside Front Vert Accel	Input
10	Btm Drwbr CS Edge (L) strain	Ignored	40	Curbside Front Trans Accel	Input
11	Btm Drwbr CS Edge Aft (T) strain	Ignored	41	Curbside Front Long Accel	Input
12	Btm Drwbr CS Edge Aft (45) strain	Ignored	42	Curbside Rear Vert Accel	Input
13	Btm Drwbr CS Edge Aft (L) strain	Ignored	43	Curbside Rear Trans Accel	Input
14	Top Triang Plate Corner (T) strain	Ignored	44	Curbside Rear Long Accel	Input
15	Top Triang Plate Corner (45) strain	Ignored	45	Roadside Front Vert Accel	Input
16	Top Triang Plate Corner (L) strain	Ignored	46	Roadside Front Trans Accel	Input
17	Btm Triang Plate Corner (T) strain	Ignored	47	Roadside Front Long Accel	Input
18	Btm Triang PlateA Corner (45) strain	Ignored	48	Roadside Rear Vert Accel	Input
19	Btm Triang Plate Corner (L) strain	Ignored	49	Roadside Rear Trans Accel	Input
20	Left Angle Plate Lower (V) strain	Ignored	50	Roadside Rear Long Accel	Input
21	Left Angle Plate Lower (45) strain	Ignored	51	Pitch Rate	Input
22	Left Angle Plate Lower (L) strain	Ignored	52	Roll Rate	Input
23	Left Angle Plate Upper (V) strain	Ignored	53	Yaw Rate	Input
24	Left Angle Plate Upper (45) strain	Ignored	54	Curbside Shock Length	Input
25	Left Angle Plate Upper (L) strain	Ignored	55	Roadside Shock Length	Input
26	Curbside Axle Vert Accel	Input	56	Master Cylinder Pressure	Input
27	Curbside Frame Vert Accel	Input	57	Curbside Brake Pressure	Input
28	Roadside Axle Vert Accel	Input	58	Roadside Brake Pressure	Input
29	Roadside Frame Vert Accel	Input	59	Tow vehicle speed	Ignored
30	Lunette Vert Accel	Input			

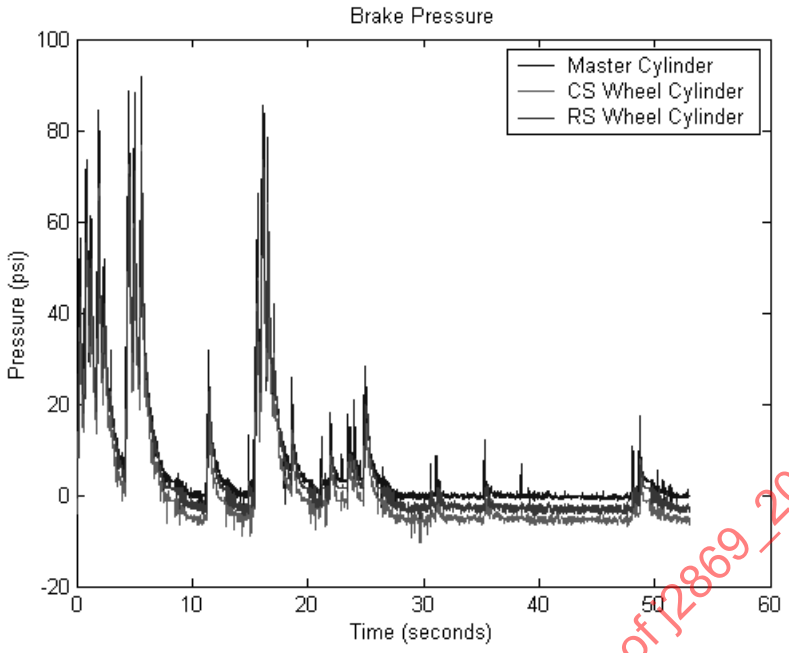

FIGURE 48 - SURGE BRAKE PRESSURES FOR TEST COURSE B

TABLE 17 - STATISTICS FOR BRAKE SYSTEM VARIABLE (BRAKES ENABLED)

	Min. Pressure (psi)	Max. Pressure (psi)
Master Cylinder	-3.61	91.74
Curbside Wheel Cylinder	-10.45	76.61
Roadside Wheel Cylinder	-4.98	75.39

TABLE 18 - CORRELATION COEFFICIENT FOR TEST COURSE B BRAKE PRESSURES

a	Master Cylinder	Right Wheel Cylinder	Left Wheel Cylinder
Master Cylinder	1.0000		
Right Wheel Cylinder (curbside)	0.9889	1.0000	
Left Wheel Cylinder (roadside)	0.9639	0.9857	1.0000

Statistics for the brake system pressure variables are given in Table 19. The variations in the master cylinder and roadside wheel cylinder pressures were very small and can be attributed to the sensor noise in data collection. The curbside wheel cylinder pressure variation was enough to affect the regression model. This was not expected since the surge brake was disabled and the brake pressures should remain constant. From the data, it cannot be determined if the variation in the curbside wheel cylinder pressure was from the sensor calibration, noise, or if the brake was dragging slightly.

TABLE 19 - STATISTICS FOR BRAKE SYSTE4M VARIABLES (BRAKES DISABLED)

	Min. Pressure (psi)	Mean (psi)	Max. Pressure (psi)
Master Cylinder	3.0166	3.5226	4.8359
Curbside Wheel Cylinder	-6.5763	-0.2867	4.5523
Roadside Wheel Cylinder	0.1862	1.5529	1.7714

5.1 Analysis Method

The two test runs, with the brakes enabled and disabled, on the same test course, need to be evaluated to compare the effects of the surge brake on the measured strain. Assuming that the brake torques, which are generated by the brake pressure, have a direct relationship to the measured strain, a regression model can be developed to represent this relationship. However, other measured responses, such as longitudinal acceleration may also affect the relationship. Given that 59 channels of data were measured for each run, and 33 of those were considered as input variables, the task of determining which of the data channels was relevant to the observed response (strain) and which were non-relevant was required to reduce the size of the dataset.

The non-relevant variables were determined by using principal component analysis and multivariate regression. Several regression models were created:

a. Brakes enabled, brake pressure data included in regression

b. Brakes enabled, brake pressure data removed from regression

c. Brakes disabled, brake pressure data removed from regression

d. Concatenated dataset, combining both brakes enabled and disabled

The regression models were developed using both the data as measured, and using the principal component variables, which form an uncorrelated, orthogonal set of predictor variables.

5.1.1 Regression Analysis

Regression analysis is used for description, control, and prediction of data. To determine the relationship between the input data and the strain; at the expected point of failure, a regression analysis was performed.

The linear regression model has the general form

$$Y = \beta_0 + \mathbf{X}^T\beta + \varepsilon = \beta_0 + X_1\beta_1 + X_2\beta_2 + \cdots + \varepsilon \quad \text{(Eq. 4)}$$

where Y is the response (output) variable, β_i are the model parameters, X_i are the independent (input) variables, and ε is an error term.

The goodness-of-fit for a regression mode can be measured by the coefficient of determination, R^2 which is simply the proportion of variance between the measured and predicted values of the response variable, Y_m. It reflects the ratio of the regression sum of squares to the total sum of squares, and is given by

$$R^2 = \frac{\sum_{i=1}^{n}(Y_{hi} - Y_m)^2}{\sum_{i=1}^{n}\left[(Y_{hi} - Y_m)^2 + (Y_i - Y_{hi})^2\right]} = \frac{\sum_{i=1}^{n}(Y_{hi} - Y_m)^2}{\sum_{i=1}^{n}(Y_i - Y_m)^2} \quad \text{(Eq. 5)}$$

where the regression sum of squares is the squared sum of the differences between the fitted value, Y_{hi}, and the mean of the fitted values, Y_m, for n observations. The total sum of squares measures the uncertainty of predicting Y when the predictor variables are not considered. The total sum of squares is the sum of both the error and regression sum of squares. The error sum of squares is the squared sum differences between the observation, Y_i, and the mean of the fitted values, Y_m. It measures the variation in the measured values, Y_i, when the predictor variables, X, are considered.

The closer the value of R^2 is to unity, the closer the observations, Y, are to the regression model and the greater the degree of linear association between the input variables, X, and the predicted response variable, Y.

5.1.2 Regression with Operational Surge Brake

Three regression models were created from the test run data where the brake system was normally operational. These regressions are used to determine which variables contained the least amount of significant information, by progressively eliminating variables from the regression and examining the effect on the R^2 value.

The first regression model predicted the transverse strain using all 33 input variables. Using stepwise regression, the value for the model is 0.7879. Eliminating the brake pressure variables from the model inputs, the value drops to 0.7832, a change of 0.0045. Progressively eliminating the roll, pitch and yaw rates, and the longitudinal lunette acceleration from the model input variables, the value drops to 0.7716. This pattern of reducing the value by eliminating input variables continues, without significantly changing, until only input variables, which are highly correlated with the predicted transverse strain, remain.

The second regression model predicted the 45-degree strain. Again using a stepwise regression model with all 33 independent input variables, the value is 0.8016. Eliminating the brake pressure variables from the model input reduced the value to 0.7957, a decrease of 0.0059. If longitudinal lunette acceleration, transverse curbside aft acceleration, and CG pitch, roll, and yaw rates are also eliminated, the value drops to 0.7862.

The third regression model predicted the longitudinal strain. Using all 33 independent input variables and a stepwise regression model the value is 0.8143. Eliminating the brake pressure variables reduced the value to 0.8081, a change of 0.0062. If the CG roll and yaw rates are then eliminated the value drops to 0.8072. If longitudinal lunette acceleration and CG pitch rate are also eliminated the value drops to 0.7951. If the transverse lunette acceleration and longitudinal ground speed are eliminated the value drops to 0.7941.

Interaction effects can be added to the regression model. An interaction effect is the effect one predictor variable X1 has on the interaction between another predictor variable X2 and the response variable Y. With the addition of pair-wise interaction effects, the regression model has the addition of all possible pairs if predictor variables multiplied together and added to X.

With the addition of interaction terms the linear regression model has the form

$$Y = \beta_0 + \mathbf{X}^T \beta + \varepsilon = \beta_0 + X_1\beta_1 + X_2\beta_2 + X_1X_2\beta_{12} + \cdots + \varepsilon \quad \text{(Eq. 6)}$$

In order to determine if there were any significant interactions between the measured brake pressures and the strains, a multivariate regression model, including pair-wise interaction effects, was created. The model for predicting transverse strain had an overall R^2 of 0.8666. The model for predicting 45-degree strain had an overall R^2 of 0.8925. The model for predicting longitudinal strain had an overall R^2 of 0.9068.

A multivariate regression with main effects and interactions was again created with the brake pressure variables eliminated. The model for transverse, 45-degree, and longitudinal strains had overall R^2 values of 0.8577, 0.8818, and 0.8975, respectively.

A summary of R^2 values resulting from the strain predictions, using the experimental data with the surge brake system operating normally, is given in Table 20. In general, the models with interaction effects had higher R^2 values than the models without interaction terms. The R^2 values for the models with the brake pressure data included had only slightly higher R^2 values than the models without the brake pressure data. For the models with interaction terms, elimination of the brake pressure data only reduced the R^2 value by an average of 0.0097. For the models without interaction terms, elimination of the brake pressure data only reduced the R^2 value by an average of 0.0056. Due to this insignificant change in the R^2 value, the brake pressure data can be eliminated without having a significant effect on the model.

TABLE 20 - R^2 VALUES FOR STRAIN PREDITION (BRAKES NORMALLY OPERATIONAL)

	With Brake Pressures		Brake Pressures Eliminated	
	Interaction	No Interaction	Interaction	No Interaction
Transverse	0.8666	0.7879	0.8577	0.7832
45-degree	0.8926	0.8015	0.8818	0.7957
Longitudinal	0.9068	0.8143	0.8975	0.8081

5.1.3 Regression with Disabled Surge Brake

A second analysis was performed to help explain and validate the findings using the data from the experimental test run where the surge brake system was disabled. This was a multivariate regression analysis, using all 33 input variables that examined the main effects only, without any interactions.

The R^2 values for the strain prediction models, with the surge brake system disabled, and the benefit of adding interaction terms to the models are shown in Table 21. The results that are labeled 'with brake pressures' are only for showing the effect of the pressure transducer noise on the regression model, since ideally the brake pressures should have been constant and would have no effect on the model. The strain prediction models that included interaction terms and no brake pressure data had overall R^2 values of 0.8049, 0.8133, and 0.8269, for transverse, 45-degree, and longitudinal strains, respectively. Without interaction terms, the models for transverse, 45-degree, and longitudinal strains, had R^2 values of 0.7280, 0.7259, and 0.7373, respectively.

TABLE 21 - R^2 VALUES FOR STRAIN PREDICTION (SURGE BRAKE SYSTEM DISABLED)

	With Brake Pressures		Brake Pressures Eliminated	
	Interaction	No Interaction	Interaction	No Interaction
Transverse	0.8121	0.7283	0.8049	0.728
45-degree	0.8206	0.7264	0.8133	0.7259
Longitudinal	0.8338	0.7383	0.8269	0.7373

The overall R^2 values when the surge brakes were disabled were lower than the R^2 values when the surge brakes were operating normally, previously shown in Table 20. The average difference in the overall R^2 value between the models, developed from data where the brake system was enabled and disabled was 0.06397, with interaction terms included, and 0.0668, with no interaction terms. In both cases, the brake pressure variables were eliminated from the input variable set.

5.1.4 Regression with Concatenated Data

To determine if the reduced R^2 values were due to information lost with the surge brake disabled and if the disabling of the surge brake had a significant effect on the strains, a third data set was analyzed. This data set was created by concatenating the two previous data sets. The brake pressure data for the test case where the surge brake was disabled was set to zero to minimize its effects. The test cases were also separated into classes based on whether the surge brake was enabled or disabled. By adding classes, the effect of the surge brake being enabled or disabled can be directly analyzed.

A multivariate regression with main effects and interactions was created for the third data set using all 33 independent variables and 1 classification variable. The models for transverse, 45-degree, and longitudinal strains had R^2 values of 0.8194, 0.8351, and 0.8512, respectively. The models showed significant interaction effects between the class variable and several other independent variables. With these interaction effects, the main effect of the classification variable could not be determined.

To determine the effect of the classification variable on the model, the classification variable was removed and another multivariate regression with main effects and interactions was created using all 33 independent variables. The models for transverse, 45-degree, and longitudinal strains had overall R^2 values of 0.8119, 0.8260, and 0.8430, respectively.

To determine the effect of the brake pressures on the model, the brake pressure variables were then removed from the model, leaving 30 independent variables. This yielded models for transverse, 45-degree, and longitudinal strains with overall R^2 values of 0.8106, 0.8243, and 0.8413, respectively. Reductions of 0.0013, 0.0017, and 0.0017 from the regression model with the brakes included, respectively.

The effect of the classification variable without the brake pressure variables was also studied by creating a multivariate regression with main effects and interactions using the 30 independent variables left after the brake pressure variables were removed and the 1 classification variable. The models for transverse, 45-degree, and longitudinal strains had R^2 values of 0.8130, 0.8271, and 0.8442, respectively. This improves 0.0011, 0.0011, and 0.0012, from the model, which had the brake system variables included, but no classification variable.

The brake pressure data parameters are small in comparison to the other parameters. The other parameters with large values do not drastically change when the brake pressure parameters are removed.

As shown in Table 22 and Table 23, the models with interaction effects that included the brake pressure data and classification variable had the highest R^2 values. For the models with interaction terms, the removal of the brake pressure variables decreased the overall R^2 value of the models with the classification variable by an average of 0.0072, and an average of 0.0015 for the models without the classification variable. Therefore, the brake pressure variables can also be eliminated without having a significant effect on the model. The removal of the classification variable from the models with interaction terms decreased the R^2 value by an average of 0.0083 for the models with all 33 independent variables and 0.0027 for the models with the brake pressure data eliminated. Therefore, the classification variable can be eliminated without having a significant effect on the model. The average R^2 value for the model with interaction terms and all 33 independent variables and one classification variable was 0.8353, with the brake pressure variables and classification variable removed, the R^2 value drops to 0.8269. The difference between the values is only 0.0083. This means that the enabling or disabling the surge brake has very little effect on the strains. Therefore, modeling of the surge brake is not necessary for an analysis of the trailer.

TABLE 22 - R^2 VALUES FOR STRAIN PREDICTION
(SURGE BRAKE SYSTEM DISABLED, BRAKE VARIABLES INCLUDED)

	Class		No Class	
	Interactions	No interactions	Interactions	No interactions
Transverse	0.8194	0.7427	0.8119	0.7427
45-degree	0.8351	0.7462	0.8260	0.7464
Longitudinal	0.8513	0.7660	0.8430	0.7655

TABLE 23 - R^2 VALUES FOR STRAIN PREDICTION
(SURGE BRAKE SYSTEM DISABLED, BRAKE VARIABLES ELIMINATED)

	Class		No Class	
	Interactions	No interactions	Interactions	No interactions
Transverse	0.8130	0.7394	0.8106	0.7394
45-degree	0.8271	0.7424	0.8243	0.7424
Longitudinal	0.8442	0.7615	0.8413	0.7611

5.1.5 Principal Component Analysis

Principal component analysis identifies variables or groups of variables that represent the driving behavior of the system. Each principal component is a linear combination of the original data and thus forms a vector basis for the data. Since there are an infinite number of ways to construct the vector basis, the principal component technique defines the basis to be constructed such that the first principal component describes the direction of maximum variance, and each succeeding principal component is defined to be orthogonal to all previous principal components and to have the maximum variance of all remaining choices.

In the context of this study, the input space X, which consists of all the accelerometer, rate gyro, linear position and brake pressure data, is transformed into an orthogonal space Z using a transformation matrix α:

$$\{z\} = [\alpha]\{x\} \quad \text{(Eq. 7)}$$

This transformation is performed sequentially by first creating a variable z_1 that is a linear combination of the input data channels x_j , and has maximum variance with respect to the data.

$$z_1 = \alpha_{11}x_1 + \alpha_{12}x_2 + \cdots + \alpha_{1p}x_p = \sum_{j=1}^{p} \alpha_{1j}x_j \quad \text{(Eq. 8)}$$

A second variable, z_2, is then created. This variable has maximum variance with respect to the remaining data, and is uncorrelated (i.e. orthogonal) to z_1.

$$z_2 = \alpha_{21}x_1 + \alpha_{22}x_2 + \cdots + \alpha_{2p}x_p = \sum_{j=1}^{p} \alpha_{2j}x_j \quad \text{(Eq. 9)}$$

This process continues until p uncorrelated principal components (PCs) are found and are arranged in order of decreasing variance. The values of the PC scores show how each input variable is weighted. The percent explained by each principal component shows how much variance is explained in by each PC.

$$\%\ \text{explained} = 100\% \times \frac{\text{variance}_j}{\sum_{j=1}^{p} \text{variance}_j} \quad \text{(Eq. 10)}$$

Since the principal components are ordered in terms of decreasing variance, the higher numbered principal components contain little information which can be used to characterize the input data. Figure 49 shows the percent explained by the first principal component is slightly over 14% of the information (variance) in the input data.

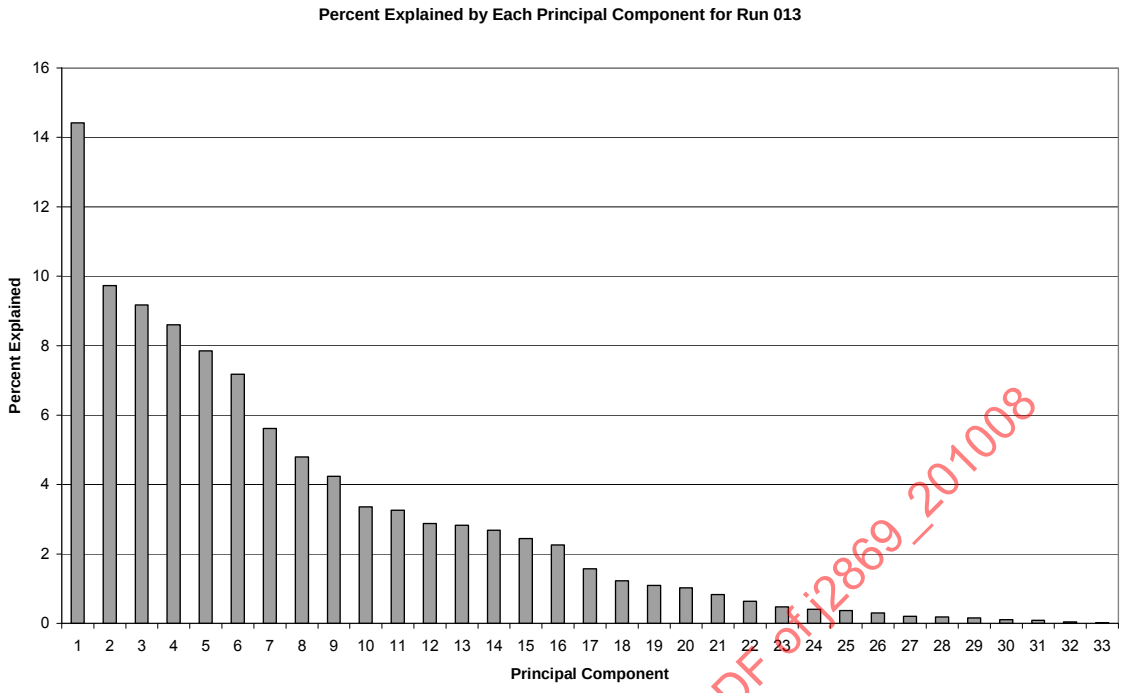

FIGURE 49 - PERCENT OF DATA EXPLAINED BY EACH PRINCIPAL COMPONENT (BRAKES ENABLED)

TABLE 24 - PRINCIPAL COMPONENT VALUES FOR THE MEASURED BRAKE SYSTEM PRESSURES

	PC SCORES				PC SCORES		
PC	Master Cyl.	CS Wheel Cyl.	RS Wheel Cyl.	PC	Master Cyl.	CS Wheel Cyl.	RS Wheel Cyl.
1	-0.1036	-0.1273	-0.1528	18	-0.0042	0.003	0.0139
2	-0.3804	-0.3742	-0.3454	19	0.005	0.0057	0.0092
3	-0.2724	-0.2644	-0.2524	20	0.0019	-0.004	-0.0084
4	0.1977	0.1963	0.2023	21	-0.0431	0.0182	0.0656
5	-0.2124	-0.2166	-0.2229	22	-0.0061	0.0004	0.0028
6	0.0076	-0.0012	-0.0069	23	-0.0043	-0.006	0.008
7	0.0014	0.0079	0.0199	24	0.0206	0.0073	-0.0302
8	-0.0309	-0.02	-0.0236	25	-0.0175	0.0025	0.0164
9	0.0182	0.0187	0.028	26	0.0123	-0.0112	-0.0005
10	0.0354	0.0559	0.0892	27	0.009	-0.0033	-0.0189
11	-0.0884	-0.1245	-0.1618	28	0.0167	-0.006	-0.0104
12	0.0116	0.0156	0.0176	29	0.013	-0.0055	-0.0025
13	0.0387	0.0529	0.0837	30	-0.2788	-0.0012	-0.2749
14	0.018	0.029	0.043	31	-0.6526	-0.0024	0.6334
15	-0.0211	-0.0297	0.0509	32	-0.0304	0.0155	0.016
16	0.0049	0.0135	0.0155	33	0.4508	-0.8142	0.4137
17	-0.0256	-0.0058	0.024				

From the PC scores, shown in Table 24 and Table 25 principal components 2, 31, and 33 are weighted toward the brake variables. Referring back to Figure 51 it can be seen that principal component 2 explains 9.73% of the information in the input data while principal components 31 and 33 explain only 0.091% and 0.020% of the information in the input data, respectively. The effect of these three principal components on the prediction of strain data is examined by regression analysis.

Also, the PC scores seen in Table 24 show that the values for the roadside and curbside cylinders are not equal. This is primarily due to the variation in the curbside wheel cylinder pressure data, which contained variations that were large enough to affect the regression models. This variation was discussed previously in Section 5.

5.1.6 Regression Using Principal Components

As in previous regression models, the data was divided into two sets, one for training the regression model, and the other to calculate the model's prediction capabilities. The error in the training model was calculated to be 68.2306 µinch/inch. The regression model was then used to predict the y test set from the x test set. The error was the calculated to be 54.8989 µinch/inch. Removing the principal components that is weighted toward the brake data (2, 31, and 33) drops the predicted strain error to 54.3704 µinch/inch, an improvement of 0.5285 µinch/inch or approximately 1%.

The effect of the principal components on the strain prediction error was determined by progressively removing each principal component from the regression, starting with the last principal component (PC). Figure 50 shows the resulting average strain error. Initially, there is decrease in the average error to a minimum of 54.3424 µinch/inch when the last 4 principal components (29-33) are removed. As additional principal components are removed, the average error in the predicted strain increases.

TABLE 25 - INPUT MEASUREMENT CONTRIBUTION TO PRINCIPAL COMPONENTS 2, 31, AND 33

Input Measurement	PC 2	PC 31	PC 33
1) Curbside Axle Accel (Vertical)	0.0875	0.0065	0.0027
2) Curbside Frame Accel (Vertical)	0.0919	-0.0117	-0.0001
3) Roadside Axle Accel (Vertical)	-0.116	0.0021	-0.0028
4) Roadside Frame Accel (Vertical)	-0.0687	-0.0045	0.0084
5) Lunette Accel (Vertical)	-0.0176	0.0042	0.0005
6) Lunette Accel (Transverse)	-0.1182	0.0077	0.0002
7) Lunette Accel (Longitudinal)	0.0149	0.0161	-0.0017
8) Tongue Accel (Vertical)	0.0352	0.024	-0.002
9) Tongue Accel (Transverse)	-0.2508	-0.0045	0.0028
10) Tongue Accel (Longitudinal)	0.1111	-0.0703	-0.0025
11) Trailer CG Accel (Vertical)	0.0467	0.0452	0.0038
12) Trailer CG Accel (Transverse)	-0.2735	0.0065	-0.0109
13) Trailer CG Accel (Longitudinal)	0.1462	-0.0765	-0.0032
14) Curbside Front Accel (Vertical)	0.1954	0.0338	-0.0058
15) Curbside Front Accel (Transverse)	-0.1446	0.0217	0.0048
16) Curbside Front Accel (Longitudinal)	-0.0968	-0.1636	0.0026
17) Curbside Rear Accel (Vertical)	0.0223	-0.0095	-0.0158
18) Curbside Rear Accel (Transverse)	-0.017	0.0342	0.0044
19) Curbside Rear Accel (Longitudinal)	-0.1116	0.2339	-0.0054
20) Roadside Front Accel (Vertical)	-0.122	0.0398	0.0148
21) Roadside Front Accel (Transverse)	-0.1174	-0.0225	0.0103
22) Roadside Front Accel (Longitudinal)	0.2106	-0.1182	-0.0009
23) Roadside Rear Accel (Vertical)	-0.0571	-0.0599	-0.0057
24) Roadside Rear Accel (Transverse)	-0.0068	-0.0101	-0.0033
25) Roadside Rear Accel (Longitudinal)	0.2242	0.2046	0.0013
26) Trailer CG Pitch Rate	-0.1617	-0.0032	0.0059
27) Trailer CG Roll Rate	-0.2535	-0.0037	0.0042
28) Trailer CG Yaw Rate	-0.0788	0.0135	0.004
29) Curbside Shock Absorber Displacement	-0.052	0.059	-0.0012
30) Roadside Shock Absorber Displacement	-0.2543	0.0964	0.0087
31) Master Cylinder Pressure	-0.3804	-0.6526	0.4058
32) Curbside Brake Pressure	-0.3742	-0.0024	-0.8142
33) Roadside Brake Pressure	-0.3454	0.6334	0.4137

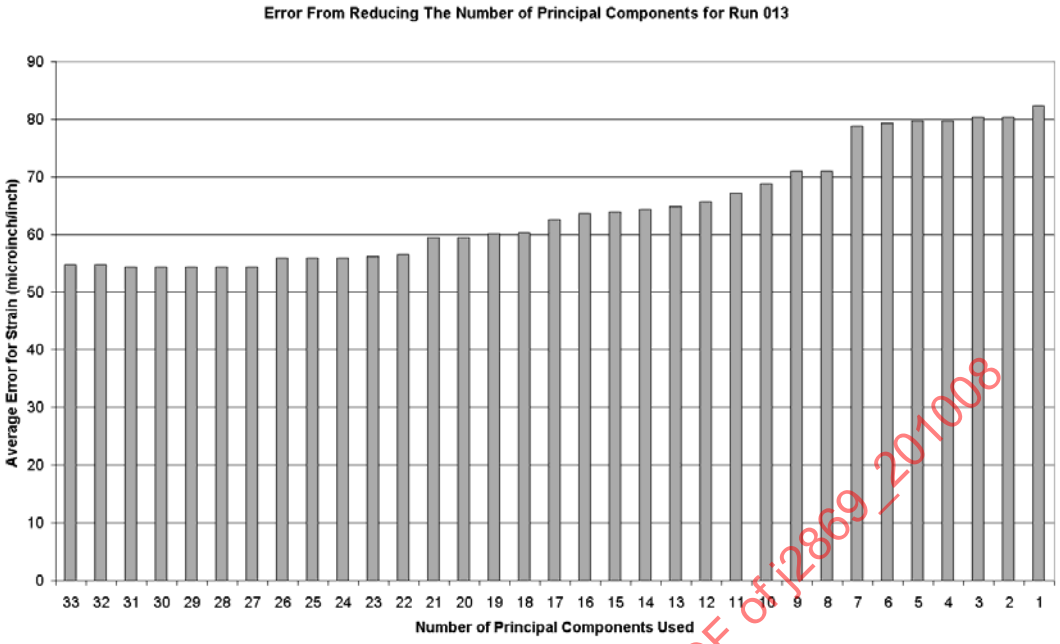

FIGURE 50 - AVERAGE STRAIN PREDICTION ERROR

A correlation coefficient matrix of the z and y training data was made to determine which principal components are most useful in predicting acceleration. The absolute values of the correlation coefficients are shown in Figure 51. From the figure it can be seen that principal components 2, 4, 8, 18, 20, 22, 24, 27, 28, 29, 30, and 32 are the least correlated, below 0.05, with the data. With these PC's removed the error only increased to 55.3605. Additional principal components: 6, 13, 14, 16, 19, 25, and 33 were removed and the error increased to 58.7066. Principal components 3, 5, and 31 were then removed and yielded an error of 58.5525.

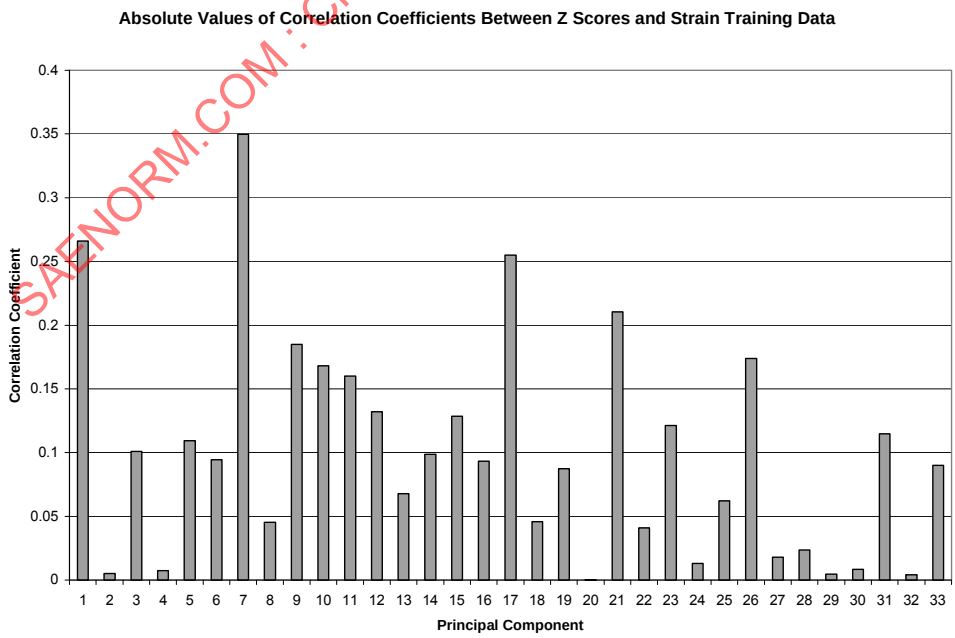

FIGURE 51 - CORRELATION COEFFICIENTS

Regression analysis of the principal components also shows that the brakes do not correlate to the longitudinal strain. The second, thirty-first and thirty-third principal components were weighted toward the brake pressure data. The second principal component did explain a large percentage of the input data relative to the other principal components, but it did not correlate to the strain data. The thirty-first and thirty-third principal components were slightly correlated to the strain data, but explained a negligible percentage of information from the input data. The removal of these three principal components reduced the average error by 0.5205 µinch/inch, reinforcing the conclusion that the activation of the surge brake does not affect the life of the trailer.

5.2 Experimental Analysis Conclusion

It was originally hypothesized that the hydraulic surge brakes contributed to the fatigue-related failures of the trailer drawbar. The trailer was instrumented and test data was acquired for a variety of different terrain profiles and tow vehicle speeds. One particular terrain profile, Test Course B, at a nominal speed of 12 mph, was selected to develop linear regression models between some of the measured data and the measured strain response near the expected point of failure.

Predictive models of the strain response for longitudinal, transverse and 45-degree strains were developed, using accelerations, angular rates, shock absorber displacement and brake pressure as the input variables. In all cases, the brake pressure variables had little effect on the goodness-of-fit of the model, and in some cases, eliminating the brake pressure variables improved the goodness-of-fit. This identifies the original hypothesis as incorrect. The brake pressure and the surge brakes have little effect on the strain.

In order to further verify this, a principal component analysis was performed for the group of input variables. The principal component analysis identified groups of variables, which represent the driving behavior of the system. In this case, only one principal component, the second one, contained both a large contribution from the brake pressures, and a high degree of variance. Two other principal components, the 31st and the 33rd, had little associated variance, but large contributions from the brake pressure variables. Another regression model to predict the longitudinal strain was developed from the set of principal component variables. This model showed that the ability to predict the strain improved slightly when the three principal components (2, 31, and 33) were removed. Again this shows little influence by the brake pressures on the strain near the expected point of failure.

Finally a correlation was done between the principal component variables and the measured longitudinal strain. This showed that the second principal component, which did explain a large percentage of the input data, was not correlated with the strain gauge output. The brake system pressures did not contribute to the measured response. The input variables that did show a correlation to the measured strain were primarily composed of the vertical accelerations and yaw rate.

6. DYNAMIC MODEL COMPARISON

The first step in validating the PoF computer simulation models is to compare the accelerations predicted by the multi-body dynamics model implemented in DADS to the experimental data. The intent of this project was to generate the flexible multi-body dynamics model directly from the CAD and FEA models.

Two versions of the DADS model were implemented: one that did not include the surge brake, and another that implemented the surge brake model using Simulink. As was shown previously through mathematical regression, the use of the surge brakes did not correlate with the strain gauge output. Due to this, and also due to the faster execution speed, the DADS-only version of the trailer model was used for validation.

6.1 Modifications to Dynamic Analysis Design System (DADS) Model

The DADS model was modified to include points of interest that are close to the points where the accelerometers were attached to the trailer during testing. Since these points were not known precisely, they were estimated from the pictures of the test configuration and the Pro/E CAD model. Most of the accelerometers were attached to the cargo bed or trailer frame, which were modeled using flexible bodies in the DADS simulation. These accelerometers must be associated with a node from the finite element model.

Table 26 lists the CAD model coordinates of the accelerometers with respect to the body on which they are attached. The closest node number from the finite element mesh is listed for accelerometers attached to the trailer frame, which is modeled as a flexible body. Since these nodes do not exactly correspond to the selected locations, the distance from the tabulated location to the FE node is also given. The modified model is shown in Figure 52, where triads show the CAD model coordinates, and circles show the FE nodal coordinates. All of the distances are less than the original uncertainty in location.

TABLE 26 - ACCELEROMETER LOCATION IN DADS MODEL

Location	Body	'X' (in)	'Y' (in)	'Z' (in)	Node #	(in)
Trailer CG	Frame	-32	0	4	5995	1.74
Left Front Corner	Frame	-0.2	40	22	4615	0.458
Right Front Corner	Frame	-0.2	-40	22	4547	0.458
Left Rear Corner	Frame	-85	40	22	4599	0.964
Right Rear Corner	Frame	-85	-40	22	4530	0.964
Drawbar	Frame	27	0	-4	4099	0.79
Lunette	Lunette	-1	0	-9	rigid	

No GPS data was acquired during the experimental testing, so it is not possible to directly relate the position and velocity of the trailer to its actual location on the test courses. This limits the comparison of the simulation and experimental data to PSD frequency domain comparisons and to statistical distributions in the time domain. For all comparisons, the simulation data was generated at 126.58 Hz, and the experimental data, with an original sample rate of 1262.626 Hz, was decimated by a factor of 10 to obtain the same frequency. The simulations were run for a total of 25 seconds, of which the first 3 seconds were discarded since the model was undergoing dynamic settling to an equilibrium condition. Thus, each simulation sequence is a total of 22 seconds in length. The total time sequence of the experimental data was used to formulate the PSD's and the statistical distributions. This was done due to the lack of knowledge of the trailer position, relative to the test courses, and the non-stationary terrain elevation statistics of the test courses. The frequency range for the PSD's was plotted with a limit of 25 Hz, since it was known that the fatigue damage occurred for low frequencies, and also that data above this value was questionable.

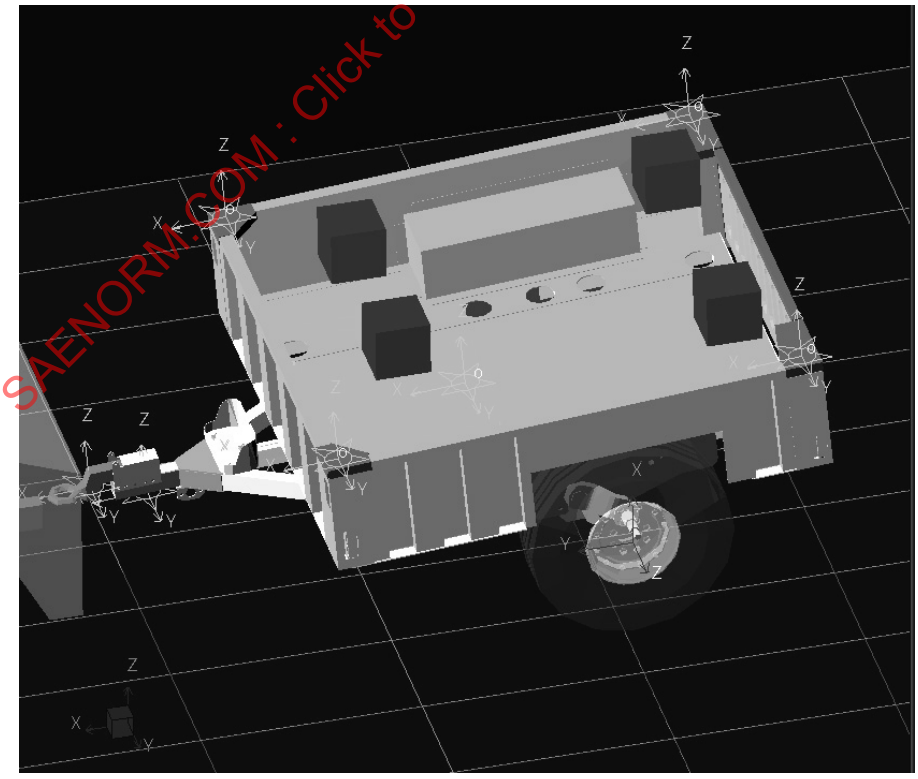

FIGURE 52 - MODIFIED DADS MODEL WITH POINTS OF INTEREST

6.2 Test Course A Comparison

The Test Course A comparison was performed for a nominal speed of 15 mph (14.75 mph average actual). This course was selected for simulation comparisons because it was known that fatigue failures of the trailer occurred for fairly low mileage tests on the course. The test course elevations were measured every 3 inches for the length of the course using the ATC profilometer and detrended using standard procedures.

PSD's of the accelerations for the trailer center-of-gravity (CG) are shown in Figures 53 through 55. Given that these figures are plotted using a decibel scale, they do not show a particular goodness of fit, except for the vertical accelerations for frequencies less than 5 Hz.

Statistical distributions of the CG acceleration data are shown in Figure 56. The major finding here is that the 90th percentile distribution is much greater for the experimental data than for the simulation data. Also, the transverse accelerations are much less for the simulation model than for the experimental data.

PSD's of the angular velocities of the trailer are shown in Figures 57 through 59. The trailer roll rate, shown in Figure 57, appears to match reasonably up to 5 Hz, but the simulation model shows a resonance peak at approximately 15 Hz, which is not present in the experimental data. The trailer pitch rate data, shown in Figure 58, matches very well up to 15 Hz, and does not significantly deviate until about 22 Hz, which is higher than the frequency of the body vibration modes included in the flexible body model. The worst match by far, is the yaw rate PSD, shown in Figure 59. There are definite problems with the yaw rate simulation and experimental data comparisons, even at 0 Hz.

Statistical distributions of the angular velocities are shown in Figure 60. Roll and pitch velocities are very comparable between the simulation and experimental data, however the simulation yaw velocities show smaller magnitudes.

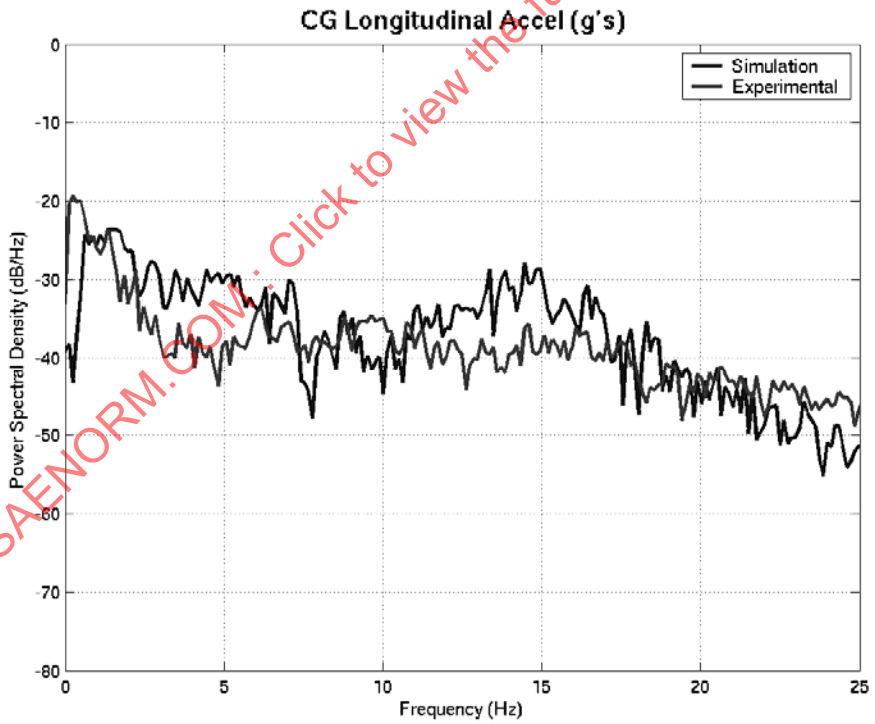

FIGURE 53 - TEST COURSE A CG LONGITUDINAL ACCELERATION PSD COMPARISON

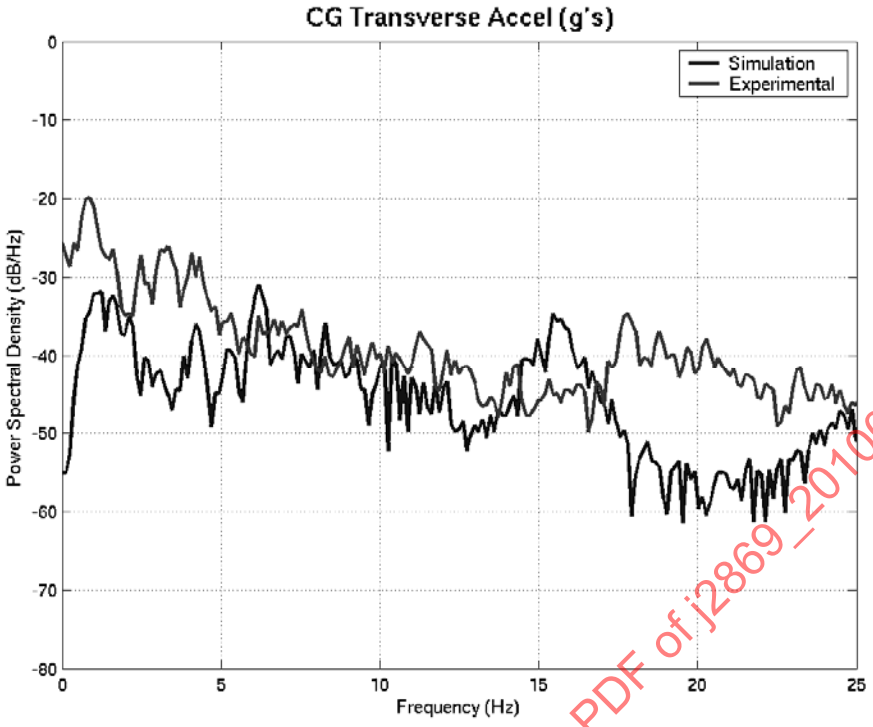

FIGURE 54 - TEST COURSE A CG TRANSVERSE ACCELERATION PSD COMPARISON

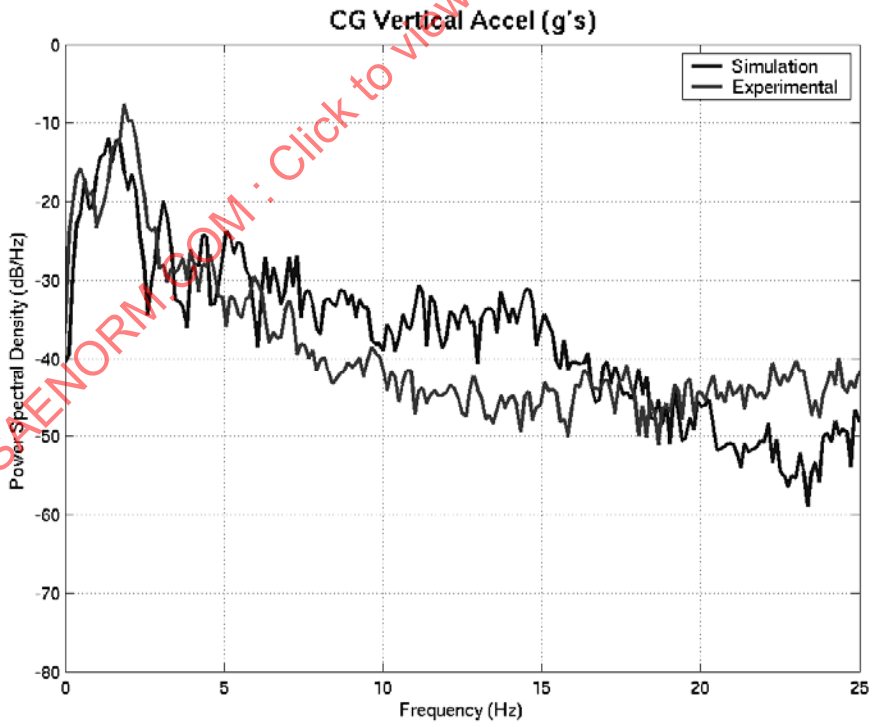

FIGURE 55 - TEST COURSE A CG VERTICAL ACCELERATION PSD COMPARISON

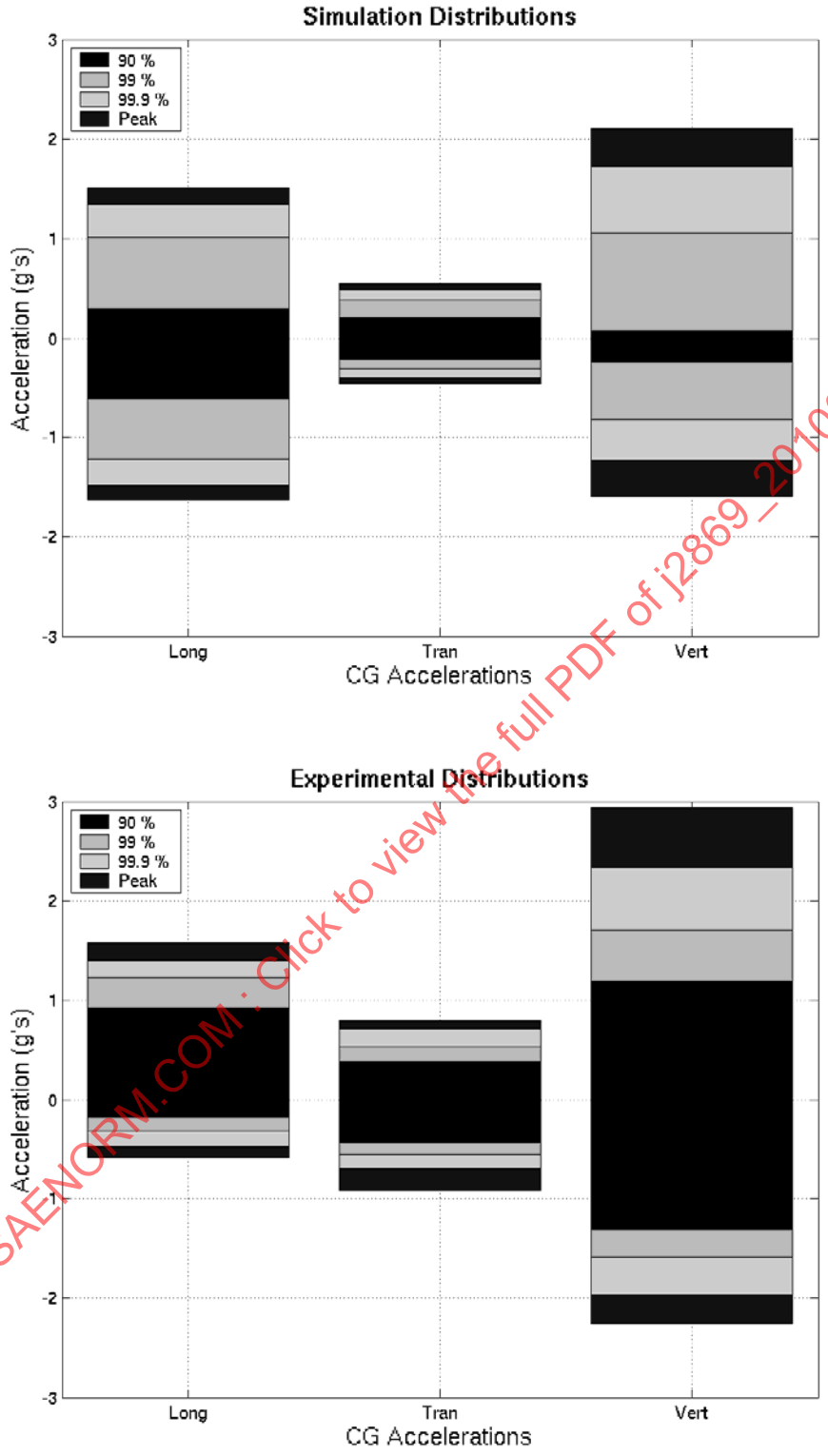

FIGURE 56 - TEST COURSE A CG ACCELERATION STATISTICAL DISTRIBUTIONS

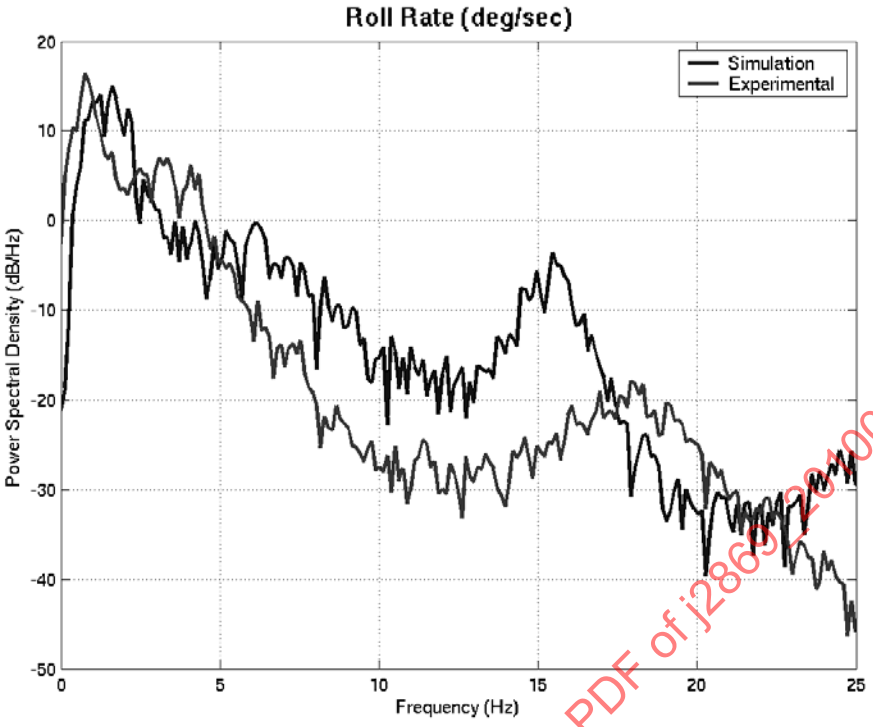

FIGURE 57 - TEST COURSE A TRAILER ROLL RATE PSD COMPARISON

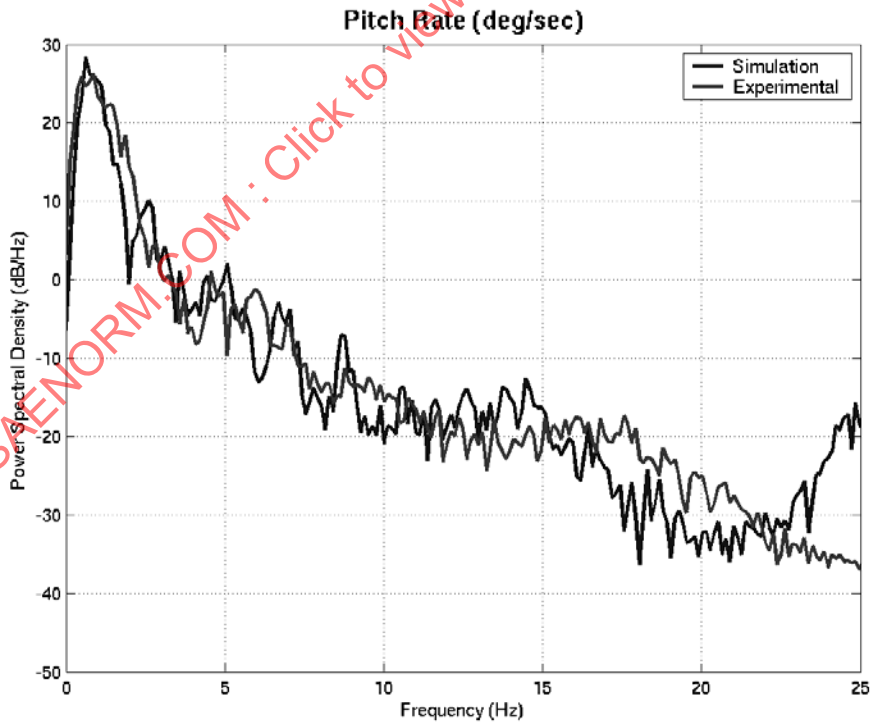

FIGURE 58 - TRAILER PITCH RATE PSD COMPARISON

FIGURE 59 - TEST COURSE A TRAILER YAW RATE PSD COMPARISON

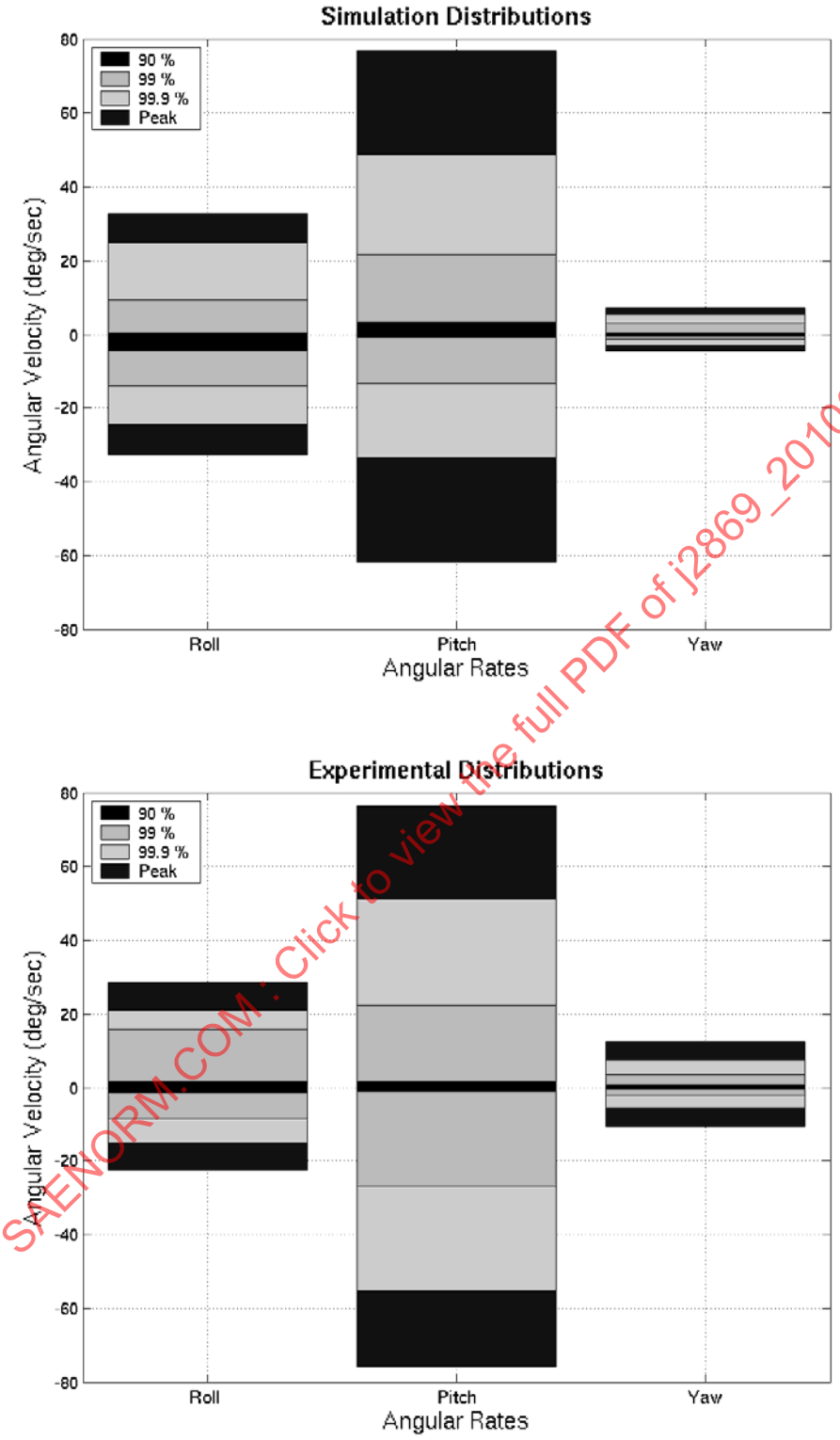

FIGURE 60 - TEST COURSE A TEST COURSE A ANGULAR RATE DISTRIBUTIONS

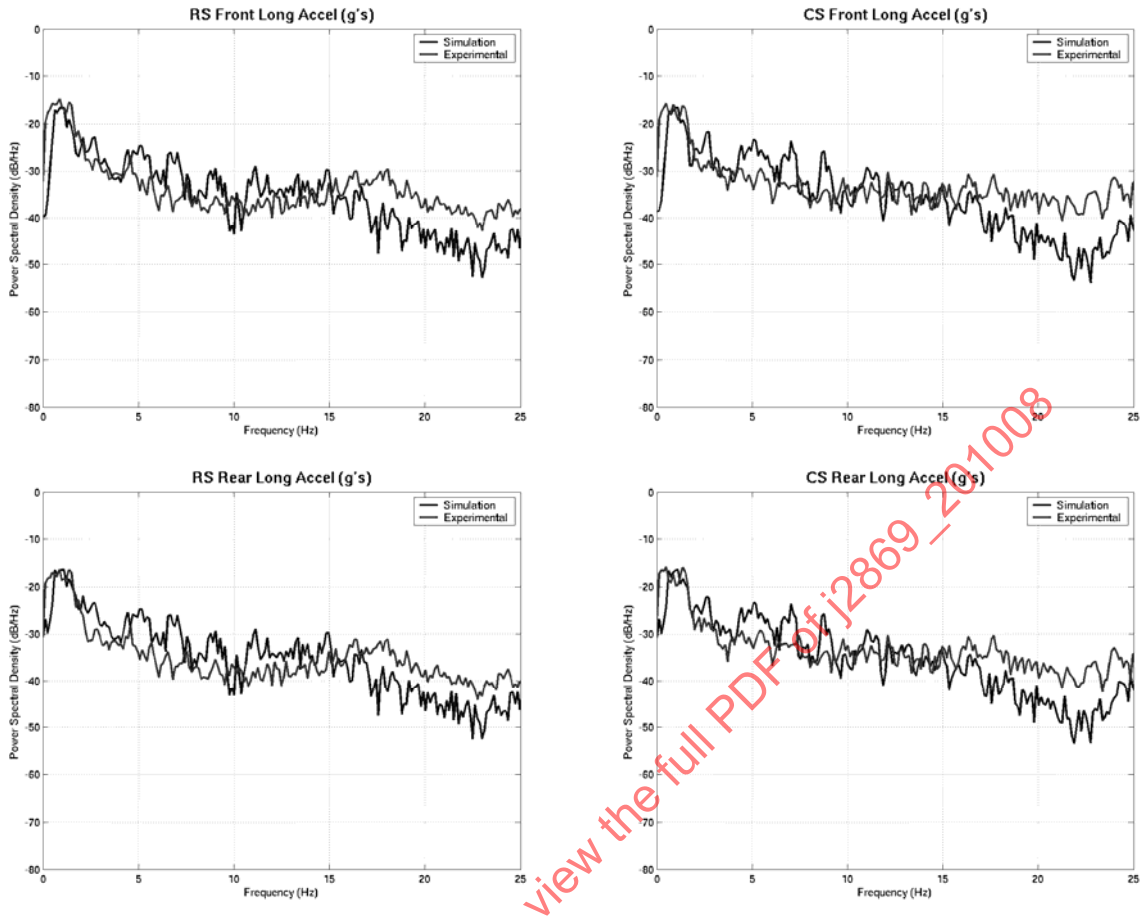

FIGURE 61 - TEST COURSE A TRAILER CORNER LONGITUDINAL ACCELERATION PSD COMPARISON

PSD's of the longitudinal accelerations of the four corners of the trailer are shown in Figure 61. All of these show a better fit than the CG longitudinal acceleration from Figure 53.

Statistical distributions of the four corner longitudinal accelerations are shown in Figure 62. The simulation results are remarkably consistent, whereas the experimental results show relative differences between the four locations. Additionally, the experimental data shows much larger ranges, especially for the 90th percentile.

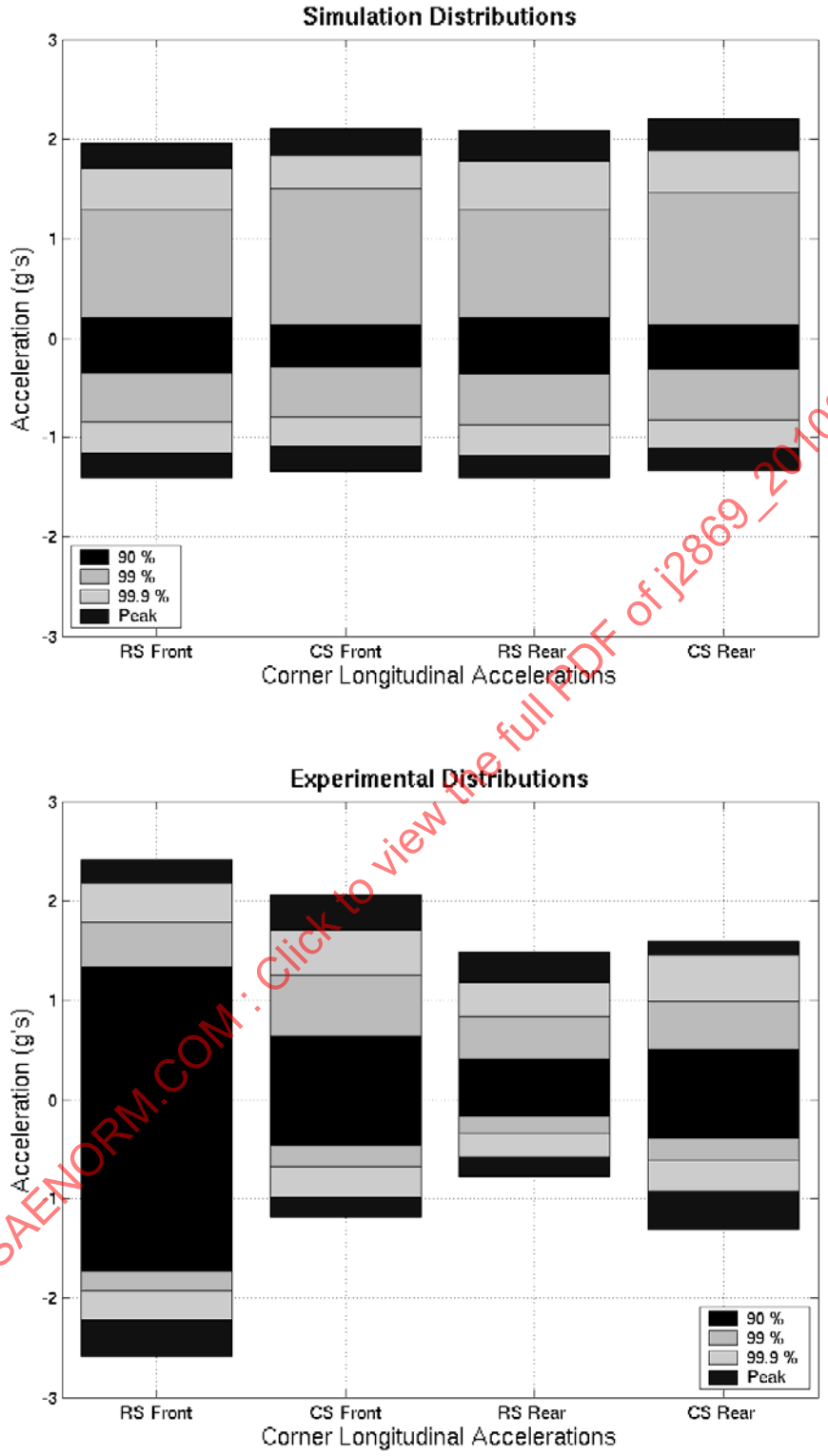

FIGURE 62 - TEST COURSE A TRAILER CORNER LONGITUDINAL ACCELERATION DISTRIBUTIONS

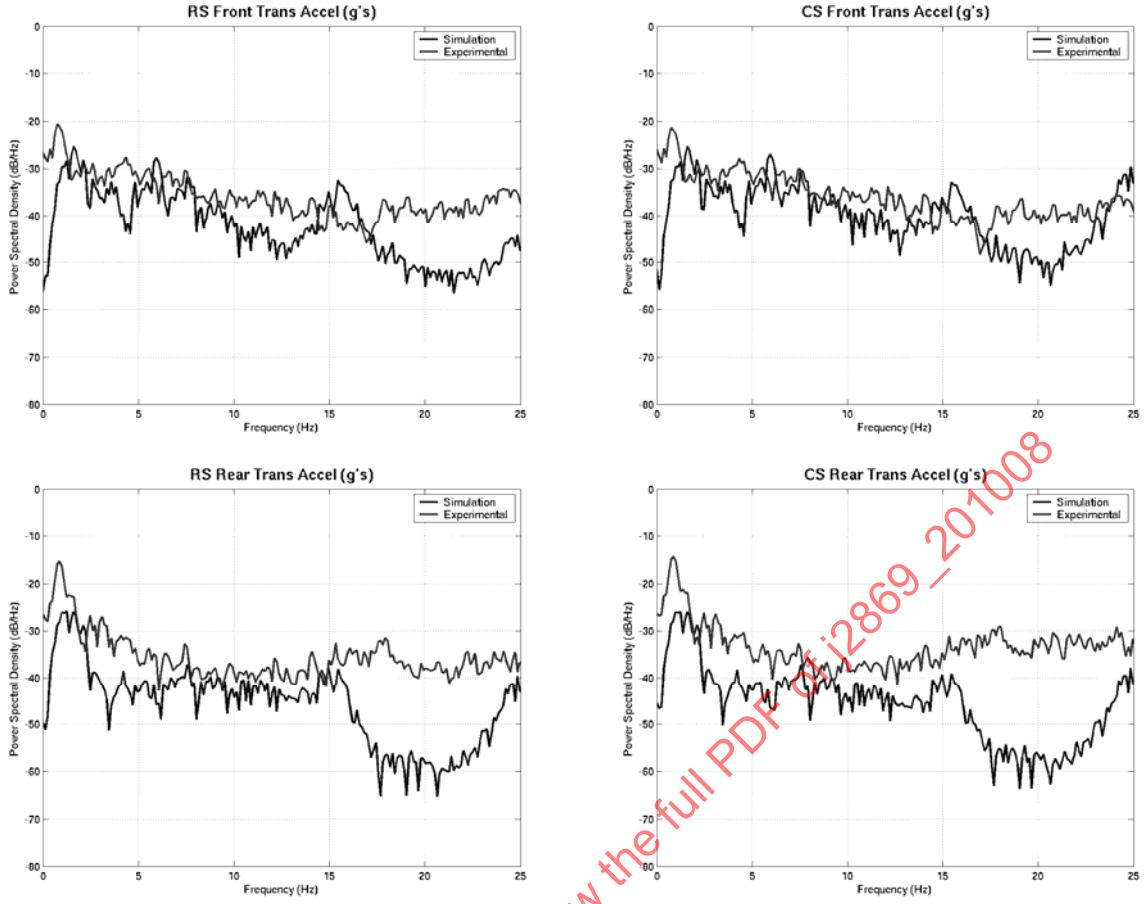

FIGURE 63 - TEST COURSE A TRAILER CORNER TRANSVERSE ACCELERATION PSD COMPARISON

PSD's of the transverse accelerations at the corners of the trailer are shown in Figure 63. The PSD's show the front roadside and curbside results are marginally better than the CG transverse acceleration, previously shown in Figure 54. Results from the rear of the trailer are worse. This makes sense, in light of the poor match for the trailer yaw rate signals, and the fact that the trailer rotates about the hitch location.

The statistical distributions, shown in Figure 64, confirm the poor match of results for the rear corners of the trailer. The simulation model shows the distributions for the rear accelerometers to be lower than the front accelerometers, which is opposite of the experimental data. Also, all simulation transverse accelerations occur at much lower levels than the experimental data.

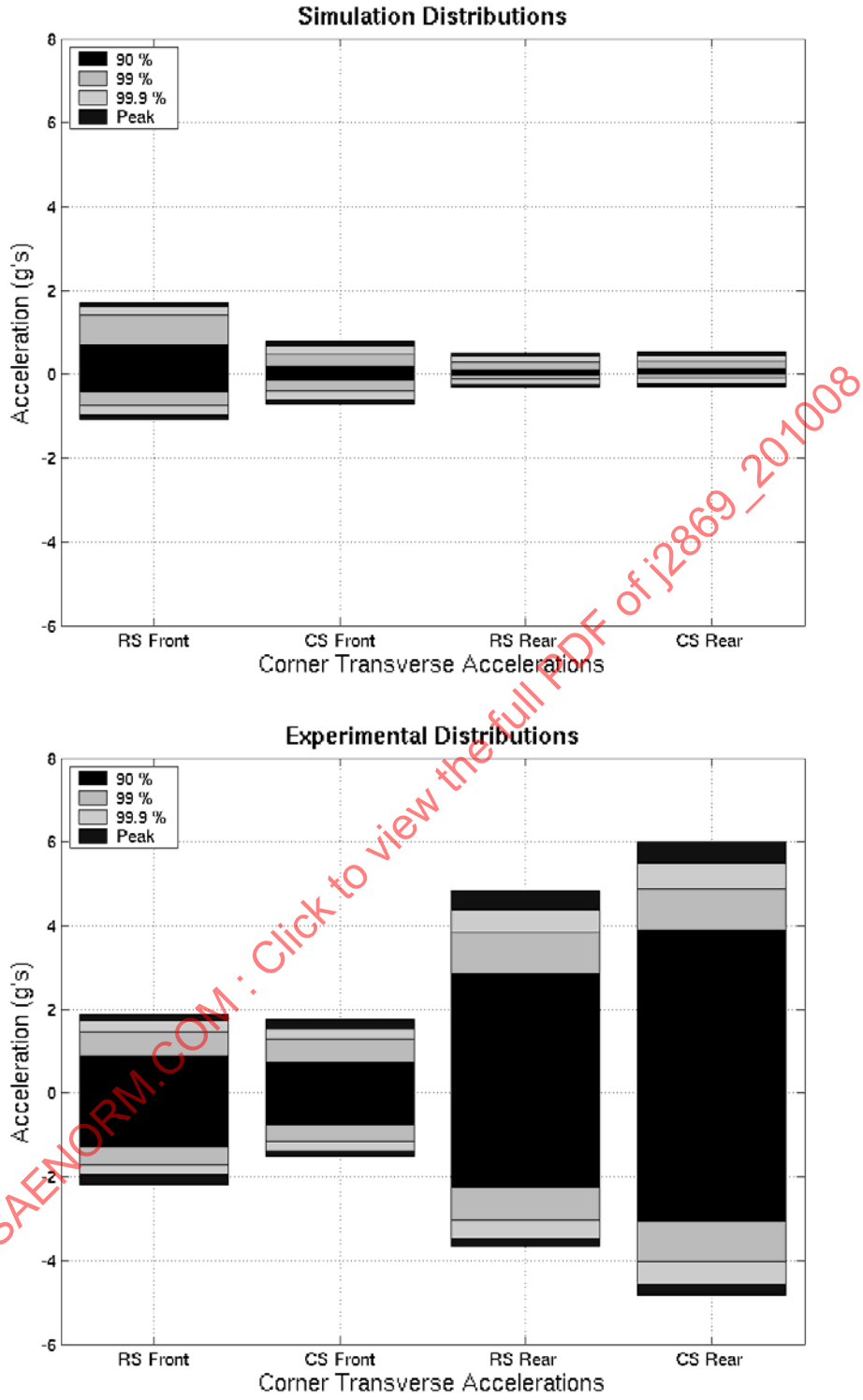

FIGURE 64 - TEST COURSE ATRAILER CORNER TRANSVERSE ACCELERATION DISTRIBUTIONS

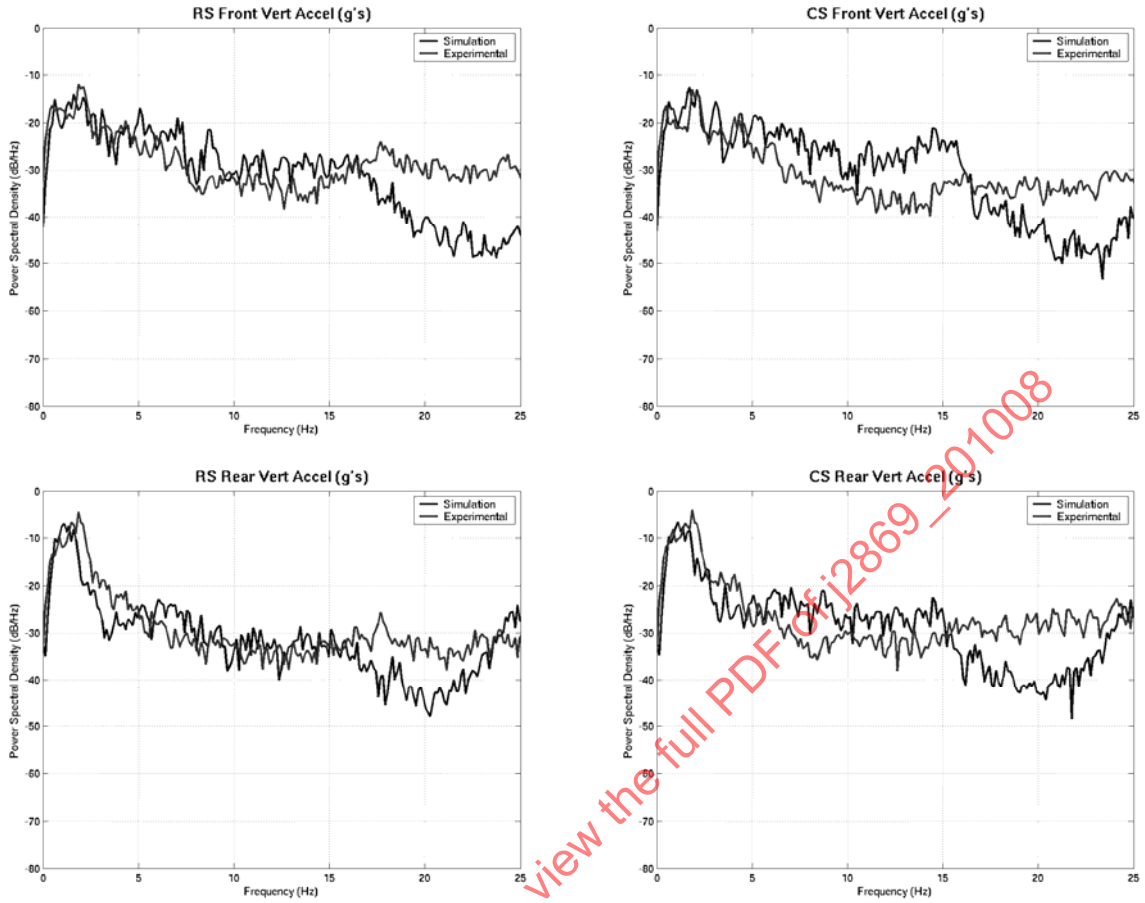

FIGURE 65 - TEST COURSE A TRAILER CORNER VERTICAL ACCELERATION PSD COMPARISON

PSD's of the trailer corner vertical accelerations are shown in Figure 65. Both roadside plots appear to be better matches than the CG vertical acceleration, shown previously in Figure 55, while both curbside plots appear to be about the same as the CG plot.

Once again, the statistical distribution plots show much smaller magnitudes for all the simulated acceleration distributions. In this case, the roadside rear accelerations have comparable peak-to-peak values, but the 90th percentile simulation values are still lower than the experimental ones.

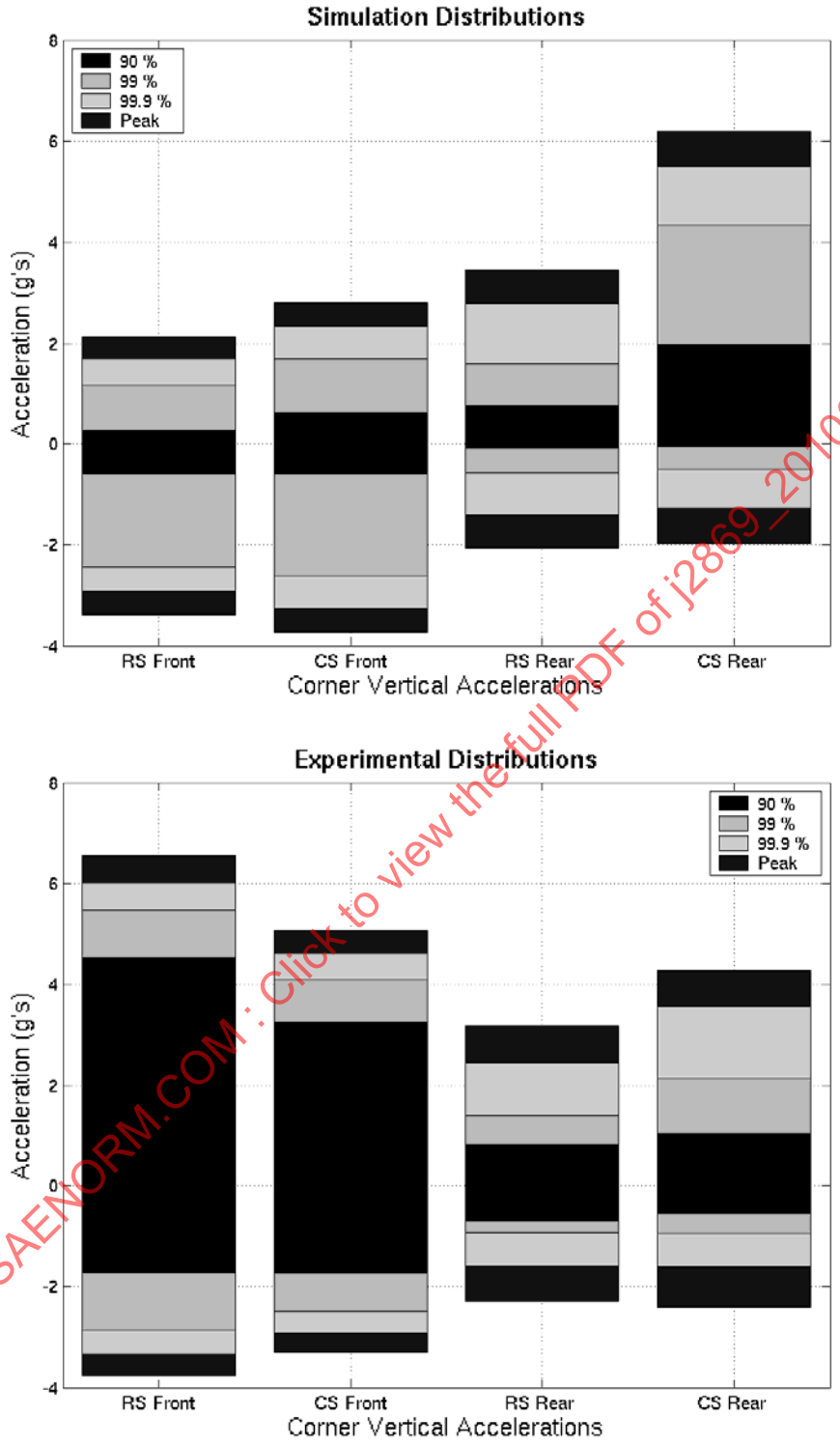

FIGURE 66 - TEST COURSE A TRAILER CORNER VERTICAL ACCELERATION DISTRIBUTIONS

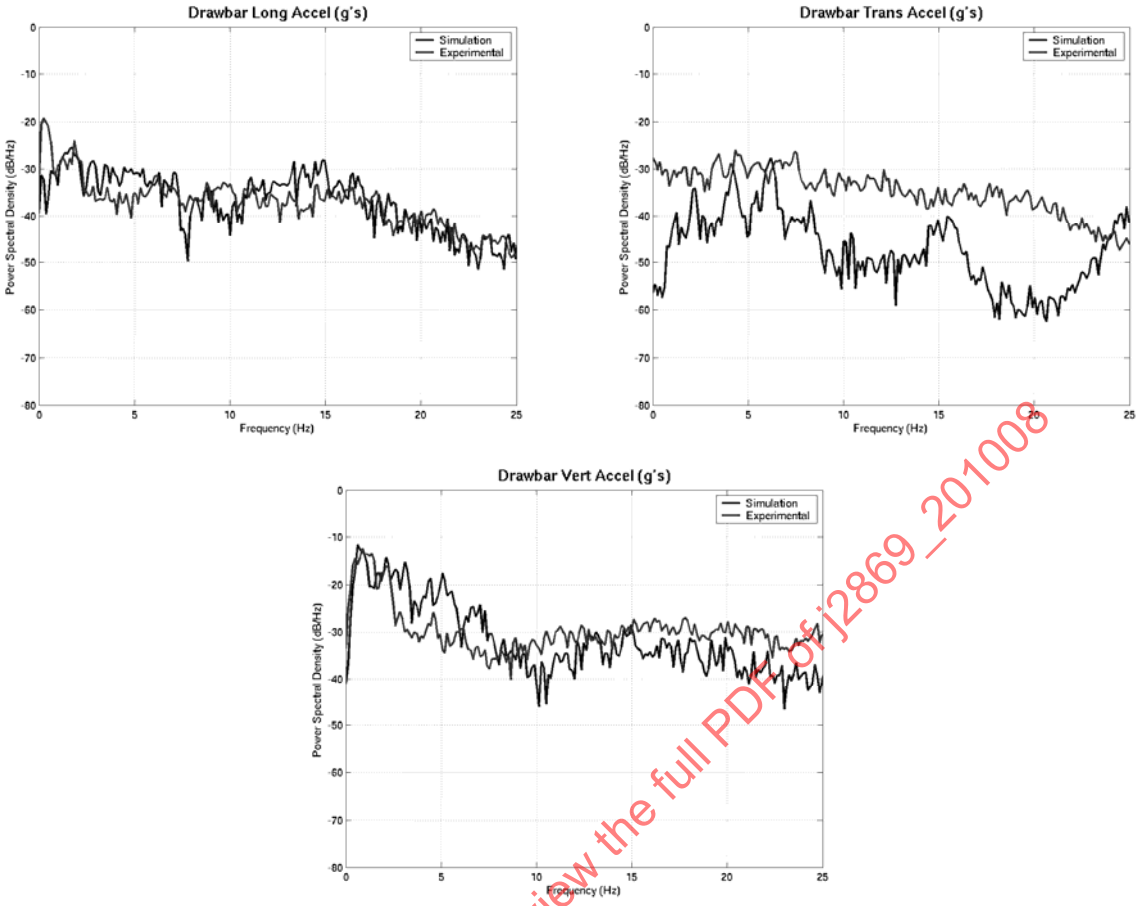

FIGURE 67 - TEST COURSE A DRAWBAR ACCELERATIONS

PSD's for the drawbar accelerations are shown in Figure 67. Like previous acceleration PSD's, a good match is shown for the longitudinal accelerations, an acceptable one is shown for the vertical accelerations, and a poor match is shown for the transverse accelerations.

This is confirmed by the statistical distributions of the accelerations (Figure 68). The longitudinal component comes closest to matching simulation and experimental results, other distributions again show the simulation to be under predicting the magnitudes of the response.

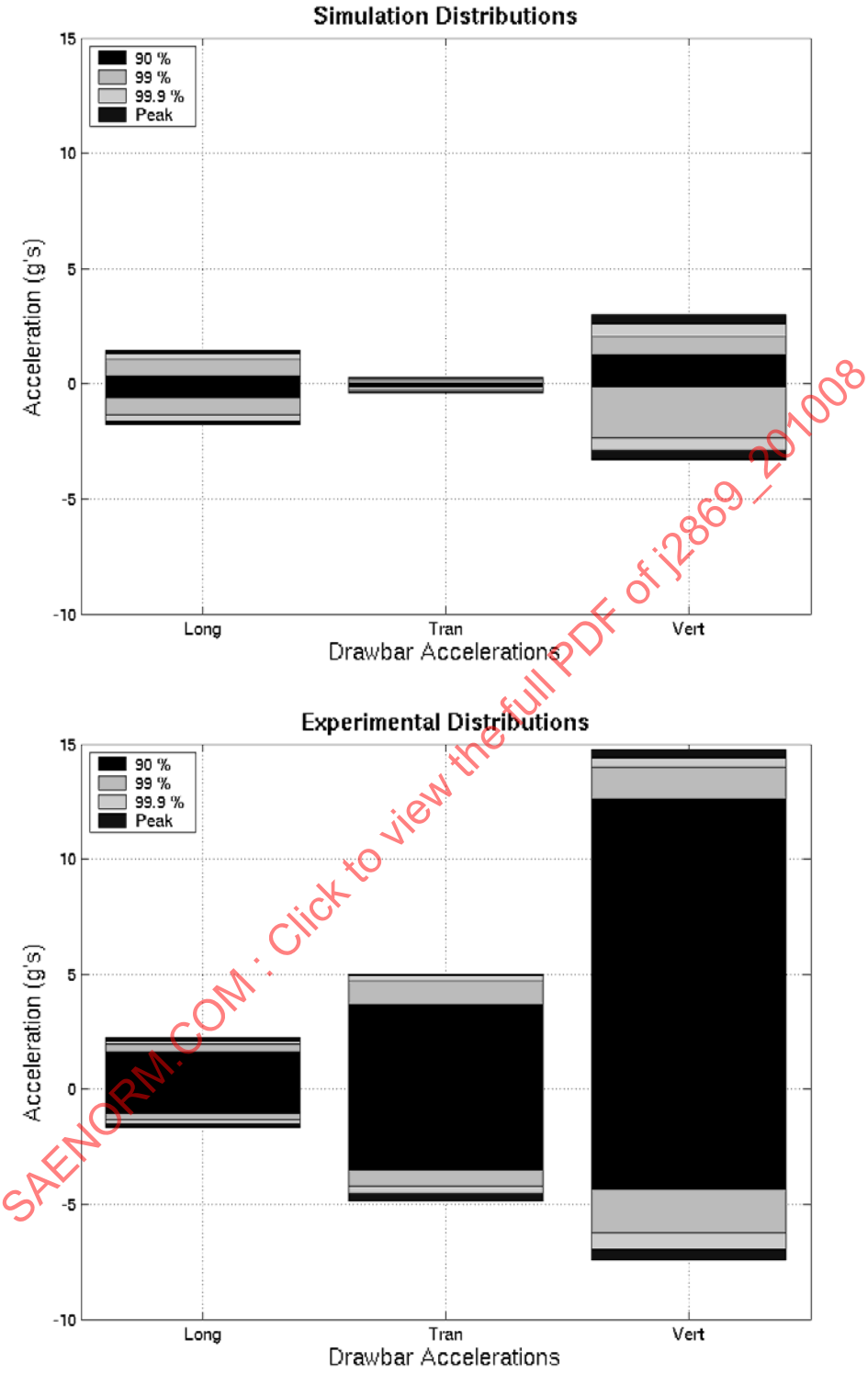

FIGURE 68 - TEST COURSE A DRAWBAR ACCELERATION DISTRIBUTIONS

6.3 Test Course B Comparison

The Test Course B comparison was performed for a nominal speed of 15 mph (16.16 mph average actual). This course was selected for simulation comparisons because it has a nearly normal distribution of terrain elevation. Unfortunately, the elevation distribution is non-stationary, which causes some problems since the position of the trailer, relative to the test course, is not known, and the direction of motion was not documented.

Like Test Course A, Test Course B elevations were measured every 3 inches for the length of the course using the ATC profilometer and detrended using standard procedures [6].

PSD's of the trailer CG accelerations are shown in Figures 69 through 71. The longitudinal acceleration, shown in Figure 69, is much worse than the corresponding plot, Figure 53, of the Test Course A data. Interestingly, the experimental data shows a high magnitude across most of the frequency band, which is opposite of the Test Course A data.

The transverse acceleration data, Figure 70, is also much worse than the Test Course A data, Figure 54. Given the varying transverse geometry of Test Course B, this points toward a deficiency of the tire model used in the simulation.

Up to 15 Hz, the vertical accelerations, shown in Figure 71, are a good match. However, none of the statistical distributions, shown in Figure 72, of the simulated and experimental data are comparable. The simulated data has much lower distributions than the experimental data.

PSD's of the angular velocities are shown in Figures 73 through 75. The pitch rate, shown in Figure 74, matches well up to about 7 Hz. The roll rate, shown in Figure 73, has a good match up through about 8 Hz, except for one resonant peak in the experimental data. The yaw rate, shown in Figure 75, is a poor match.

The statistical distributions of the angular rates are shown in Figure 76. Both the roll and pitch rate distributions are very comparable, but the yaw rate distributions are not.

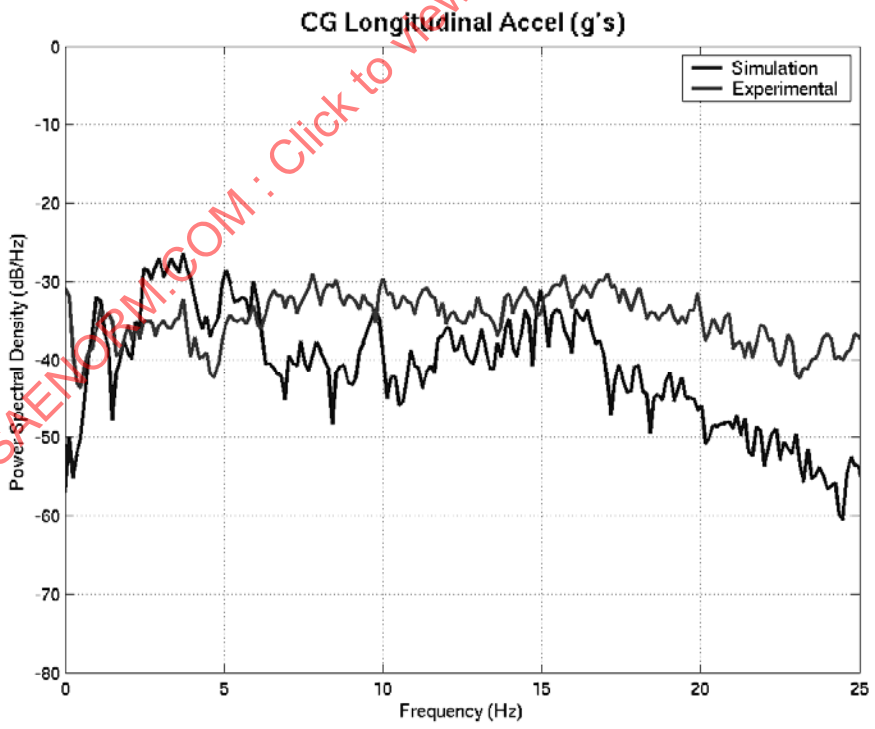

FIGURE 69 - TEST COURSE B CG LONGITUDINAL ACCELERATION PSD COMPARISON

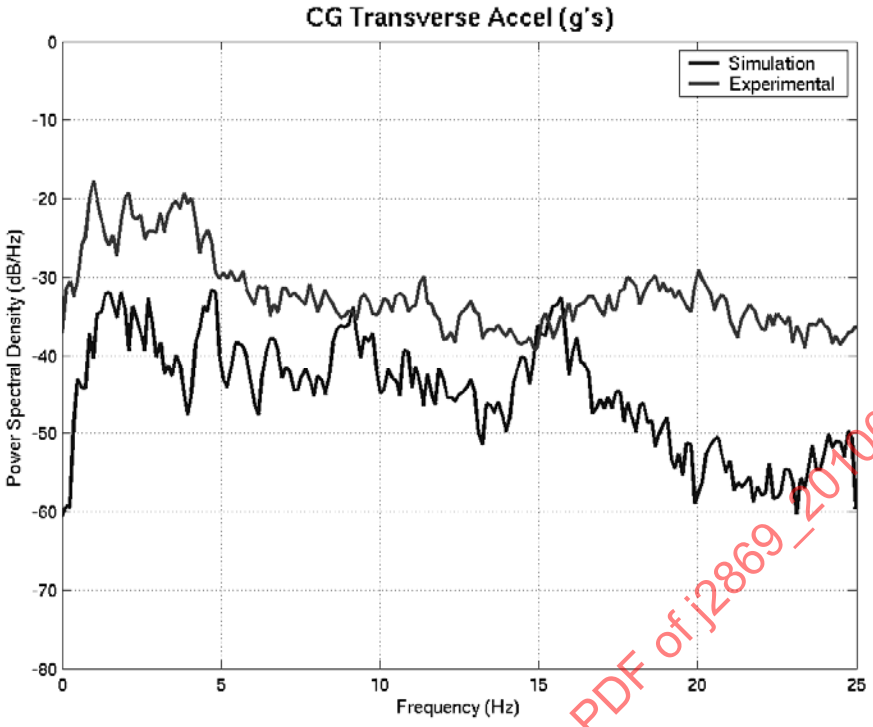

FIGURE 70 - TEST COURSE B CG TRANSVERSE ACCELERATION PSD COMPARISON

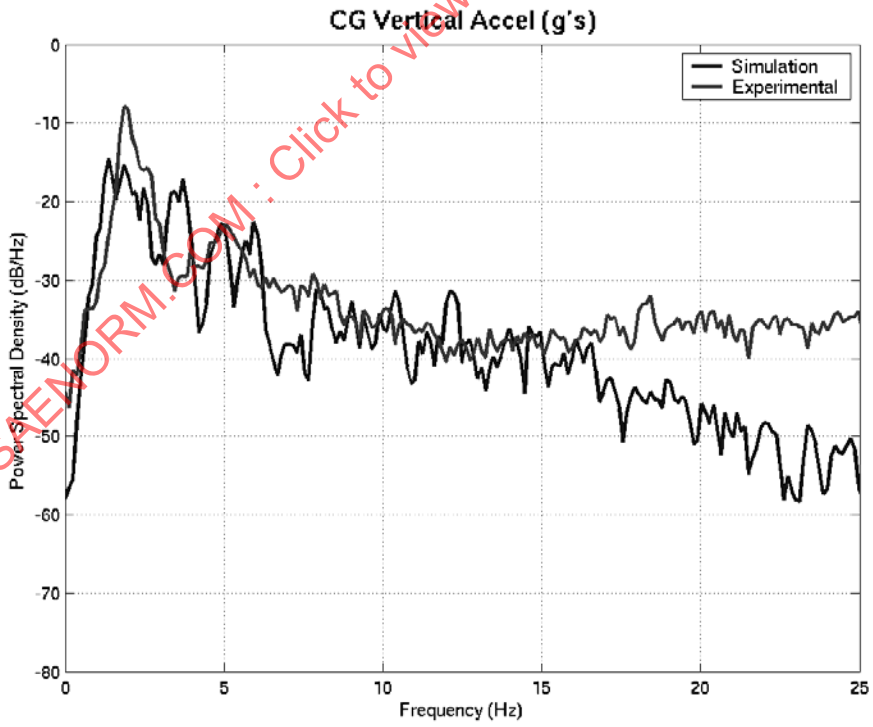

FIGURE 71 - TEST COURSE B CG VERTICAL ACCELERATION PSD COMPARISON

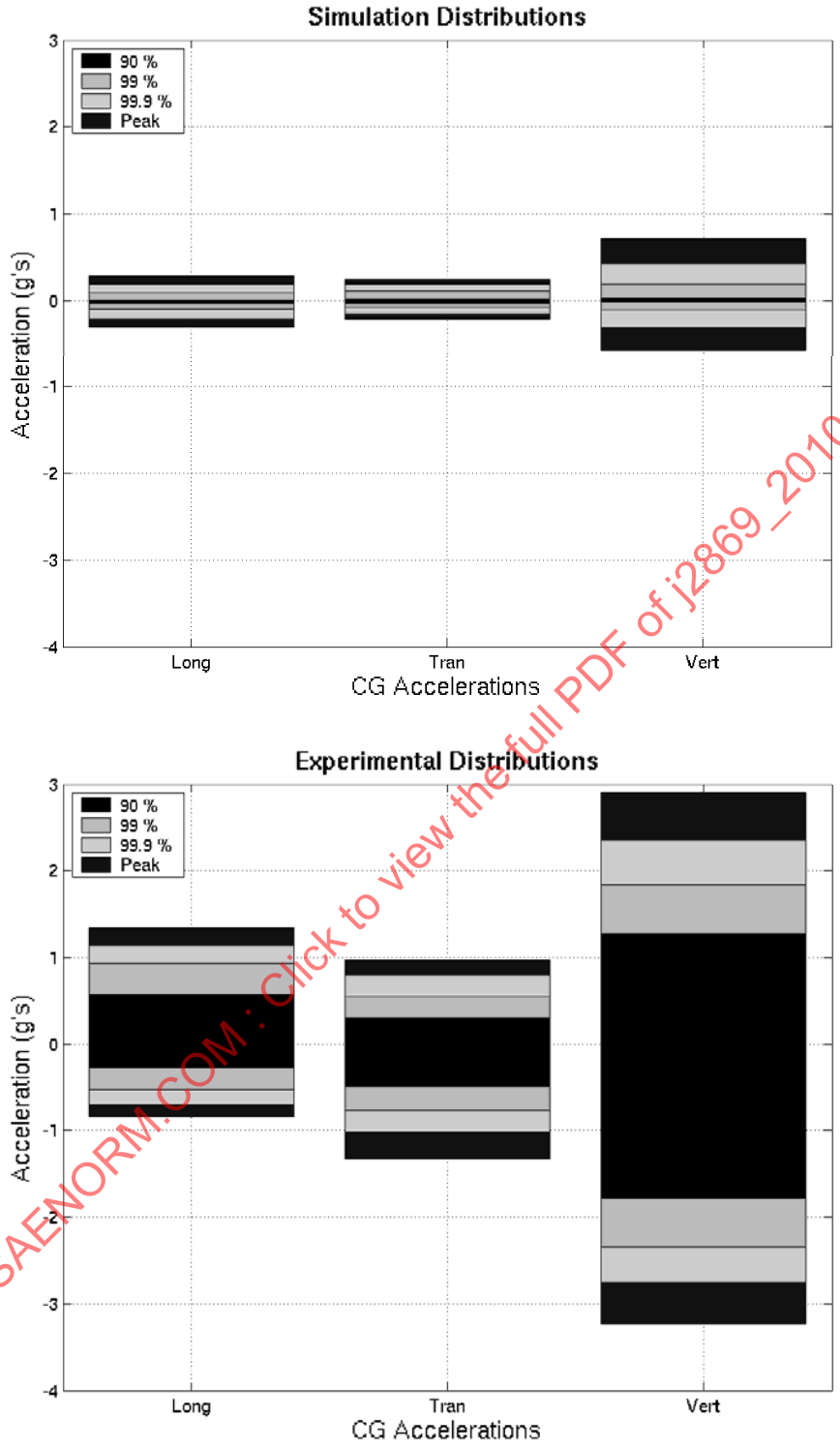

FIGURE 72 - TEST COURSE B CG ACCELERATION STATISTICAL DISTRIBUTIONS

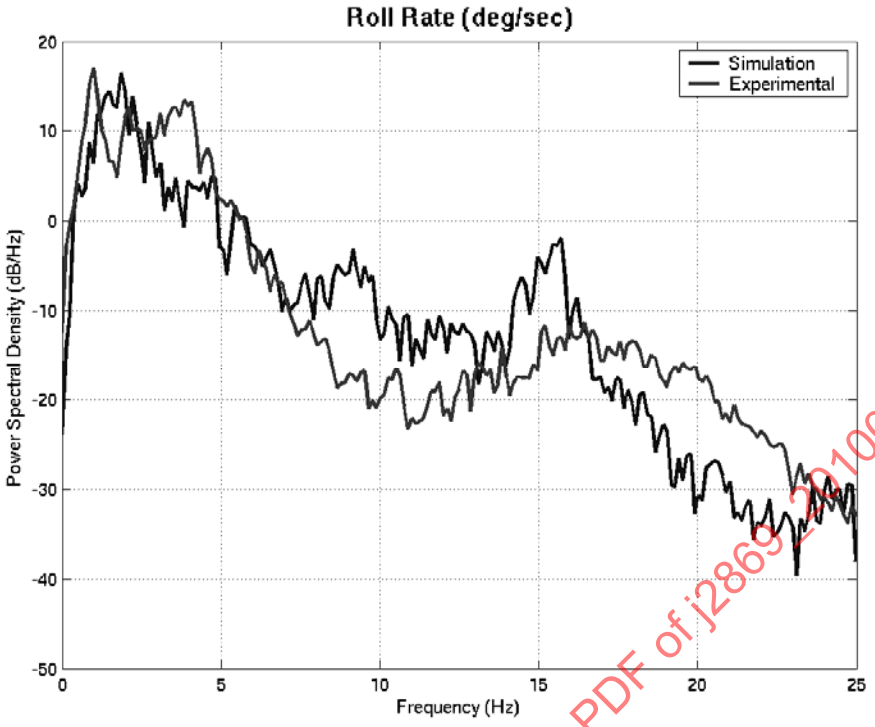

FIGURE 73 - TEST COURSE B TRAILER ROLL RATE PSD COMPARISON

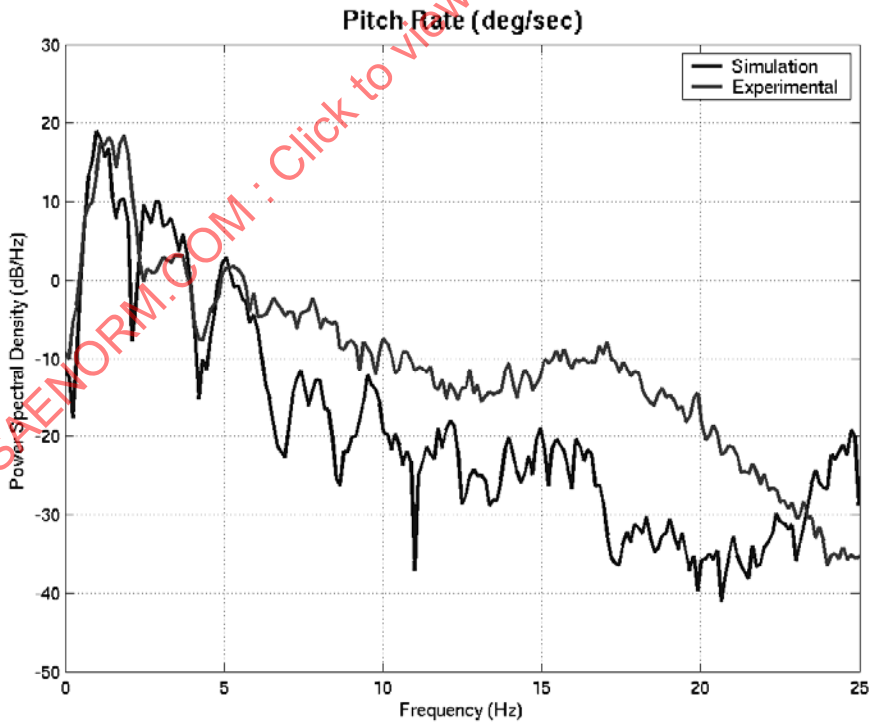

FIGURE 74 - TEST COURSE B TRAILER PITCH RATE PSD COMPARISON

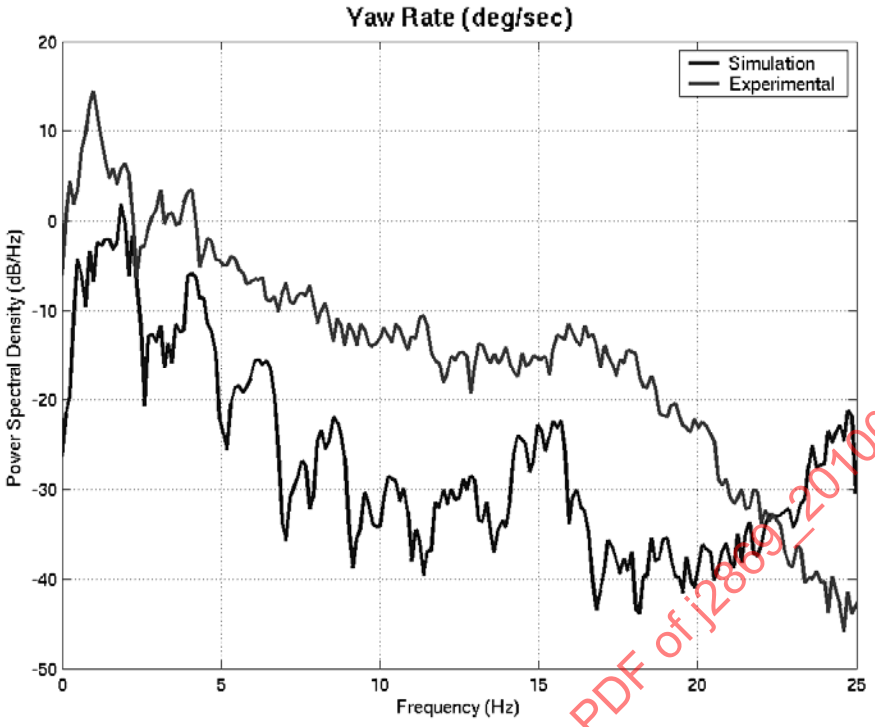

FIGURE 75 - TEST COURSE B TRAILER YAW RATE PSD COMPARISON

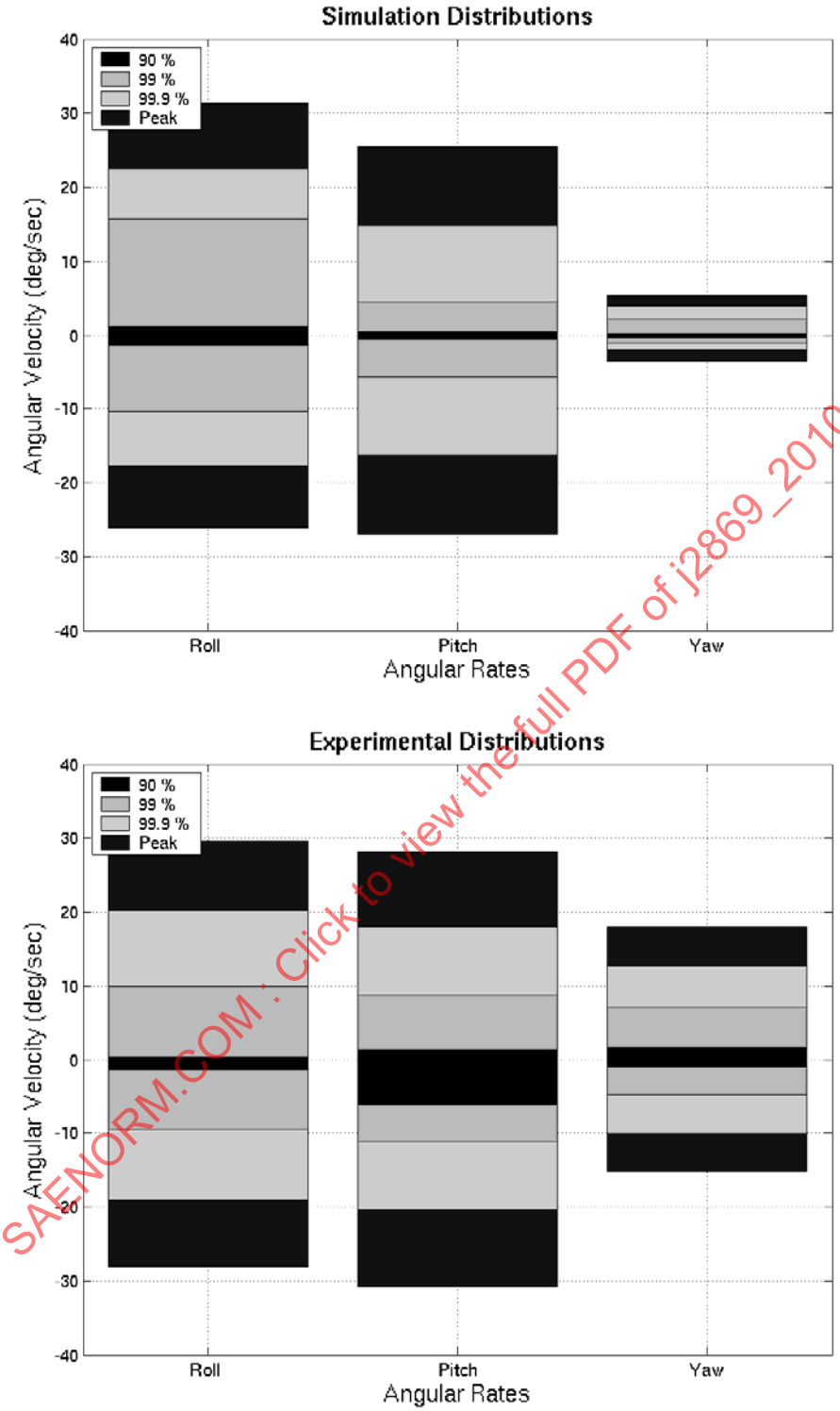

FIGURE 76 - TEST COURSE B ANGULAR RATE DISTRIBUTIONS

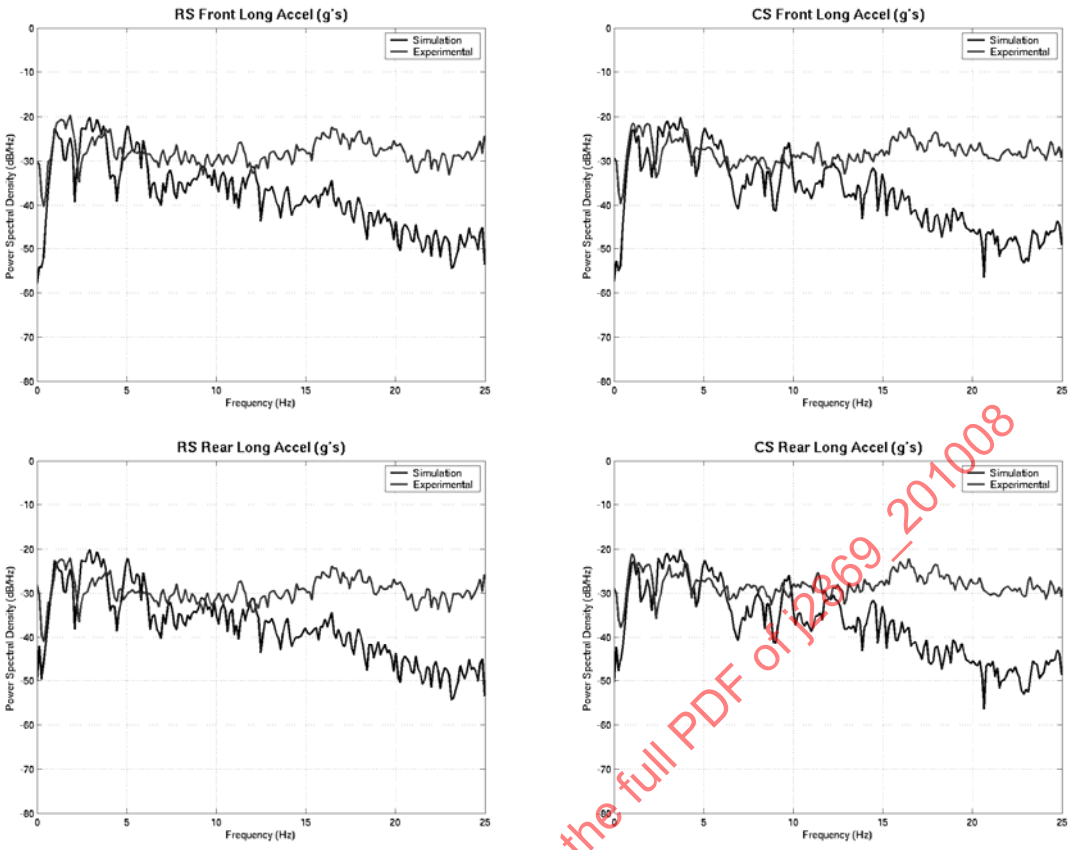

FIGURE 77 - TEST COURSE B TRAILER CORNER LONGITUDINAL ACCELERATION PSD COMPARISON

PSD's of the trailer's corner longitudinal accelerations are shown in Figure 77. Unlike the Test Course A PSD's, shown previously in Figure 61, Test Course B shows a decreasing goodness-of-fit as the frequency increases. This is due to the structure of the test course, where the individual blocks create a higher frequency input to the trailer. This is also reflected in the statistical distributions, shown in Figure 78. None of the four corner simulated accelerations show the same distribution ranges as the experimental data.

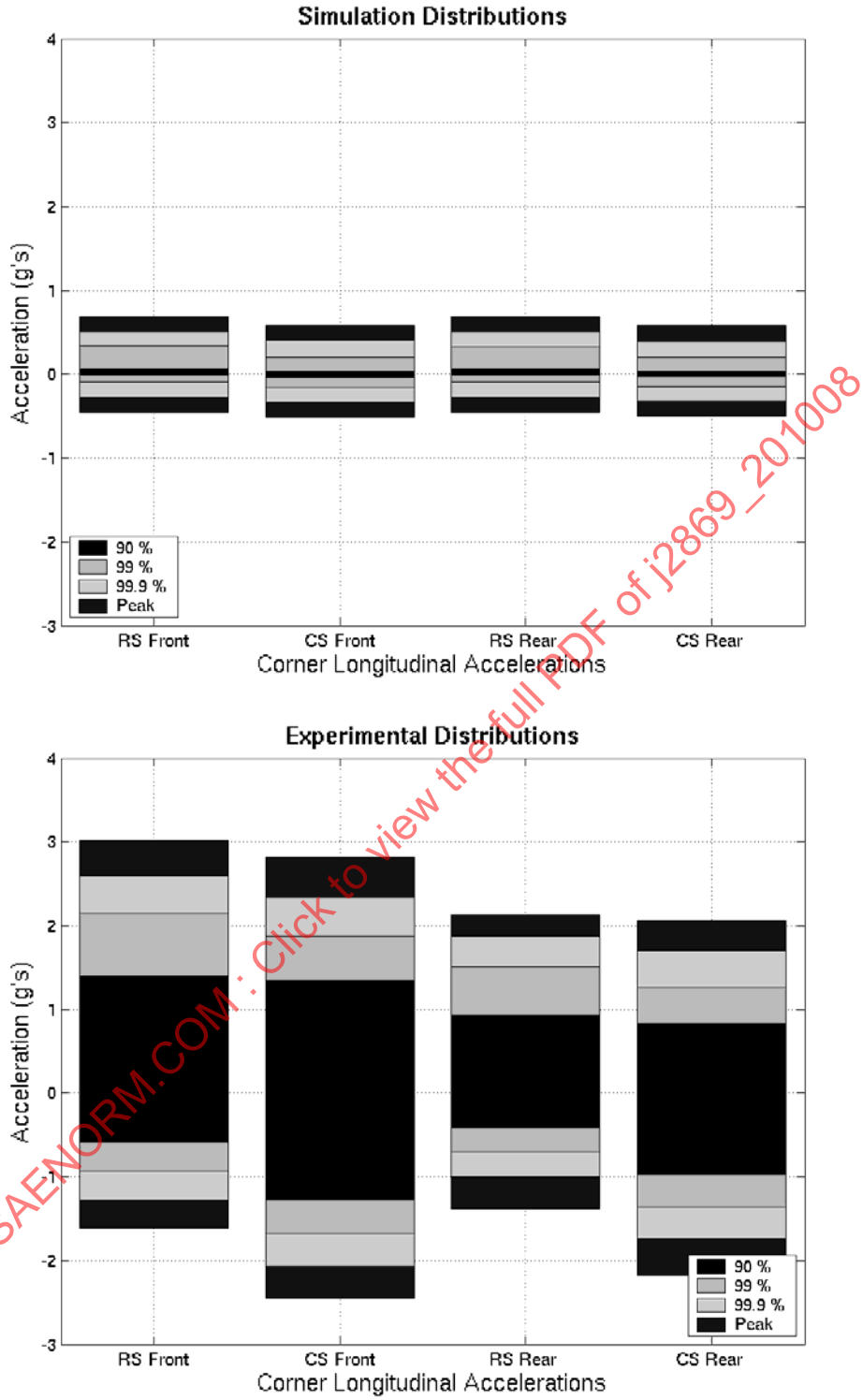

FIGURE 78 - TEST COURSE B TRAILER CORNER LONGITUDINAL ACCELERATION DISTRIBUTIONS

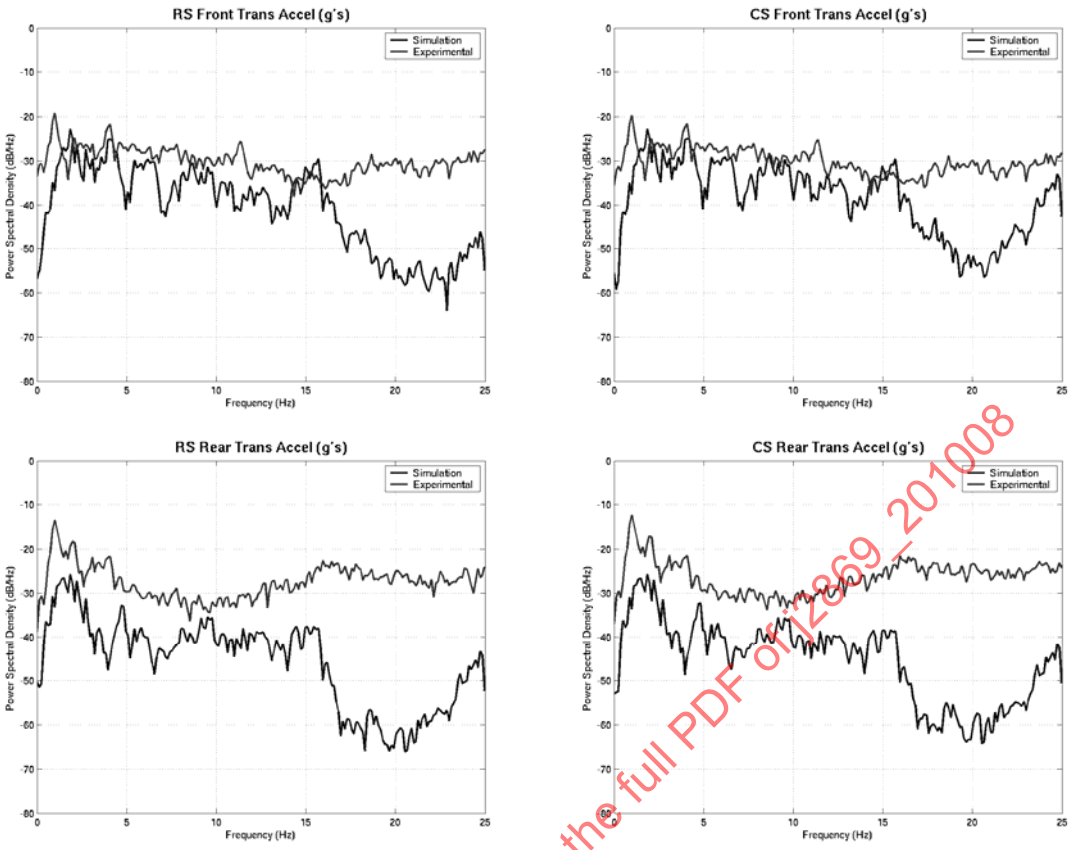

FIGURE 79 - TEST COURSE B TRAILER CORNER TRANSVERSE ACCELERATION PSD COMPARISON

PSD's of the trailer corner transverse accelerations are shown in Figure 79. Like previously shown transverse acceleration PSD's, the fit is not very good, especially at the rear of the trailer. This is a result of under predicting the value of the yaw acceleration.

The statistical distributions of the transverse corner accelerations are shown in Figure 80. Again, the statistical distributions of the simulation have much lower magnitudes than those from the experimental test data.

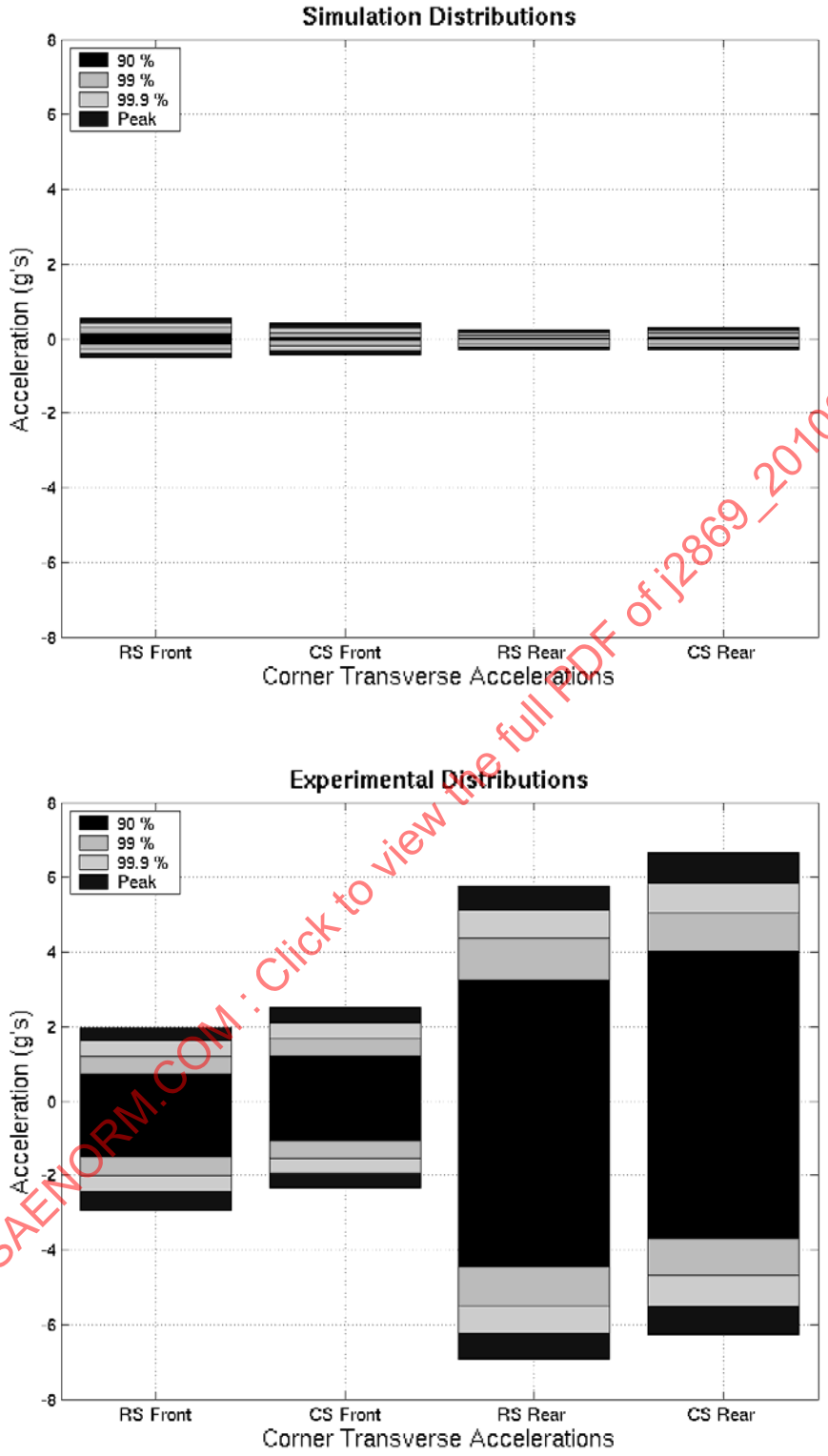

FIGURE 80 - TEST COURSE B TRAILER CORNER TRANSVERSE ACCELERATION DISTRIBUTIONS

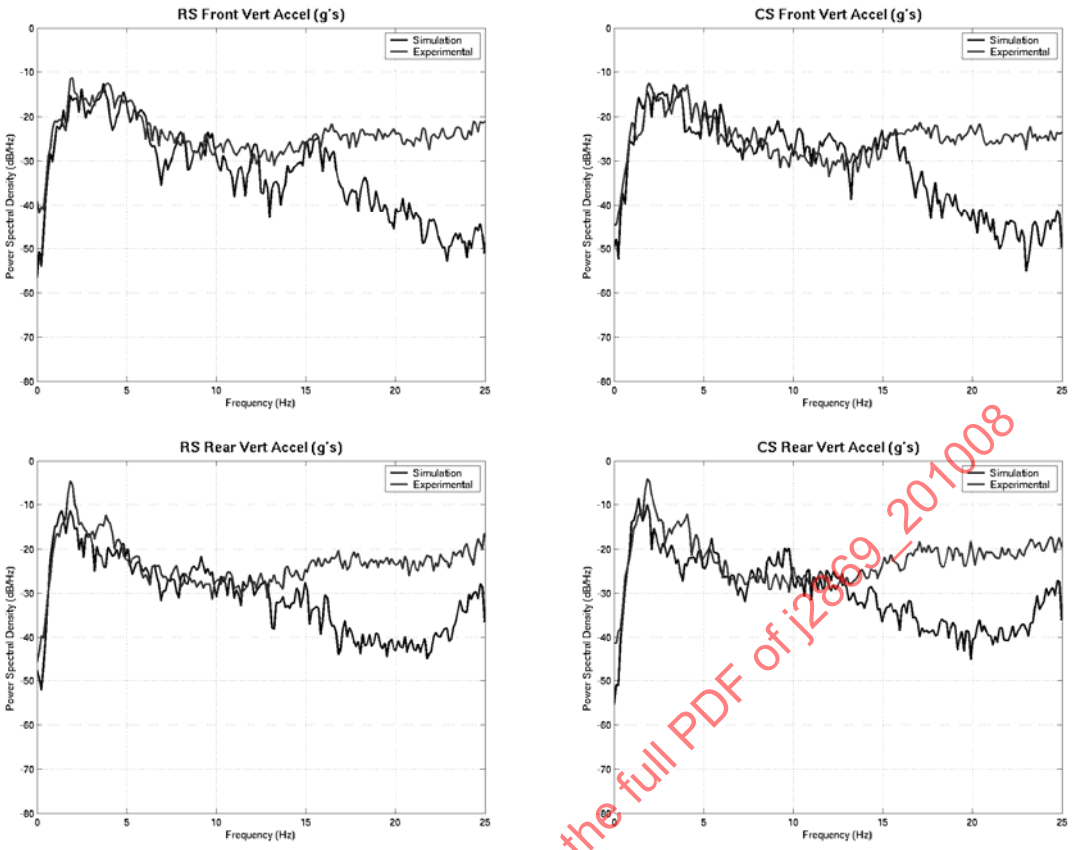

FIGURE 81 - TEST COURSE B TRAILER CORNER VERTICAL ACCELERATION PSD COMPARISON

PSD's of the trailer corner vertical accelerations for Test Course B are shown in Figure 81. All four corners have a good match up to about a 12 Hz frequency. Beyond 12 Hz, the experimental data has a much greater amount of energy than the simulation data.

Statistical distributions of the trailer corner vertical accelerations are shown in Figure 82. The simulation model data has approximately the same distributions at all four corners. Unfortunately, the magnitudes of the distributions are all lower than those determined from the experimental data.

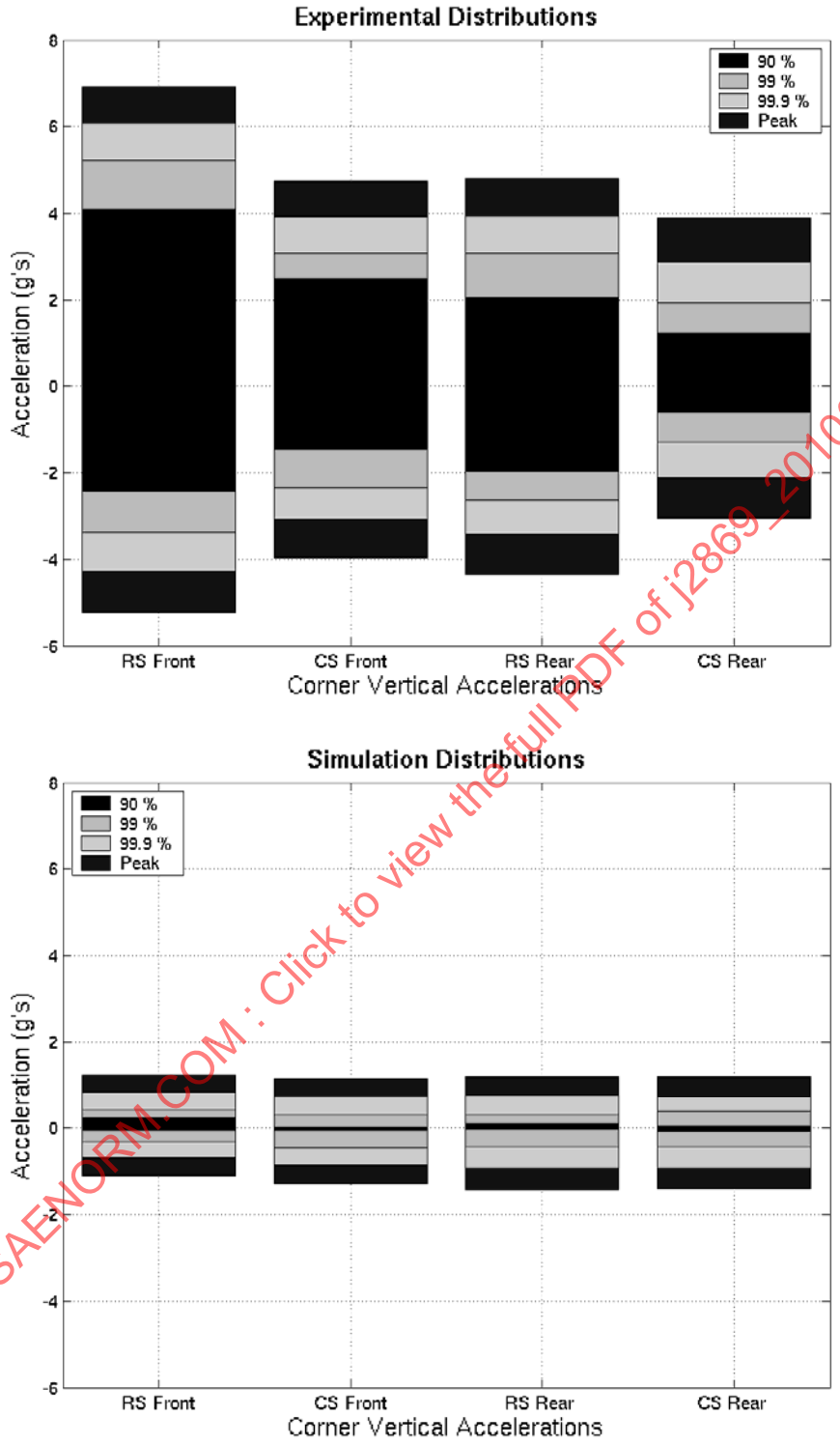

FIGURE 82 - TEST COURSE B TRAILER CORNER VERTICAL ACCELERATION DISTRIBUTIONS

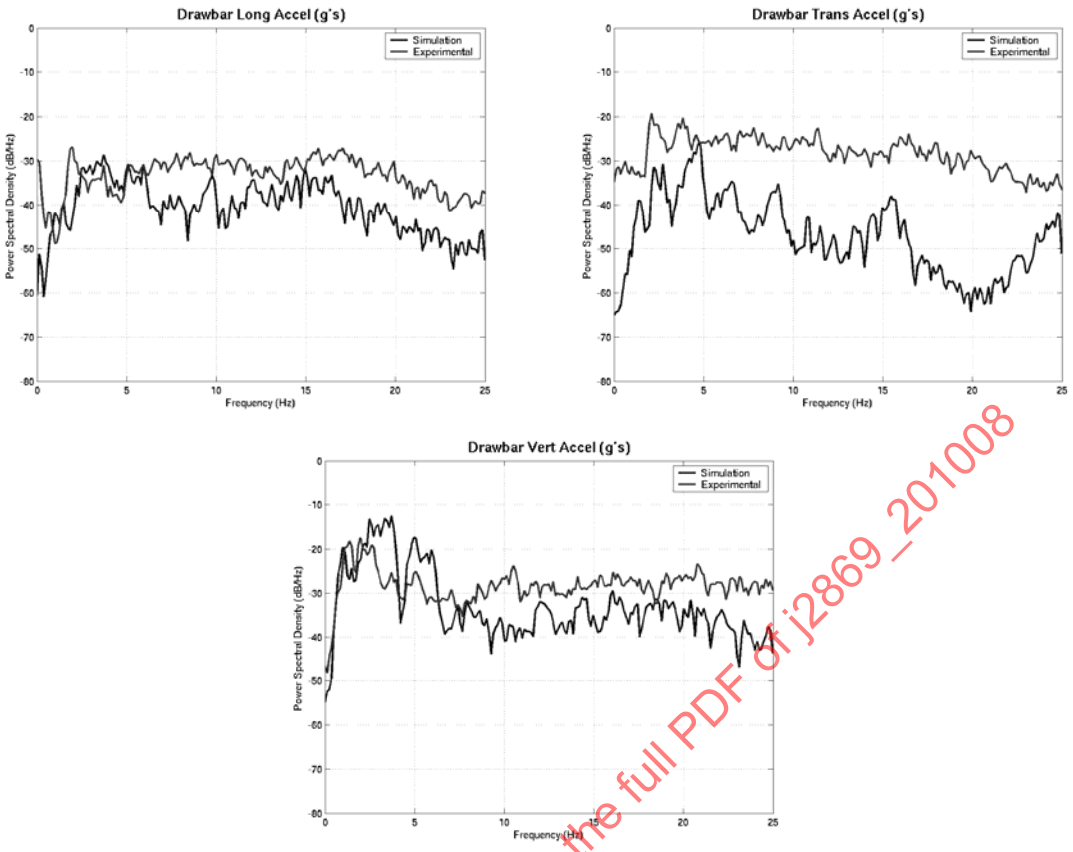

FIGURE 83 - TEST COURSE B TRAILER DRAWBAR ACCELERATION PSD COMPARISON

PSD's of the trailer drawbar accelerations for Test Course B are shown in Figure 83. As with Test Course A, the longitudinal accelerations match best, the vertical accelerations match for low (<3 Hz) frequencies, and the transverse accelerations do not match.

Statistical distributions of the drawbar accelerations are shown in Figure 84. As with most other cases, the magnitudes of the simulated accelerations are much lower than the magnitudes of the experimental data.

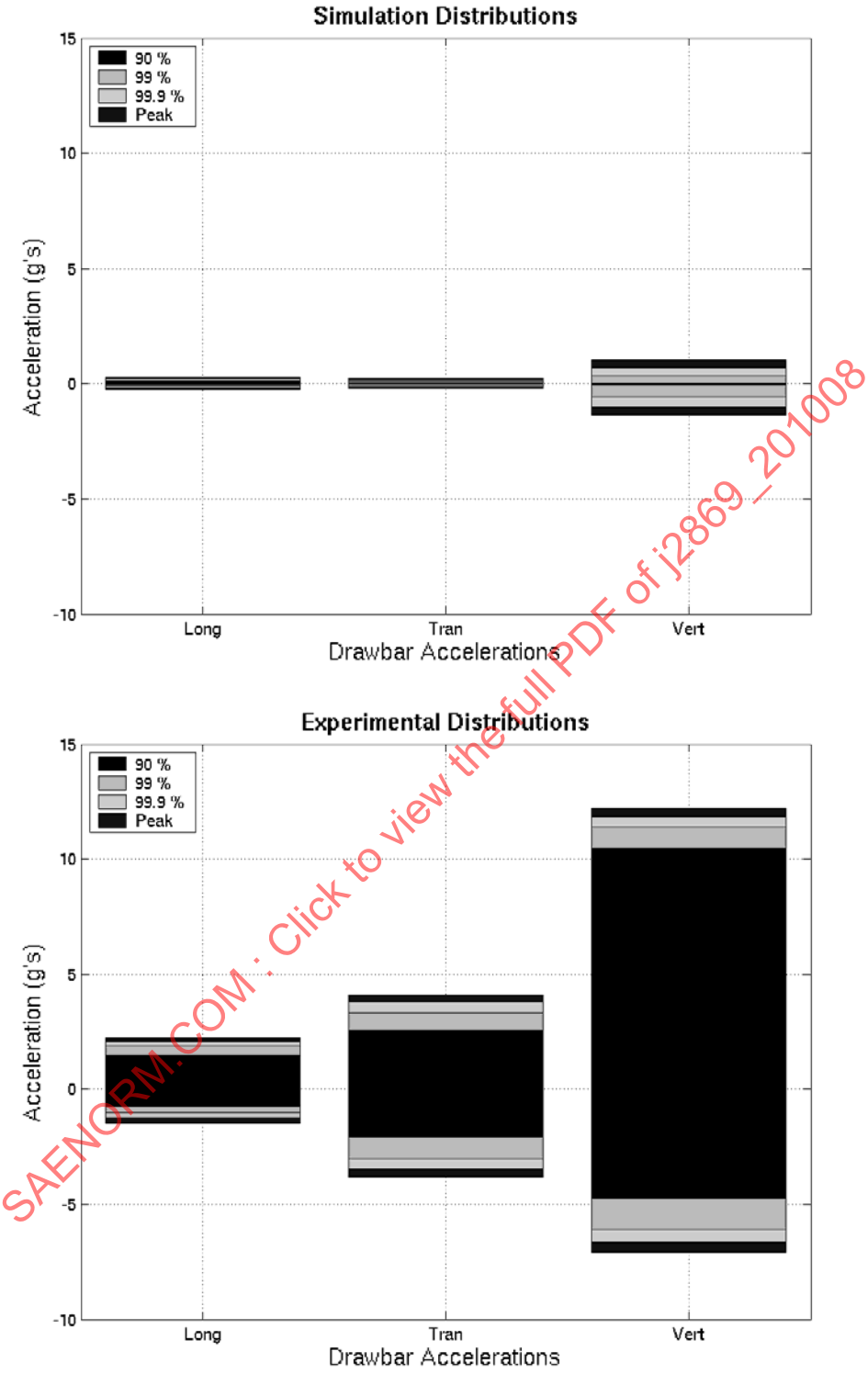

FIGURE 84 - TEST COURSE B DRAWBAR ACCELERATION DISTRIBUTIONS

6.4 Conclusions

One goal of the project was to model the trailer, independent of the experimental testing, and then compare the results. The outputs of the DADS trailer model have been compared to the experimental results for two test courses. Since the location of the trailer, relative to the test course, was not known, comparisons have been limited to PSD's and statistical distributions of the accelerations for several locations on the trailer. Several problems have been identified by this comparison process:

a. Transverse accelerations of the simulation model have much lower statistical distribution magnitudes and frequency content than the experimentally measured transverse accelerations.

b. The transverse accelerations match better for Test Course A than for Test Course B.

c. Yaw rate angular velocities of the simulation model have much lower statistical distribution magnitudes and frequency content than the experimentally measured yaw rates.

d. Generally, the simulated accelerations (longitudinal, transverse, and vertical) had significantly lower magnitudes than the corresponding experimentally measured accelerations.

These problems can be related to several modeling issues. The first issue occurred during the development of the flexible-body trailer model. In this case, the bed and walls of the trailer are made from corrugated aluminum, but in the interest of reducing the size of the FE model, the corrugations were removed and the shell elements were given composite mass and stiffness properties. These properties were estimated and no sensitivity analysis was done. This could have had an effect on both the CG and corner mounted accelerometers. Also, only the first three constrained normal modes and three static correction modes were used for the flexible-body model. The mode selection was done based on the modal analysis test, but may not be representative of the forced response frequencies from operation on some test courses. This could explain some differences in the higher frequency regions of the Test Course B PSD's.

The second issue is the modeling of the test mass, shown in Figure 85. Not much was known about how the test mass was to be affixed to the trailer bed when the simulation model was created. What was known were the mass/inertia properties, and the locations where the mass contacted the trailer bed. In the simulation model, the test mass was divided into four separate masses, with the same mass and approximate inertia properties, which were attached to the bed using bracket joints. Given that the physical test mass was chained to the trailer bed, it probably increased the stiffness. In retrospect, the simulation model should have used a single mass, with contact elements, and should have used stiff springs to represent the chains.

The third issue relates to the modeling of the hitch. The first study examined two methods for modeling the hitch: one using contact elements, and the second using a spherical joint. The actual trailer hitch is a lunette/pintle combination, which allows for much more relative motion than a more typical ball hitch. It was decided to use the spherical joint, or ball hitch, model for this validation study because the frequency that the dynamic simulation data was passed to the fatigue analysis did not allow for correct results when the contact element model was used. The contact element model of the hitch generated higher acceleration shocks, which could improve the magnitudes of the statistical distributions.

The fourth issue involves both the tire model used in the multi-body software and the representation of the terrain. The DADS tire model queries the terrain along a single line, and the tire has no width component. Likewise, the profilometer, used to measure the test courses, measured the left and right wheel tracks as lines. The tire model was developed to generate lateral forces due to wheel slip angle and not terrain geometry. This is particularly evident by comparing the transverse acceleration results from Test Course A and Test Course B. Test Course A has a fairly flat lateral terrain profile, while Test Course B undulates considerably. Thus, the Test Course B comparisons show a much worse estimation of the transverse accelerations. This also causes the underestimation of the trailer yaw rate, since, in the simulation, the tire force is the only lateral load applied to the trailer.

Lastly, not having GPS data from the tests did not allow for correlation of the position of the trailer with the test course profilometry. This would allow for time domain comparison of the results. Also, on some courses, particularly Test Course A, the speed of the trailer varied considerably and using the average speed for the simulations may not be as representative as the actual measured speed.

In all, the dynamic model comparison can be considered a qualified success. The modeled accelerations and angular rates that best matched the experimental data happened to be the ones most closely associated with the forces that cause the fatigue damage.

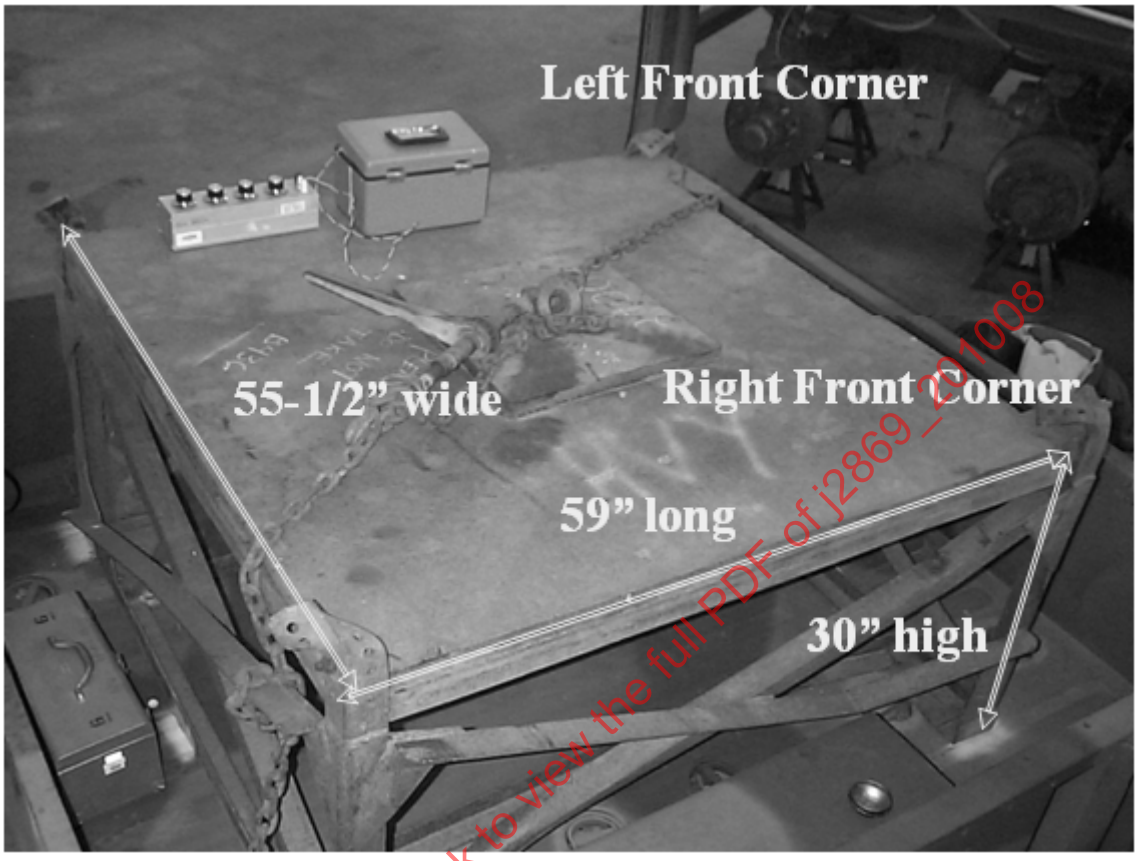

FIGURE 85 - TEST MASS USED FOR TRAILER EXPERIMENTAL TESTS

7. STRAIN VALIDATION

7.1 Test Courses

The trailer traversed a number of different test courses at multiple speeds to produce the validation strain data. Each run represents operation on a particular course at a set constant speed with fixed operating constraints. All of the runs selected for strain validation had the hydraulic surge brakes disabled. The runs are:

a. Run011 – Test Course B at 20 mph

b. Run022 – Test Course C at 10 mph

c. Run055 – Test Course A at 15 mph

7.2 Validation Process and Procedure

The validation process focuses on comparing experimental and simulation results at the critical points, FE nodes 424 and 425 illustrate the evaluation procedure. Steps include:

a. Compute the principal strain for both simulated and measured strain data.

b. Develop Histograms of strain data for both simulated and measured strain data.

c. Check the normality of the strain data to both simulated and measured strain data.

d. Calculate statistical parameters (Mean, RMS, skewness, kurtosis) for both simulated and measured strain data.

e. Generate and compare PSD curves for both simulated and measured strain data.

f. Predict the fatigue life using measured strain data and compare it with predicted simulation fatigue life.

7.3 Data Sanity Check and Initial Reduction: Filter and Decimate Data

The simulation data was analyzed at a frequency of 100 Hz. The decision to use the 100 Hz rate was primarily due to the flexible-body vibration mode frequencies, which were all less than 40 Hz, and the computational time required by DRAW to perform the fatigue life prediction. This computational time is directly proportional to the frequency (i.e., 200 Hz takes twice the time as 100 Hz). In this regard, the simulation models contain data with varying frequency content. For example, the rigid-body DADS model has a natural frequency for each rigid-body motion, and it has a forced-response frequency spectrum due to the motion of the prime mover and the irregularity of the terrain. The flexible-body DADS model adds the frequencies for the three eigenmodes used in the simulation model.

In order to properly compare the simulation and experimental test data, the experimental test data must be filtered to reduce the effect of noise and deterministic responses that occur at higher frequencies than what has been modeled. This filtering will also reduce the effect of aliasing in the signal. Proper filtering involves selecting a normalized cutoff frequency, and applying the filter both forwards and backwards in time to eliminate phase distortion. Since the experimental test data is being post-processed, the filter can be applied phaselessly (both forward and backward in time).

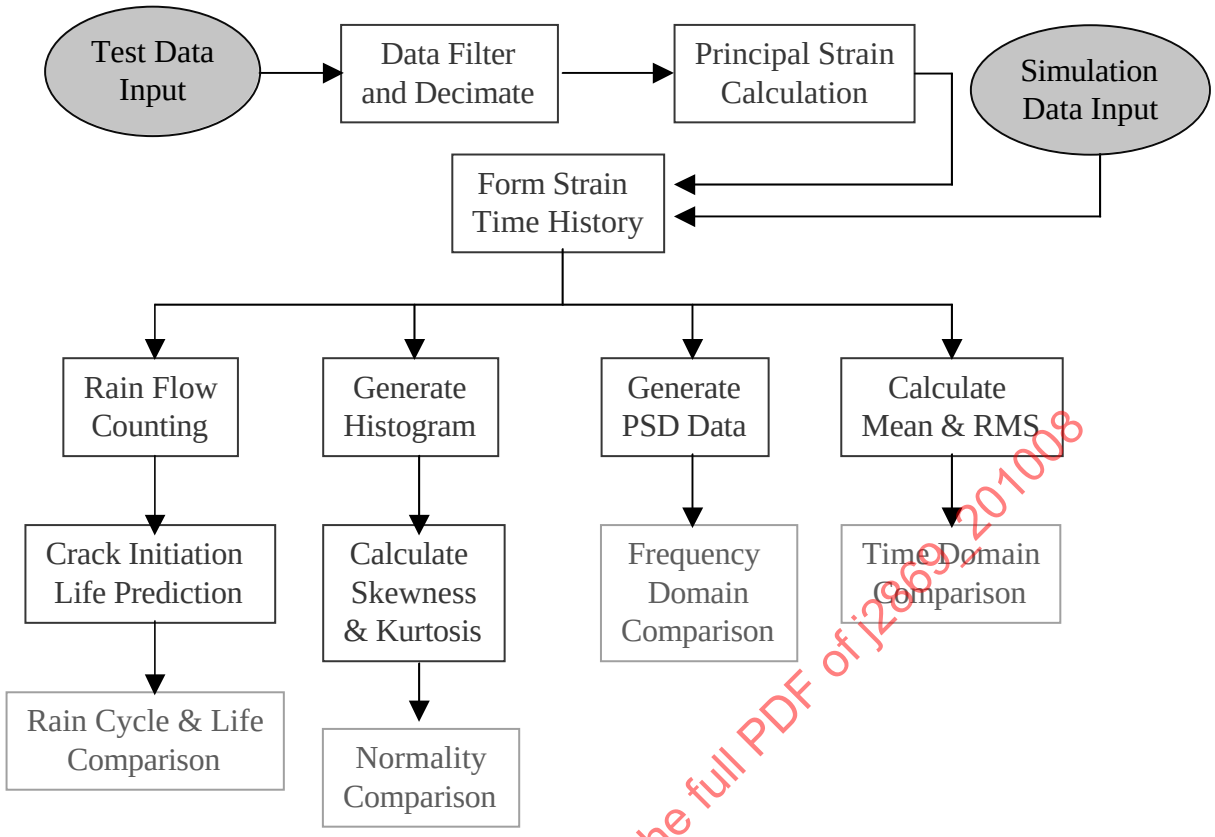

FIGURE 86 - EVALUATION PROCEDURE

Matlab includes a function '`decimate`' as part of the Signal Processing Toolkit. This decimation involves both filtering and re-sampling data. This function employs an eighth-order phaseless Chebyshev type-1 low pass filter whose cutoff frequency is set to the Nyquist-rate of the re-sampled data. The filter is applied to the data before it is re-sampled.

For example, in this case the data is originally sampled at 1262.626 Hz and we want to decimate it by a factor of 13, so the re-sampled frequency is 97.13 Hz, which is close to the 100 Hz simulation data. The '`decimate`' function will first filter the original data at 40 Hz, and then resample, using every 13th point. In this validation, the Chebyshev filter is used.

For simulation, DRAW obtains the dynamic information from DADS output data. Therefore, the data need to be filtered. Since DRAW itself does not produce any varying frequency content, it has more sense of reality that may filter the input data of DRAW (DADS output data) instead of filter the DRAW output data. In this regard, the dynamic analysis simulation data has been filtered first and then sent to DRAW.

Since the validation will performed through three experimental test data runs, which are Test Course A at 15 mph, Test Course B at 20 mph, and Test Course C at 10 mph, the corresponding simulations are performed. They are Test Course A at 15 mph for flexible dynamic body simulation, Test Course A at 15 mph for rigid body dynamic simulation, Test Course B at 20 mph flexible body simulation, Test Course B at 20 mph rigid body simulation, and Test Course C at 10 mph flexible body simulation. The comparison is also carried out for them.

7.4 Strain Time History

In order to compare the simulation and experimental results, statistical parameters of the strain time histories are calculated. The statistical parameters are the mean, RMS, standard deviation, skewness and kurtosis of the strain time histories.

The statistical differences between simulation and experimental test are shown in Figure 87 to Figure 94. In these figures, the horizontal axes indicates the node number, in which, node numbers 1 to 8 indicate the real node number 382, 383, 424, 425, 469, 471, 504, 531, respectively.

Figure 87 and Figure 91 show a side-by-side comparison of the mean values of principal strains 1 and 2,
Figure 88 and Figure 92 show the comparison of RMS values of principal strains 1 and 2,
Figure 89 and Figure 93 show the comparison of skewness of principal strains 1 and 2,
Figure 90 and Figure 94 show the comparison of kurtosis of principal strains 1 and 2.

a. The mean, RMS, and skewness graphs show that the values of nodes 382(1), 383(2), 424(3), 425(4) are much more consistent and comparable than the values of other four nodes. Nodes 382, 383, 424 and 425 are the nodes which are located on the bottom of the straight drawbar, and node 424 is the node which was closest to the point of failure.

b. All the statistical values for the principal strain 1 (longitudinal) match each other more closely than the statistical parameters for the principal strain 2 (lateral). Especially, for those nodes 469, 471, 504, and 531 that are located at the corner attached angular plates.

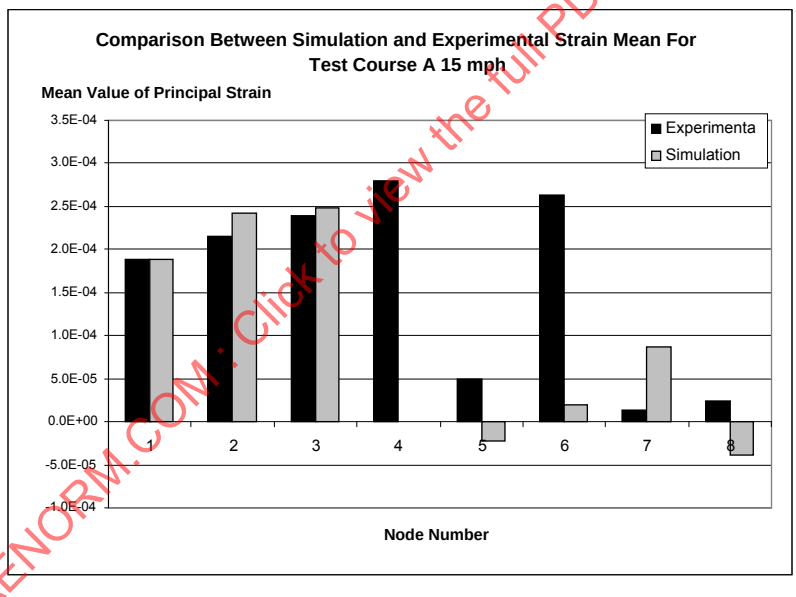

FIGURE 87 - MEAN VALUE COMPARISON OF PRINCIPAL STRAIN 1

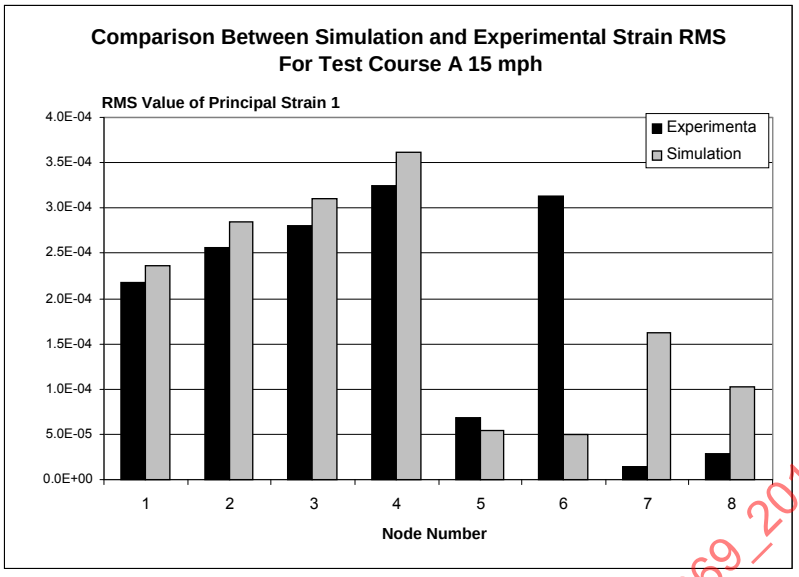

FIGURE 88 - RMS VALUE COMPARISON OF PRINCIPAL STRAIN 1

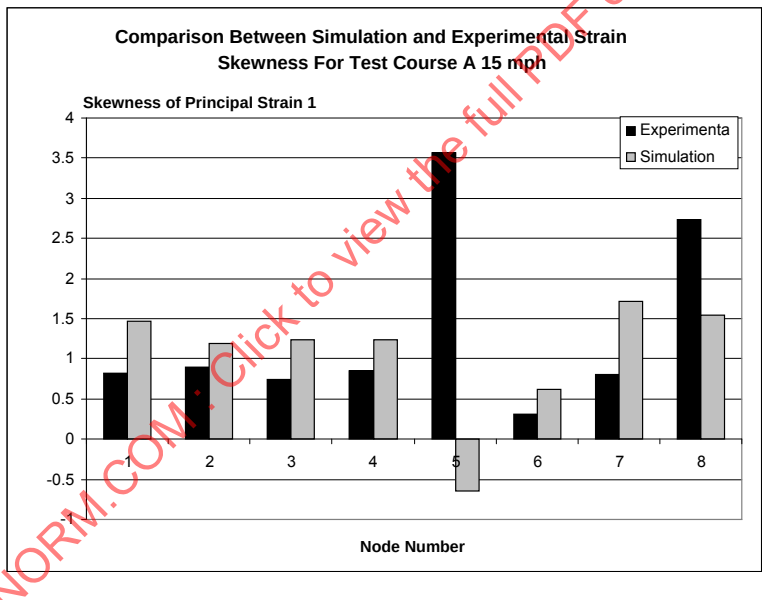

FIGURE 89 - SKEWNESS COMPARISON OF PRINCIPAL STRAIN 1

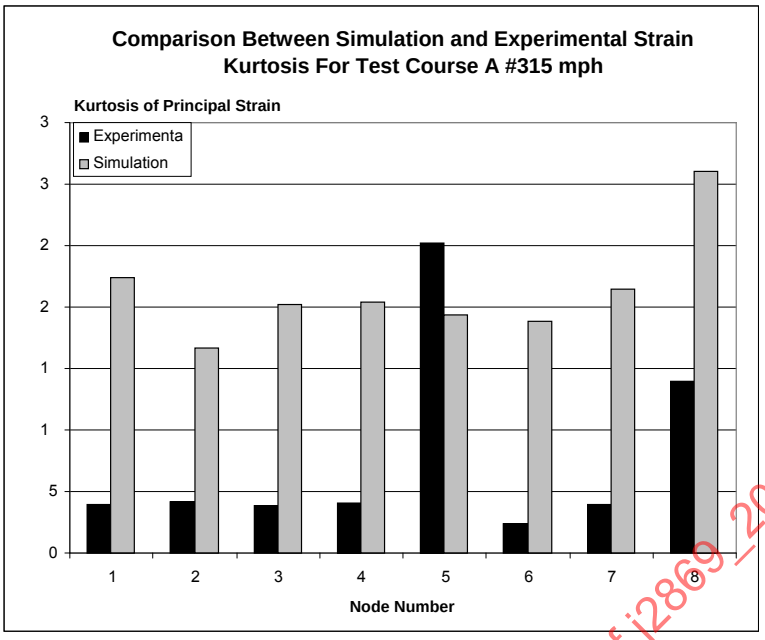

FIGURE 90 - KURTOSIS COMPARISON OF PRINCIPAL STRAIN 1

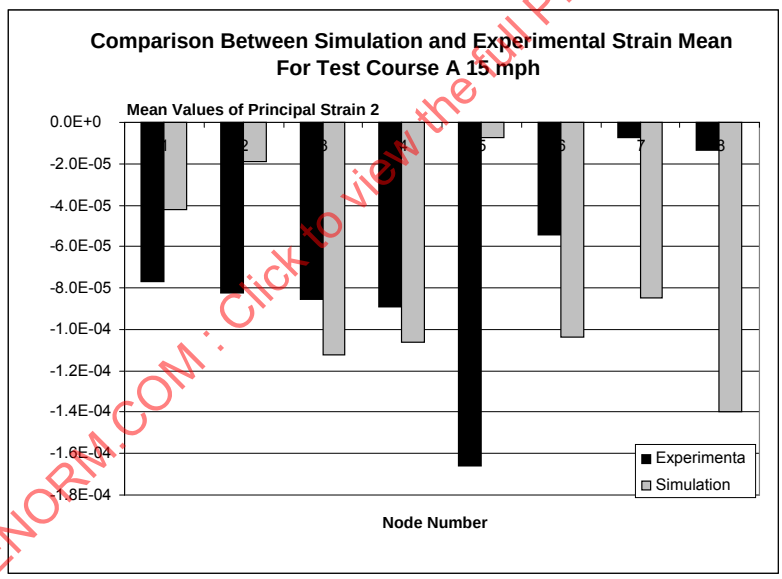

FIGURE 91 - MEAN VALUE COMPARISON OF PRINCIPAL STRAIN 2

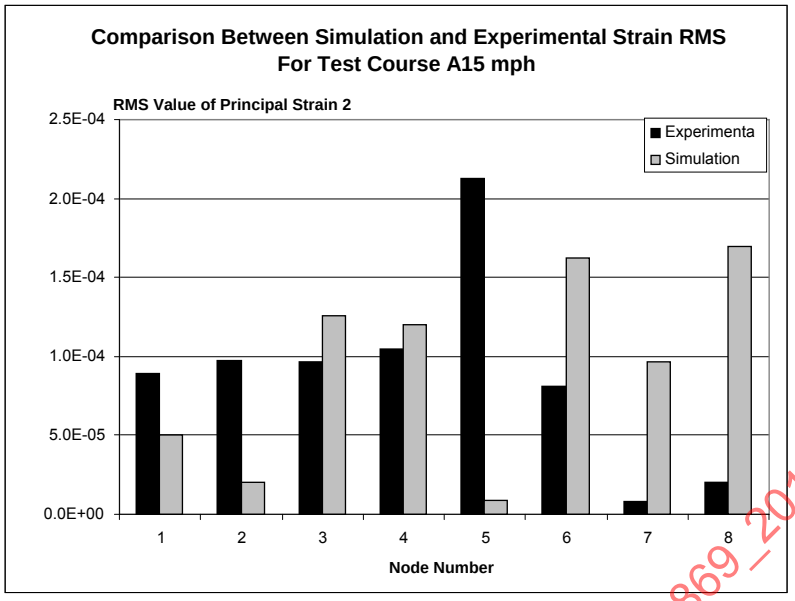

FIGURE 92 - RMS VALUE COMPARISON OF PRINCIPAL STRAIN 2

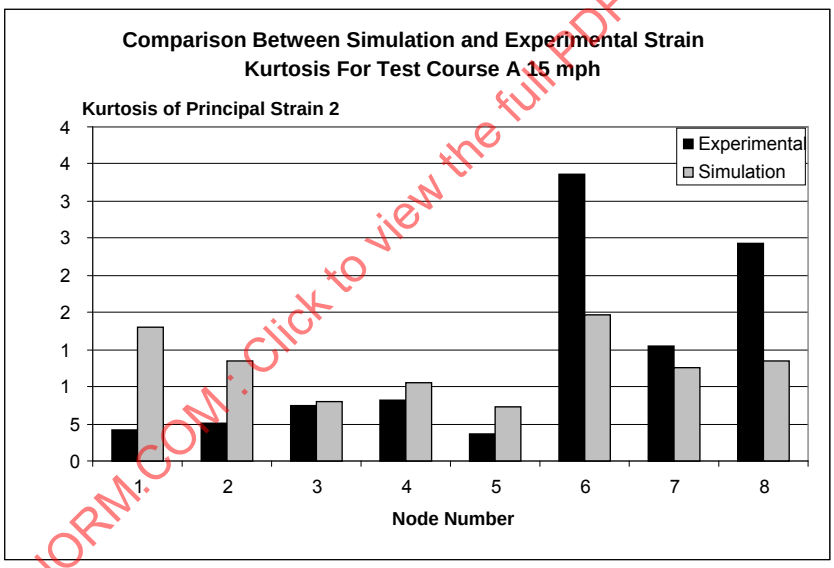

FIGURE 93 - SKEWNESS COMPARISON OF PRINCIPAL STRAIN 2

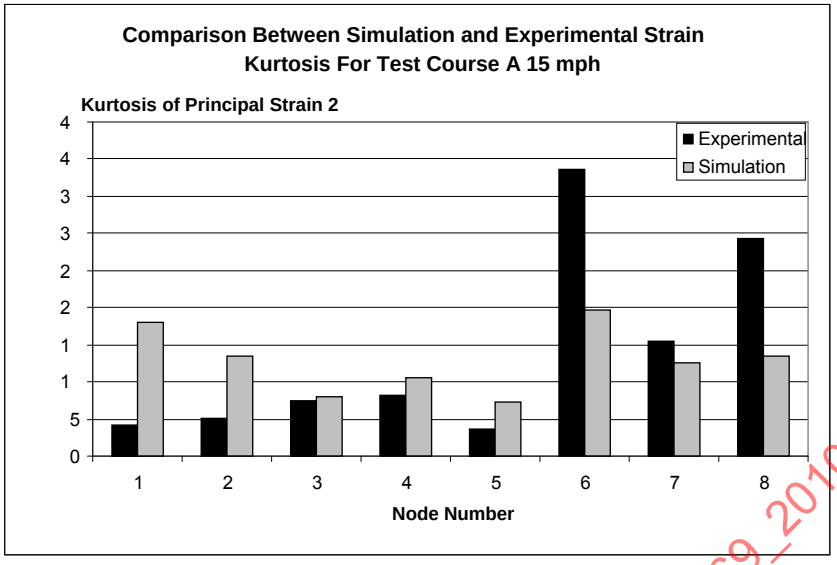

FIGURE 94 - KURTOSIS COMPARISON OF PRINCIPAL STRAIN 2

7.5 Normality Check of Strain Data

To check normality of both simulation and experimental test strain data and make a comparison with them, histograms have been generated. From these histograms, the normality of each data set can be explored. In these histograms, the number of bins is 101.

Figures 95 and 96 show the histograms of longitudinal strain P1 and lateral strain P2 of nodes 424 and 425 for Test Course A, respectively. Comparisons between the flexible body simulation and experimental test strain data for critical nodes 424 and 425 are also indicated. For the other six nodes that correspond with the other six strain gauges of Test Course A, the histograms and comparisons are shown in the Appendix C, Figures C7 to C12.

Figures 97 and 98 show the histograms of strain P1 and P2 of nodes 424 and 425 for Test Course B, respectively. Figure 97 shows the comparison between flexible body simulation and experimental strain P1 and P2 of node 424, while Figure 98 is the node 425.

Figures 99 and 100 show the histograms of strain P1 and P2 of nodes 424 and 425 for Test Course C, respectively. Figure 99 shows the comparison between flexible body simulation and experimental strain P1 and P2 of node 424, while Figure 100 is the node 425.

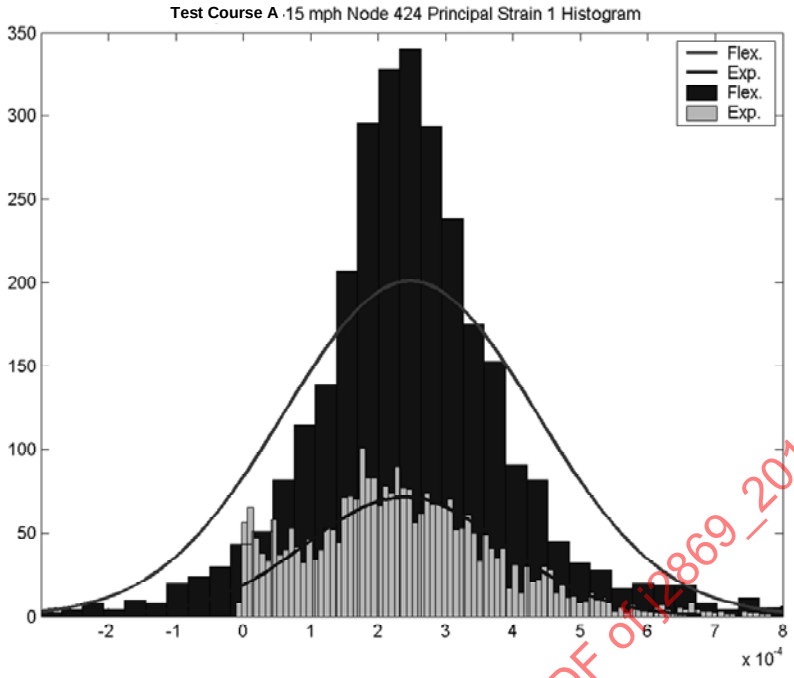

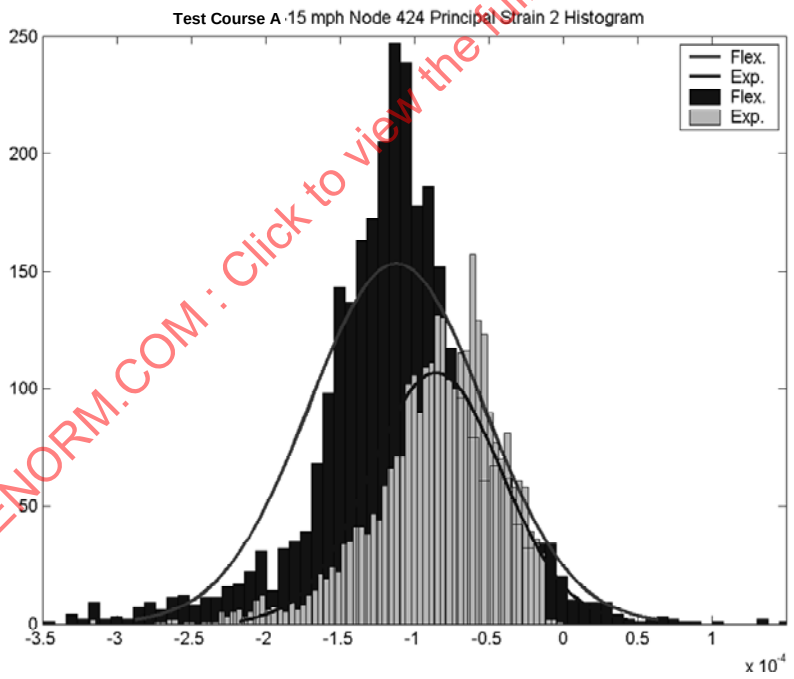

FIGURE 95 - TEST COURSE A HISTOGRAM FOR BOTH SIMULATION AND EXPERIMENT OF NODE 424

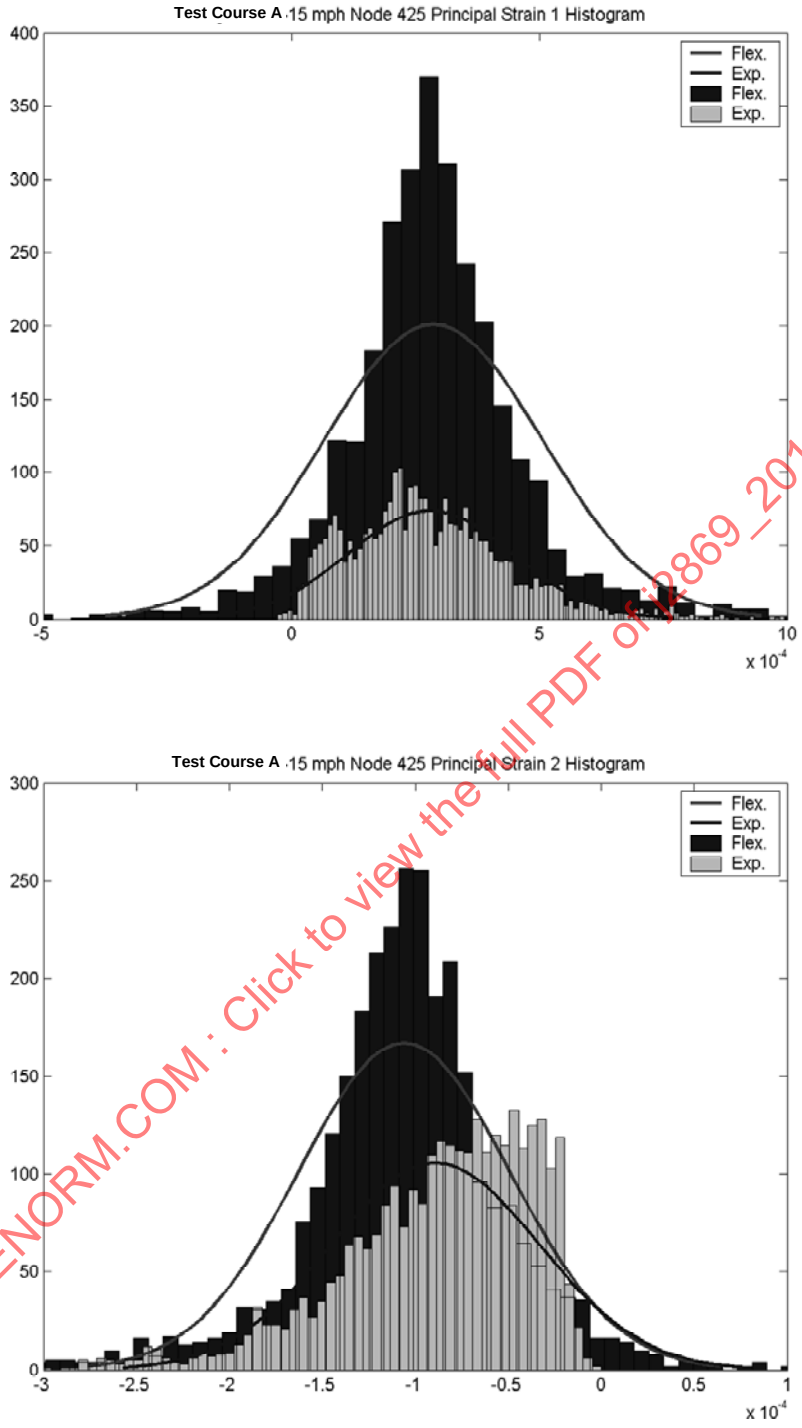

FIGURE 96 - TEST COURSE A HISTOGRAM FOR BOTH SIMULATION AND EXPERIMENT OF NODE 425

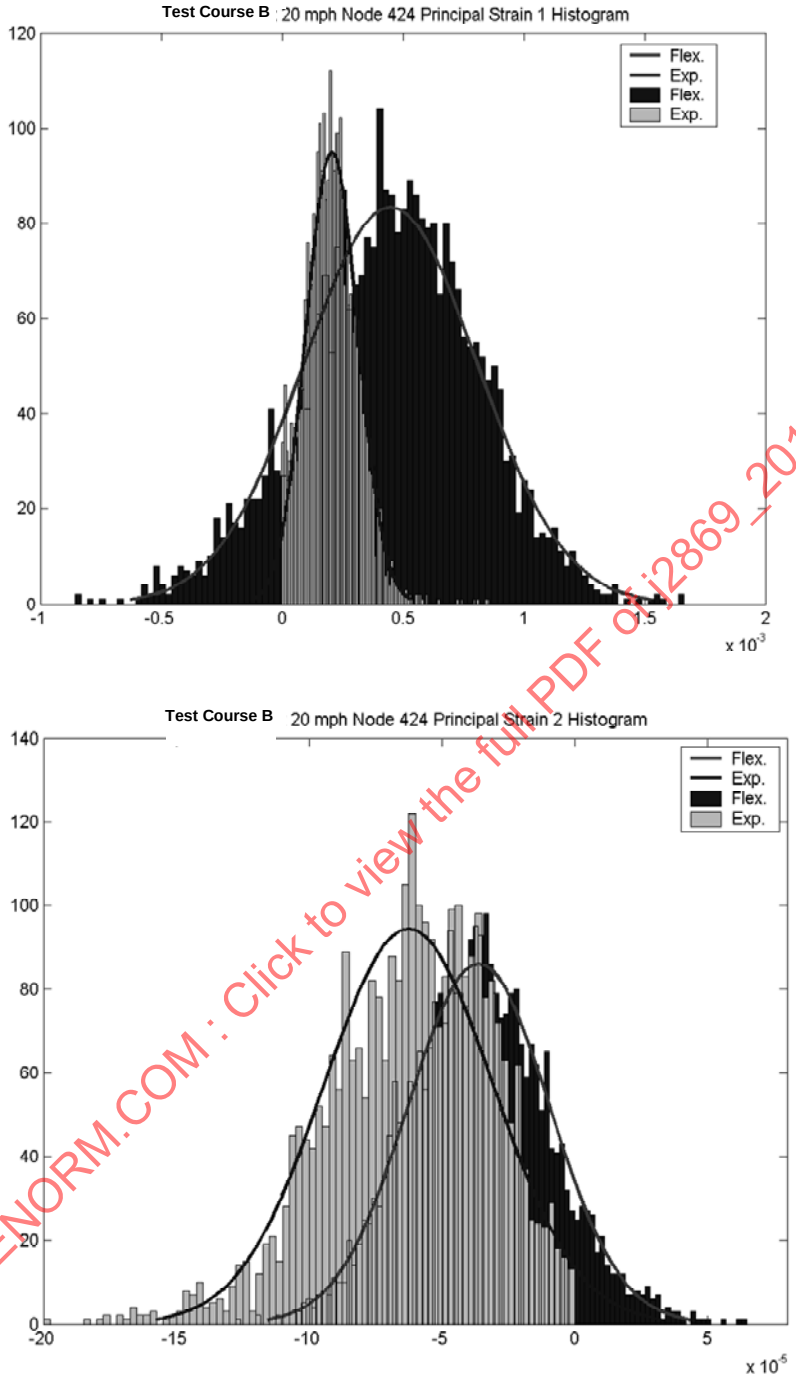

FIGURE 97 - TEST COURSE B HISTOGRAM FOR BOTH SIMULATION AND EXPERIMENT OF NODE 424

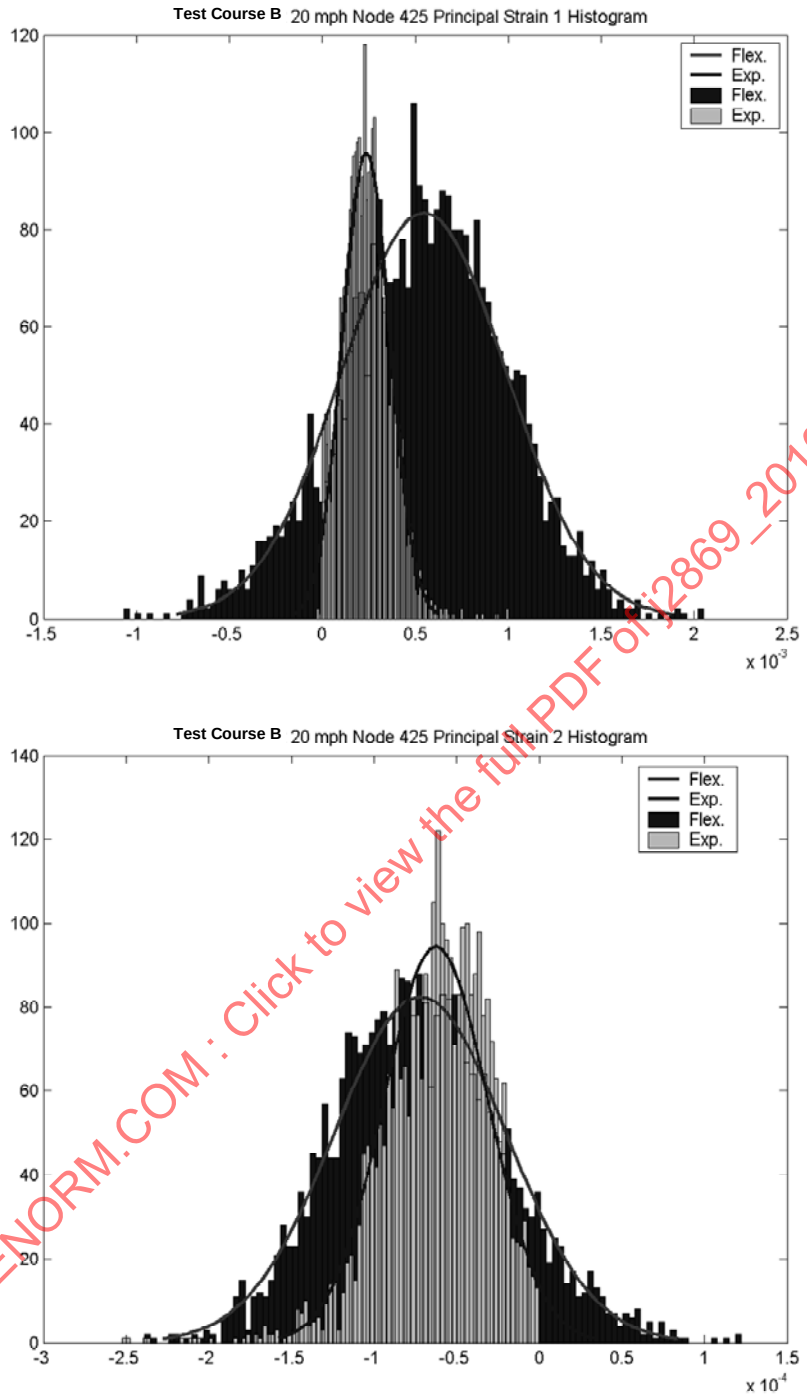

FIGURE 98 - TEST COURSE B HISTOGRAM FOR BOTH SIMULATION AND EXPERIMENT OF NODE 425

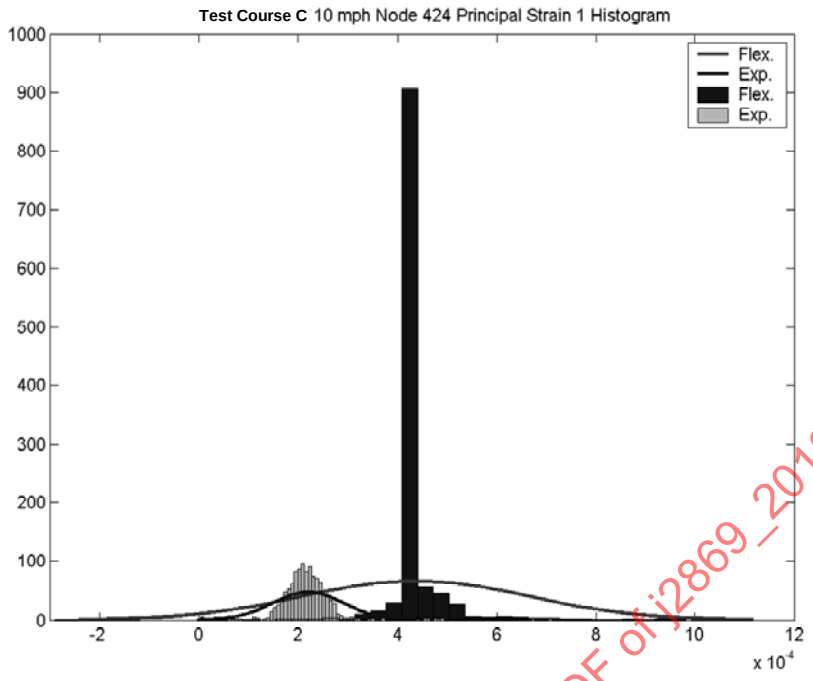

FIGURE 99 - TEST COURSE C HISTOGRAM FOR BOTH SIMULATION AND EXPERIMENT OF NODE 424

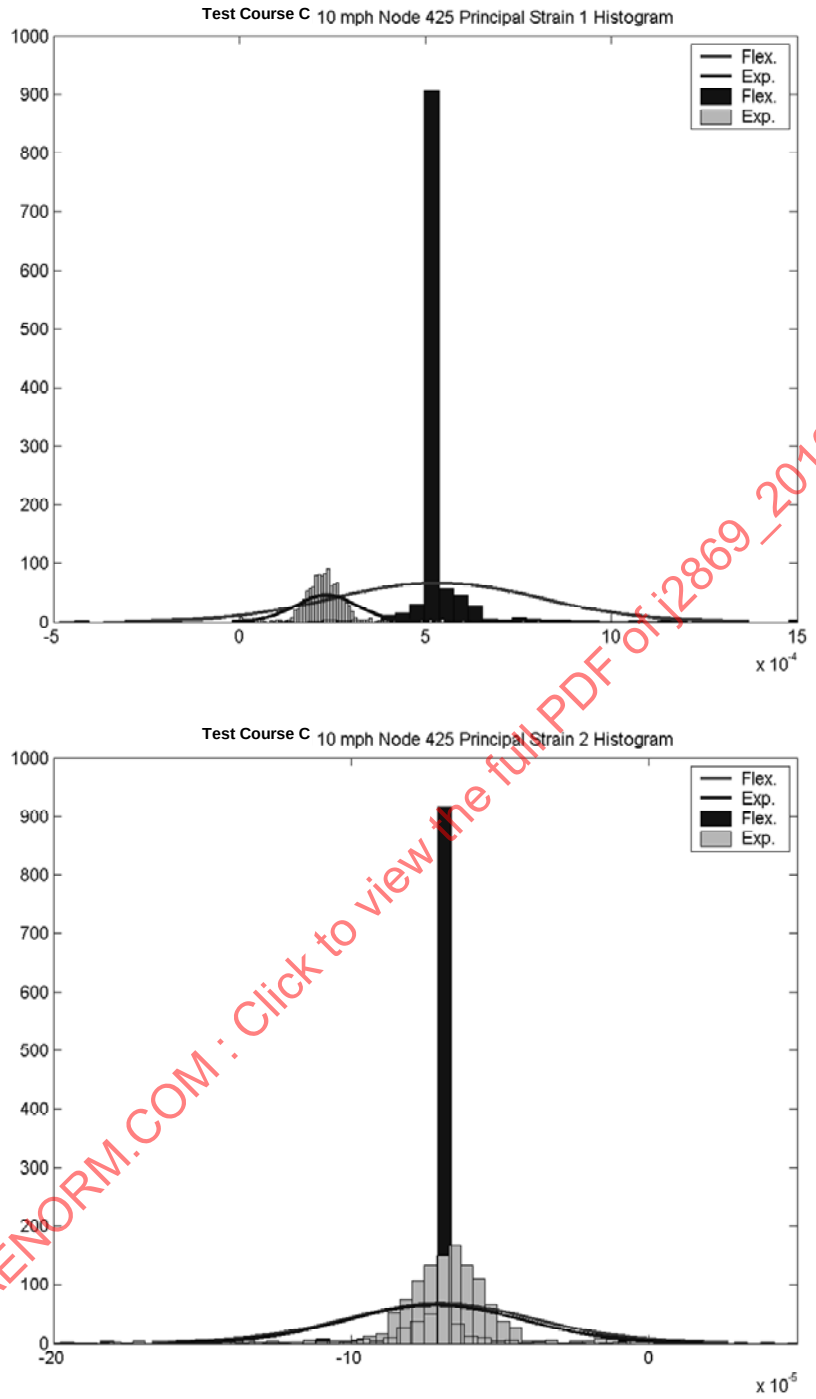

FIGURE 100 - TEST COURSE C HISTOGRAM FOR BOTH SIMULATION AND EXPERIMENT OF NODE 425

From these plots, it can be seen that the normality of node 424 for both Test Course A and Test Course B is pretty good, especially for Test Course A. On Test Course C, distribution does not appear to be normal since there are less data used. For Test Course A the mean values of both simulation and experiment are also very close, especially for longitudinal strain P1. After comparing the strain histograms of all eight nodes for Test Course A at 15 mph, we found the normality of the four nodes that are located on the bottom of the straight drawbar look good, while for the other four nodes the histograms show that the normality is not very good. The histograms for those nodes are shown in Appendix C, Figures C7 to C12. This is the same phenomenon that we have seen in the time history curves and their statistical parameters. This is because the four gauges at the bottom of the straight drawbar are attached on the drawbar directly, while the other four gauges are attached on the corner of the connected angular plates. These corners are a connection of several parts. Therefore, for the experimental test data, the signals of strain gauges are transmitted through other parts; this induces some problems with the fidelity of the transmission of the stress/strain. These same connections in the simulation also show low accuracy due to the limitations of these connections in the finite element model. These errors lead to a much higher strain fluctuation in the simulation than in the experimental time histories. This will cause the fatigue life estimate to be shorter. This situation will be discussed in more depth later in this section.

7.6 Power Spectral Density (PSD) Comparison

A more effective and meaningful comparison of dynamic related data is done in the frequency domain. Time histories of the simulation and experimental test data need to be converted into the frequency domain for comparison. Welch's technique which averages a number of periodograms, in order to reduce the variance, is used for this purpose. The analysis parameters were set to be a 256-point block-size, a Hanning window, and no overlap.

Figures 101 and 102 depict the PSD curves of both the flexible body simulation and the experimental test principal strains for the critical nodes 425 and 424, respectively. The test condition was Test Course A at 15 mph. Data for the other six node/strain gauge pairs are shown in the Figures C13 to C18 in Appendix C.

Figures 103 and 104 show the PSD curves and the principal strain of nodes 424 and 425, respectively, for Test Course B at 20 mph using both the flexible body simulation and experimental tests.

The corresponding Test Course C PSD curve comparisons are shown in Figures 105 and 106.

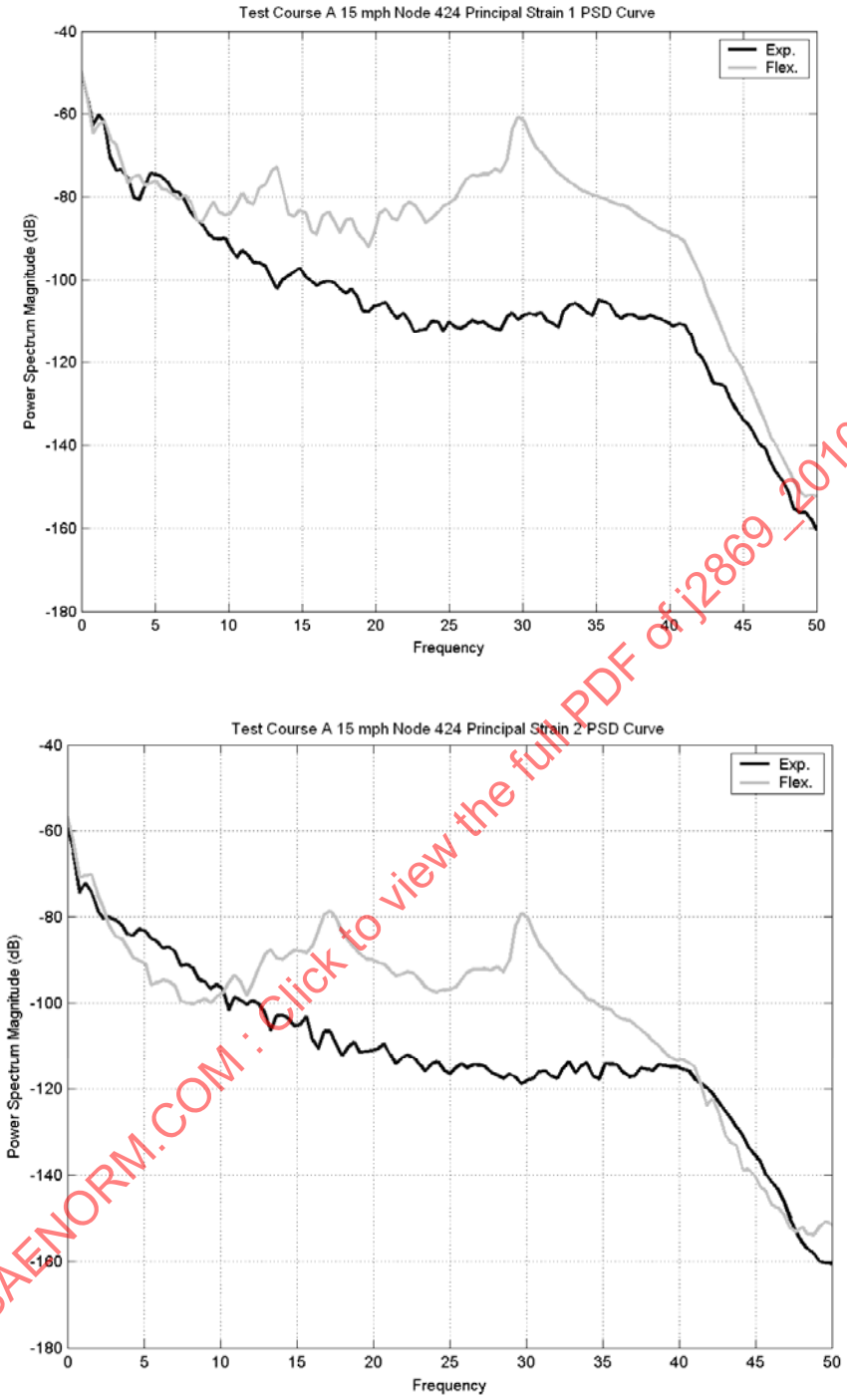

FIGURE 101 - TEST COURSE A PSD CURVES OF SIMULATION AND EXPERIMENT STRAIN DATA OF NODE 424

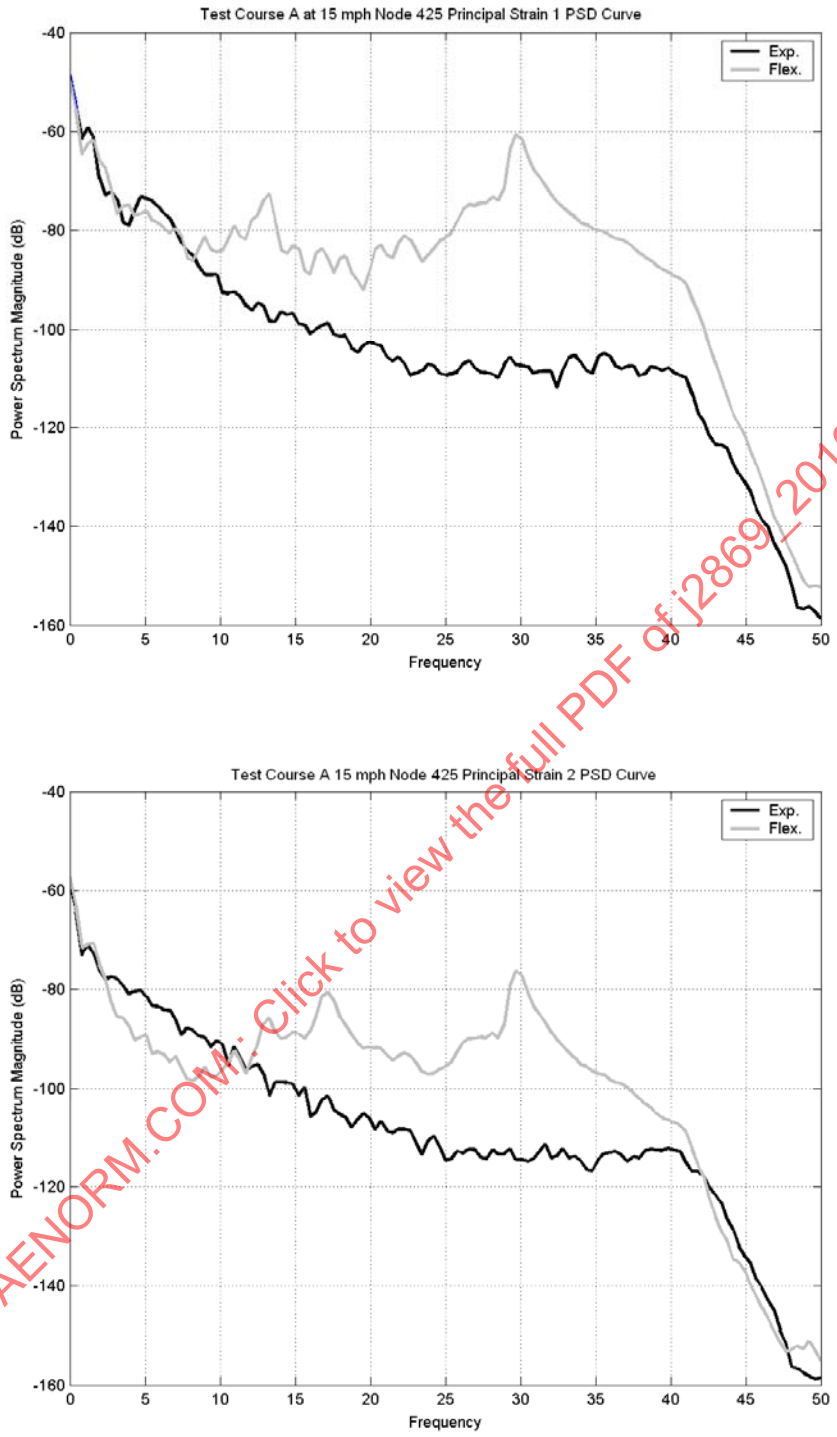

FIGURE 102 - TEST COURSE A PSD CURVES OF SIMULATION AND EXPERIMENT STRAIN DATA OF NODE 425

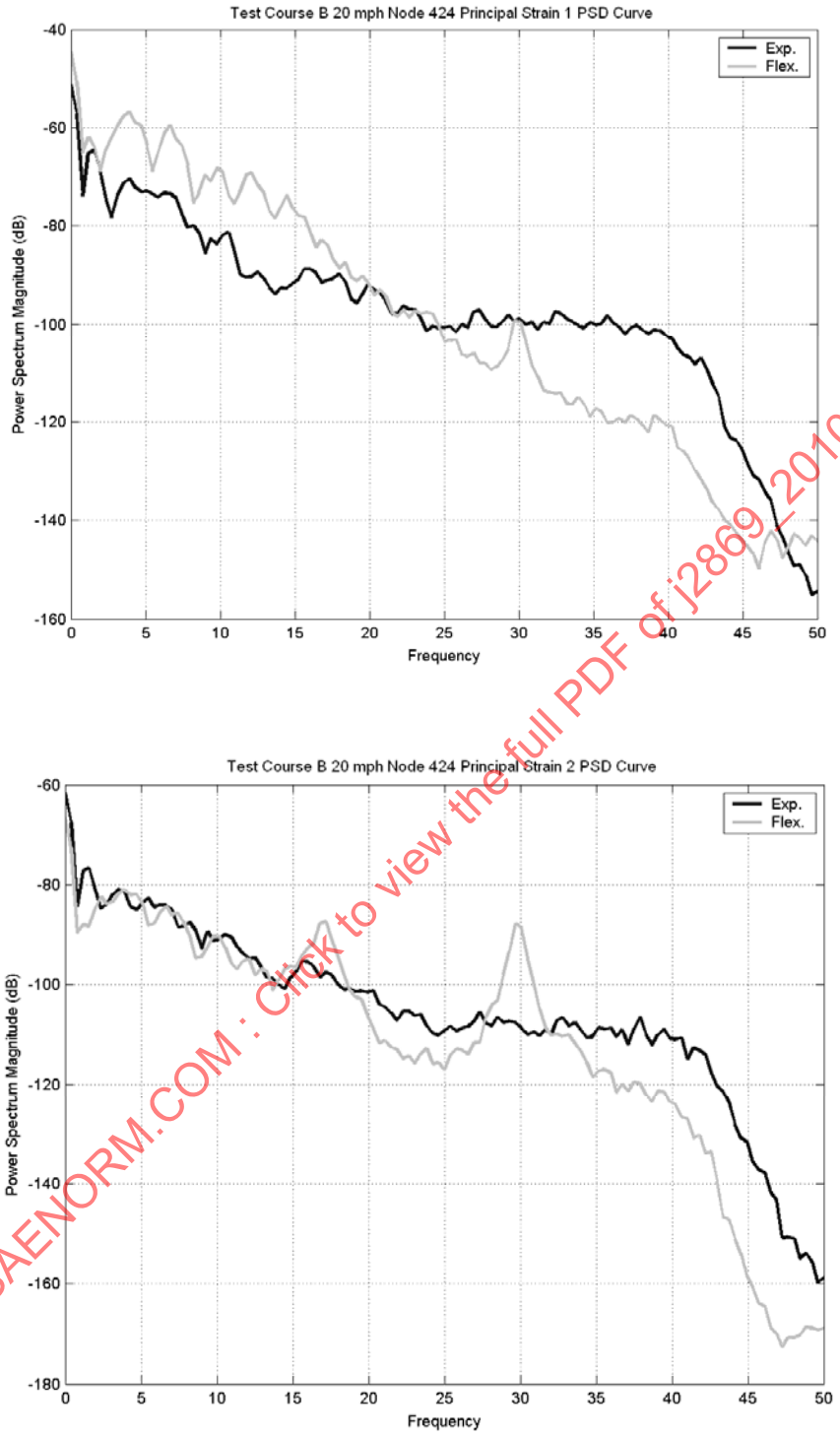

FIGURE 103 - TEST COURSE B PSD CURVES OF SIMULATION & EXPERIMENT STRAIN DATA OF NODE 424

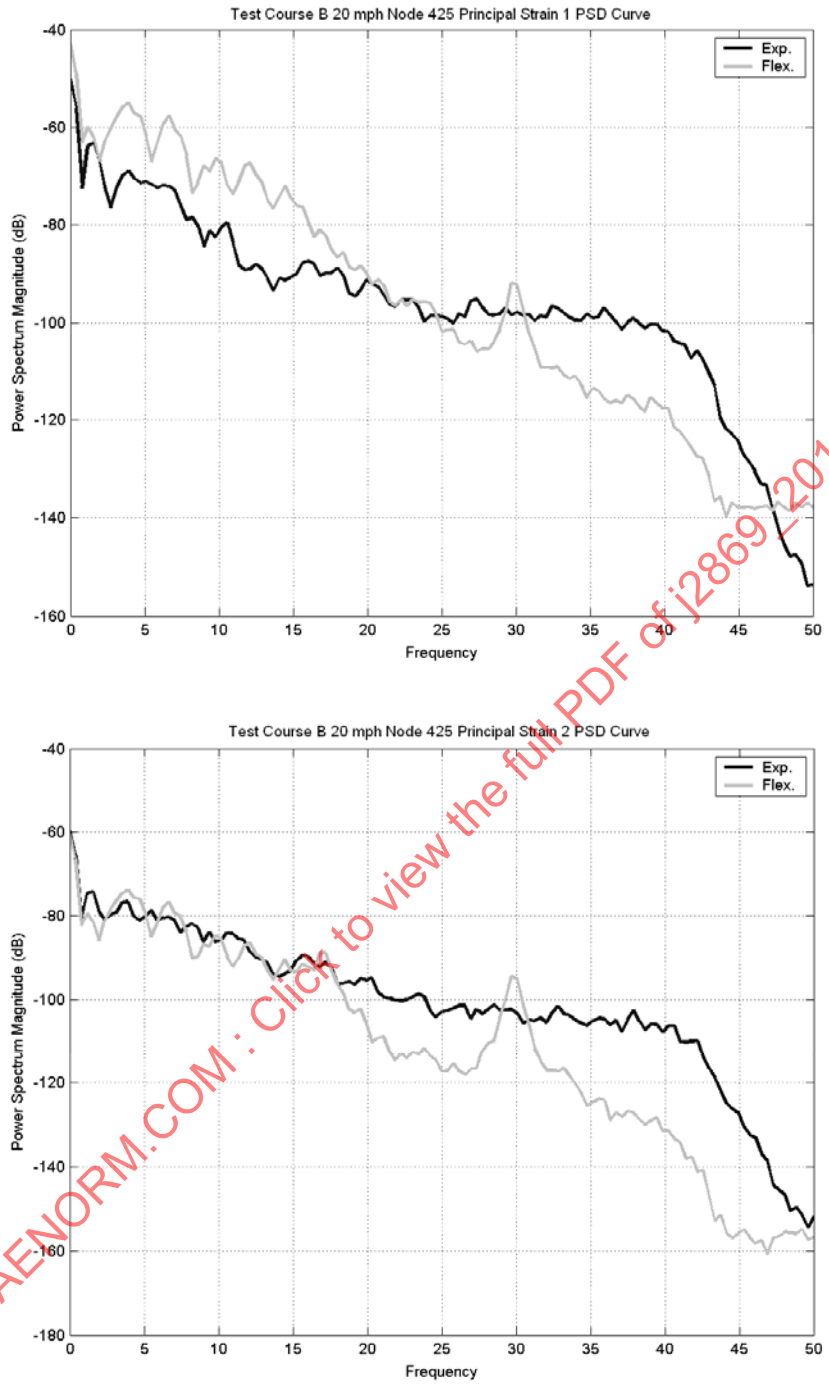

FIGURE 104 - TEST COURSE B PSD CURVES OF SIMULATION AND EXPERIMENT STRAIN DATA OF NODE 425

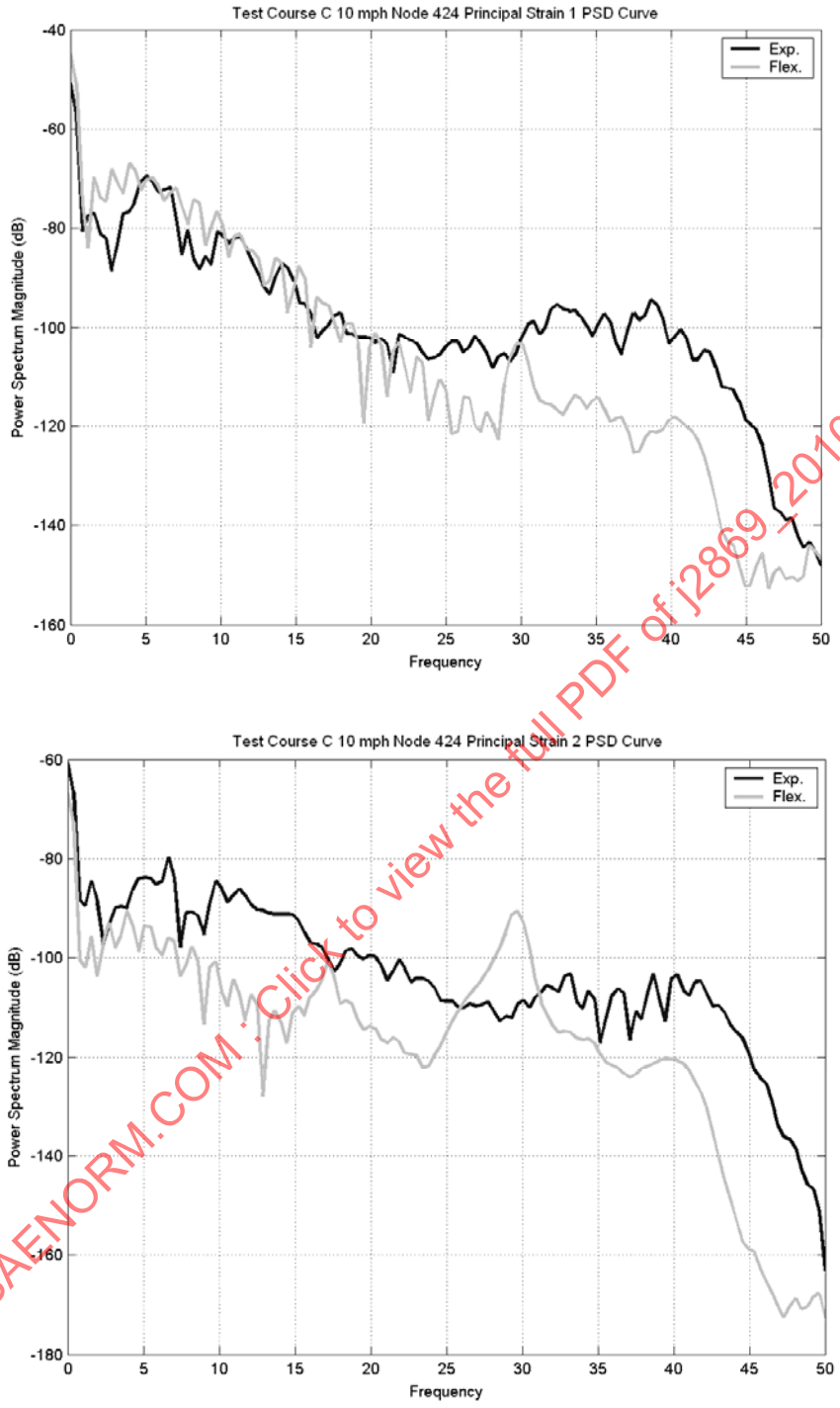

FIGURE 105 - TEST COURSE C PSD CURVES OF SIMULATION AND EXPERIMENT STRAIN DATA OF NODE 424

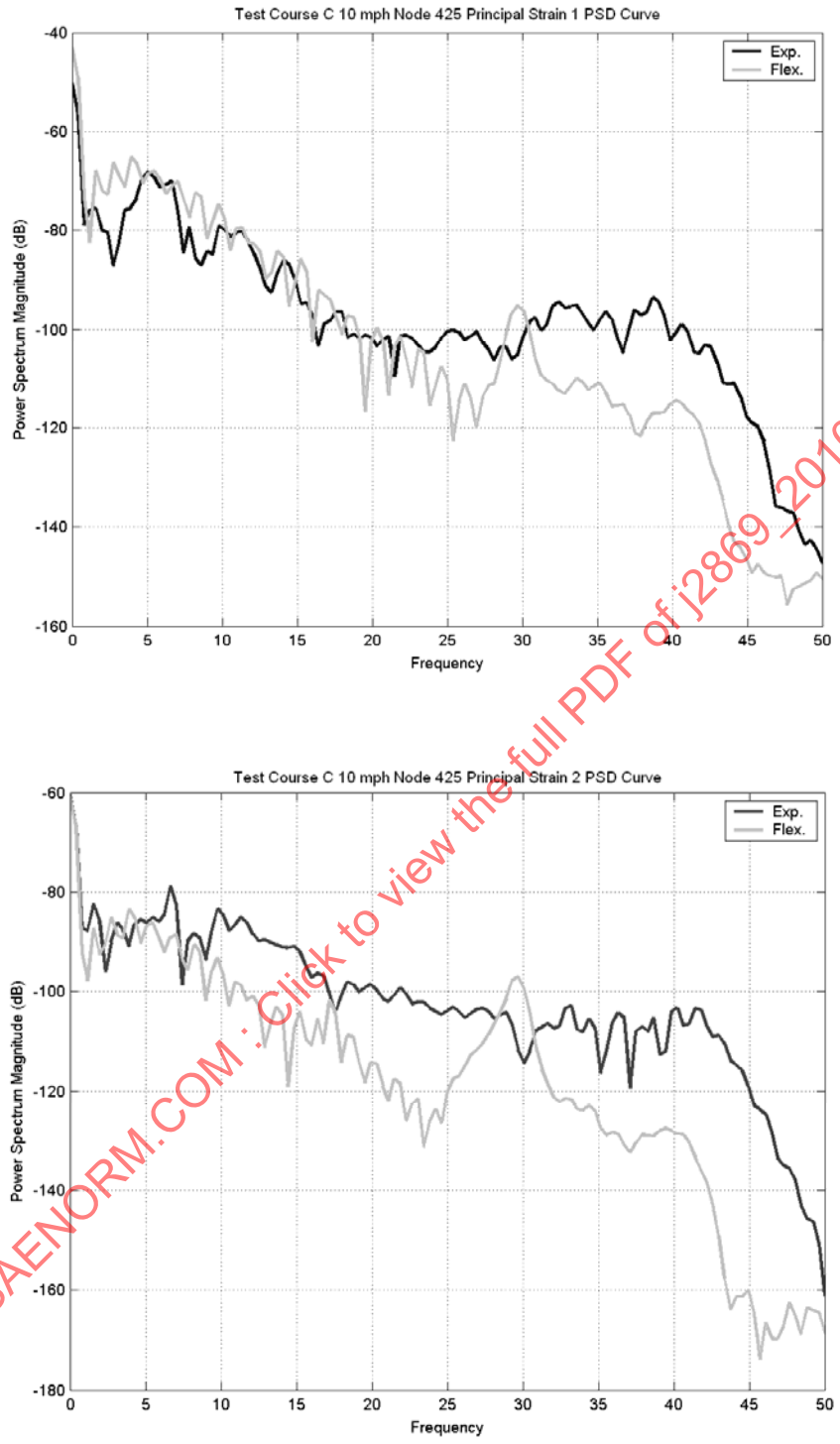

FIGURE 106 - TEST COURSE C PSD CURVES OF SIMULATION AND EXPERIMENT STRAIN DATA OF NODE 425

There are some differences between the simulation and experimental psd curves shown in Figures 101 to 106:

a. It can be seen that all simulation curves have two obvious peaks, one large peak around 30 Hz, and another peak between 10 and 15 Hz, while the experimental curves do not have them.

b. Except for a small part of low frequency, both simulation and experimental PSD curves do not match well.

7.7 Fatigue Crack Initiation Life

In this section, the simulation-based fatigue life values will be compared with the fatigue life values based on the experimental test data. The simulation-based fatigue durability analysis is based on one of the critical-plane methods implemented by the DRAW software. The experimental data was evaluated using the strain time histories.

Comparisons of the fatigue lives at critical node 425 and node 424 for the three validation runs, are presented in Figures 107 to 109 and in Table 27 to Table 29, respectively.

7.7.1 Fatigue Results: Test Course A at 15 mph

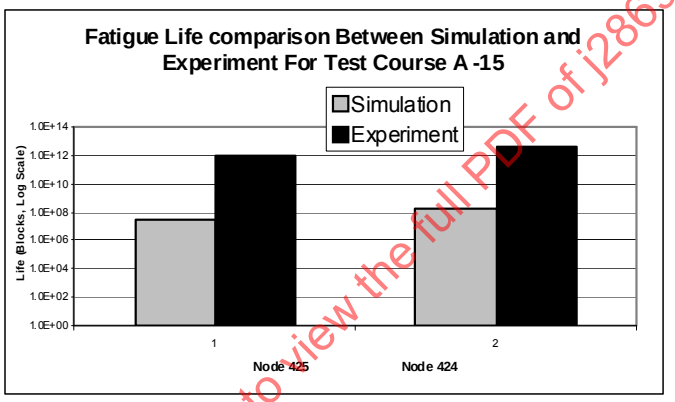

FIGURE 107 - COMPARISON OF LIVES BETWEEN SIMULATION AND EXPERIMENT FOR TEST COURSE A AT 15 MPH

TABLE 27 - LIFE COMPARISON BETWEEN FLEX SIMULATION AND EXPERIMENT FOR TEST COURSE A AT 15 MPH

Node No.	Flexible Body Simulation		Experimental Test	
	Blocks	Miles	Blocks	Miles
425	2.736E+7	3.421E+6	9.404E+11	1.176E+11
424	1.837E+8	2.297E+7	4.340E+12	5.425E+11

7.7.2 Fatigue Results: Test Course B at 20 mph

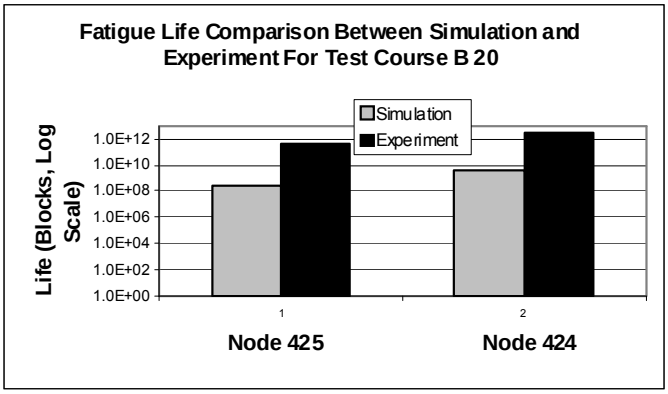

FIGURE 108 - COMPARISON OF LIVES BETWEEN SIMULATION AND EXPERIMENT FOR TEST COURSE B AT 20 MPH

TABLE 28 - LIFE COMPARISON BETWEEN FLEX SIMULATION TABLE AND EXPERIMENT FOR TEST COURSE B AT 20 MPH

Node No.	Flexible Body Simulation		Experimental Test	
	Blocks	Miles	Blocks	Miles
425	3.035E+8	3.794E+7	4.466E+11	5.583E+10
424	4.631E+9	5.789E+8	3.049E+12	3.811E+11

7.7.3 Fatigue Results: Test Course C at 10 mph

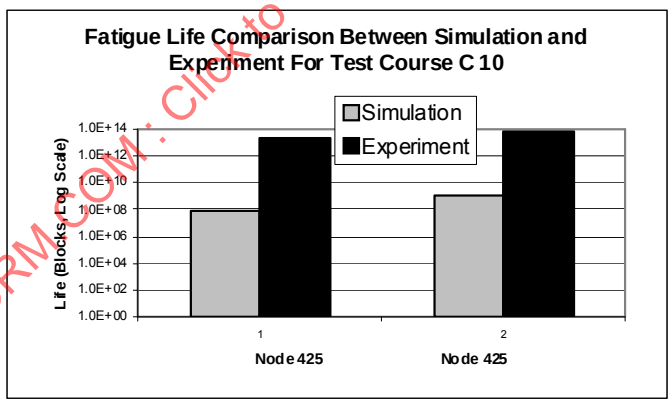

FIGURE 109 - COMPARISON OF LIVES BETWEEN SIMULATION AND EXPERIMENT FOR TEST COURSE C AT 10 MPH

TABLE 29 - LIFE COMPARISON BETWEEN FLEX SIMULATION AND EXPERIMENT FOR TEST COURSE C AT 10 MPH

Node No.	Flexible Body Simulation		Experimental Test	
	Blocks	Miles	Blocks	Miles
425	6.882E+7	1.912E+6	2.180E+13	6.056E+11
424	1.209E+9	3.358E+7	6.759E+17	1.878E+12

From these comparisons, we can see that the simulation lives are much shorter than experimental test. However, the mean values of strain for both simulation and experimental test are close. We need to explore the reasons that cause this phenomenon. In the next section, factors that affect fatigue life will be discussed. Based on these factors, reasons that cause the fatigue life differences will be discussed.

7.8 Prediction of Fatigue Crack Initiation Life and Factors That Affect Life

The fatigue analysis has used the strain-based fatigue life approach for crack initiation life prediction. The strain-life approach is the most important method used for Low Cycle Fatigue (LCF) life. Failure is defined by the development of a crack having a specified length. The strain-life curves (μ-N curves) were used to characterize the material of component response to cyclic loading. In this method, a single strain-life relation, μ-N curve that is applicable in LCF regimes is constructed. However, a μ-N curve is determined by fatigue tests or by empirical relations among some basic material property parameters (Bannantine et al., 1990). The experimental data of the μ-N diagram is actually obtained based on constant amplitude strain cycles (the stress and/or strain time-histories are sinusoid), the μ-N curve is an “average” drawn through a scatter band of points plotted from the failure of individual fatigue specimens. On the other hand, the environmental loading on a component is varied in time in a random fashion; the stress/strain variation in a component will also be varied in time and be a stochastic process. This means that a given varied amplitude history of operating stress or strain is expressed as a function of time within certain time interval (called a “block”).

In order to predict life using μ-N relationship, it is often advantageous to consider a quasi-constant loading level life. Thus, the stress and strain time history is always broken down into a series of defined constant amplitude cycles using a cycle-counting approach, in most cases; it is the rain-flow counting method. That is, after a rain-flow counting, an irregular stress or strain history has been transformed through hysteresis curves (stress-strain loops) into an equivalent sequence of closed loop constant amplitude stress and strain histories. The cycle counting method plays a very important role in the fatigue life prediction process. It is generally regarded as the method leading to the best estimators of fatigue life. It is designed to catch both slow and rapid variation in the load process by forming cycle amplitudes and by pairing high maxim with low minima even if they are separated by intermediate extremes. Due to the great importance of the cycle-count, a strain/strain process can be decomposed (broken down) into several cycles in which the stress/strain time-histories are sinusoid and to be used to predict life using S/ μ-N curves.

Cycle counting yields many cycles which can then be utilized to predict a life, associated with a specific cycle, by using μ-N curve. Since the fatigue effect is likely to gradually weaken the capacity of the component, it does not consider those affected in a separated problem. To obtain the life of whole loading history (block), a widely accepted damage summation model, such as Palmgren-Miner rule, will then be used to combine the individual life found for each defined cycle into the predicted life of the whole history. The Palmgren-Miner cumulative damage criterion is a definition of fatigue damage. With this definition, through cycle counting methods and a mathematical characterization of strain-life (μ-N) fatigue curve, the fatigue life has been predicted.

It is then clear that the life value not only relies on the amplitude of strain but the fluctuation as well. Large amplitudes will lead to a shorter fatigue life. Additionally, the greater the fluctuation in the strain history, the greater the number of cycles the cycle counting algorithm will find for a given block. Since, a larger number of cycles will lead to more accumulated damage; this increase in damage will also cause the fatigue life to shorten.

7.9 The Reasons That Cause the Fatigue Life Differences in Trailer Model

To prove this conclusion, we have filtered the strain time history by discarding the high frequencies above 10 Hz using low pass 8-pole Butterworth filter. By using the filtered data, the fatigue life of critical Node 425 is predicted. When comparing the fatigue life obtained based on the filtered strain history with the fatigue life predicted from experimental strain, it shows they are very close. The fatigue life results and comparison are shown in Table 30 and illustrated in Figure 110.

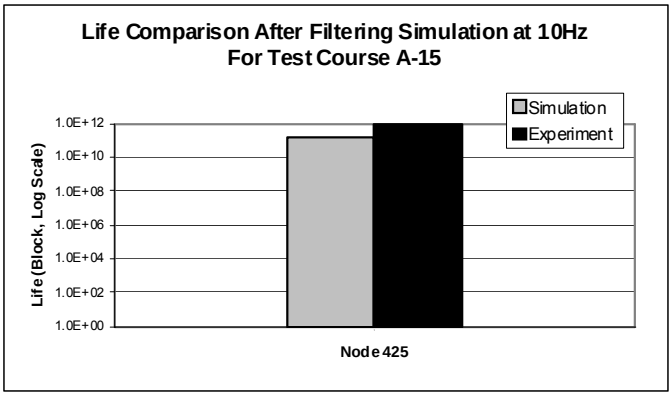

FIGURE 110 - LIFE COMPARISON BETWEEN FILTERED SIMULATION STRAIN AND EXPERIMENTAL STRAIN

TABLE 30 - LIFE COMPARISON BETWEEN SIMULATION (AFTER FILTERING) AND EXPERIMENT

Node No.	Flexible Body Simulation		Experimental Test	
	Blocks	Miles	Blocks	Miles
425	1.42E+11	1.77E+10	9.40E+11	1.18E+11

The next question that needs to be discussed is why the high frequency sparks (fluctuation) were formed in the simulation result. In order to answer this question, the loading histories have been studied first since the load and stress/strain should be synchronous. The loading histories were obtained from dynamics simulation; it then has a forced-response frequency spectrum due to the motion of the prime mover and the irregularity of the terrain. Figure 111 shows one of the regular joint reaction force histories and one of the flexible motion induced inertia force histories. From this figure, we can see that the inertia force induced by flexible motion has a higher fluctuation than the joint force. We also magnified these histories partially to be sure. The magnified curve is shown in Figure 112. The two histories indicate clearly that the inertia force has high fluctuation. This is one of the reasons the high fluctuation in the simulation strain history.

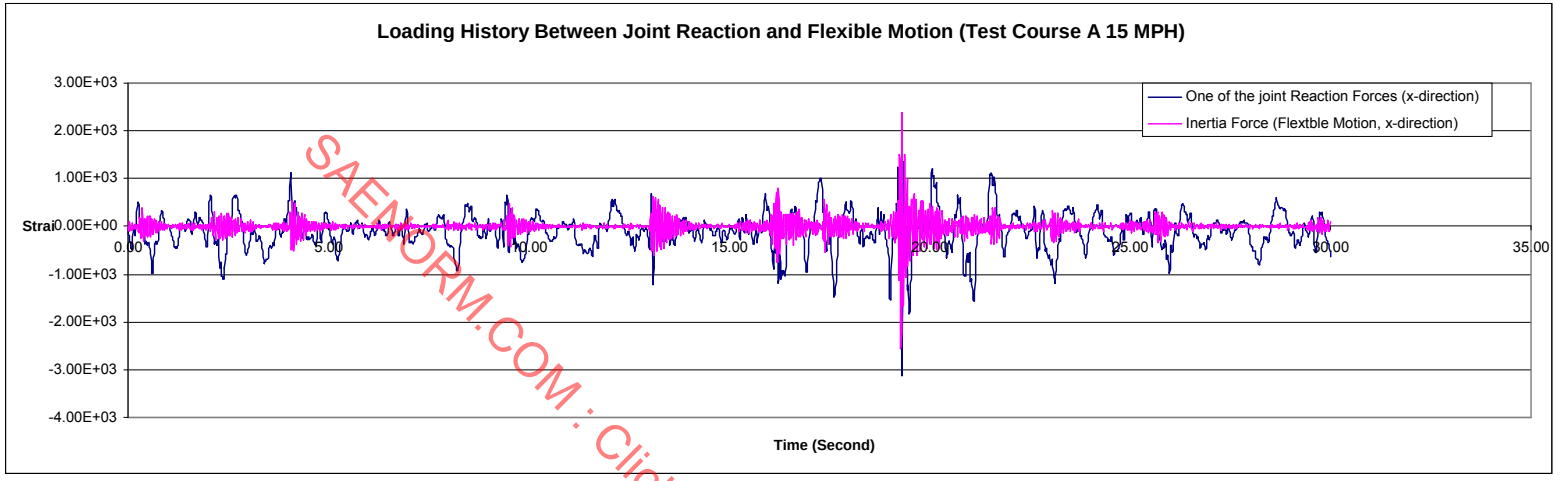

FIGURE 111 - ONE OF THE JOINT REACTION FORCES AND FLEXIBLE MOTION INERTIA FORCES HISTORY

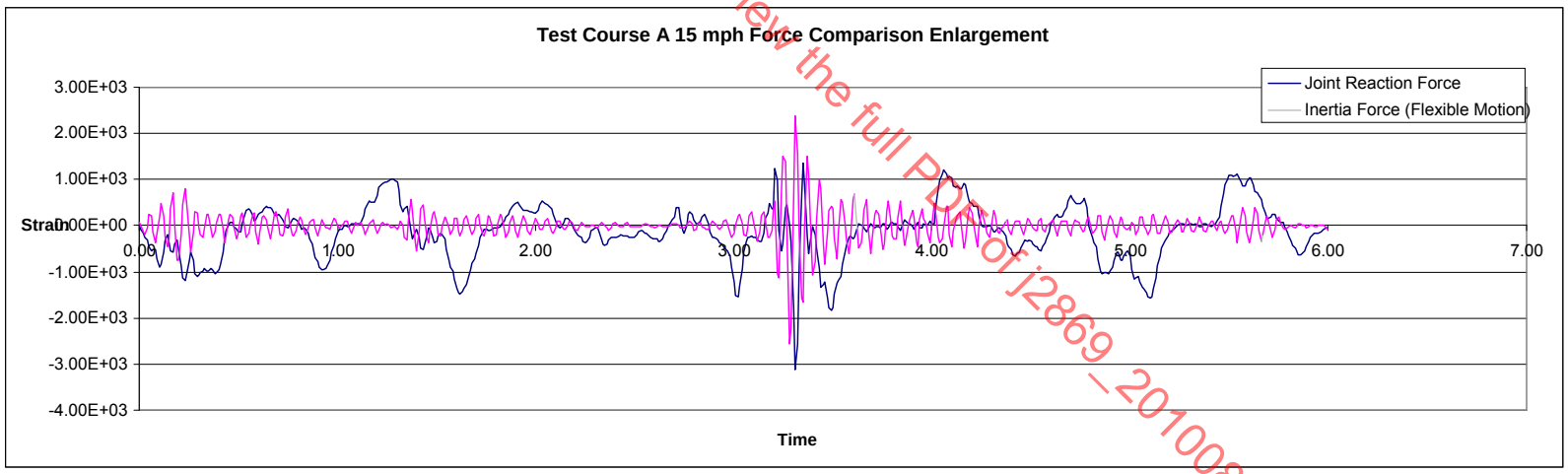

FIGURE 112 - PARTIAL ENLARGEMENT (16 TO 22 INCHES)

By studying more loading cases, we found that not only the flexible motion induced inertia forces have high fluctuation, but also the payload-joint reaction forces have high fluctuation too. The following pictures illustrated inertial force induced rigid gross motion and payload joint reaction forces. Figure 113 depicted inertia force induced by rigid motion. Figures 114 to 117 are one of the reaction forces of the payload-joints, in which Figures 114 and 115 are one of the joint reaction forces of all four payload-joints and their partial magnifications, while Figures 116 and 117 are one of the joint reaction forces of the front-left payload-joint and their partial magnification, respectively. These history curves indicate that the payload-joints also contribute the high fluctuation to the strain. Even the inertia force induced by rigid motion has some contribution to the high fluctuation in the strain. That contribution however is very small, and should be considered negligible when compared with others.

After this study, we realized that the flexible dynamic model is not perfect because of the selection of the static correction mode shapes. The static correction mode shapes are very sensitive for the dynamic response. Therefore, the static mode shape selection is very important for flexible dynamic analysis. However, the static correction mode shapes for the payload-joint are not included and other static correction mode shapes may not be accurate enough in the current dynamic model. This causes the high fluctuation in the simulation strain histories.

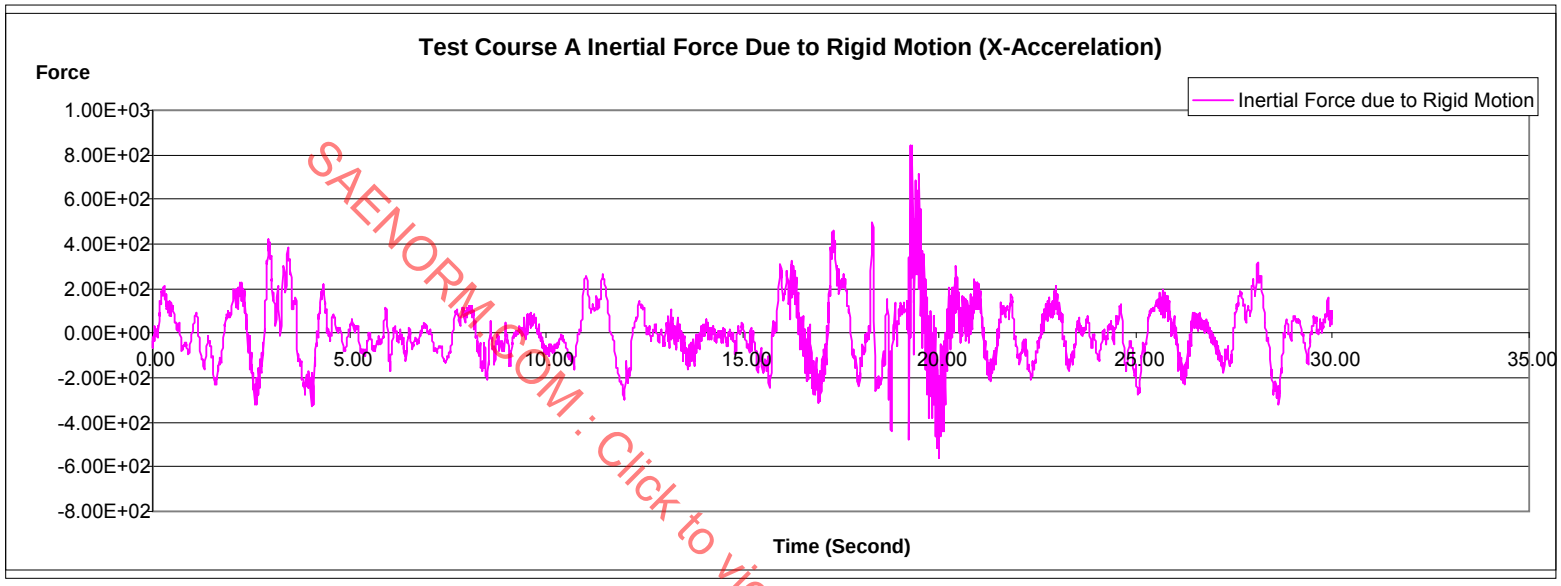

FIGURE 113 - INERTIA FORCE HISTORY INDUCED BY RIGID GROSS MOTION

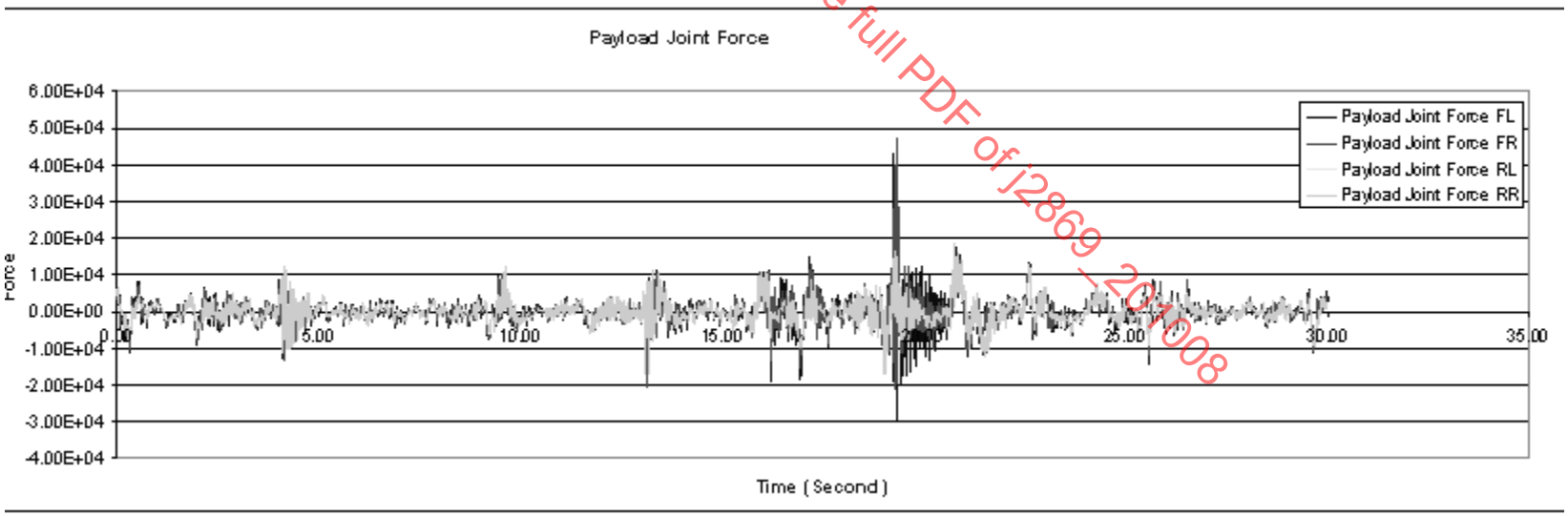

FIGURE 114 - JOINT REACTION FORCE HISTORY OF FOUR PAYLOAD JOINTS

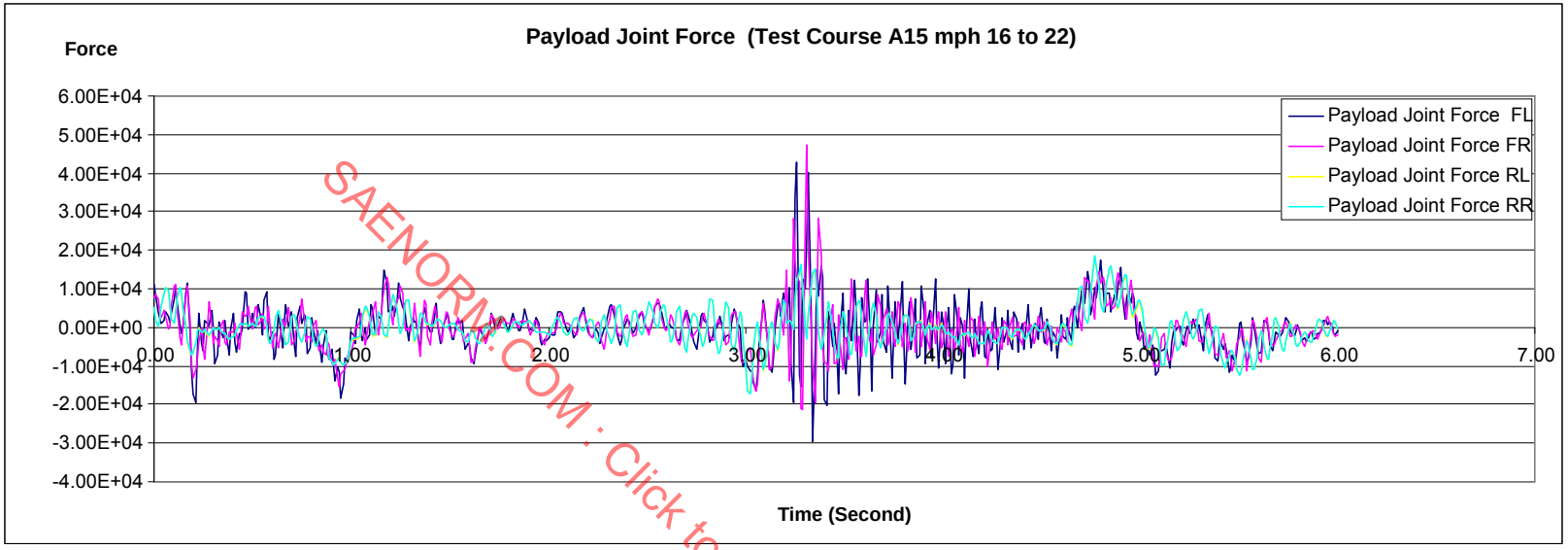

FIGURE 115 - PARTIAL ENLARGEMENT (16 TO 22 INCHES)

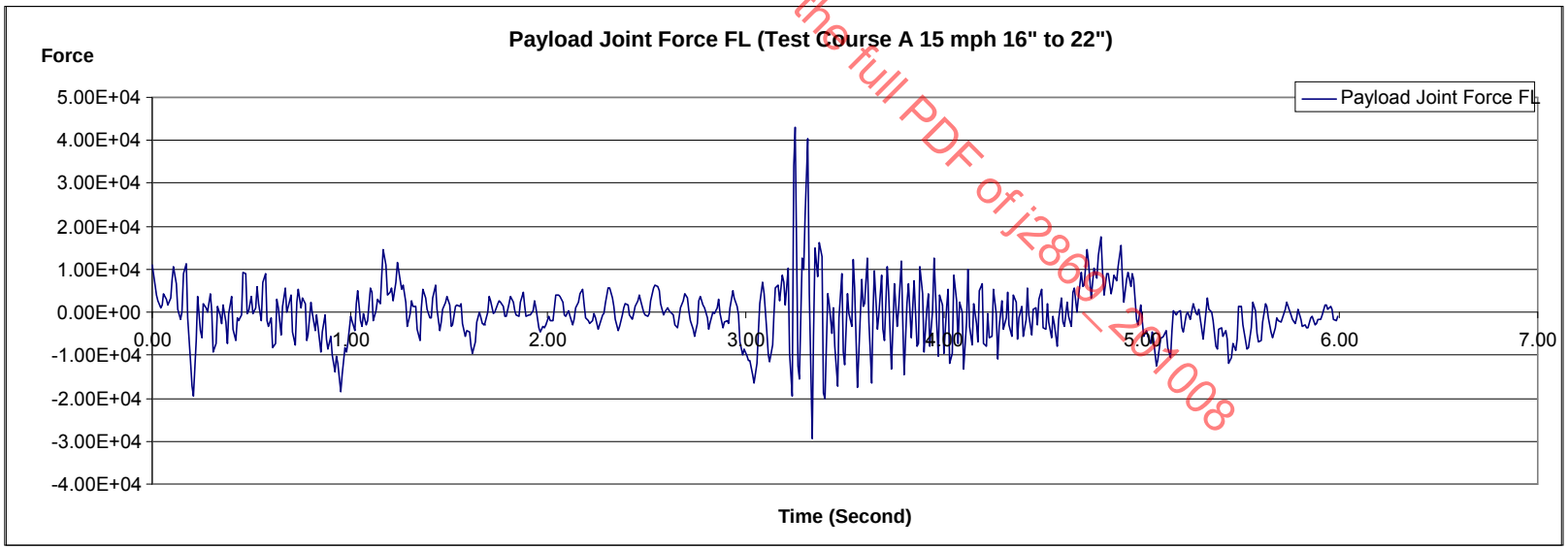

FIGURE 116 - JOINT REACTION FORCE HISTORY OF FRONT-LEFT PAYLOAD JOINTS

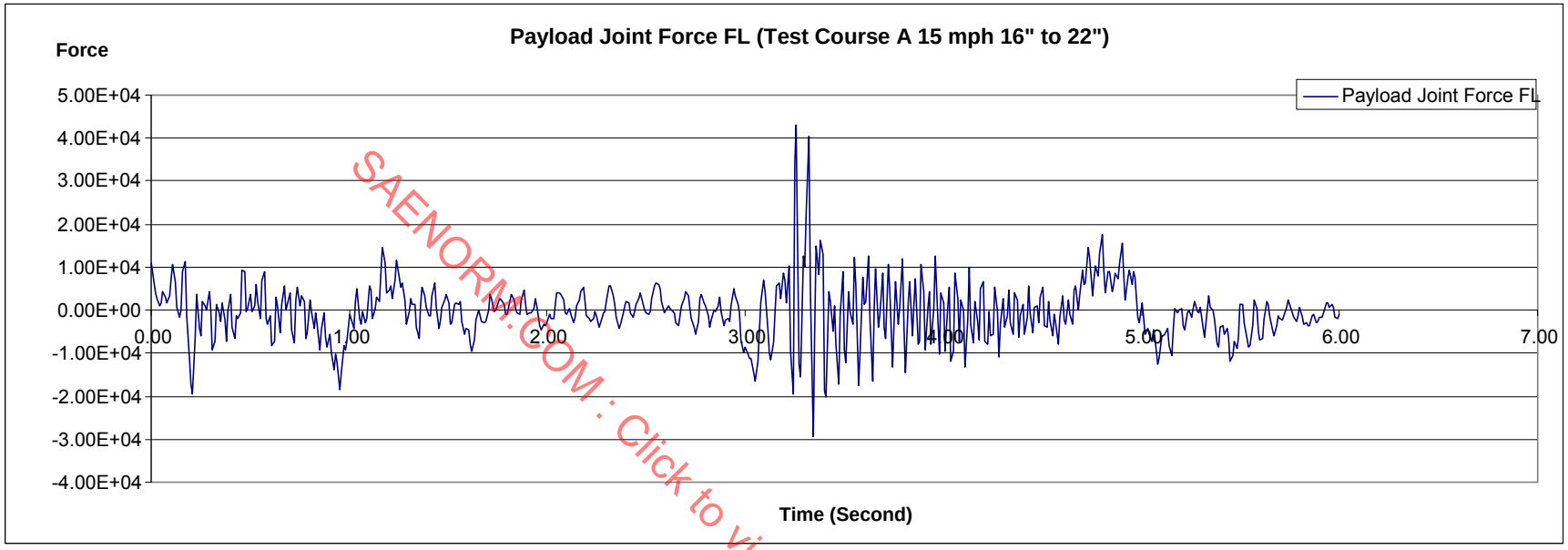

FIGURE 117 - PARTIAL ENLARGEMENT (16 TO 22 INCHES)

7.10 Comparison With Rigid Body Dynamic Model

As was shown in 7.9, the static correction mode shapes present in the flexible model cause a high fluctuation in the strain histories. Therefore, a rigid body dynamic simulation, which by definition should have only a minimal influence on the strain history, was used in order to explore the necessity of the flexible body simulation. The rigid body dynamics simulations have been performed and their dynamic information was used to perform durability analyses for comparison. The rigid body dynamics simulations are performed only for Test Course A and Test Course B courses.

Figures 118 and 121 are the Test Course A 15 mph strain time histories of both rigid body simulation and experimental principal strain of nodes 425 and 424, respectively.

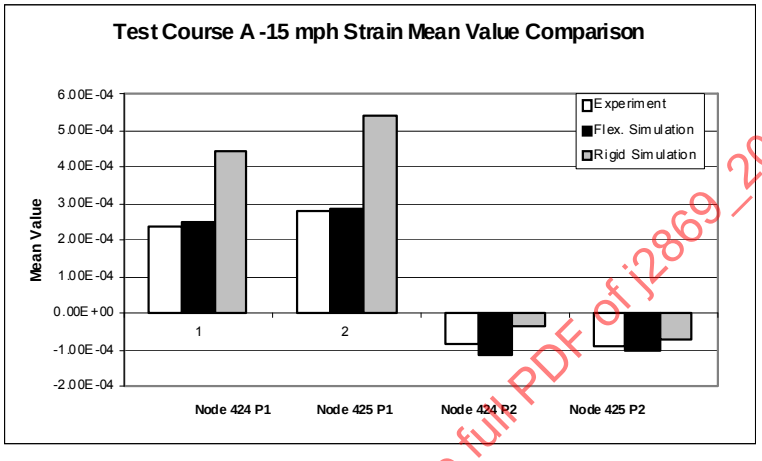

FIGURE 118 - MEAN VALUE COMPARISON OF STRAIN FOR TEST COURSE A

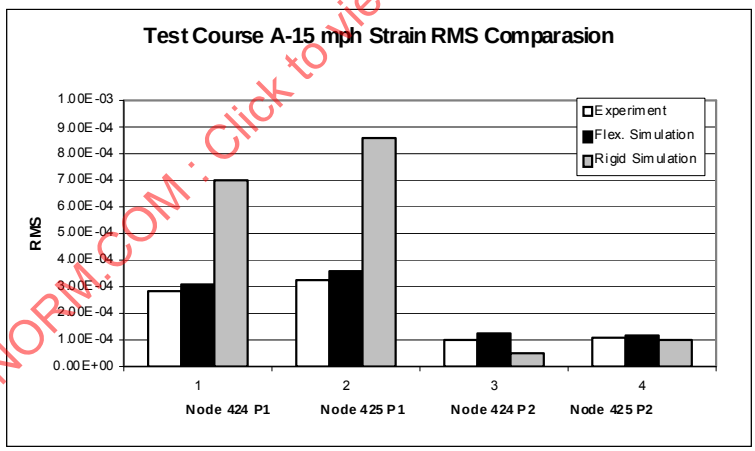

FIGURE 119 - RMS COMPARISON OF STRAIN FOR TEST COURSE A

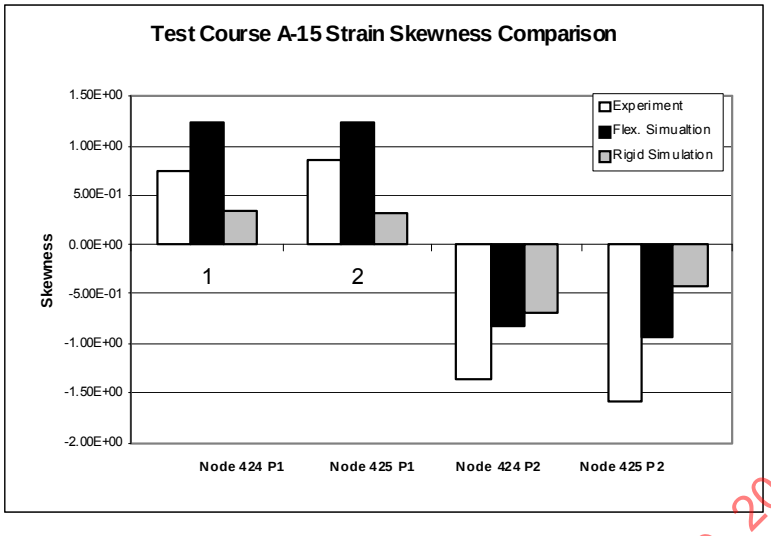

FIGURE 120 - SKEWNESS COMPARISON OF STRAIN FOR TEST COURSE A

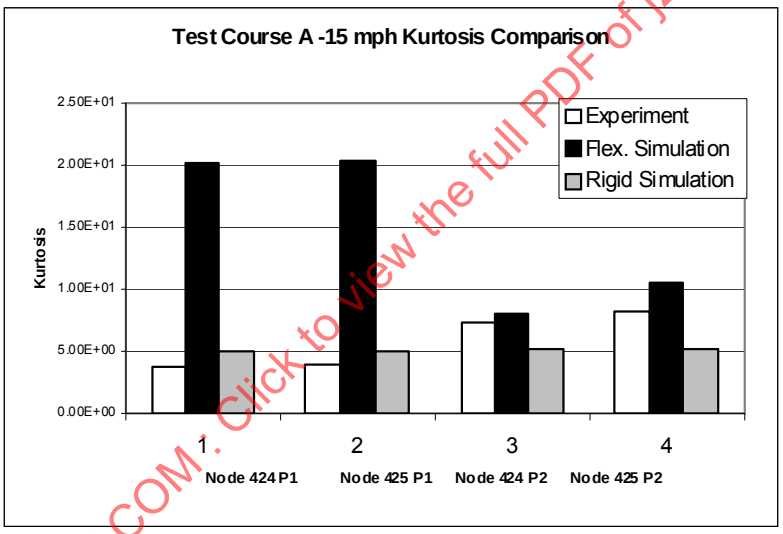

FIGURE 121 – KURTOSIS COMPARISON OF STRAIN FOR TEST COURSE A

The comparison of these simulation and experimental test statistic parameters are depicted in Figures 124 to 127. These figures illustrate the comparison of each item, such as mean, RMS, skewness, and kurtosis, respectively. In these figures, the horizontal axes indicates the node number, in which, the strain P1 and P2 of node numbers 424 and 425 are indicated, respectively.

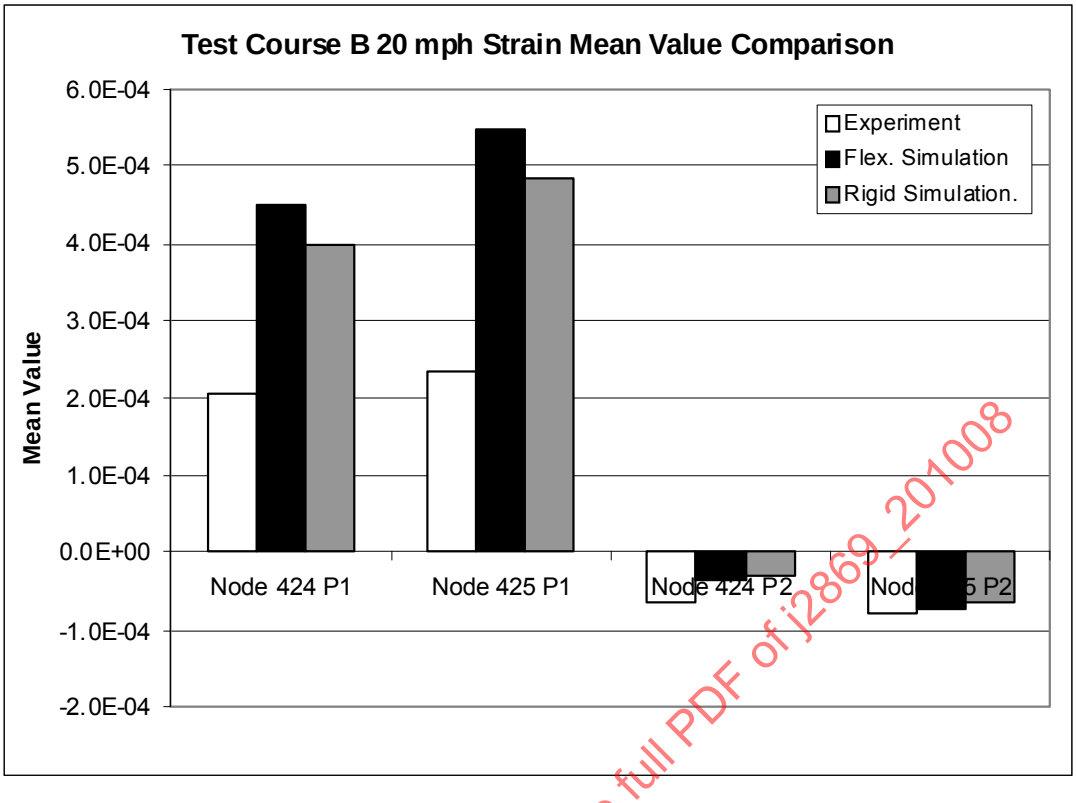

FIGURE 122 - COMPARISON OF FLEX., RIGID, AND EXPERIMENT MEAN FOR NODES 424 AND 425

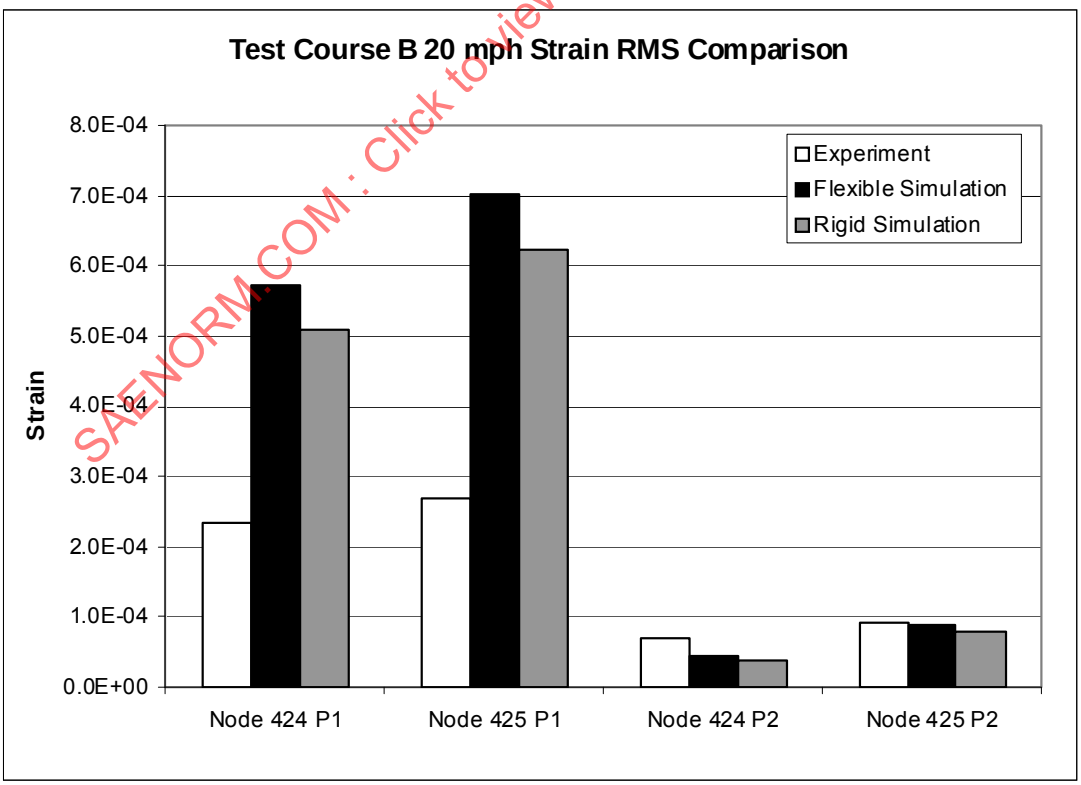

FIGURE 123 - COMPARISON OF FLEX., RIGID, AND EXPERIMENT RMS FOR NODES 424 AND 425

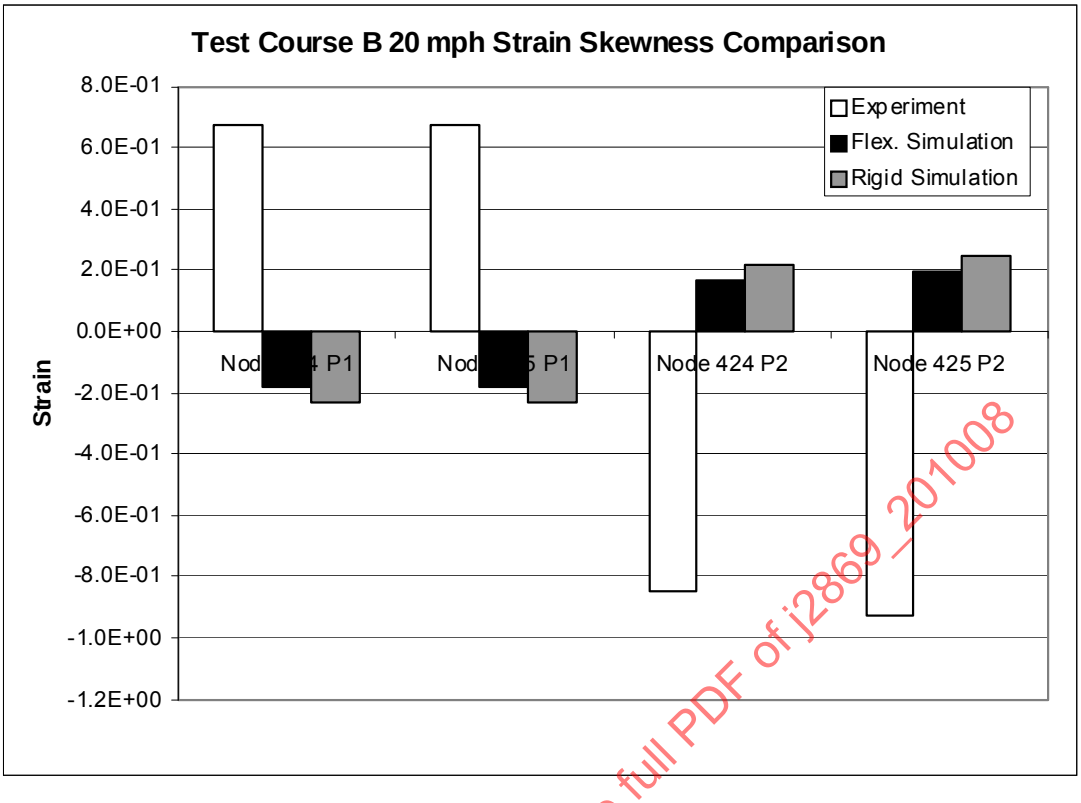

FIGURE 124 - COMPARISON OF FLEX., RIGID, AND EXPERIMENT SKEWNESS FOR NODES 424 AND 425

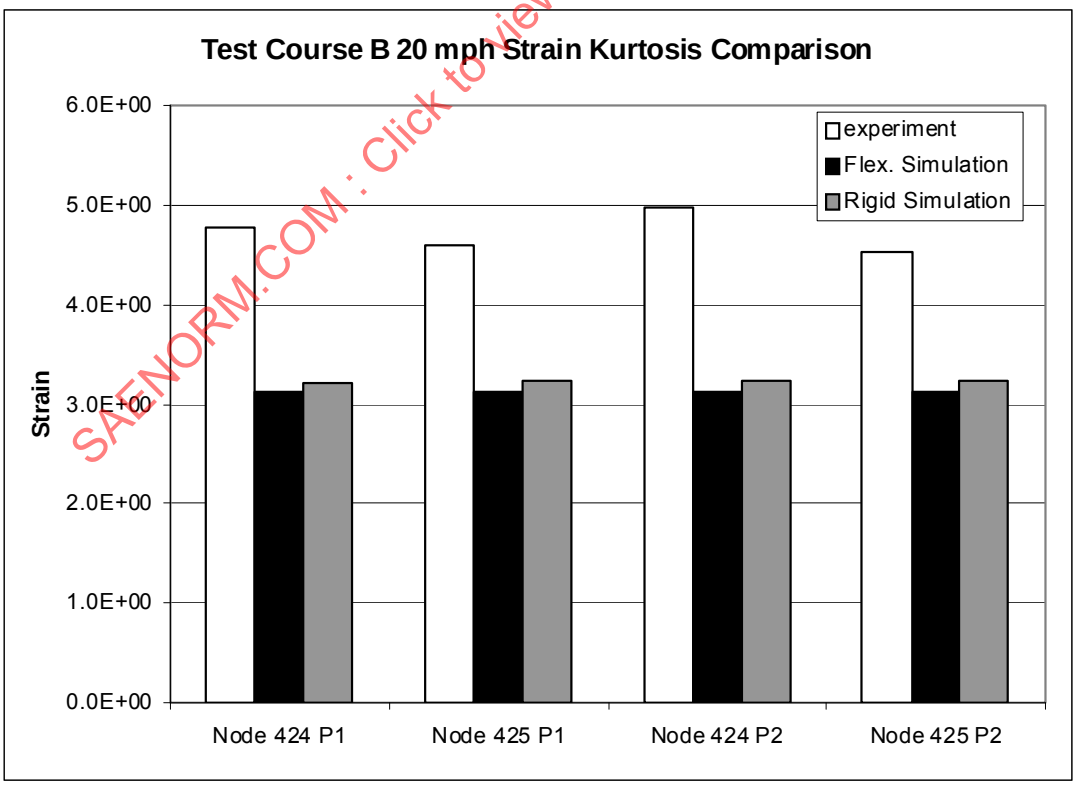

FIGURE 125 - COMPARISON OF FLEX., RIGID, AND EXPERIMENT KURTOSIS FOR NODES 424 AND 425

The comparisons of the statistical parameters, show the strain values of the rigid simulation for Test Course A are much larger than both flexible and experimental values. This is obvious from mean values and RMS values, and was expected since the actual Test Course A is a coarse road. It has a forced-response frequency spectrum due to the motion of the prime mover and the irregularity of the terrain, and, therefore, the rigid body results have large peaks that are induced by large impact energy accumulated in the simulation in the stress/strain time histories. This makes the rigid body results far larger than the experimental results. However, for Test Course B, the flexible and rigid simulation results are very close. It is because Test Course B is smoother than Test Course A so there is no such large impact energy that produces large peaks in the stress/strain time histories accumulated in the simulation. However, both results are not close with experimental data.

In order to make a thorough investigation and probe deeply into the essence of the effect of rigid and flexible simulation to the durability, the normality and PSD of the rigid simulation strain have been checked. The following figures depict the histogram of both Test Course A and Test Course B strain data for rigid, flexible simulation and experiment.

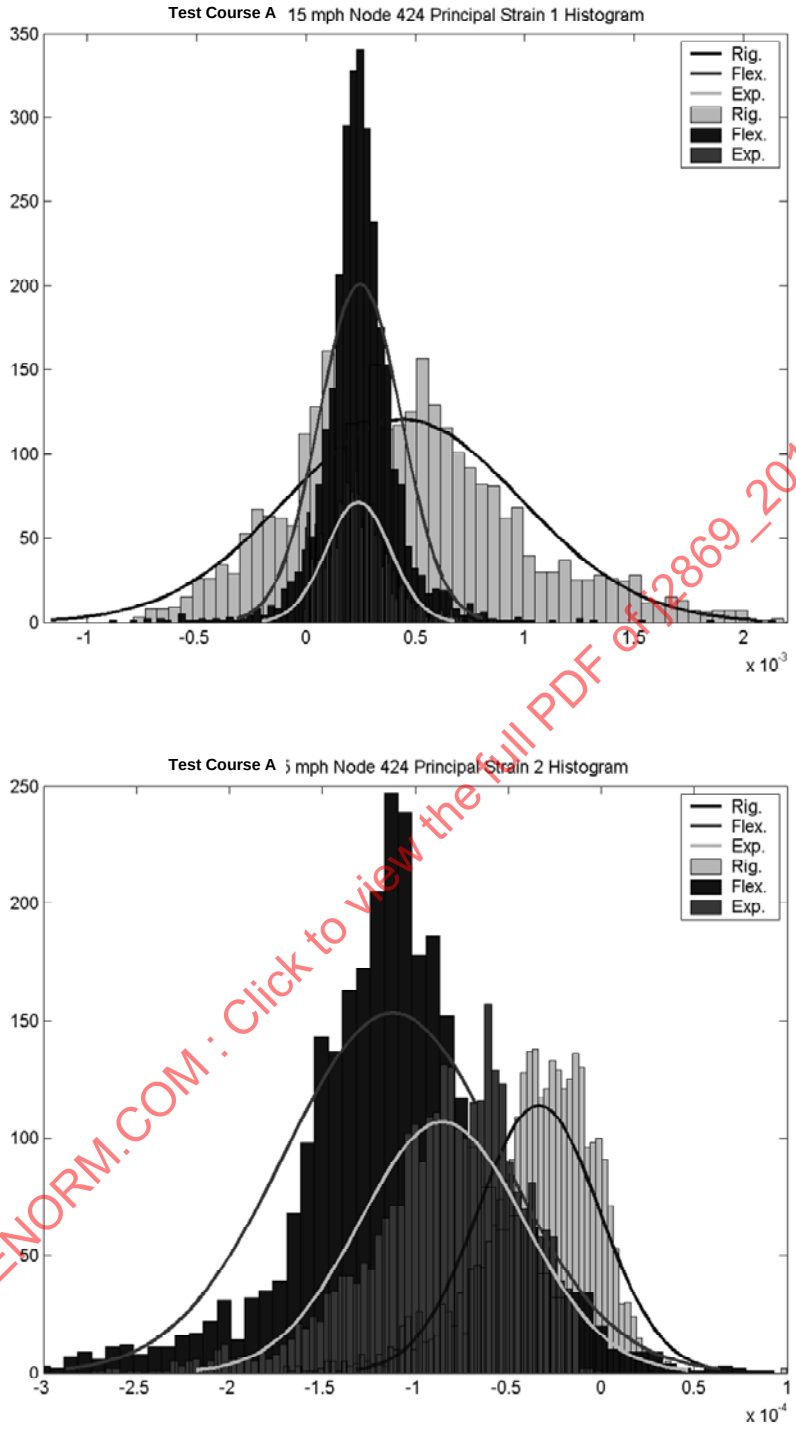

FIGURE 126 - THE HISTOGRAM FOR BOTH RIGID AND FLEXIBLE BODY SIMULATION AND EXPERIMENT OF NODE 424

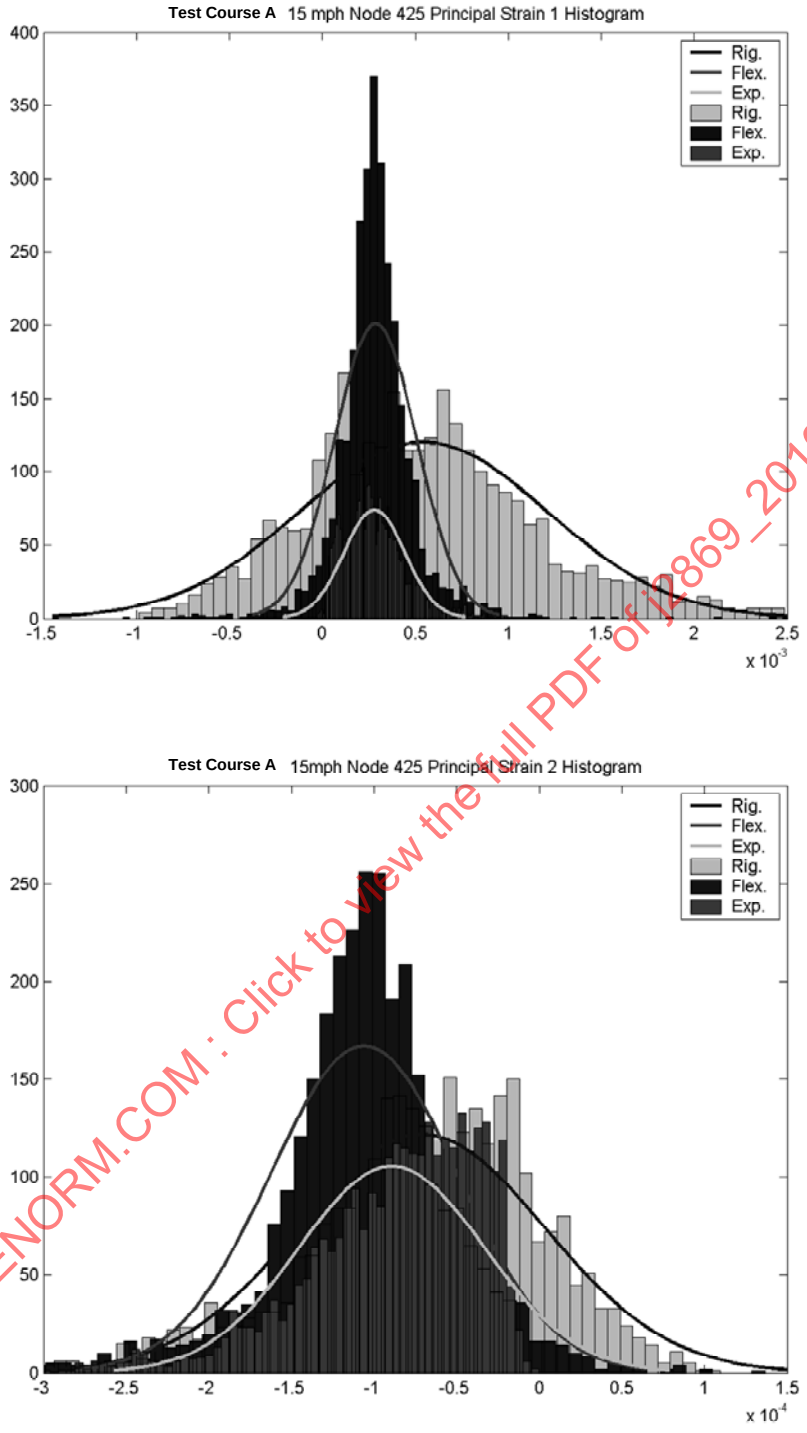

FIGURE 127 - HISTOGRAM FOR BOTH RIGID AND FLEXIBLE BODY SIMULATION AND EXPERIMENT OF NODE 425

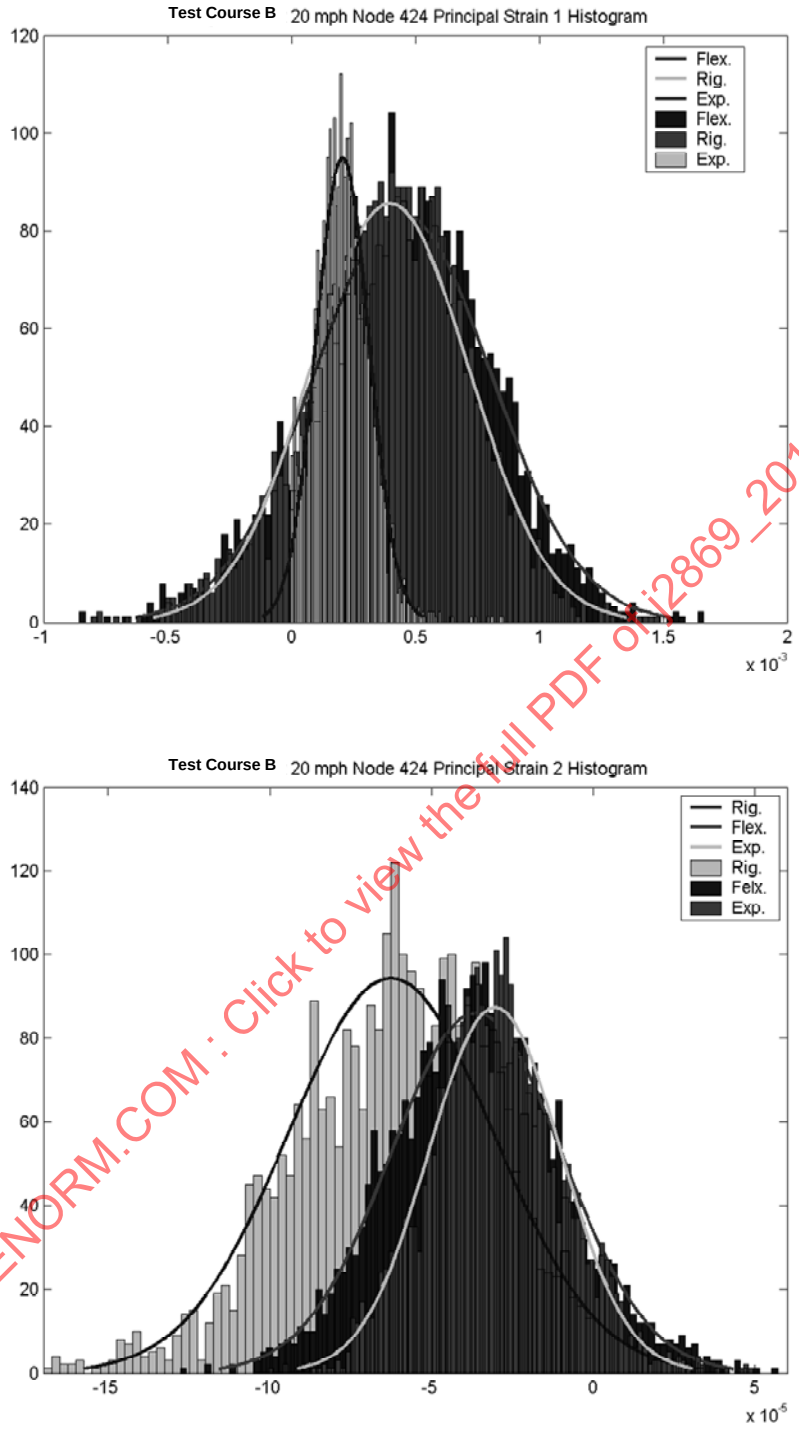

FIGURE 128 - HISTOGRAM FOR BOTH RIGID AND FLEXIBLE BODY SIMULATION AND EXPERIMENT OF NODE 424

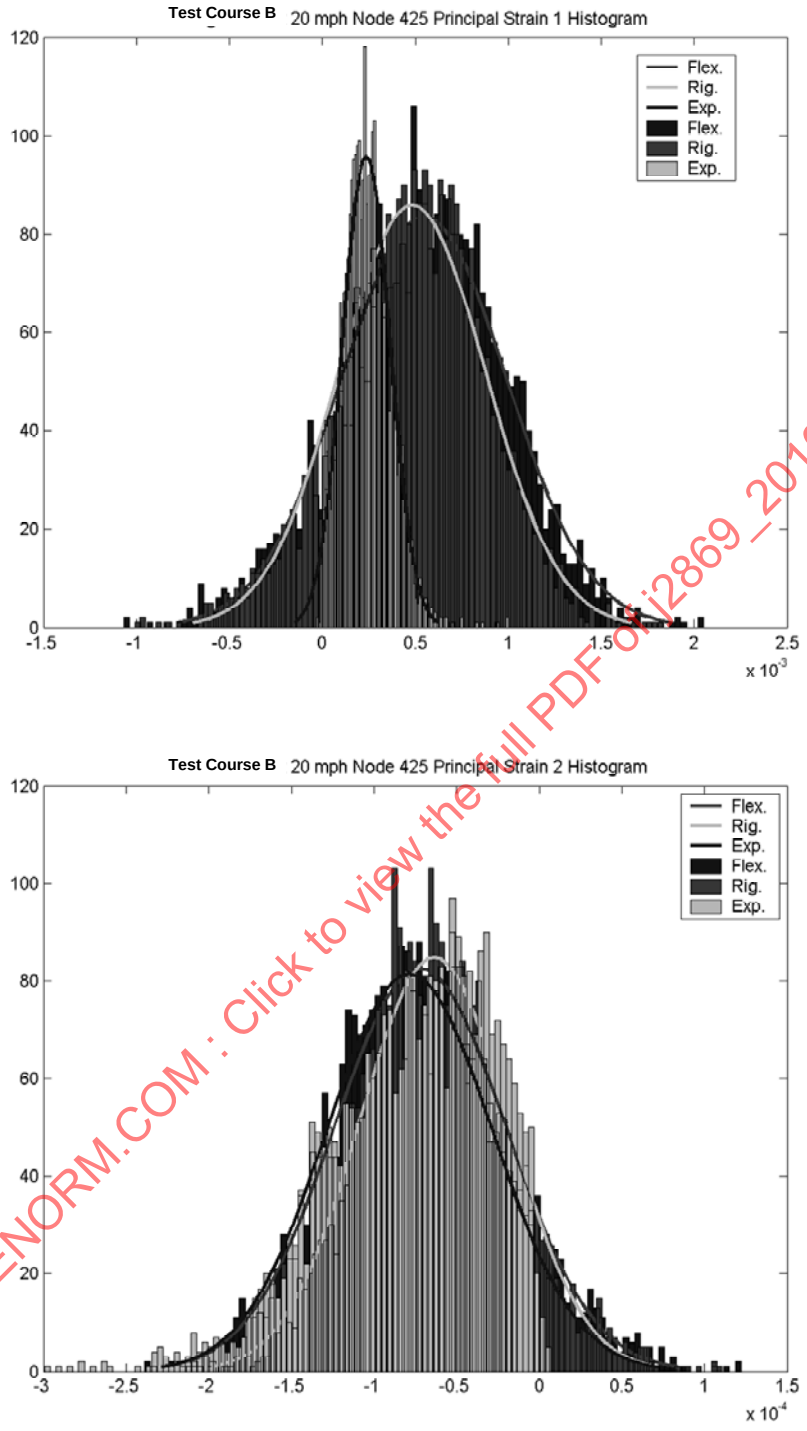

FIGURE 129 - HISTOGRAM FOR BOTH RIGID AND FLEXIBLE BODY SIMULATION AND EXPERIMENT OF NODE 425

Figures 130 to 133 are the strain PSD curves of nodes 425 and 424 for Test Course A and Test Course B, in which the Figures 130 and 131 are the strain PSD curves for Test Course A, while Figures 132 and 133 are Test Course B.

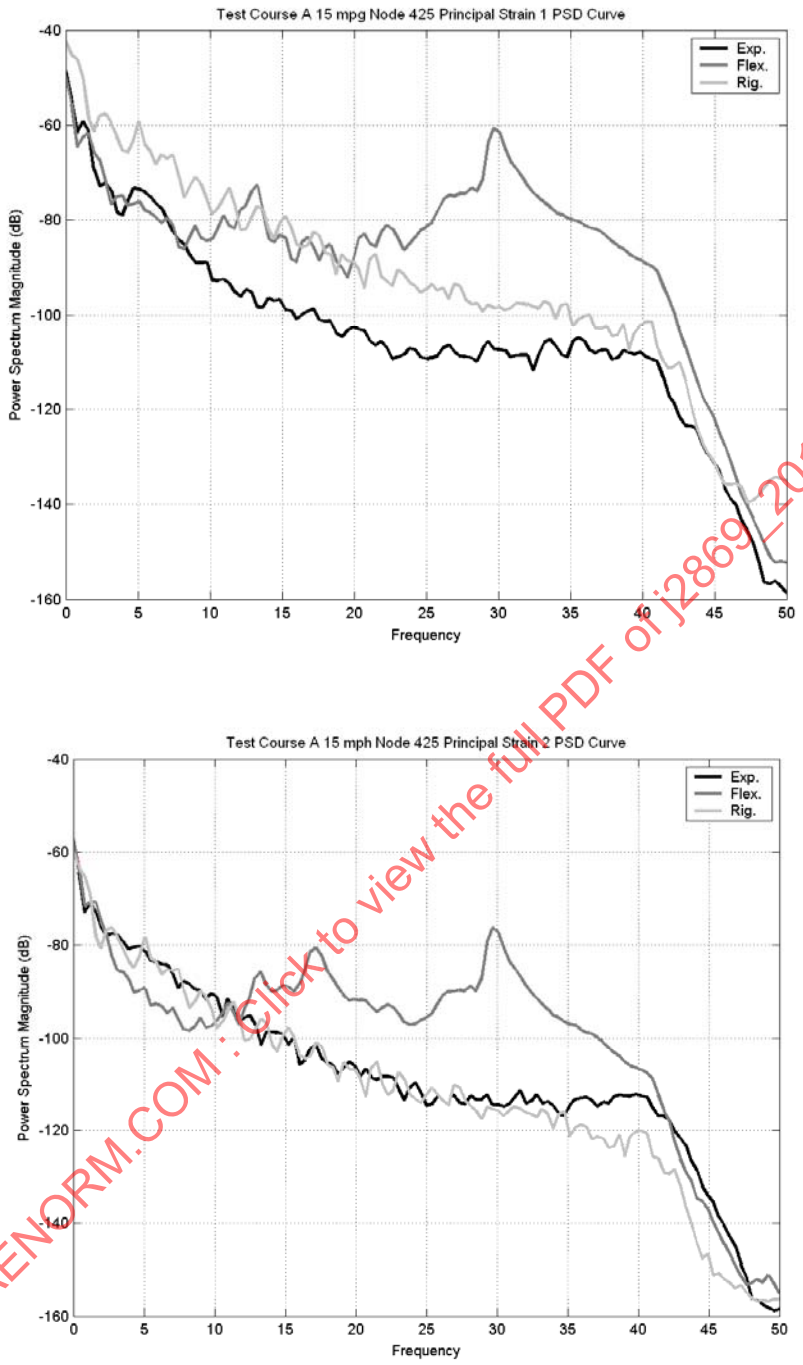

FIGURE 130 - NODE 425 PSD COMPARISON BETWEEN RIGID, FLEX., AND EXPERIMENT FOR TEST COURSE A

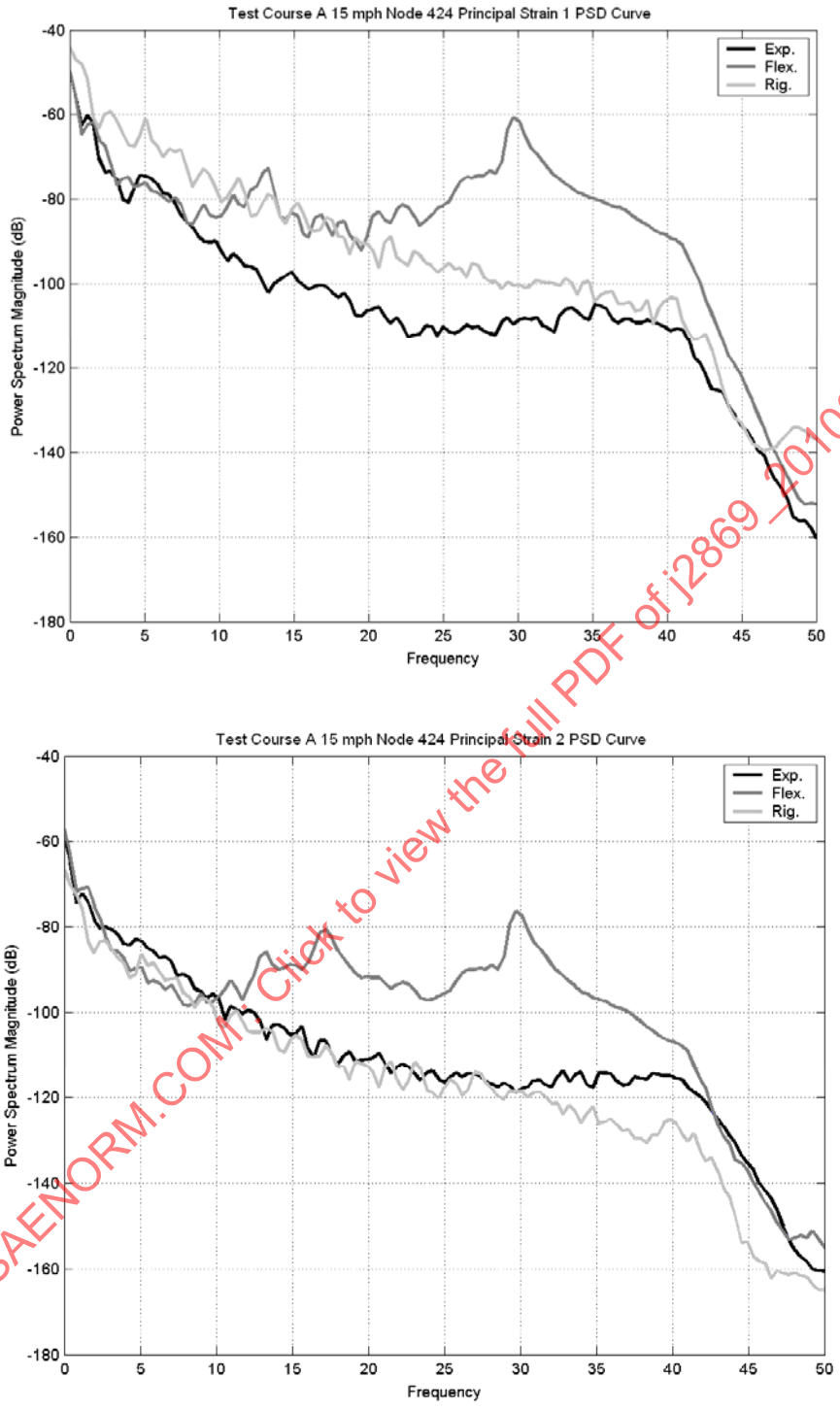

FIGURE 131 - NODE 424 PSD COMPARISON BETWEEN RIGID, FLEX., AND EXPERIMENT FOR TEST COURSE A

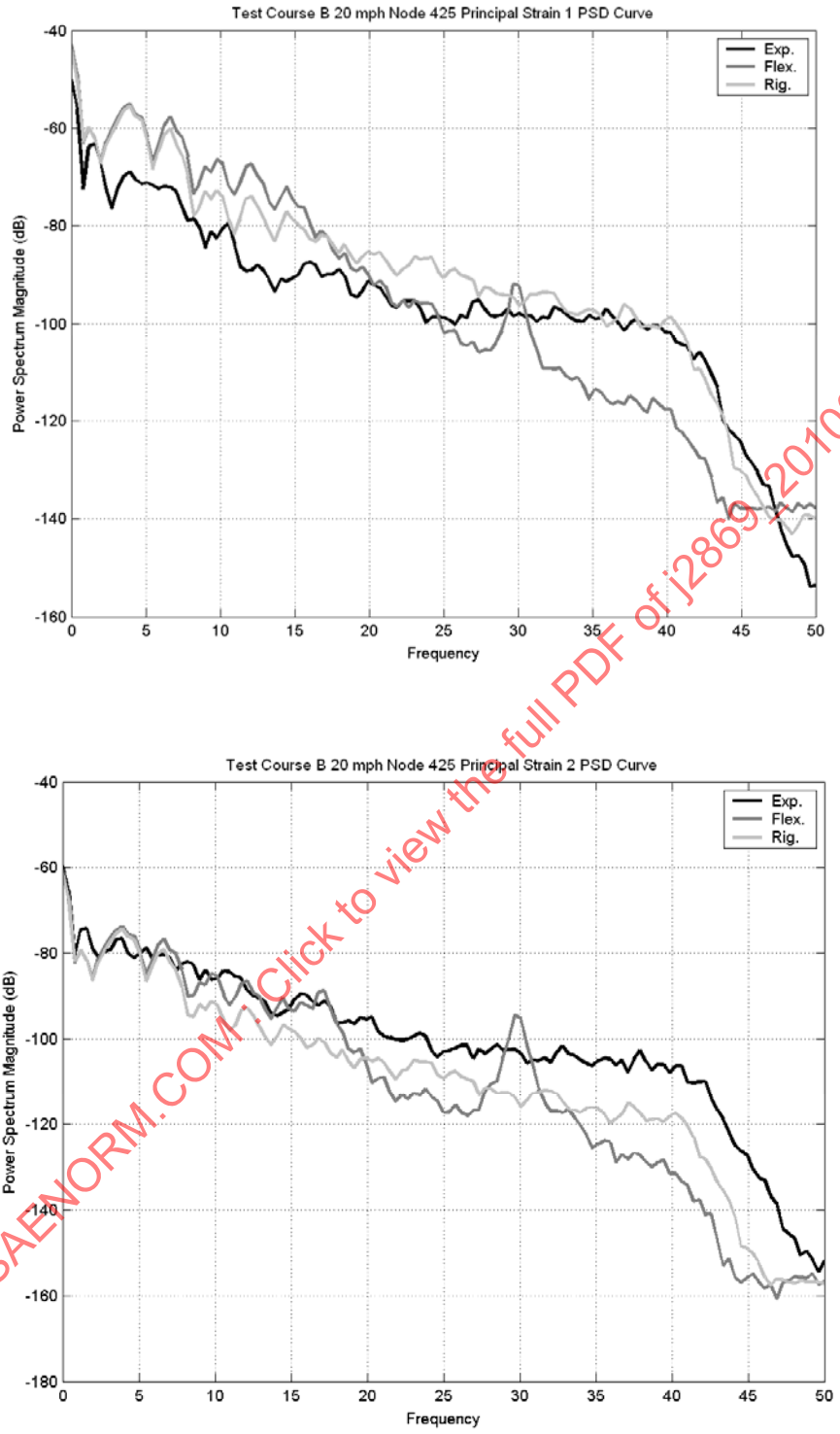

FIGURE 132 - NODE 425 PSD COMPARISON BETWEEN RIGID, FLEXIBLE, AND EXPERIMENT FOR TEST COURSE B

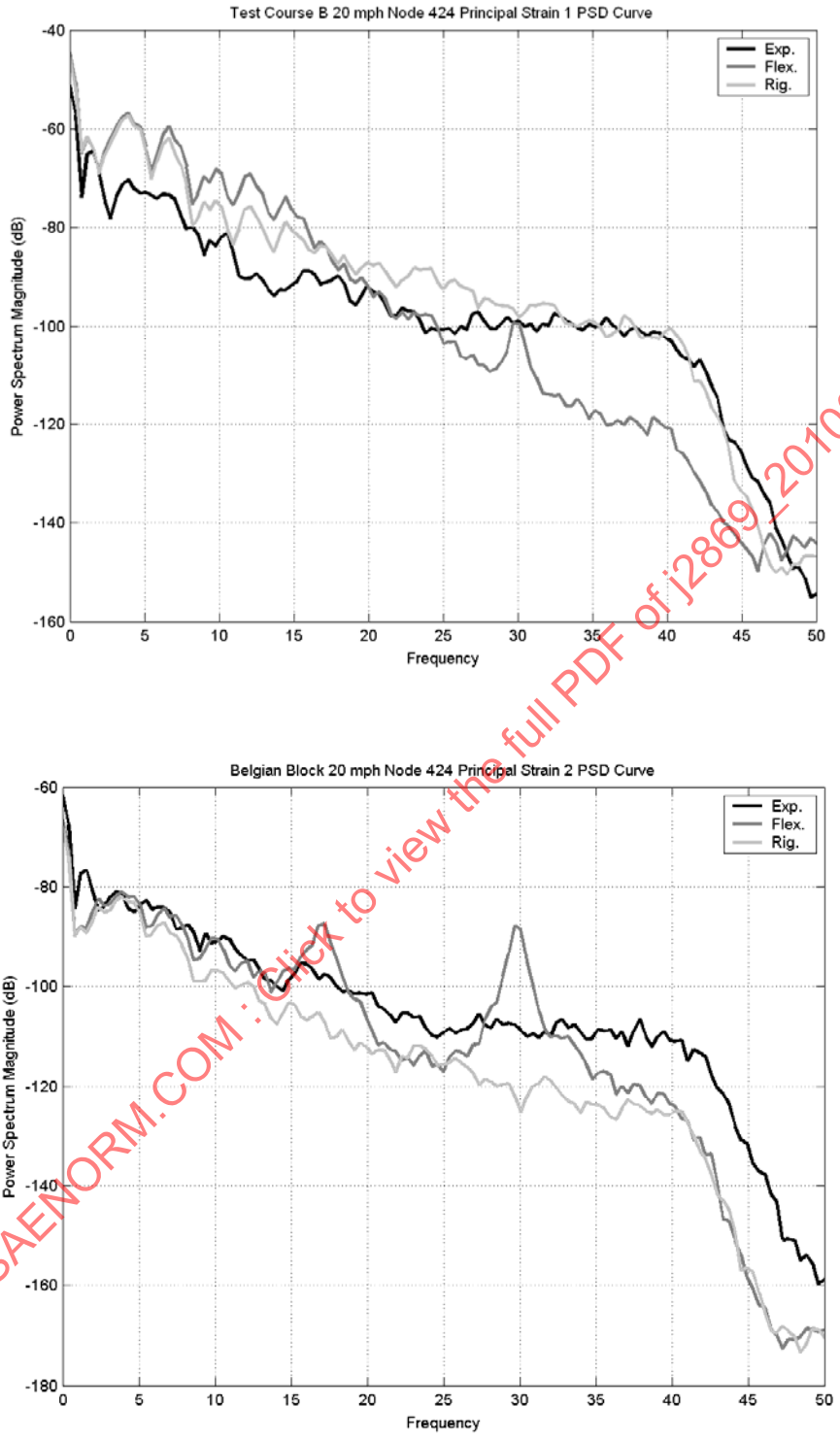

FIGURE 133 - NODE 424 PSD COMPARISON BETWEEN RIGID, FLEX., AND EXPERIMENT FOR TEST COURSE B

The normality of these histograms looks good. From these histograms, we can obtain the same conclusion as before. That is, for Test Course A the mean values of rigid simulation are much larger than both flexible simulation and experimental values; while for Test Course B the two simulation results are very close but both are not close to the experiment. Meanwhile, it was indicated that the fluctuations are very interesting from these histograms. For Test Course A, the fluctuations of the three histograms have the following relationship: The flexible fluctuation is greater than the rigid fluctuation, and both are greater than the experimental one. And, the rigid fluctuation is more close to the experimental fluctuation. In the Test Course B case, the mean values of both simulations are close, especially for principal strain 1 (longitude), and are larger than the experimental one. However, the fluctuations for the three histograms are extremely close. As mentioned before, these situations were expected by analyzing the physical courses.

From PSD curves, it is interesting that the two peaks in the flexible simulation curve disappeared in the rigid simulation curve, and the rigid simulation PSD curves are close to the experimental curves. Therefore, we understood that due to the flexibility of the dynamic model some unexpected noise information would be induced if the flexible model has some shortages.

Finally, the fatigue life was compared between the rigid simulation and experimental results. The following tables describe the fatigue life results obtained from three cases, i.e., flexible dynamics analysis, rigid dynamics analysis, and experimental strain data sets. Tables 31 and 32 list all three results for Test Course A and Test Course B for comparison. And, figures, Figures 134 and 135 have been depicted to illustrate the differences of the three life results for Test Course A and Test Course B, respectively.

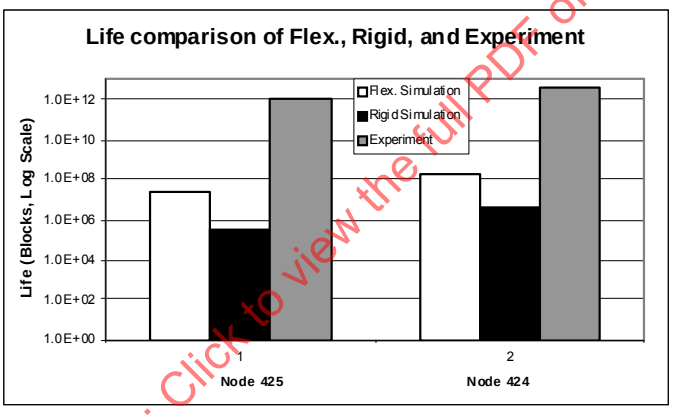

FIGURE 134 - LIFE COMPARISON OF FLEXIBLE, RIGID SIMULATION AND EXPERIMENT FOR TEST COURSE A

TABLE 31 - FATIGUE LIFE COMPARISON FOR TEST COURSE A

	Flex. Body Simulation		Rigid Body Simulation		Experimental Test	
Node No.	Blocks	Miles	Blocks	Miles	Blocks	Miles
425	2.736E+7	3.421E+6	3.430E+5	4.288E+4	9.404E+11	1.176E+11
424	1.837E+8	2.297E+7	4.462E+6	5.577E+5	4.340E+12	5.425E+11

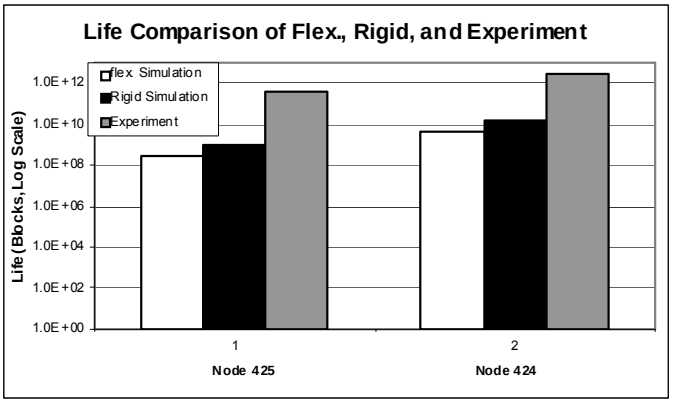

FIGURE 135 - LIFE COMPARISON OF FLEXIBLE, RIGID SIMULATION AND EXPERIMENT FOR TEST COURSE B

TABLE 32 - FATIGUE LIFE COMPARISON FOR TEST COURSE B

	Flex. Body Simulation		Rigid Body Simulation		Experimental Test	
Node No.	Blocks	Miles	Blocks	Miles	Blocks	Miles
425	3.035E+8	3.794E+7	1.044E+9	1.305E+8	4.466E+11	5.583E+10
424	4.631E+9	5.789E+8	1.610E+10	2.013E+9	3.049E+12	3.811E+11

It is clear from Tables 37 and 38 and Figures 134 and 135 that for Test Course A the rigid simulation fatigue life is less than flexible simulation life, while for Test Course B both rigid and flexible life results are very similar. These results are consistent with the behavior observed in the strain histories, which was, as discussed previously, that the large impact energies observed in the rigid model cause much higher strains on Test Course A.

7.11 Conclusion

After comparing the results of durability analyses that corresponded to rigid and flexible multi-body simulation dynamics information, we can sum up with the following conclusions:

a. For the trailer model, the flexible body model of the frame is necessary. It is very useful for obtaining accurate life results. However, for simulation of the flexible model, the static correction mode shapes of the frame are not only necessary, but also need to be selected carefully. In the current trailer model, all possible mode shapes that will induce the elastic deflection mode need to be included, such as payload joints.

b. The selected normal modes should not include the high frequency modes since the proper frequency of trailer frame is a low frequency structure. In addition, the high frequency noise that was induced during the simulation, such as the flexible-body dynamic simulation, needs to be filtered before the durability analysis.

c. Generally speaking, the simulation procedure that uses an integrated Computer Aided Engineering environment for durability analysis is feasible. The procedure of this integrated system started from a CAD model and included dynamics simulation in order to obtain joint reaction force histories and motion histories that are used for calculating the inertia forces of the component. Then the process continues through finite element analysis to compute stress/strain time histories by superposition; and finally to predict fatigue life using the strain-life prediction approaches based on the stress/strain time histories obtained from superposition.

d. Since the dynamic model is very important for fatigue life results, whether the flexible or rigid model needs to be used is a very sensitive problem. It should be dealt with as precisely as possible. As for the flexible model, the mode shape selection requires significant attention.

8. NOTES

8.1 Marginal Indicia

A change bar (I) located in the left margin is for the convenience of the user in locating areas where technical revisions, not editorial changes, have been made to the previous issue of this document. An (R) symbol to the left of the document title indicates a complete revision of the document, including technical revisions. Change bars and (R) are not used in original publications, nor in documents that contain editorial changes only.

PREPARED BY ???

APPENDIX A - INSTRUMENTATION

Channel Information from the data acquisition system is provided in Table A1. These raw data files have been converted to ASCII files, with time as the first column, and the remaining 58 columns are composed of the active channels in Table A1. The sample time was computed from the 1262.626 Hz sample rate.

TABLE A1 - DATA ACQUISITION SYSTEM CHANNEL ASSIGNMENTS

Channel #	Description	
5	Bottom Drawbar Center	Transverse strain
6		45 degree strain
7		Longitudinal strain
8	Bottom Drawbar Center Aft	Transverse strain
9		45 degree strain
10		Longitudinal strain
11	Bottom Drawbar Curbside Edge	Transverse strain
12		45 degree strain
13		Longitudinal strain
14	Bottom Drawbar Curbside Aft Edge	Transverse strain
15		45 degree strain
16		Longitudinal strain
17	Top Triangle Plate Corner	Transverse strain
18		45 degree strain
19		Longitudinal strain
20	Bottom Triangle Plate Corner	Transverse strain
21		45 degree strain
22		Longitudinal strain
23	Left Angle Plate Lower	Vertical strain
24		45 degree strain
25		Longitudinal strain
26	Left Angle Plate Upper	Vertical strain
27		45 degree strain
28		Longitudinal strain
29	Curbside Axle Acceleration	
30	Curbside Frame Acceleration	
31	Roadside Axle Acceleration	
32	Roadside Frame Acceleration	
33	Lunette Acceleration	Vertical (z)
34		Transverse (y)
35		Longitudinal (x)
36	Tongue Acceleration	Vertical (z)
37		Transverse (y)
38		Longitudinal (x)
39	Trailer CG Acceleration	Vertical (z)
40		Transverse (y)
41		Longitudinal (x)

42	Curbside Acceleration Forward	Vertical (z)
43		Transverse (y)
44		Longitudinal (x)
45	Curbside Acceleration Aft	Vertical (z)
46		Transverse (y)
47		Longitudinal (x)
48	Roadside Acceleration Forward	Vertical (z)
49		Transverse (y)
50		Longitudinal (x)
51	Roadside Acceleration Aft	Vertical (z)
52		Transverse (y)
53		Longitudinal (x)
54	Trailer CG	Vertical (z)
55		Transverse (y)
56		Longitudinal (x)
57	Curbside Shock Displacement	
58	Roadside Shock Displacement	
59	Longitudinal Ground Speed	
60	(not used)	
61	Master Cylinder Brake Pressure	
62	Curbside Wheel Brake Pressure	
63	Roadside Wheel Brake Pressure	

APPENDIX B - MATLAB FILES

The Matlab program has been extensively used during the data reduction process. This appendix provides example source code for many of the calculations shown in this report.

B.1 READING THE DATA FILES

The data files can be opened and the contents read by calling the `read_run` function.

```
[data,label]=read_run('run055.csv');
```

The Matlab function is specific to the data files provided by ATC. It skips the top 9 lines, and then reads 59 columns of data until the end of the file. One problem with the `*.csv` files provided by ATC is that Matlab improperly reads commas while importing data. All of the commas need to be removed from the *.csv file for this routine to work properly.

```
function [data,label]=read_run(file)
fid = fopen(file);
for i=1:9
tmp=fgetl(fid);
end
mask = '%g';
for i=1:58
mask = strcat(mask,' %g');
end
data = fscanf(fid,mask,[59 inf]);
label = char( 'Time', …
'bdc_t', 'bdc_45', 'bdc_l',
                    'bdca_t','bdca_45','bdca_l', …
                    'bde_t', 'bde_45', 'bde_l', …
                    'bdea_t','bdea_45','bdea_l', …
                    'ttc_t', 'ttc_45', 'ttc_l', …
                    'btc_t', 'btc_45', 'btc_l', …
                    'lal_v', 'lal_45', 'lal_l', …
                    'lau_v', 'lau_45', 'lau_l', …
                    'csa', 'csf', 'rsa', 'rsf', …
                    'la_v', 'la_t', 'la_l', …
                    'ta_v', 'ta_t', 'ta_l', …
                    'tcg_v', 'tcg_t', 'tcg_l', …
                    'csf_v', 'csf_t', 'csf_l', …
                    'csa_v', 'csa_t', 'csa_l', …
                    'rsf_v', 'rsf_t', 'rsf_l', …
                    'rsa_v', 'rsa_t', 'rsa_l', …
                    'pitch', 'roll', 'yaw', …
                    'cs_dp', 'rs_dp', …
                    'mc_pr', 'cs_pr', 'rs_pr', …
                    'speed');
```

The data labels correspond to the individual channels. Table B1 matches the labels with their respective details.

TABLE B1 - LABELS WITH THEIR RESPECTIVE DETAILS

Label	Description	Label	Description
Time	Time (sec)	la_v	Lunette Accel. Vert
bdc_t	Bottom Drawbar Center Trans	la_t	Lunette Accel Trans
bdc_45	Bottom Drawbar Center 45	la_l	Lunette Accel Long
bdc_l	Bottom Drawbar Center Long	ta_v	Tongue Accel Vert
bdca_t	Bottom Drawbar Center Aft Trans	ta_t	Tongue Accel Trans
bdca_45	Bottom Drawbar Center Aft 45	ta_l	Tongue Accel Long
bdca_l	Bottom Drawbar Center Aft Long	tcg_v	Trailer CG Accel Vert
bde_t	Bottom Drawbar Edge Trans	tcg_t	Trailer CG Accel Trans
bde_45	Bottom Drawbar Edge 45	tcg_l	Trailer CG Accel Long
bde_l	Bottom Drawbar Edge Long	csf_v	CS Forward Accel Vert
bdea_t	Bottom Drawbar Edge Aft Trans	csf_t	CS Forward Accel Trans
bdea_45	Bottom Drawbar Edge Aft 45	csf_l	CS Forward Accel Long
bdea_l	Bottom Drawbar Edge Aft Long	csa_v	CS Aft Accel Vert
ttc_t	Top Triang Plate Corner Trans	csa_t	CS Aft Accel Trans
ttc_45	Top Triang Plate Corner 45	csa_l	CS Aft Accel Long
ttc_l	Top Triang Plate Corner Long	rsf_v	RS Forward Accel Vert
btc_t	Bottom Triang Plate Corner Trans	rsf_t	RS Forward Accel Trans
btc_45	Bottom Triang Plate Corner 45	rsf_l	RS Forward Accel Long
btc_l	Bottom Triang Plate Corner Long	rsa_v	RS Aft Accel Vert
lal_v	Left Angle Plate Lower Vert	rsa_t	RS Aft Accel Trans
lal_45	Left Angle Plate Lower 45	rsa_l	RS Aft Accel Long
lal_l	Left Angle Plate Lower Long	pitch	Pitch Rate
lau_v	Left Angle Plate Upper Vert	roll	Roll Rate
lau_45	Left Angle Plate Upper 45	yaw	Yaw Rate
lau_l	Left Angle Plate Upper Long	cs_ds	Curbside Shock Disp
csa	Curbside Axle Accel Vert	rs_ds	Roadside Shock Disp
csf	Curbside Frame Accel Vert	mc_pr	Master Cyln Pres
rsa	Roadside Axle Accel Vert	cs_pr	Curbside Brake Pres
rsf	Roadside Frame Accel Vert	rs_pr	Roadside Brake Pres
		speed	Speed (mph)

B.2 FILTERING THE DATA

Proper filtering of the data is required for good comparisons with the simulation. The experimental data contains both noise and deterministic responses which occur at higher frequencies than what has been modeled. Proper filtering in Matlab involves selecting a normalized cutoff frequency, and applying the filter both forwards and backwards in time to eliminate phase distortion. For example, to create a 30 Hz lowpass, 8-pole Butterworth filter, and apply it to a column of the data which was sampled at 1262.626 Hz the following commands are used

```
[b,a]=butter(8,30/1262.626);
filt_data=filtfilt(b,a,data(i,:));
```

The effect of this on the trailer CG longitudinal acceleration is shown in Figure B1oth filtered and unfiltered time responses.

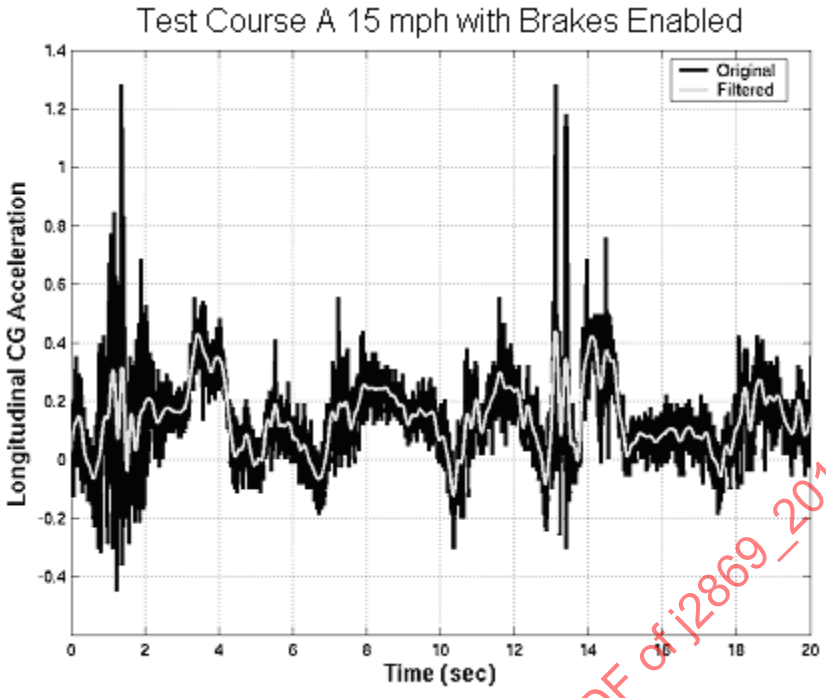

FIGURE B1 - FILTERED AND UNFILTERED LONGITUDINAL ACCELERATION TIME RESPONSES

B.3 DECIMATION

Decimation in Matlab can be performed manually or using the automated '`decimate`' command. In order to perform decimation manually, an appropriate filter must be created and applied to the data before re-sampling. For example, the original experimental data was sampled at 1262.626 Hz, while the simulation data was sampled at 60 Hz. In order to compare the responses, it is appropriate to decimate the experimental data by a factor of 20, so that its re-sampled rate is 63.1313 Hz. The following commands can be used to do this when the size of the original data is 'x'

```
[b,a] = butter(8,1/40);
filt_data = filtfilt(b,a,data(i,:));
deci_data = filt_data(1:20:'x');
```

This creates an 8th order, low-pass Butterworth filter, with a normalized cutoff frequency of $\frac{1}{40}$ (or $\frac{1}{2}\left(\frac{63.1313}{1262.626}\right)$). The filter is phaselessly applied to one channel of the data, which is then re-sampled using every 20th data point.

An equivalent decimation can be performed using the `decimate` command as

```
deci_data = decimate(data(i,:),20);
```

The `decimate` command creates a Type 1 Chebyshev low-pass filter at the same normalize frequency used in the Butterworth filter example, and then re-samples the data.

B.4 PRINCIPAL STRAINS

Strain gauges are used in vehicle testing, especially for validation of flexible-body simulation models. Depending on the application, strain gauges are typically either uniaxial, or a rosette of three gauges.

Rosettes are either oriented at $0^\circ - 45^\circ - 90^\circ$, $0^\circ - 60^\circ - 120^\circ$, or at $0^\circ - 120^\circ - 240^\circ$. Regardless, strain gauge rosettes are mounted on the surface of the part, and are assumed to be a measure of plane stress (stress perpendicular to the surface is assumed to be zero). In the most general orientation case, shown in Figure B4, the relationship between the measured strains, $\{\varepsilon_a\ \varepsilon_b\ \varepsilon_c\}$, and the strains oriented along the xy coordinate axis, $\{\varepsilon_x\ \varepsilon_y\ \gamma_{xy}\}$, is given by

$$\begin{aligned}\varepsilon_a &= \varepsilon_x \cos^2\theta_a + \varepsilon_y \sin^2\theta_a + \gamma_{xy}\sin\theta_a\cos\theta_a \\ \varepsilon_b &= \varepsilon_x \cos^2\theta_b + \varepsilon_y \sin^2\theta_b + \gamma_{xy}\sin\theta_b\cos\theta_b \\ \varepsilon_c &= \varepsilon_x \cos^2\theta_c + \varepsilon_y \sin^2\theta_c + \gamma_{xy}\sin\theta_c\cos\theta_c\end{aligned} \qquad \text{(Eq. B1)}$$

which can be re-written as

$$\begin{Bmatrix}\varepsilon_x \\ \varepsilon_y \\ \gamma_{xy}\end{Bmatrix} = \begin{bmatrix}\cos^2\theta_a & \sin^2\theta_a & \sin\theta_a\cos\theta_a \\ \cos^2\theta_b & \sin^2\theta_b & \sin\theta_b\cos\theta_b \\ \cos^2\theta_c & \sin^2\theta_c & \sin\theta_c\cos\theta_c\end{bmatrix}^{-1}\begin{Bmatrix}\varepsilon_a \\ \varepsilon_b \\ \varepsilon_c\end{Bmatrix} \qquad \text{(Eq. B2)}$$

when θ_a corresponds to the x axis, this simplifies to

$$\begin{Bmatrix}\varepsilon_x \\ \varepsilon_y \\ \gamma_{xy}\end{Bmatrix} = \begin{bmatrix}1 & 0 & 0 \\ \cos^2\theta_b & \sin^2\theta_b & \sin\theta_b\cos\theta_b \\ \cos^2\theta_c & \sin^2\theta_c & \sin\theta_c\cos\theta_c\end{bmatrix}^{-1}\begin{Bmatrix}\varepsilon_a \\ \varepsilon_b \\ \varepsilon_c\end{Bmatrix} \qquad \text{(Eq. B3)}$$

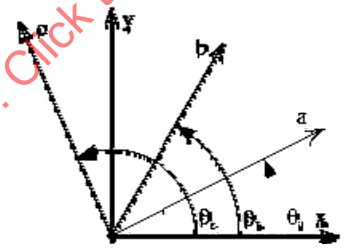

FIGURE B2 - GENERALIZED STRAIN-GAUGE ROSETTE ORIENTATIONS

The relationship between the in-plane principal strains, $\{\varepsilon_{p1}\ \varepsilon_{p2}\}$, in terms of $\{\varepsilon_x\ \varepsilon_y\ \gamma_{xy}\}$, is given by

$$\varepsilon_{p1},\varepsilon_{p2} = \left(\frac{\varepsilon_x + \varepsilon_y}{2}\right) \pm \sqrt{\left(\frac{\varepsilon_x - \varepsilon_y}{2}\right)^2 + \left(\frac{\gamma_{xy}}{2}\right)^2} \qquad \text{(Eq. B4)}$$

and the angle, θ_p, between the in-plane principal strain axes and the xy axis is expressed as

$$\theta_p = \frac{1}{2}\tan^{-1}\left(\frac{\gamma_{xy}}{\varepsilon_x - \varepsilon_y}\right) \qquad \text{(Eq. B5)}$$

Using Poisson's ratio, ν, the third principal strain, ε_{p3}, which is normal to the plane of the strain-gauge rosette can be determined.

$$\varepsilon_{p3} = -\frac{\nu}{1-\nu}\left(\varepsilon_x + \varepsilon_y\right) \quad \text{(Eq. B6)}$$

The principal strains can then be compared to those predicted by a finite-element model, using the same loading conditions.

B.4.1 Example

The strain gauge rosette data can be reduced to principal strains, strain orientation, and radius of the Mohr's circle by calling the `prin_strain` function. This is done as

```
[eta1,eta2,eta3,theta]=prin_strain(ex,eb,ec,tb,tc,nu);
```

where `ex`, `eb`, and `ec` are the measured strains, `tb` and `tc` are the angles of the rosette, `eta1`, `eta2`, and `eta3` are the principal strains, and `theta` is the angle from the x axis to the principal strain (`eta1`) axis.

This Matlab function can be written as

```
function [eta1,eta2,eta3,theta]=prin_strain(ea,eb,ec,tb,tc,nu)
      [ir,ic]=size(ea);
      eta1=zeros(ir,1); eta2=zeros(ir,1);
      eta3=zeros(ir,1); theta=zeros(ir,1);
      %
      for i=1:ir
            cb=cos(tb(i)); sb=sin(tb(i));
            cc=cos(tc(i)); sc=sin(tc(i));
            A=[1,0,0; cb^2,sb^2,sb*cb; cc^2,sc^2,sc*cc];
            %
            str_xy = inv(A)*[ea(i);eb(i);ec(i)];
            %
            tmp1 = (str_xy(1)+str_xy(2))/2;
            tmp2 = (str_xy(1)-str_xy(2))/2;
            tmp3 = sqrt( tmp2^2 + (str_xy^2)/4)
            %
            eta1(i) = tmp1 + tmp3;
            eta2(i) = tmp1 - tmp3;
            eta3(i) = -nu*(str_xy(1)+str_xy(2))/(1-nu);
            theta(i)= atan2(str_xy(3),(str_xy(1)-str_xy(2))/2;
      end
end
```


B.4.2 Histogram Calculation

Histograms are useful for visually portraying the distribution of data. Many of the statistical methods used to analyze the data assume that it follows a normal distribution, with a particular mean, $\bar{x}$, and standard deviation, σ. The probability density function for a normally distributed variable, x, is defined as

$$p(x) = \frac{1}{\sigma(2\pi)^{1/2}} \exp\left[-\frac{(x-\bar{x})^2}{2\sigma^2}\right] \quad \text{(Eq. B7)}$$

The histogram plots both the tendency and probability density by dividing the abscissa into M intervals (bins) between the maximum and minimum values of x. The number of times, n, that the value of x lies in the interval $x-\delta x \le x < x+\delta x$ is plotted on the ordinate axis. If the values of the ordinate are non-dimensionalized by dividing by the total number of measurements, N, the histogram represents the frequency distribution of x. This is the preferred method of plotting vehicle data for comparison, since the number of samples used to create two histograms does not need to be identical.

B.4.3 Example

The histogram should always be plotted with a representation of the normal distribution for the dataset. The Matlab function `histfit` has been developed to do this. The syntax is

```
h = histfit(x,m);
```

Using profilometry data for Test Course B, and 100 bins, the resulting histogram appears as Figure B3, which shows the numbers of instances of each measurement in the data.

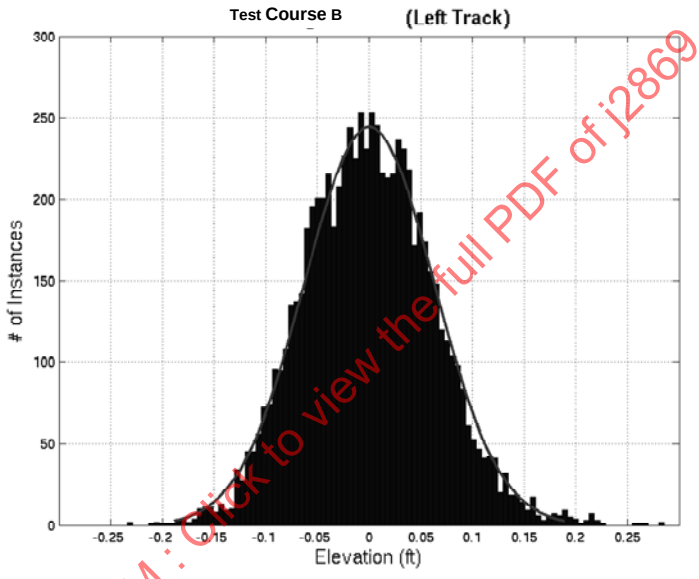

FIGURE B3 - NUMBER OF INSTANCES HISTOGRAM OF TEST COURSE B PROFILE

Making a small change in the Matlab routine, and renaming it `histfit2`, the normalized frequency distribution of the data, or relative histogram, can be plotted, as shown in Figure B4. The relative histogram is the preferable method when comparing experimental and simulated vehicle responses, since it is independent of the sizes of the datasets.

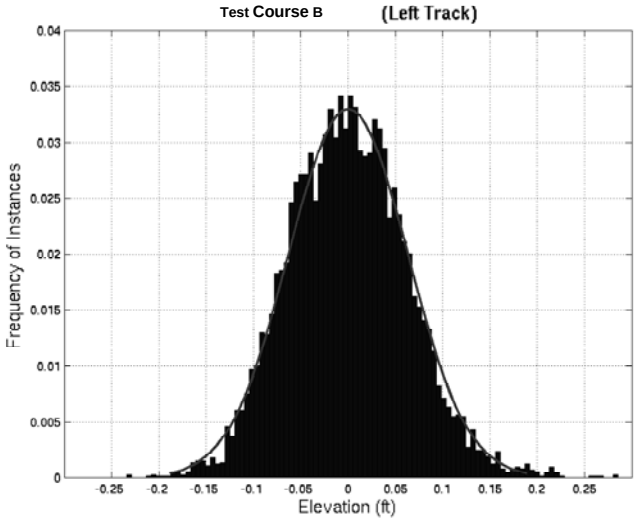

FIGURE B4 - FREQUENCY DISTRIBUTION HISTOGRAM OF TEST COURSE B PROFILE

An example of non-normal distribution is shown in Figure B5. Clearly the statistical normal distribution from Eq. (B13) does not match the frequency distribution shown by the histogram. For this type of distribution, comparison using statistical moments (mean, variance, skewness, kurtosis) does not have a good basis.

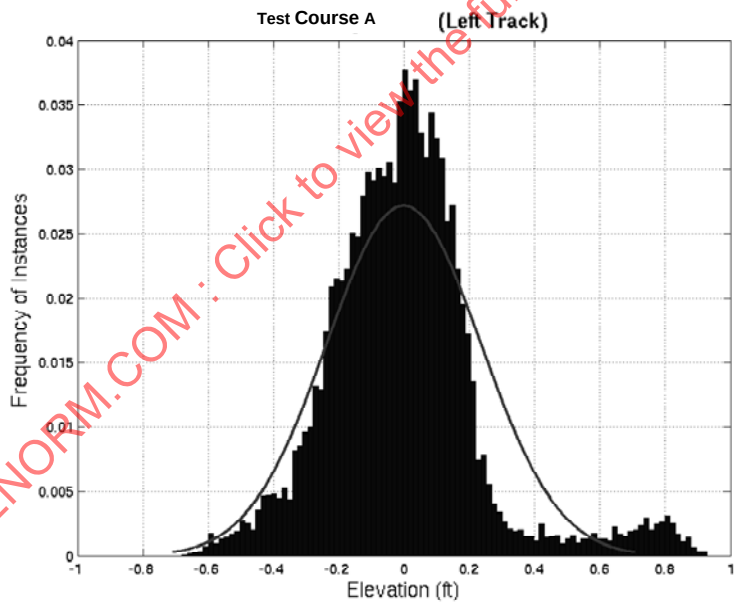

FIGURE B5 - FREQUENCY DISTRIBUTION HISTOGRAM TEST COURSE A PROFILE

B.4.4 Statistical Distributions

The Army has historically used statistical distributions for data comparison. These distributions include the mean, ±90, ±99, and ±99.9 percentiles. Use of the percentile distributions doesn't make a lot of sense, unless the underlying dataset follows a normal distribution pattern.

B.4.5 Example

A Matlab function to calculate the relevant statistics, using the `prctile` command from the Statistics Toolbox, is

```
function [vec]=process(dat)
    vec=zeros(1,11);
    vec(1)=mean(dat);% mean
    vec(2)=std(dat);% standard deviation
    vec(3)=rms(dat);% root mean square
    vec(4)=max(dat);% maximum
    vec(5)=min(dat);% minimum
    d=[0.05,0.5,5,95,99.5,99.95];
    tmp=prctile(dat,d);
    vec(6)=tmp(6);% +99.9
    vec(7)=tmp(1);% -99.9
    vec(8)=tmp(5);% +99
    vec(9)=tmp(2);% -99
    vec(10)=tmp(4);% +90
    vec(11)=tmp(3);% -90
```

The `prctile` command calculates the distributions on a scale of 0 to 100%, while we want the scale expressed as ±100% centered around the mean. This is responsible the value changes in the percentile distribution vector, `d`.

In the past, the data was usually presented in table format. However, greater meaning can be given to the data by viewing the results is as a stacked bar chart. This allows for visual comparison of experimental and simulation results. An example of experimental data results shown in Figure B6, the statistical distributions are shown in Figure B7. Normally both experimental and simulated distributions are shown on the same bar chart. The wide difference between the 99.9% values and the peak values is indicative of data outliers, which should probably be ignored. The outliers clearly appear at approximately 5 seconds in Figure B6. Knowledge of the experimental test being performed is required to determine if the outliers should be ignored.

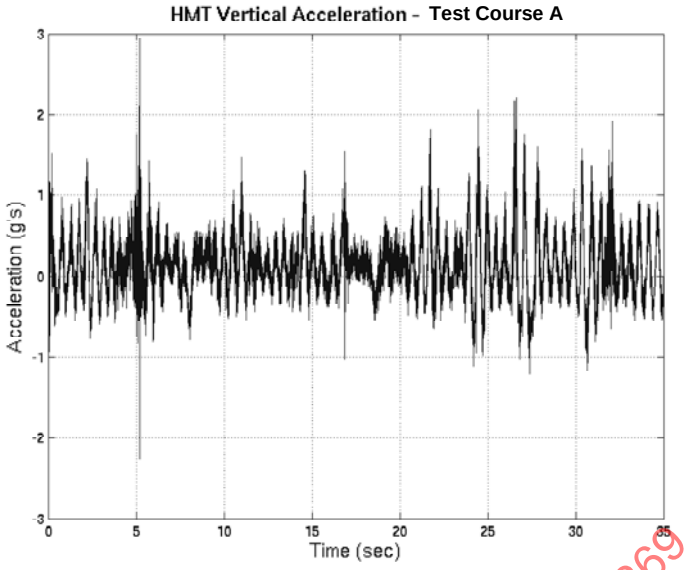

FIGURE B6 - TIME DOMAIN REPRESENTATION OF DATA

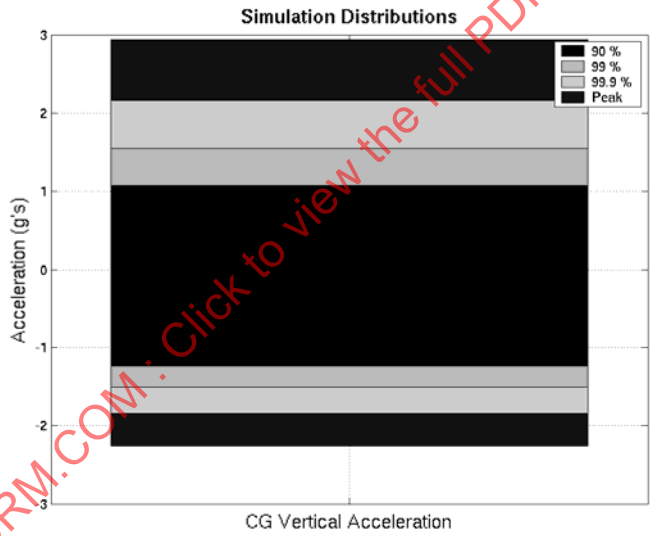

FIGURE B7 - STATISTICAL DISTRIBUTION OF DATA

The Matlab code to create the distribution plot follows. This code can easily be generalized to accommodate multiple bar charts on a single plot.

```
d = process(data(36,:));% vertical acceleration channel
p = zeros(2,4);% stacked bars don't work for only one
%
%positive bars
p(1,4) = d(1,10);
p(1,3) = d(1,8)-d(1,10);
p(1,2) = d(1,6)-d(1,8);
p(1,1) = d(1,4)-d(1,6);
h1 = bar(p,'stacked'); hold on;
%
%negative bars
p(1,4) = d(1,11);
p(1,3) = d(1,9)-d(1,11);
p(1,2) = d(1,7)-d(1,9);
p(1,1) = d(1,5)-d(1,7);
h2 = bar(p,'stacked');
%
%cosmetics
grid on;
set(gca,'XTickLabelMode','manual','XTickLabel',[]);
xlabel('CG Vertical Acceleration','FontSize',14);
ylabel('Acceleration (g''s)','FontSize',14);
title('Simulation Distributions','FontSize',14,'FontWeight','bold');
legend('90 %','99 %','99.9 %','Peak');
axis([0.5 1.5 -3 3]);
```

APPENDIX C - ADDITIONAL COURSE DATA

This appendix presents additional data for Test Course A at both 10 and 12 mph nominal speeds, and Test Course B at 15 mph nominal speed. Due to the normal distribution of the ground profile, the Test Course B data (runs 10 and 13) were used for the experimental analysis of the surge brake effects in Section 5. However, Test Course A was determined to cause the fatigue failures of the trailer drawbar. The ground elevation profile of Test Course A is not normally distributed, as shown previously in Figure B5, and thus standard statistics do no apply.

C.1 TEST COURSE A (10 mph)

Experimental data from runs #37 (brakes disabled) and #27 (brakes enabled) are presented in this section. The nominal speed was 10 mph.

C.1.1 Strain-Gauge Data

The principal strains and rotation angle were calculated from the measured strain gauge data according to the previously defined procedures. Figure C1 shows the average principal strains for each of the eight rosette positions. Unlike the 15 mph (nominal) case shown in Figure 20, this shows that the strains are typically higher for the case with the brakes enabled, particularly at the lower angle strain rosette (FE node #471). This also appears in Figure C2, showing standard deviations in the data, and Figure C3, showing RMS values of the data. Finally, the statistical distributions of the data, shown in Figure C4 for the 1st principal strain, and Figure C5 for the 2nd principal strain, show larger values for the brakes enabled case, again primarily at the lower angle strain rosette.

TABLE C1 - PRINCIPAL STRAIN AMPLITUDE DISTRIBUTION DATA (BRAKES DISABLED, 10 MPH)

Description		Ave	Std Dev	Rms	+Peak	-Peak	+99.9	-99.9	+99	-99	+90	-90
Btm Cntr	(ε_1)	211.313	94.411	231.445	656.153	-1.889	647.194	0.197	555.142	4.498	370.847	55.938
#424	(ε_2)	-65.798	28.123	71.556	0.717	-274.17	-2.429	-250.61	-7.916	-178.70	-25.310	-114.48
	(α)	-0.835	4.433	4.511	44.312	-44.820	42.134	-41.281	20.423	-17.349	3.991	-5.709
Btm Cntr Aft	(ε_1)	245.520	111.923	269.827	761.814	-13.162	754.749	-10.146	646.828	-4.707	435.968	61.196
#425	(ε_2)	-101.97	40.795	109.824	-4.784	-318.02	-9.902	-302.87	15.273	-255.02	-41.071	-172.24
	(α)	-0.766	4.208	4.277	44.808	-44.513	42.924	-40.157	19.213	-17.731	3.687	-5.057
Btm Edge	(ε_1)	157.796	71.284	173.150	491.427	15.653	483.987	-12.675	420.652	-6.151	281.552	44.004
#383	(ε_2)	-81.727	29.881	87.019	-13.763	-226.81	-18.313	-216.77	-22.123	-187.92	-36.581	-136.52
	(α)	4.372	5.840	7.295	44.924	-44.955	43.649	-44.405	30.941	-24.825	12.346	-0.583
Btm Edge Aft	(ε_1)	169.730	85.132	189.883	591.916	-5.986	582.309	0.684	496.019	9.015	324.901	39.092
#382	(ε_2)	-42.348	34.127	54.387	80.863	-296.38	70.871	-269.49	33.453	-170.18	5.646	-102.43
	(α)	-0.084	4.907	4.908	44.927	-44.933	43.296	-42.057	25.796	-27.462	4.237	-2.640
Top Plate	(ε_1)	14.262	9.210	16.977	78.971	-6.740	75.559	-3.480	59.277	-2.109	29.330	0.904
#531	(ε_2)	-9.771	4.533	10.771	-1.060	-66.656	-2.219	-58.496	-3.453	-38.353	-5.549	-14.997
	(α)	-14.754	13.735	20.158	44.027	-44.557	43.609	-44.359	40.778	-43.382	21.448	-28.148
Btm Plate	(ε_1)	24.612	2.606	24.750	36.894	13.877	34.395	15.581	31.667	17.223	28.853	20.347
#504	(ε_2)	-8.075	4.219	9.111	10.668	-33.485	8.897	-31.611	6.547	-26.567	-1.613	15.603
	(α)	29.286	4.049	29.565	41.936	0.240	39.521	6.822	37.739	15.861	35.350	22.029
Ang. Lower	(ε_1)	185.979	108.768	215.450	612.372	-1.648	577.322	1.427	499.017	6.646	381.425	27.335
#471	(ε_2)	-24.805	36.005	43.722	11.463	-517.49	8.264	-438.37	4.639	-235.44	-1.053	-77.172
	(α)	1.163	12.379	12.433	44.732	-44.97	44.591	-44.890	42.161	-42.561	23.584	-20.553
Ang. Upper	(ε_1)	52.050	23.156	56.969	284.188	-2.884	217.158	0.601	114.398	3.656	91.655	16.538
#469	(ε_2)	-172.78	92.659	196.059	-0.675	-529.74	-1.329	-525.45	-6.463	-481.552	-30.864	-350.640
	(α)	11.752	7.407	13.891	44.704	-44.69	43.885	-44.045	38.036	-33.842	23.162	5.376

TABLE C2 - PRINCIPAL STRAIN AMPLITUDE DISTRIBUTION DATA (BRAKES ENABLED, 10 MPH)

Description		Ave	Std Dev	Rms	+Peak	-Peak	+99.9	-99.9	+99	-99	+90	-90
Btm Cntr	(ε_1)	211.830	88.333	229.509	659.485	-11.676	648.027	17.612	546.706	25.602	382.803	72.100
#424	(ε_2)	-68.186	28.069	73.738	-13.449	-365.78	-17.721	-337.80	-22.875	-187.42	-33.102	-120.58
	(α)	-7.482	8.237	11.128	44.925	-44.740	44.867	-44.560	37.726	-40.413	0.326	-20.152
Btm Cntr Aft	(ε_1)	270.603	105.346	290.385	792.063	-16.291	775.795	11.685	661.303	34.768	472.514	101.847
#425	(ε_2)	-82.677	43.247	93.305	-2.154	-415.93	-4.812	-387.07	-8.822	-259.25	-22.697	-163.27
	(α)	5.023	6.781	8.439	44.990	-44.997	43.927	-43.500	37.003	-27.658	14.523	-1.221
Btm Edge	(ε_1)	162.067	71.761	177.244	516.112	-18.980	503.018	-3.399	427.513	1.333	300.189	45.800
#383	(ε_2)	-77.388	35.207	85.021	9.640	-312.63	3.075	-296.75	-4.545	-202.13	-23.829	-134.91
	(α)	0.2314	6.631	6.635	44.973	-44.773	43.333	-42.804	29.648	-26.984	9.8992	-7.911
Btm Edge Aft	(ε_1)	188.842	89.691	209.059	695.219	-82.956	645.314	-20.143	532.851	-5.270	351.737	48.064
#382	(ε_2)	-72.158	43.206	84.104	101.125	-473.23	74.561	-412.20	30.321	-230.33	-8.893	-139.60
	(α)	-1.385	2.218	2.615	43.922	-44.916	33.848	-34.806	5.879	-9.193	-0.099	-2.673
Top Plate	(ε_1)	21.8769	9.729	23.943	90.659	-3.872	84.664	-1.749	66.275	2.706	39.701	9.607
#531	(ε_2)	-18.633	7.855	20.221	-5.824	-139.02	-8.629	-123.34	-9.898	-79.606	-12.849	-28.054
	(α)	-8.369	5.482	10.005	43.140	-44.096	19.358	-31.873	5.239	-26.411	1.118	-17.278
Btm Plate	(ε_1)	9.039	2.866	9.483	26.814	-0.446	25.466	2.319	19.767	3.123	14.069	5.108
#504	(ε_2)	-1.487	3.252	3.576	11.214	-38.804	8.497	-33.584	5.246	-22.165	2.702	-5.953
	(α)	8.785	18.355	20.349	44.992	-44.999	44.919	-44.838	42.706	-44.630	35.193	-26.987
Ang. Lower	(ε_1)	315.342	135.460	343.205	921.711	-26.391	870.861	-20.700	650.259	-4.010	512.841	69.377
#471	(ε_2)	-51.98	34.661	62.475	30.099	-712.20	13.562	-629.08	4.212	-186.30	-11.177	-91.126
	(α)	-5.660	6.047	8.282	44.992	-44.986	43.652	-43.536	30.676	-28.563	1.8786	-11.323
Ang. Upper	(ε_1)	47.043	22.566	52.176	470.730	4.691	381.231	6.720	128.830	12.637	81.208	23.536
#469	(ε_2)	-163.84	86.677	185.357	-12.283	-533.56	-18.826	-526.65	-32.683	-474.987	-52.003	-347.349
	(α)	16.774	18.023	24.621	44.999	-44.989	44.979	-44.768	44.239	-44.009	38.177	-32.767

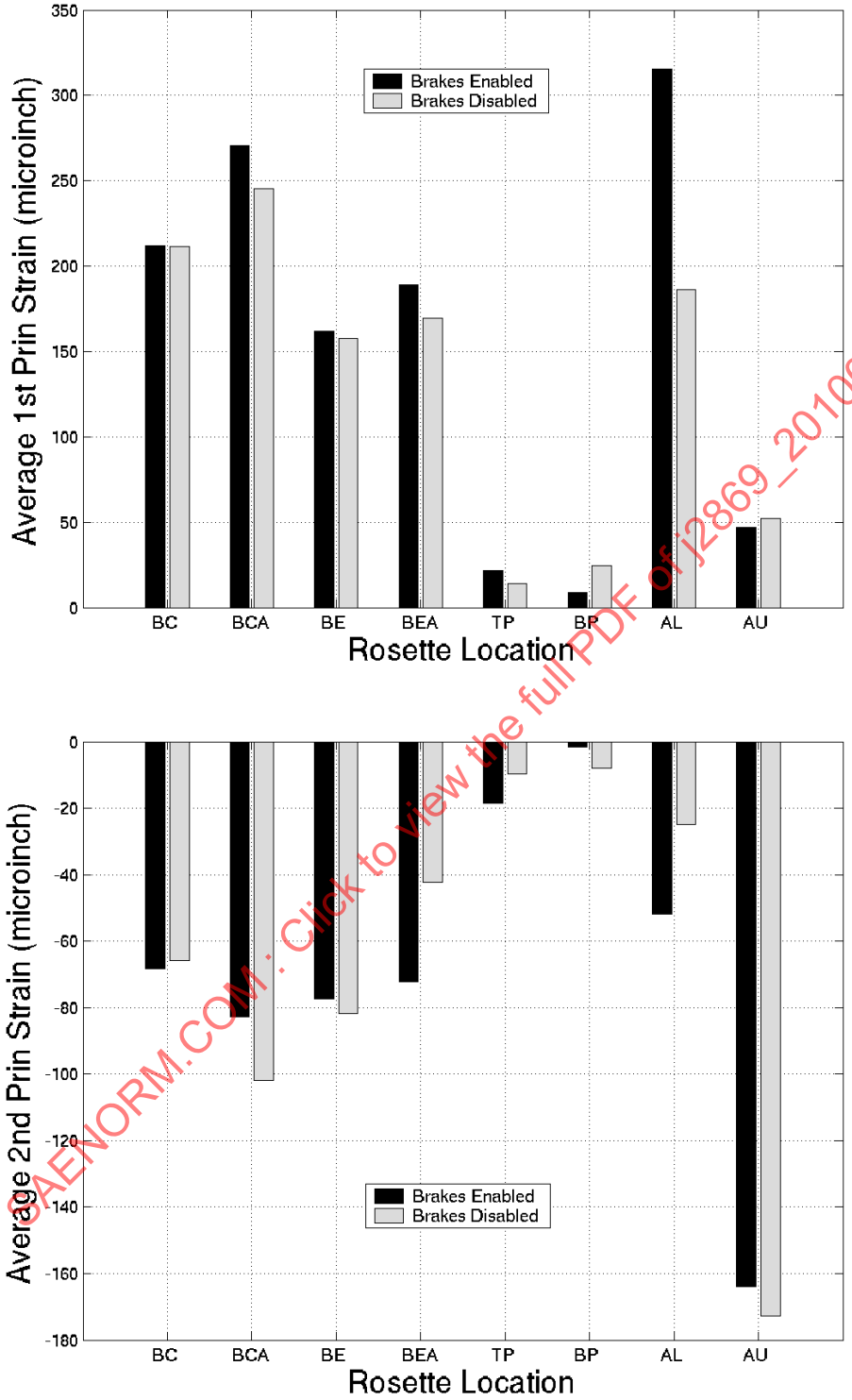

FIGURE C1 - AVERAGE PRINCIPAL STRAINS (10 MPH)

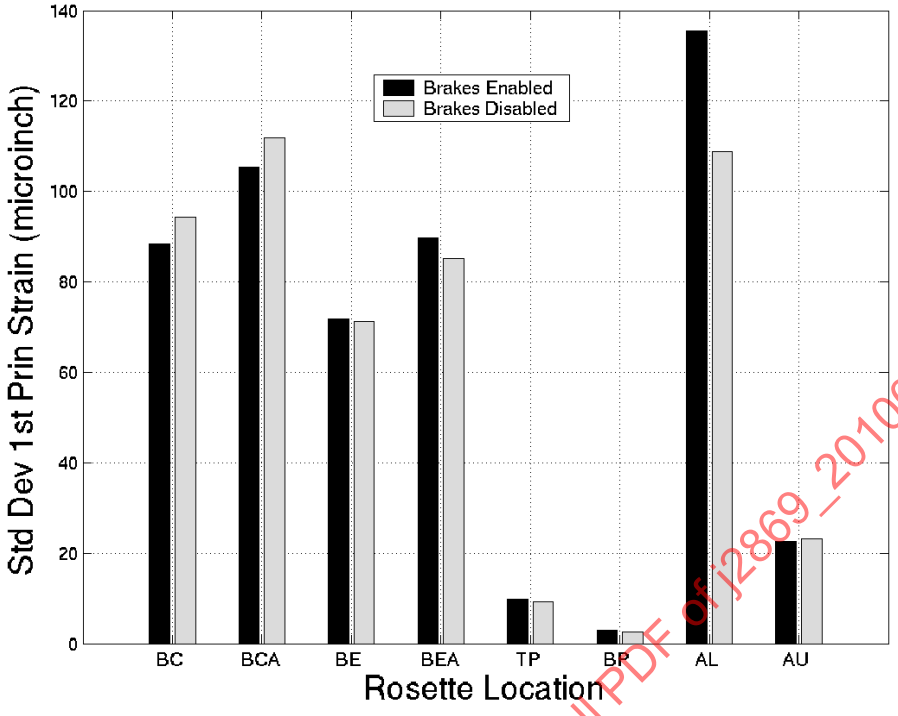

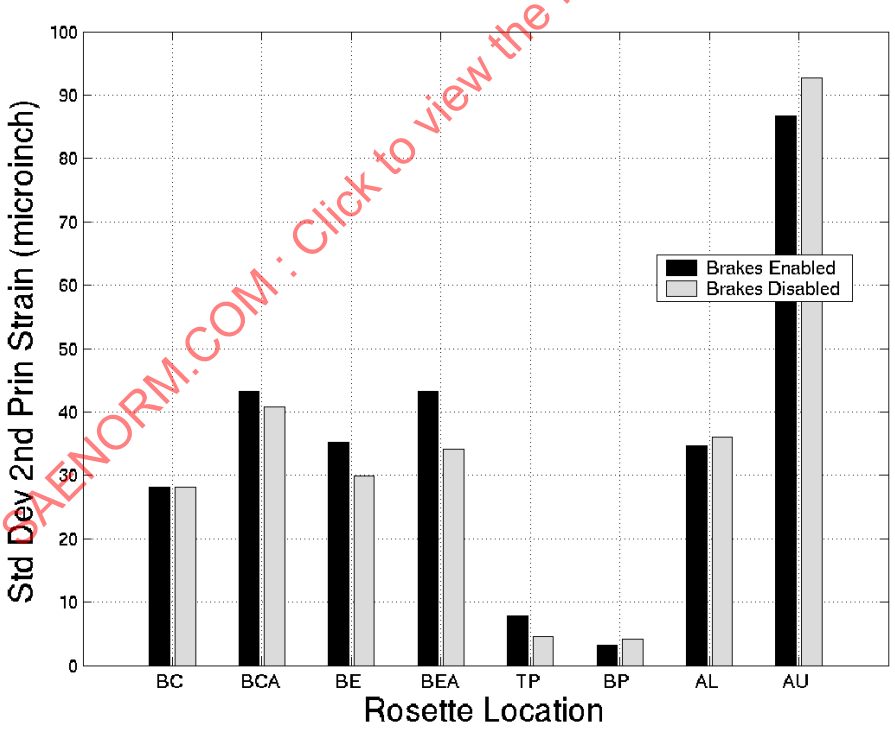

FIGURE C2 - PRINCIPAL STRAIN STANDARD DEVIATIONS (10 MPH)

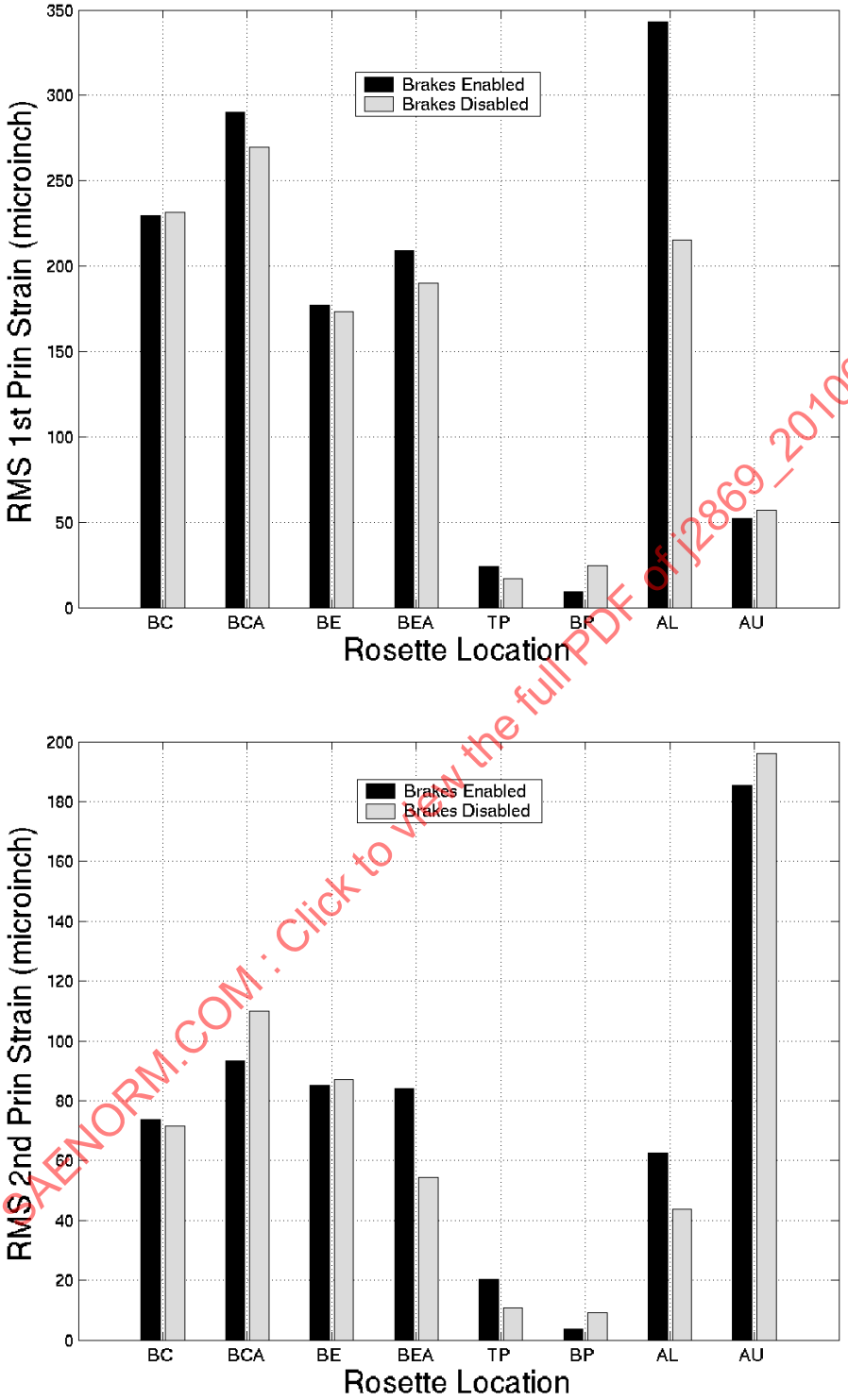

FIGURE C3 - RMS VALUES OF PRINCIPAL STRAINS (10 MPH)

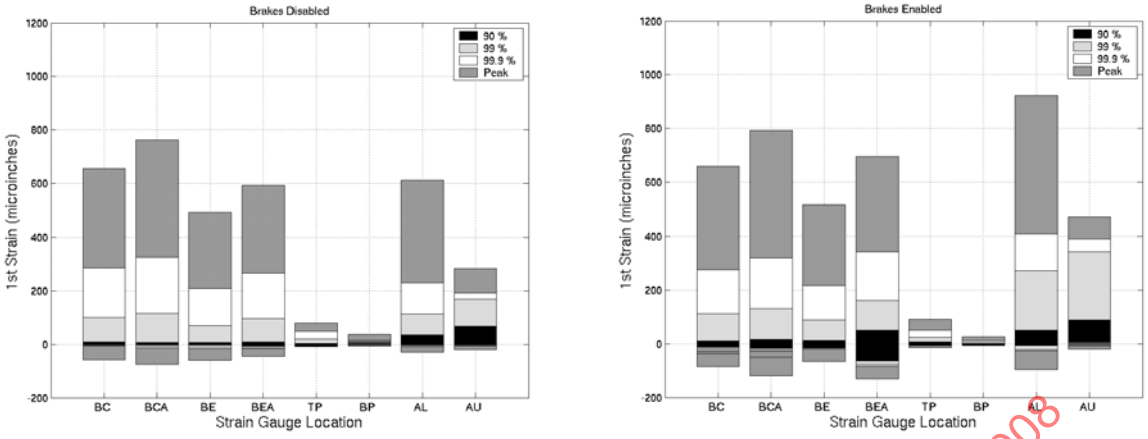

FIGURE C4 - DISTRIBUTION OF 1ST PRINCIPAL STRAINS (10 MPH)

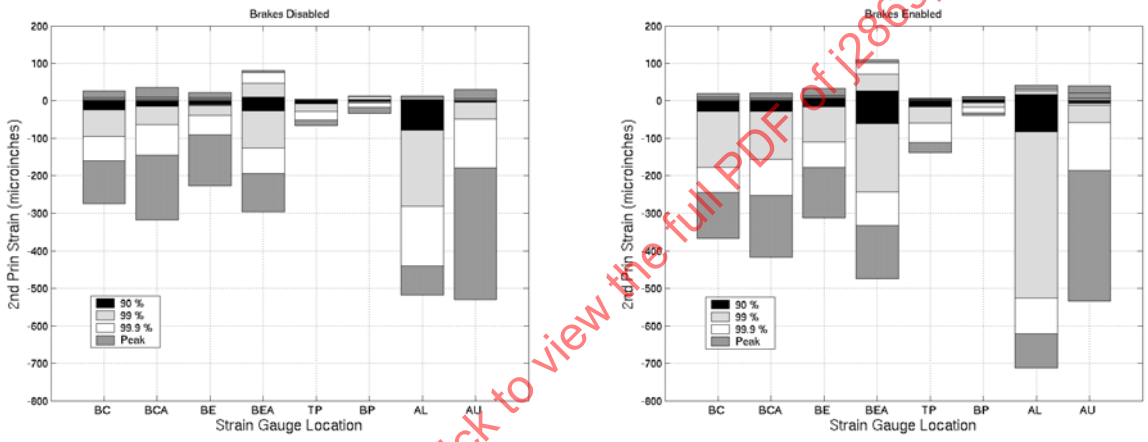

FIGURE C5 - DISTRIBUTION OF 2ND PRINCIPAL STRAINS (10 MPH)

C.1.2 Accelerometer Data

There were seven triaxial, and four vertical accelerometers mounted on the trailer. Statistics about the accelerometer data amplitude distribution is given in Table C3 for the case with disabled brakes, and Table C4 with enabled brakes. The vertical response is denoted as (V), the transverse response (T), and the longitudinal response (L). Not much is discernable from the average (Figures C6 through C8), standard deviation (Figures C9 through C11), or RMS (Figures C12 through C14) plots. However, examining the statistical distributions shown in Figures C15 through C17, the peak accelerations of the lunette were substantially greater for the lunette when the brakes were enabled, especially in the longitudinal direction.

TABLE C3 - ACCELERATION AMPLITUDE DISTRIBUTION DATA (BRAKES DISABLED, 10 MPH) IN G'S

Description		Ave	Std Dev	RMS	+Peak	-Peak	+99.9	-99.9	+99	-99	+90	-90
Lunette	(V)	-0.1021	0.3188	0.3347	3.0250	-3.3830	2.0302	-2.1760	1.0330	-1.0540	0.3900	-0.5480
	(T)	0.0155	0.2162	0.2167	1.3500	-0.7810	1.1430	-0.6440	0.8000	-0.5160	0.3780	-0.3200
	(L)	0.0381	0.2747	0.2773	2.2120	-1.9080	1.4933	-1.2600	0.9090	-0.7620	0.4860	-0.3800
Tongue	(V)	0.0423	0.2097	0.2139	1.2160	-0.7520	0.9590	-0.6170	0.7580	-0.4940	0.3890	-0.2930
	(T)	0.1772	0.2512	0.3074	12.1330	-6.7280	1.4720	-2.0101	0.8170	-0.5290	0.5160	-0.1570
	(L)	0.0687	0.1635	0.1774	8.3970	-6.2780	1.7779	-1.8685	0.5470	-0.3780	0.2220	-0.0780
CG	(V)	-0.0004	0.1221	0.1221	5.1430	-4.2810	0.8922	-0.7182	0.3280	-0.3140	0.1910	-0.1760
	(T)	-0.0779	0.2394	0.2518	5.6680	-4.4640	1.5078	-1.9474	0.5720	-0.7900	0.2760	-0.4230
	(L)	0.0036	0.1219	0.1220	3.5080	-2.8970	0.9422	-1.1340	0.4100	-0.3620	0.1680	-0.1550
CS Aft.	(V)	0.0094	0.1020	0.1024	1.9980	-1.4810	0.4883	-0.4427	0.3150	-0.2790	0.1880	-0.1510
	(T)	0.0641	0.2060	0.2157	1.8990	-1.0610	1.0592	-0.5980	0.7210	-0.4470	0.4190	-0.2560
	(L)	-0.0125	0.0944	0.0953	0.5480	-0.6450	0.4640	-0.4180	0.2850	-0.3110	0.1420	-0.1560
CS Aft.	(V)	0.0340	0.0922	0.0982	0.9400	-0.5270	0.4770	-0.3110	0.3110	-0.2310	0.2030	-0.1150
	(T)	-0.0330	0.2532	0.2553	3.2200	-2.4380	1.2250	-1.3858	0.8220	-0.7500	0.3810	-0.4150
	(L)	-0.0090	0.1281	0.1284	1.7160	-1.2370	0.6440	-0.6900	0.4150	-0.4060	0.1960	-0.1980
RS For.	(V)	0.0329	0.1698	0.1730	2.7560	-1.1620	0.8290	-0.7280	0.5540	-0.4809	0.3100	-0.2410
	(T)	0.0375	0.3705	0.3724	3.4520	-2.2070	2.1796	-1.3783	1.4500	-0.8910	0.6230	-0.5240
	(L)	0.0153	0.3031	0.3035	4.3840	-4.1390	1.4259	-1.4772	0.8590	-0.8640	0.4840	-0.4690
RS Aft	(V)	-0.0349	0.1620	0.1657	1.9210	-1.1160	0.7580	-0.7440	0.4530	-0.5180	0.2270	-0.2920
	(T)	-0.0086	0.2791	0.2792	3.6350	-2.3740	1.3607	-1.4420	0.8629	-0.8250	0.4470	-0.4320
	(L)	0.0000	0.1344	0.1344	2.1030	-2.1340	0.6978	-0.7440	0.4330	-0.4080	0.2090	-0.2060
CS Axle	(V)	-0.0362	0.1676	0.1714	1.6730	-1.7480	0.8822	-0.6880	0.4520	-0.5270	0.2300	-0.3150
CS Frame	(V)	-0.0117	0.3361	0.3363	2.0070	-1.5510	1.7552	-1.1312	1.1650	-0.8870	0.5300	-0.5400
RS Axle	(V)	0.0378	0.2599	0.2626	2.5270	-3.6950	1.2454	-1.2160	0.7870	-0.7660	0.4490	-0.3780
RS Frame	(V)	-0.0133	0.1441	0.1447	1.4010	-0.6950	0.7414	-0.5760	0.4030	-0.4480	0.2150	-0.2600

TABLE C4 - ACCELERATION AMPLITUDE DISTRIBUTION DATA (BRAKES ENABLED, 10 MPH) IN G'S

Description		Ave	Std Dev	RMS	+Peak	-Peak	+99.9	-99.9	+99	-99	+90	-90
Lunette	(V)	-0.0560	0.3456	0.3501	2.4810	-2.7400	1.7250	-1.7600	1.0640	-1.0100	0.5110	-0.5830
	(T)	0.0131	0.2448	0.2452	1.3790	-0.9560	1.0510	-0.8210	0.7030	-0.5900	0.4330	-0.3680
	(L)	0.0088	0.3256	0.3258	2.7690	-2.4510	2.1763	-1.6930	1.4131	-0.9970	0.4970	-0.4410
Tongue	(V)	0.0350	0.2489	0.2513	1.5760	-1.2080	1.2208	-0.8350	0.8850	-0.5940	0.4360	-0.3420
	(T)	0.0838	0.2923	0.3040	9.5960	-8.7650	2.3571	-3.1758	0.8790	-0.7406	0.4590	-0.2570
	(L)	-0.1961	0.3012	0.3594	11.0350	-11.3670	3.3155	-4.1492	0.7310	-1.1870	0.0180	-0.3750
CG	(V)	0.0381	0.3361	0.3383	18.8040	-24.6460	3.7819	-3.7301	0.9590	-1.0260	0.2830	-0.2140
	(T)	0.0476	0.2468	0.2513	5.0110	-4.6870	1.9812	-2.2228	0.7810	-0.6960	0.4010	-0.2780
	(L)	-0.0028	0.2189	0.2189	8.4520	-14.1210	2.0255	-2.1680	0.6590	-0.6140	0.2270	-0.1930
CS For.	(V)	-0.0446	0.1095	0.1183	1.8400	-1.7180	0.7280	-0.7030	0.3110	-0.3980	0.1310	-0.2030
	(T)	0.0559	0.2471	0.2534	3.2930	-2.8930	1.3732	-1.1346	0.8210	-0.5600	0.4630	-0.3110
	(L)	-0.0381	0.1234	0.1292	1.2290	-0.9680	0.8014	-0.6510	0.4180	-0.4160	0.1600	-0.2160
CS Aft.	(V)	0.0333	0.0978	0.1033	1.5470	-1.3030	0.7477	-0.4783	0.3560	-0.2400	0.2000	-0.1120
	(T)	-0.0484	0.3207	0.3243	2.6830	-2.6430	1.6843	-1.8078	1.0080	-1.0050	0.4630	-0.5350
	(L)	-0.0085	0.1616	0.1618	2.4790	-2.2200	1.1270	-0.8470	0.5480	-0.4820	0.2370	-0.2460
RS For.	(V)	0.0120	0.1872	0.1876	2.3510	-2.6040	1.1430	-0.9204	0.6020	-0.5220	0.3100	-0.2830
	(T)	-0.0177	0.4199	0.4203	3.2390	-3.1440	2.3550	-1.4916	1.3880	-1.1170	0.6600	-0.6570
	(L)	0.0388	0.3365	0.3387	4.3560	-4.5840	2.3808	-1.6890	1.0260	-0.8850	0.5530	-0.4690
RS Aft	(V)	-0.0094	0.1796	0.1798	1.9580	-1.8720	1.1390	-0.8388	0.5520	-0.5220	0.2750	-0.2890
	(T)	-0.0529	0.3432	0.3472	3.4130	-3.9560	1.8904	-2.2790	1.0590	-1.0500	0.4940	-0.5480
	(L)	0.0899	0.1672	0.1898	1.8200	-2.2530	1.3700	-0.8438	0.6460	-0.3970	0.3490	-0.1560
CS Axle	(V)	-0.0605	0.1785	0.1885	3.0180	-2.4870	1.1256	-0.9420	0.5230	-0.5860	0.2160	-0.3380
CS Frame	(V)	-0.0327	0.3914	0.3928	3.5470	-2.5360	2.2460	-1.7706	1.3390	-1.1280	0.5880	-0.6170
RS Axle	(V)	0.0364	0.3078	0.3100	4.3100	-4.1380	2.1263	-1.7074	0.9940	-0.7980	0.5070	-0.4320
RS Frame	(V)	-0.0356	0.1512	0.1553	2.6640	-1.4460	1.0450	-0.7080	0.4800	-0.4690	0.2020	-0.2770

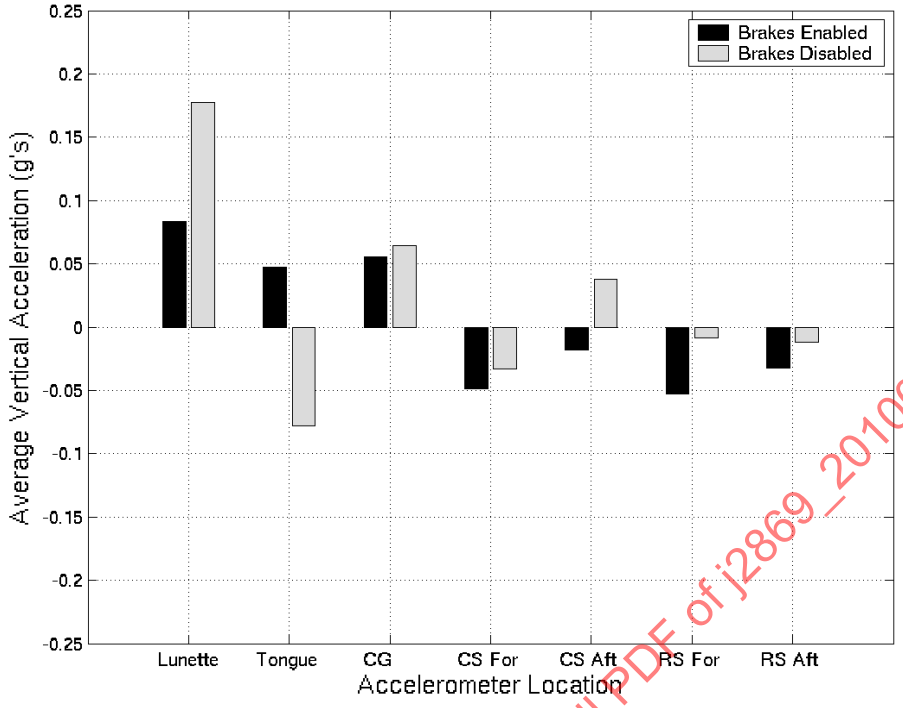

FIGURE C6 - AVERAGE VERTICAL ACCELERATIONS FOR SEVERAL TRAILER LOCATIONS (10 MPH)

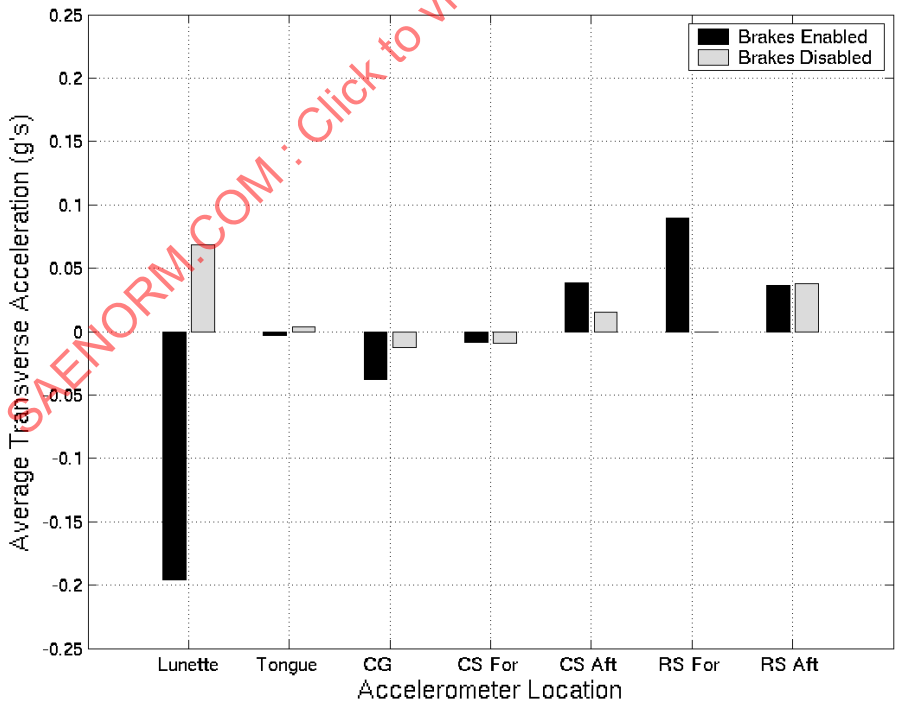

FIGURE C7 - AVERAGE TRANSVERSE ACCELERATIONS FOR SEVERAL TRAILER LOCATIONS (10 MPH)

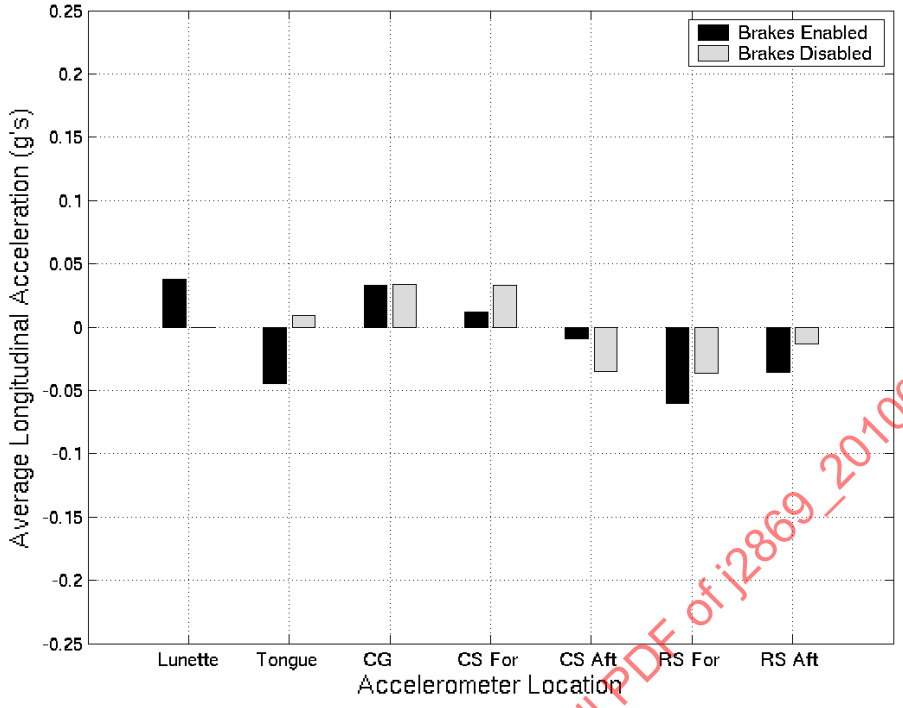

FIGURE C8 - AVERAGE LONGITUDINAL ACCELERATIONS FOR SEVERAL TRAILER LOCATIONS (10 MPH)

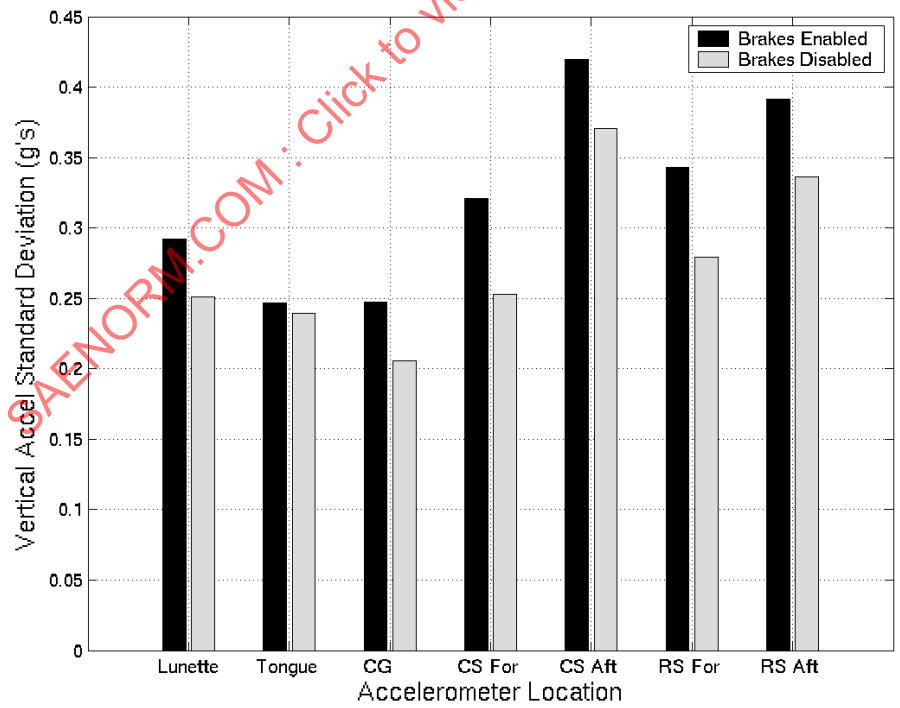

FIGURE C9 - VERTICAL ACCELERATION STANDARD DEVIATION FOR SEVERAL TRAILER LOCATIONS (10 MPH)

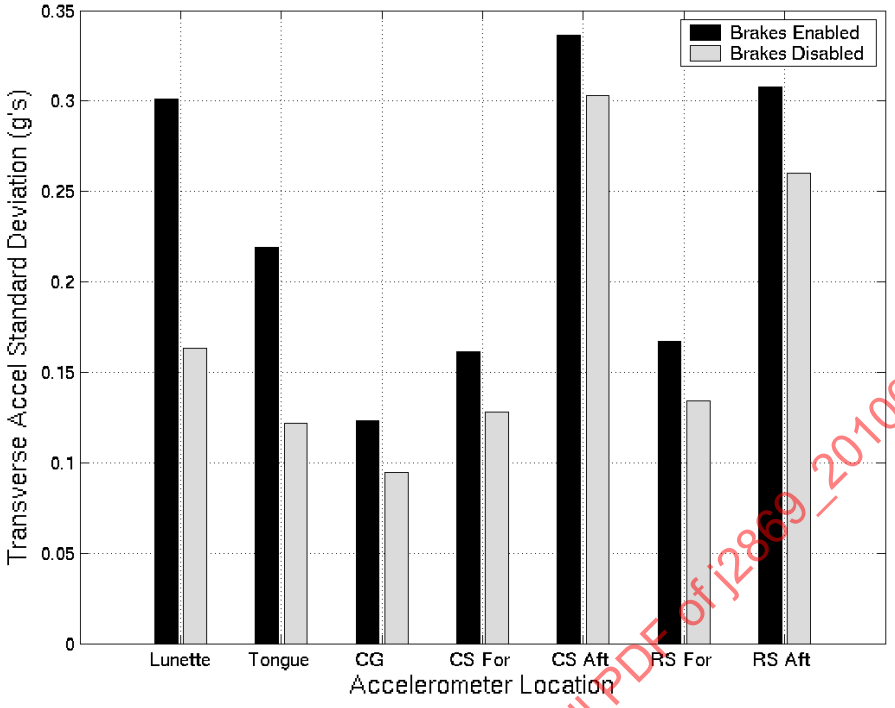

FIGURE C10 - TRANSVERSE ACCELERATION STANDARD DEVIATION FOR SEVERAL TRAILER LOCATIONS (10 MPH)

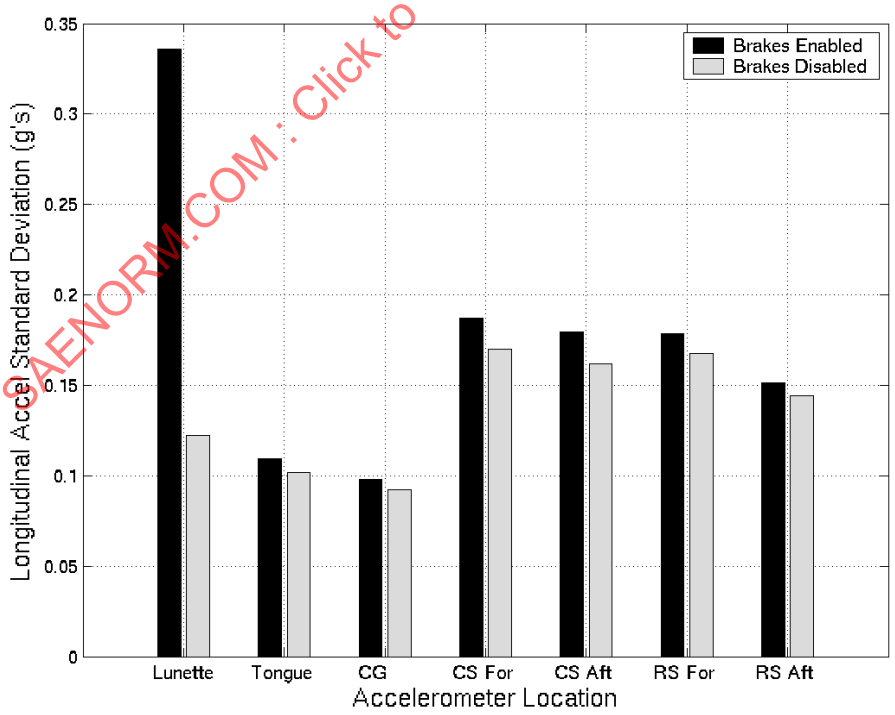

FIGURE C11 - LONGITUDINAL ACCELERATION STANDARD DEVIATION FOR SEVERAL TRAILER LOCATIONS (10 MPH)

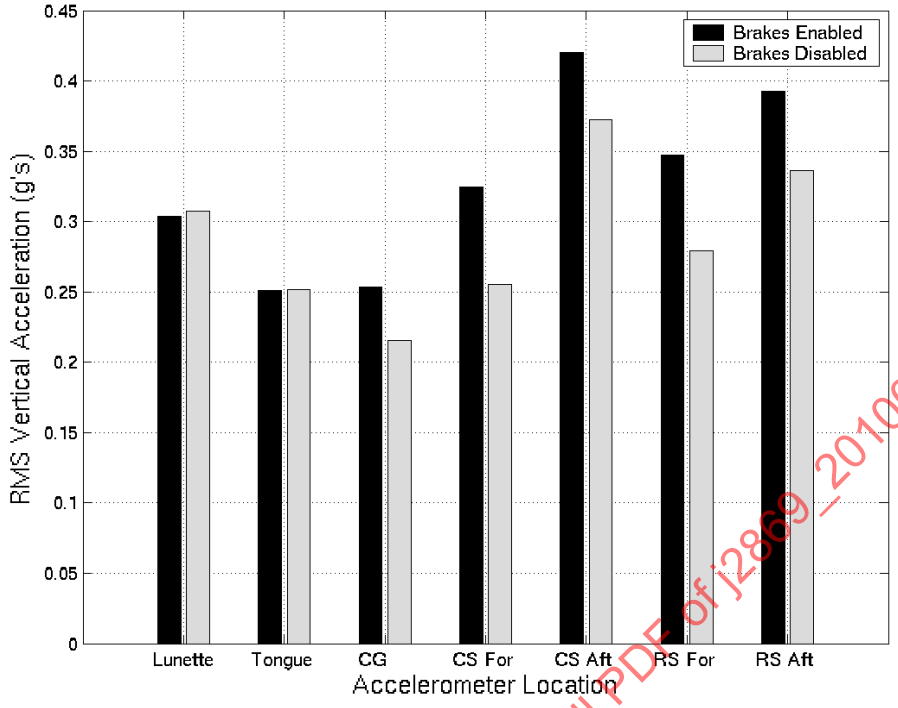

FIGURE C12 - VERTICAL RMS ACCELERATIONS FOR SEVERAL TRAILER LOCATIONS (10 MPH)

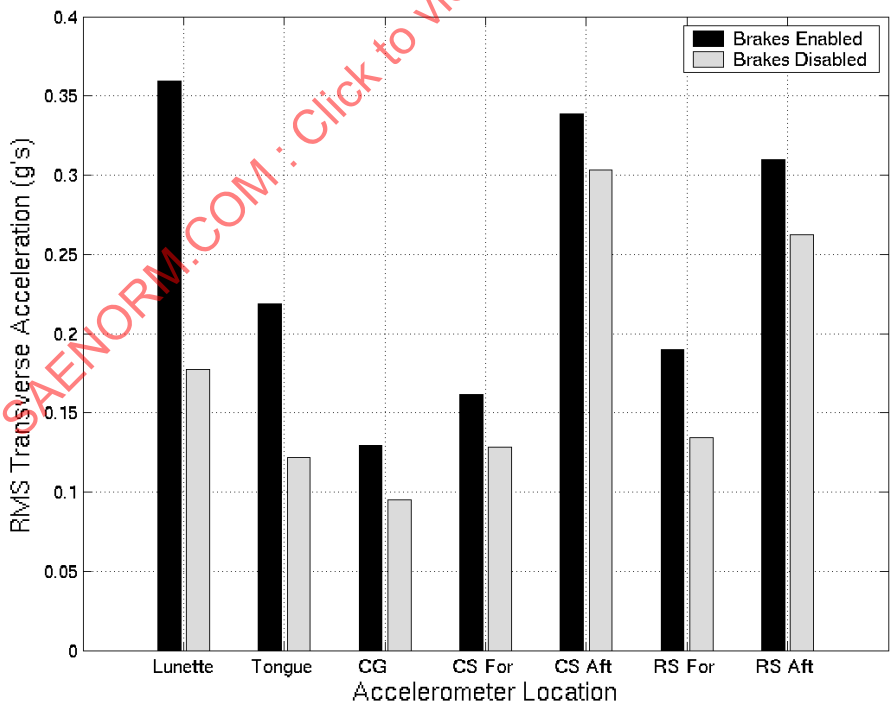

FIGURE C13 - TRANSVERSE RMS ACCELERATIONS FOR SEVERAL TRAILER LOCATIONS (10 MPH)

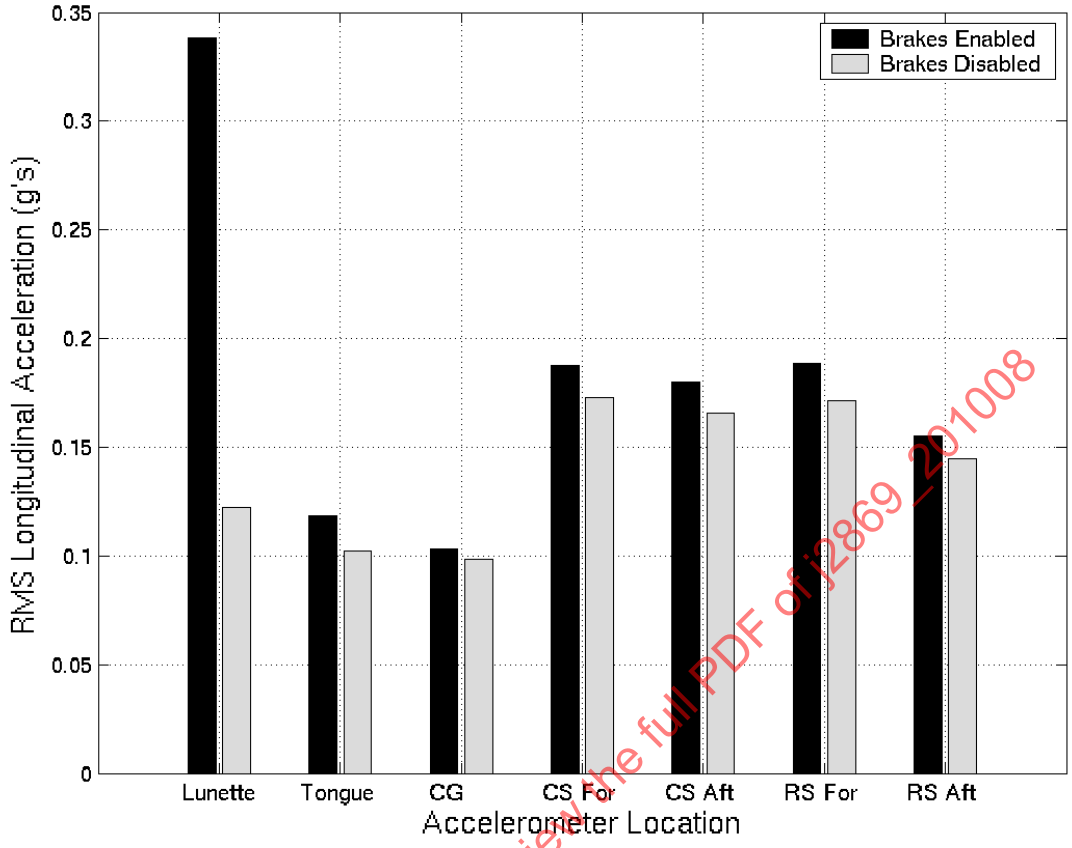

FIGURE C14 - LONGITUDINAL RMS ACCELERATIONS FOR SEVERAL TRAILER LOCATIONS (10 MPH)

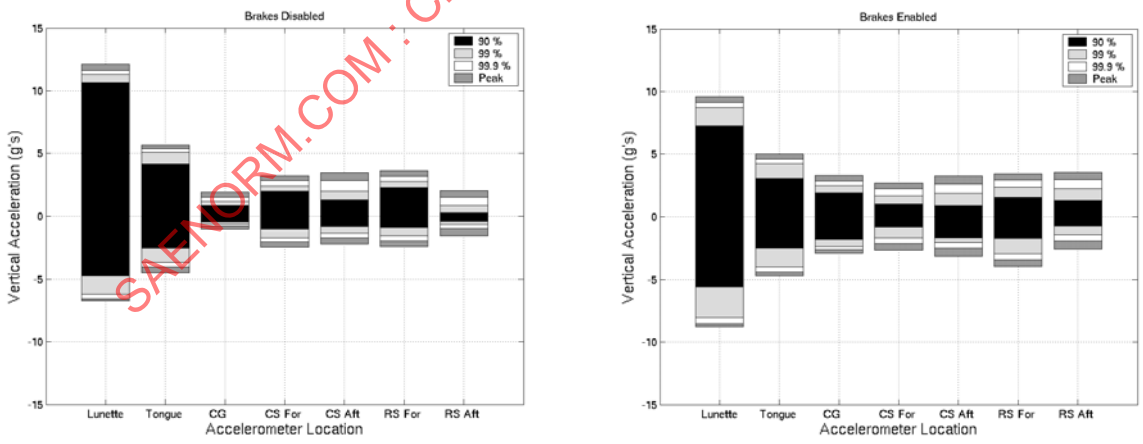

FIGURE C15 - VERTICAL ACCELERATION STATISTICS FOR SEVERAL TRAILER LOCATIONS (10 MPH)

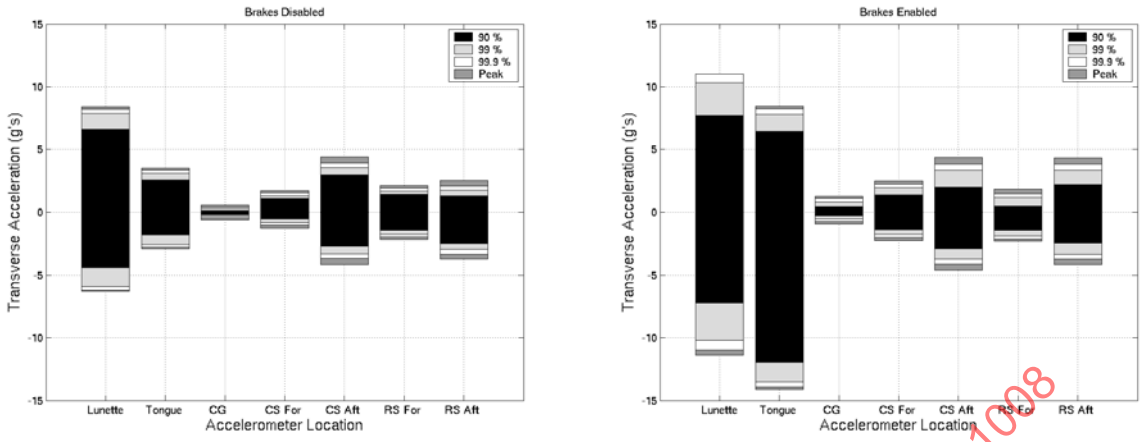

FIGURE C16 - TRANSVERSE ACCELERATION STATISTICS FOR SEVERAL TRAILER LOCATIONS (10 MPH)

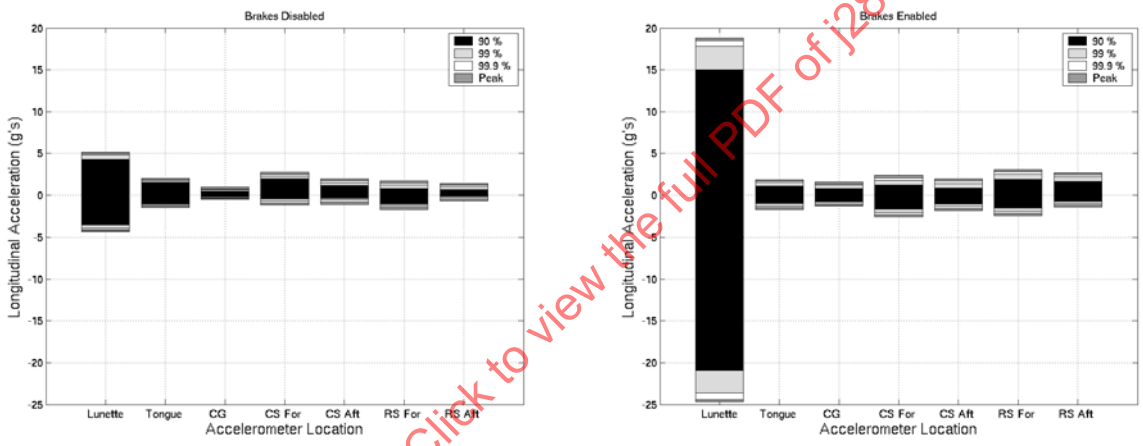

FIGURE C17 - LONGITUDINAL ACCELERATION STATISTICS FOR SEVERAL TRAILER LOCATIONS (10 MPH)

C.1.3 Rate-Gyro Data

Angular rate data for Test Course A is given in Table C5 for the braking system disabled, and in Table C6 for the brakes enabled. Since the course is straight, with elevation changes, the magnitude of the pitch rates should be much higher than the yaw or roll rates. However, for Figure C18, the average roll rate for the brakes enabled case is higher than the pitch rate. The standard deviation, and RMS values, shown in Figures C19 through C20, conform to expectations. Finally, Figure C21 shows the statistical distributions, which appear as expected, with a higher pitch rate, than roll or yaw.

TABLE C5 - RATE-GYRO DISTRIBUTION DATA (BRAKES DISABLED, 10 MPH) IN DEG/SEC

Description	Ave	Std Dev	RMS	+Peak	-Peak	+99.9	-99.9	+99	-99	+90	-90
CG Pitch Rate	0.077	12.370	12.370	49.922	-46.108	49.518	-44.693	39.961	-36.108	21.829	-19.805
CG Roll Rate	-0.065	4.405	4.406	19.743	-19.970	19.191	-17.667	13.407	-13.191	7.071	-7.260
CG Yaw Rate	0.037	2.849	2.850	11.490	-10.599	11.299	-10.484	9.049	-7.852	4.928	-4.571

TABLE C6 - RATE-GYRO DISTRIBUTION DATA (BRAKES ENABLED, 10 MPH) IN DEG/SEC

Description	Ave	Std Dev	RMS	+Peak	-Peak	+99.9	-99.9	+99	-99	+90	-90
CG Pitch Rate	0.207	12.059	12.060	60.739	-54.474	59.790	-53.501	44.552	-33.813	19.494	-20.194
CG Roll Rate	0.248	6.192	6.197	29.432	-24.833	28.866	-23.640	22.028	-16.765	10.718	-8.771
CG Yaw Rate	-0.004	4.284	4.284	23.431	-18.419	23.035	-16.879	15.381	-10.269	7.370	-5.906

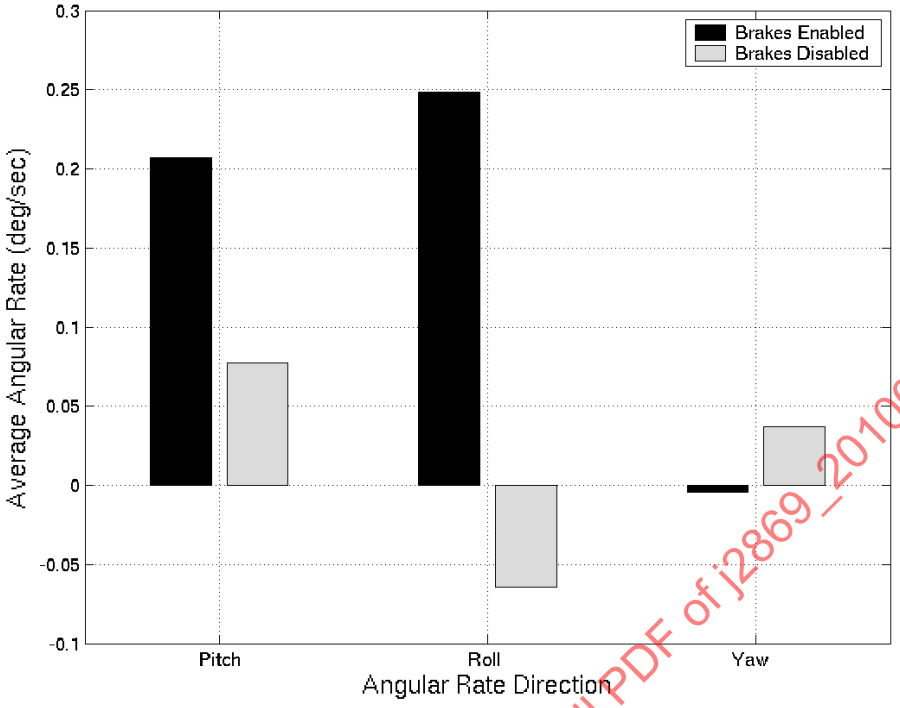

FIGURE C18 - AVERAGE RATE-GYRO ANGULAR RATES (10 MPH)

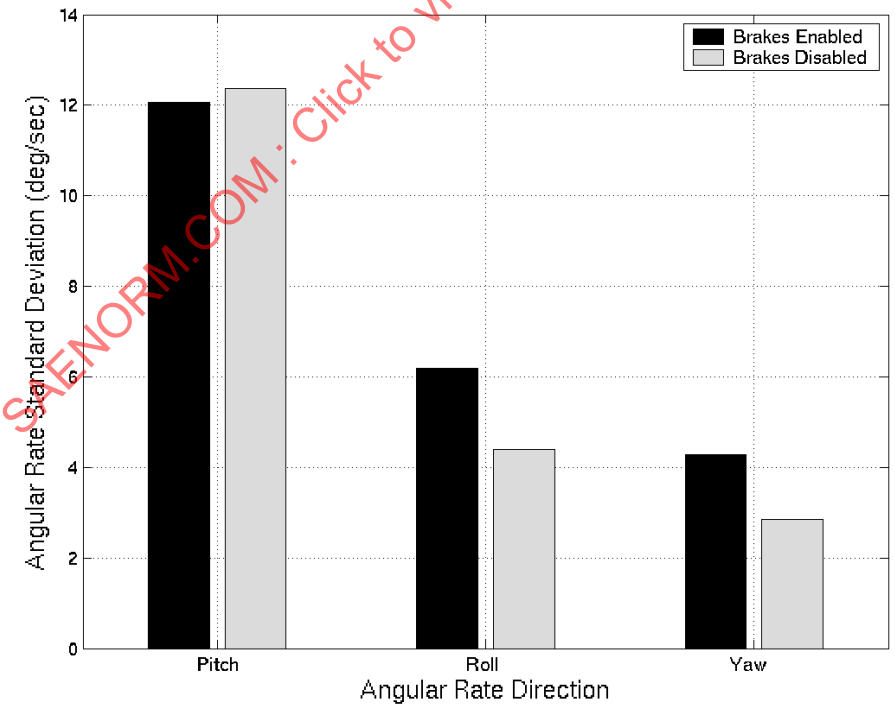

FIGURE C19 - RATE-GYRO ANGULAR STANDARD DEVIATIONS (10 MPH)

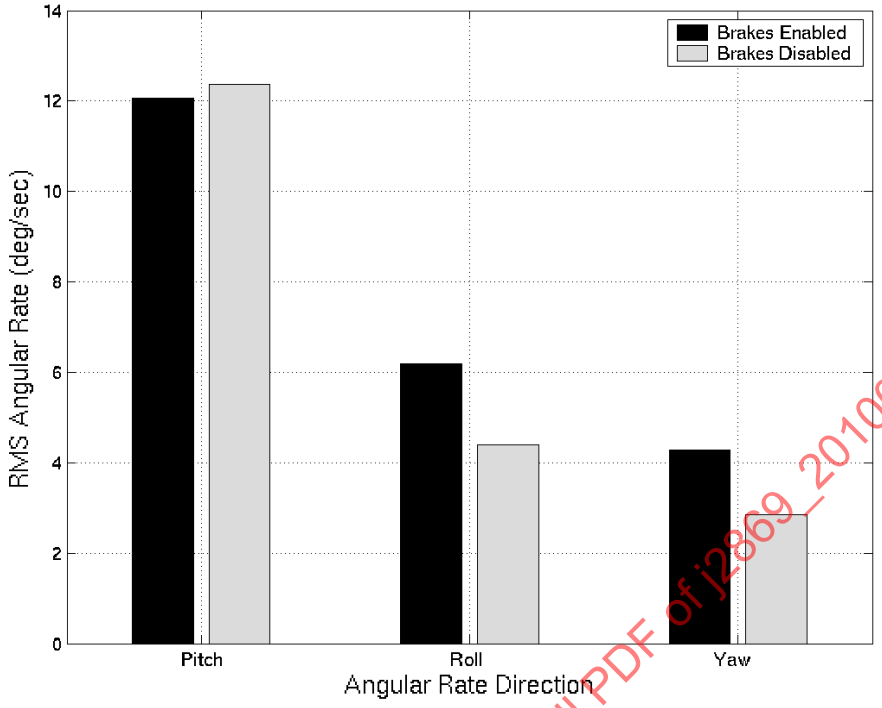

FIGURE C20 - RATE-GYRO RMS ANGULAR RATES (10 MPH)

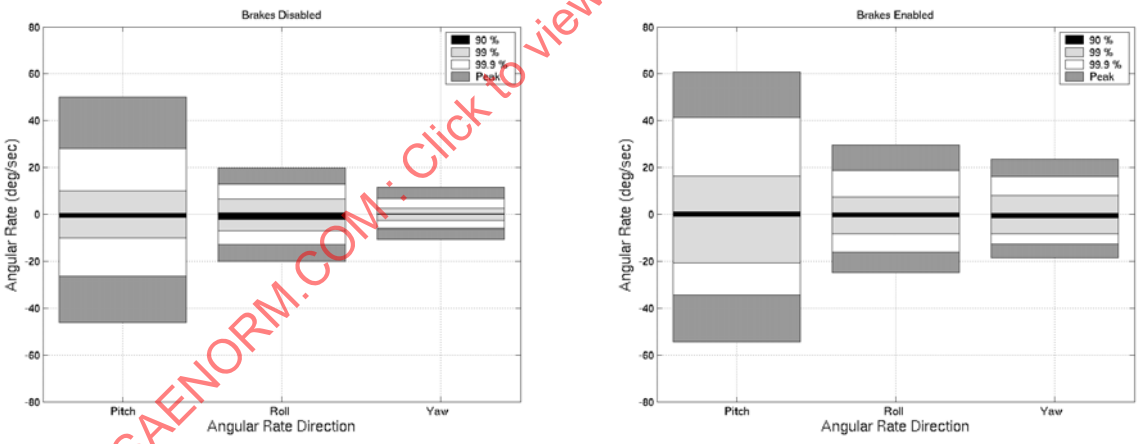

FIGURE C21 - RATE-GYRO ANGULAR RATE DISTRIBUTIONS (10 MPH)

C.1.4 Linear Displacement Transducer Data

The linear displacement transducer data shows the deflection of the trailer suspension on both the curbside and roadside. Table C7 presents the results for the braking system disabled, and Table C8 present the results for the brakes enabled. These are plotted in Figures C22 through C25. Any differences shown here are probably the result of either a difference in actual speeds during testing, or a different path on the course.

TABLE C7 - LINEAR DISPLACEMENT DISTRIBUTION DATA (BRAKES DISABLED, 10 MPH) IN INCHES

Description	Ave	Std Dev	RMS	+Peak	-Peak	+99.9	-99.9	+99	-99	+90	-90
CS Shock Displacement	0.0209	0.1149	0.1168	0.4550	-0.4800	0.4486	-0.4750	0.3820	-0.3540	0.2270	-0.1610
RS Shock Displacement	-0.0173	0.1174	0.1187	0.4580	-0.4910	0.4540	-0.4870	0.3180	-0.4460	0.1800	-0.2070

TABLE C8 - LINEAR DISPLACEMENT DISTRIBUTION DATA (BRAKES ENABLED, 10 MPH) IN INCHES

Description	Ave	Std Dev	RMS	+Peak	-Peak	+99.9	-99.9	+99	-99	+90	-90
CS Shock Displacement	0.0129	0.1344	0.1351	0.5900	-0.4060	0.5820	-0.4002	0.4560	-0.3364	0.2420	-0.2100
RS Shock Displacement	0.0181	0.1484	0.1495	0.5830	-0.5020	0.5760	-0.4910	0.4920	-0.4177	0.2730	-0.2310

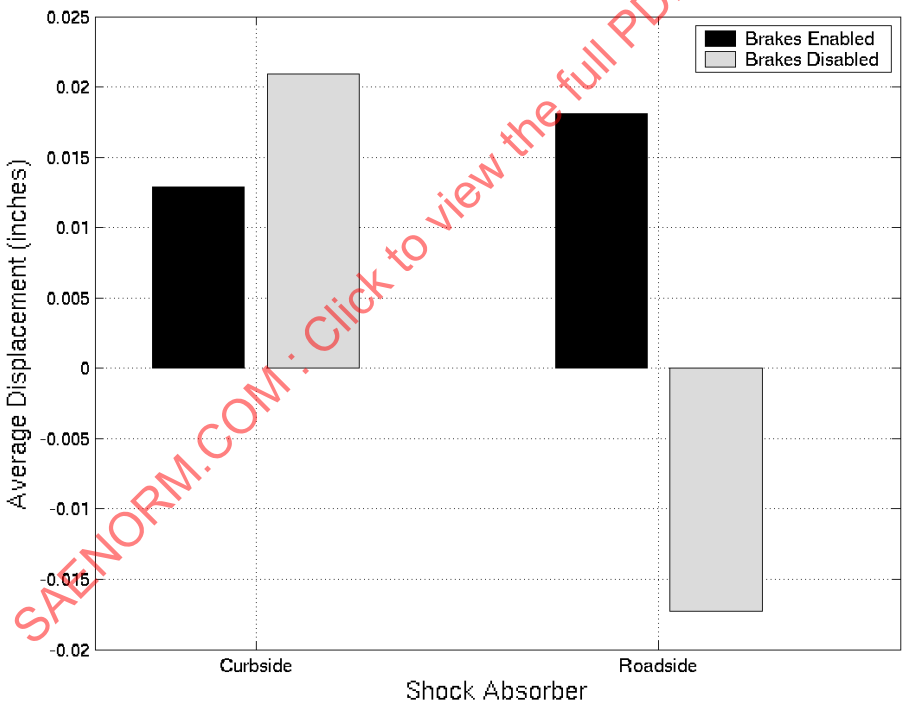

FIGURE C22 - LINEAR DISPLACEMENT AVERAGE VALUE (10 MPH)

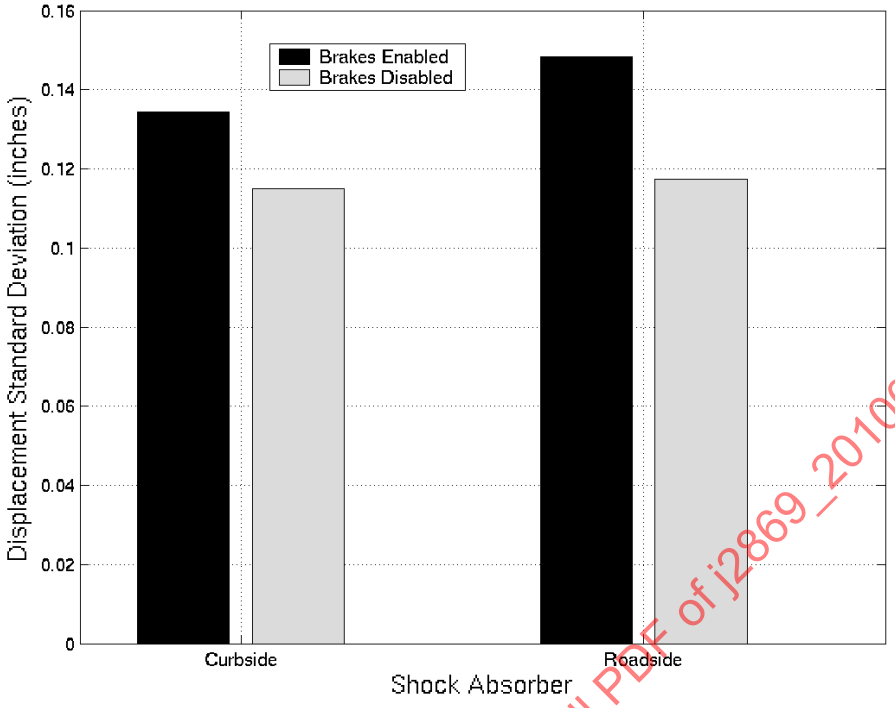

FIGURE C23 - LINEAR DISPLACEMENT STANDARD DEVIATION (10 MPH)

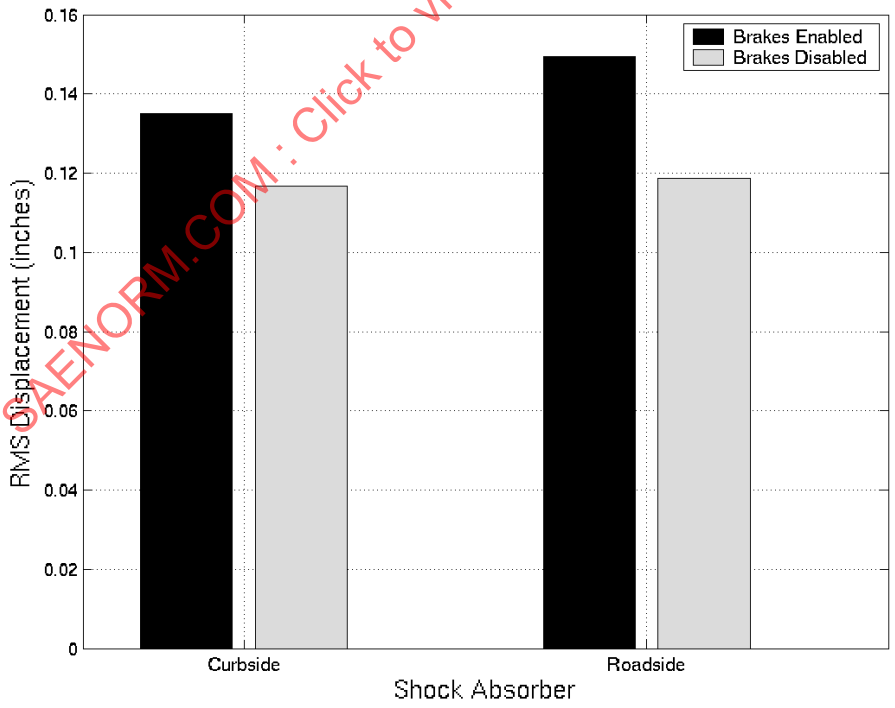

FIGURE C24 - LINEAR DISPLACEMENT RMS VALUE (10 MPH)